Quantum Transport and Nonlinear Interactions in Hybrid, Electronic, Photonic and Mechanical Systems

Doctoral thesis for obtaining the

academic degree Doctor of

Natural Science

submitted by

Hellbach, Felicitas

at the

Faculty of Science

Department of Physics

Konstanz, 2023

Date of the oral examination: 29.08.2022

1. Reviewer: Prof. Dr. Wolfgang Belzig

2. Reviewer: Dr. Gianluca Rastelli

Preface

This dissertation was written in the Quantum Transport Group in the Department of Physics at the University of Konstanz under the supervision of Prof. Dr. Wolfgang Belzig and Dr. Gianluca Rastelli and is divided into two main parts while both contain an introductory chapter based on the current literature and research indicated by the references. Furthermore, the new content that we present in Chapter 2 is published by a peer-reviewed journal[1]. This work was done in close collaboration with Prof. Dr. Fabian Pauly and parts have already been published in my Master thesis, *Coupling of Quantum Dot Systems to Microwave Cavities*, submitted 2017 at the University of Konstanz for the degree Master of Science (M.Sc.). The second part contains two different works. The content of Section 4 is already published by a peer-reviewed journal [2] and was done in close collaboration with Dr. F. Yang and the experimental group of Prof. Dr. Elke Scheer from the University of Konstanz. The content of Section 5 is currently unpublished. Since this project was initiated as Bachelor thesis some parts are similar to the work of *Nonlinear interacting quantum Duffing resonators* of Michael Saur, submitted 2020 to obtain the degree Bachelor of Science (B.Sc.). All results presented in the dissertation were obtained after many, fruitful discussions with my supervisors and the coauthors.

[1] F. Hellbach, F. Pauly, W. Belzig, G. Rastelli, *Quantum-correlated photons generated by nonlocal electron transport*, Phys. Rev. B **105**, L241407 (2022)

[2] F. Yang, F. Hellbach, F. Rochau, W. Belzig, E. M. Weig, G. Rastelli, and E. Scheer, *Persistent Response in an Ultrastrongly Driven Mechanical Membrane Resonator*, Phys. Rev. Lett. **127**, 014304 (2021)

Abstract

Hybrid devices based on semiconducting quantum circuits with integrated microwave photonics are promising for implementing quantum transducers, in which single electrons control photonic quantum states. To combine electronic with photonic degrees of freedom on-chip, quantum dots coupled to microwave photon cavities provide a novel family of coherent quantum devices. A fundamental property of the microscopic world described by quantum mechanics is the theory of nonlocality which is at the heart of quantum communication and computing in various physical implementations. An intriguing example of quantum delocalization is interference in the motion of a single electron. Our theoretical work suggests a realistic setup to generate entanglement between two spatially separated microwave cavities using quantum delocalized electrons that flow through a parallel double quantum dot connected between two electrodes. To prove the generation of entangled photons, we use a diagrammatic perturbative expansion based on Keldysh Green's functions, going beyond the theoretical studies that exist in the literature.

Another source for photon pairs with non-classical behavior are parametric oscillators. The occurring two-photon coherent states are essential in quantum optics and of enormous interest for applications in quantum communication since their noise properties are close to those of a minimum-uncertainty state, i.e. a squeezed state. We develop the theoretical basis to explain the phenomenon of persistent response and other nonlinear phenomena obtained in an experiment where membrane resonators are driven in an ultra-strong regime. We show that they are caused by the nonlinear, internal interactions between higher-order flexural modes and higher-order overtones of the driven mode, where one mode is acting as a parametric drive onto another mode. Furthermore, we consider the interaction of two parametrically driven and nonlinear coupled Duffing resonators, obtaining nonlinear phenomena like a bifurcation.

Structure and Overview

The thesis is divided into to main parts.

The first part I of the thesis deals with the quantum entanglement in the hybrid system of two microwave cavities coupled to a parallel double quantum dot. For this reason, the first introductory part, Chapter 1, gives in Section 1.2 an insight into the fundamental interaction of light and matter with a detailed view regarding the different regimes of coupling strength between the electronic and photonic subsystems and the experimental state of the art. In the following Section 1.3, we give a short overview of quantum entanglement with particular attention to the Cauchy-Schwarz inequality as quantum entanglement criterium. To prove the entanglement and determine other quantities in the hybrid system, we use a diagrammatic perturbation theory based on Keldysh Green's functions. Therefore the most extended section in the basics, i.e. Section 1.4, introduces the main steps in the nonequilibrium Green's function theory. Starting with introducing the retarded and advanced Green's function, extending them to the Keldysh contour, deriving the perturbation theory, Wick's theorem, and introducing Feynman diagrams. Parallel to the theoretical derivation of these topics, we consider as a reference example a single electronic level coupled to two fermionic leads and a single bosonic mode. In the main part, i.e. chapter 2, we introduce in section 2.1 the basic idea of how we create entanglement based on a heuristic argument. In section 2.2, we describe the Hamiltonian of the system and define the correlators in terms of lesser single-particle and two-particle Green's functions. Then we determine the Green's functions of the whole system, starting with the fermionic subsystems of a parallel double dot coupled to a common left and right lead in section 2.3. We investigate this electronic system and the simplifications we made in more detail by analyzing the transmission function. As a sanity check, we perform the calculations also for a single dot coupled to two microwave cavities simultaneously in section 2.4 and show, for completeness, in section 2.5 also the bosonic Green's functions of the microwave cavities. Afterward, we perform the perturbation expansion in the dot-lead interaction upon fourth order for the single-particle and two-particle Green's functions in section 2.6 and perform the integration in section 2.7. With these, we are finally able to calculate and discuss the main quantities in the last section, 2.8.

In Part II, we move on to driven and nonlinear interacting Duffing resonators. We begin Chapter 3, which explains the basics with Section 3.1, in which we give an overview of nonlinear resonances in mechanical and optical resonators and its wide field of applications to motivate the following work. The Duffing resonator plays a central role in this part since we model most modes with cubic nonlinearity. Since we consider two different

kinds of the driving mechanism, we first determine the solution, stability conditions, and physics behind a Duffing resonator driven by an external linear force in Section 3.2.1 and move on to a Duffing resonator that is driven parametrically in Section 3.2.2. The parametric drive reveals various nontrivial effects while we give special attention to an effect called bifurcation in Section 3.2.3. We consider two different works: In Section 4.3, we derive the theory from an experiment done by F. Yang et al. in the Scheer Group at University of Konstanz. Driving a vibrating membrane resonator in the ultra-strong regime reveals several nonlinear effects based on internal, nonlinear mode coupling. In Section 4.3, we explain the persistent response based on the coupling of the fundamental modes to its higher harmonics. In Section 4.4, we focus on direct and indirect parametric excitation, each between two specific modes, to explain nonlinear features occurring in the persistent response. In Section 5, we consider two nonlinear coupled Duffing resonators driven by a parametric force. We investigate the system first in the classical regime in Section 5.1. We study stability conditions and the nonlinear effect of bifurcation for various parameters. In Section 5.2, we move to the quantum regime introducing quantum fluctuations to determine possible squeezed states and entanglement criteria.

Acknowledgement

First of all, I would like to express my deepest appreciation to my supervisors, Prof. Dr. Wolfgang Belzig and Dr. Gianluca Rastelli, who offered me the opportunity to perform my doctoral studies in this group.

They generously provided their knowledge and expertise with invaluable patience and lots of feedback and challenged and motivated me at the same time.

The culture of always having an open ear - or an open door, made it very pleasant to work with. They offered me great opportunities to present my work and deepen my knowledge in workshops, schools, and conferences.

This endeavor would not have been possible without the great support of Prof. Dr. Fabian Pauly, who supervised me during my master thesis, inspired me for this exciting topic and was also part of the following journey.

I am also thankful for my long-term office mates, Raffael and Ali. For various coffee breaks, funny things to lighten up busy days, and intense and enriching discussions in and outside physics, with special thanks to Raffael, who proofread the whole thesis and gave me valuable feedback.

I had the pleasure of collaborating with Fan Yang and Prof. Dr. Elke Scheer on an exciting project. I appreciated the exchange we had during that time.

Of course, I'd like to acknowledge all of my group members and friends. Thanks for all the lovely evenings, board game events, pup quizzes, barbeques, and so much more.

Last but not least, I would like to thank my parents for their love and support on my long journey. Their belief in me has kept my spirits and motivation high during this time. And also, many thanks to my partner, who believed in me and supported me unconditionally, especially in the final phase.

And with a few final words, I would like to thank my physics teacher Dr. Fleig, who sparked my interest and passion for physics, and without whom, I would not be standing here today.

Deutsche Zusammenfassung

Im ersten Teil unserer Arbeit geht es um die Möglichkeit zur Erzeugung quantenverschränkter Photonen in einem elektro-photonischen hybriden System.

Die Theorie der Nichtlokalität ist eine grundlegende Eigenschaft der Quantenmechanik. Die Delokalisierung eines Quantenteilchens im Raum entsprechend seiner zugehörigen Wellenfunktion oder seine Überlagerung und die dementsprechenden Korrelationen zwischen räumlich getrennten Teilen eines Quantensystems sind von großem Interesse für hybride Geräte aus Halbleiter-Quantenschaltungen mit integrierter Mikrowellenphotonik. In unserer theoretischen Arbeit schlagen wir einen realistischen Aufbau zur Erzeugung von Verschränkung zwischen zwei räumlich getrennten Mikrowellenkavitäten vor, bei dem delokalisierte Elektronen durch einen parallelen Doppelquantenpunkt fließen, der zwischen zwei Elektroden angeschlossen ist. In Abschnitt 2.1 führen wir ein erstes heuristisches Argument an. Wenn die Energieniveaus der Quantenpunkte nahe beieinander liegen, bewegt sich das Elektron delokalisiert durch den parallelen Doppelquantenpunkt. Die im elektronischen Teil des Systems auftretende Korrelation wird auf die gekoppelten Mikrowellenkavitäten ausgedehnt und bleibt auch dann bestehen, wenn das Elektron das System verlässt, was einer nichtlokalen Messung entspricht, da das Elektron entfernt wird, ohne zu wissen, welchen Arm es durchlaufen hat. In Abschnitt 2.2 drücken wir die Kovarianz und einen weiteren Parameter, der auf der Cauchy-Schwarz-Ungleichung basiert, mit Hilfe von Keldysh-Green'schen Funktionen aus. Ersteres ist ein Nachweis für klassische Korrelation, letzteres für Quantenkorrelation. Um diese Größen zu bestimmen, betrachten wir das elektronische Teilsystem in Abschnitt 2.3 und das bosonische in Abschnitt 2.5 getrennt, und berechnen die Wechselwirkung beider durch eine Störungsentwicklung in der Kopplung zwischen Quantenpunkten und Kavitäten. Da wir die Kopplungsparameter zwischen den elektronischen Niveaus der Quantenpunkte und den fermionischen Leitern identisch gewählt haben, untersuchen wir das elektronische System anhand der Transmission näher, um aufzuzeigen, dass dies keinerlei Einschränkung für unsere Berechnungen bedeutet. In Abschnitt 2.6 führen wir dann die Störungsentwicklung bis zur vierten Ordnung durch, welche zu drei unterschiedlichen Arten von Feynman-Diagrammen führt. Durch Transformation der entsprechenden Integrale in den Energieraum und unter Verwendung des Residuensatzes führen wir die Integration der entwickelten Green'schen Funktionen in Abschnitt 2.7 durch. Schließlich fassen wir die Ergebnisse in Abschnitt 2.8 zusammen. Wir präsentieren die durchschnittliche Photonenzahl, die Fluktuation und den Fano-Faktor und finden sub-poissonisches Verhalten für identische Energielevel, was einem Anti-Bunching der Photonen in der lokalen Kavität entspricht, und ansonsten super-

poissonisches Verhalten. Wir bestimmen die Kovarianz, die für identische Energielevel oder einen einzelnen Quantenpunkt endlich ist und damit klassische Korrelation zeigt. Die Cauchy-Schwarz-Ungleichung wird jedoch nur für den Doppel-Quantenpunkt gleichen Energieleveln verletzt, was die Quantenkorrelation, d. h. die Verschränkung, beweist.

Im zweiten Teil fokussieren wir uns nun auf nichtlineare Wechselwirkung zwischen linearen und nichtlinearen Resonatoren beziehungsweise Moden.

Nanomechanische Oszillatoren können mittlerweile Dimensionen auf atomarer Ebene haben und zeigen daher schon bei kleinen Amplituden nichtlineares Verhalten ihrer Schwingungen, wie parametrische Schwingung oder Verzweigungen. Das Anwendungsfeld ist riesig, da die Anregung von Biegemoden den Weg für hybride technische Systeme ebnet, da sie leicht mit anderen Freiheitsgraden wie Licht oder Atomen gekoppelt werden können. Interne Resonanzen wie die 1:3-Resonanz führen zu nicht-trivialen Aspekten, wie der Selbstbegrenzung der Amplitude. In diesem Zusammenhang entwickelte die Scheer Gruppe der Universität Konstanz, insbesondere Dr. F. Yang, ein Experiment mit einem schwingenden Membranresonator getrieben von einer Kraft im ultrastarken Regime. Durch Entwicklung der Theorie für dieses Experiment zeigen wir, dass die Antwort des Systems, die einen Schwingungszustand mit nahezu konstanter, hoher Amplitude über einen Frequenzbereich von mehr als 50% der Eigenfrequenz zeigt, durch eine bisher unbeschriebene parametrische Kopplung zwischen verschiedenen Biegemoden und deren Obertönen verursacht wird. In Abschnitt 4.3.1 zeigen wir, dass die Dynamik der Grundmode (1,1) durch Wechselwirkung mit der zweiten, dritten und vierten Harmonischen durch eine effektive septische Kraft modelliert werden kann, wenn die Moden höherer Ordnung im harmonischen Bereich liegen. Unter diesem Gesichtspunkt leiten wir in Abschnitt 4.3.2 einen skalierten Ausdruck für die Amplitude her, der die im Experiment erhaltene Abflachung zeigt. Außerdem bestimmen wir die maximale Amplitude und Verstimmung. Die Messkurve zeigte jedoch Besonderheiten auf der Nanometerskala in Form von kleinen Stufen und Sprüngen. Bei der Auswertung des Ablenkungsprofils hatte die Experimentalgruppe diese als Anzeichen für eine nichtlineare Modenkopplung identifiziert. In Abschnitt 4.4 weisen wir nach, dass zwei verschiedene nichtlineare Kopplungsmechanismen diese Schwankungen verursachen. In Abschnitt 4.4.1 weisen wir eine indirekte, parametrische, nichtlineare Wechselwirkung nach, die durch die Obertöne der Grundmode ($m = n$) aktiviert wird. Im Detail untersuchen wir die Kopplung des zweiten Obertons des Grundmodus mit der (2,2)-Mode. In Abschnitt 4.4.2 betrachten wir eine direkte parametrische Wechselwirkung mit höheren Biegemoden ($m \neq n$). Die Resonanz ist nicht ganzzahlig, und wir untersuchen die Wechselwirkung der (1,1)-Mode mit der (1,2)-Mode im Detail. Der Vergleich mit dem Experiment zeigt, dass beide Kopplungsmechanismen mit den Merkmalen in der Messkurve in Verbindung gebracht werden können. Solche parametrischen Prozesse können kohärente Zweiphotonen-Zustände erzeugen. Diese Zustände sind für die Quantenoptik und die Quantenkommunikation unerlässlich. Motiviert durch den großen Anwendungsbereich und die Bedeutung verschränkter und gequetschter Zustände für

verschiedene Bereiche haben wir die nichtlineare Wechselwirkung von zwei parametrisch gesteuerten Duffing-Resonatoren untersucht. In Abschnitt 5.1.2 analysieren wir die Stabilität der trivialen Lösungen und stellen fest, dass die Kopplung zu instabilen Regionen führt, selbst wenn die Amplitude eines Resonators gleich Null ist. Bei der stationären Lösung der Amplitude stellen wir eine Verzweigung fest, wenn die treibenden Kräfte gleich sind, was wir in Abschnitt 5.1.3 analysieren. Je größer die Kräfte sind, desto ausgeprägter ist die Verzweigung. Wenn die Kopplung zunimmt, hat dies den entgegengesetzten Effekt einer erhöhten Antriebskraft. Wenn sich die Duffing-Nichtlinearitäten der beiden Resonatoren unterscheiden, kann die Verzweigung unterdrückt werden, während sich die Amplituden weiterhin kreuzen. Eine Erhöhung der Kraft hebt diesen Effekt auf. Wenn die Kräfte gleich sind, werden die beiden Zweige mit der Anfangskurve vor der Bifurkation verbunden. Unterscheiden sich die Kräfte geringfügig, verschwindet die Lösung in einem bestimmten Verstimmungsbereich und es entsteht eine Lücke in einem der beiden Zweige, was wir in Abschnitt 5.1.4 zeigten. Betrachtet man nicht nur die Amplitude, sondern auch die Phase der möglichen Lösungen, so erhält man vier verschiedene Lösungspaare mit unterschiedlichen Kombinationen eines positiven oder negativen Phasenwertes. Die relevante Information ist die konstante Phasendifferenz von π. Um das Vorhandensein möglicher gequetschter Zustände zu untersuchen und andere Verschränkungskriterien anzuwenden, untersuchen wir in Abschnitt 5.2 das System im Quantenregime. Bei der Herleitung der Bewegungsgleichung für die Quantenfluktuationen führen wir eine erste Analyse der Matrixelemente durch, wobei wir die stationären Lösungen des klassischen Regimes verwendeen, die das Vorhandensein von gequetschten Zuständen zur Folge hat, woraus wir den effektiven Hamiltonian der Quantenfluktuationen herleiten.

Contents

Part I

Entanglement of Photons in a Hybrid Platform of a Double Quantum Dot, Coupled to Two Microwave Cavities

1 Introduction and Theoretical Background

1.1 Introduction

Nonlocality is a fundamental property of quantum mechanics that manifests itself in two main ways: the delocalization of a quantum particle in space according to its associated wave function (superposition) or as correlations between spatially separated parts of a quantum system (entanglement). It is at the heart of quantum communication and computing in various physical implementations.

An intriguing example of quantum delocalization is the interference in the motion of a single electron. Quantum delocalized transport has been proven in nanodevices formed by two possible paths connecting an initial and final point, namely two electrical contacts playing the role of source and drain. Examples are parallel double dots [1, 2, 3], operating as single-electron splitter interferometer, or the electronic Mach-Zehnder interferometer [4], operating with the edge states of two-dimensional (2D) quantum Hall systems [5]. Similarly to a photon in a Mach-Zehnder interferometer, an electron wave function can split into two branches and then recombine give rise to interference in the transmitted flux. In general, semiconducting single-electron devices form a unique playground to address nonlocal electron transport and quantum interference [6, 7, 1, 2, 3].

Besides electron transport, quantum mechanics can be explored with high precision in the field of optics and photonics. In particular, microwave quantum photonics has made remarkable progress in the last decade. In the circuit quantum electrodynamics (QED) architecture [8], a large variety of quantum states in an electromagnetic microwave resonator has been prepared and measured [9, 10]. Moreover, using superconducting qubits or Josephson circuitry (Josephson parametric amplifier or wave-mixer), quantum entangled states of microwave photons have been realized in two spatially separated resonator cavities [11], in two resonator modes of different frequency [12, 13] as well as in propagating photons [14, 15, 16]. More recently, an entangled pair of two-mode cat states has been realized in two microwave cavities [17], a dc-biased Josephson junction was used to create two continuous entangled microwave beams [18].

Beyond superconducting circuits based on Josephson junctions, quantum dots realized in semiconducting nanostructures implement reliable and well-controlled qubits [19, 20] with transition frequencies in the microwave domain and with the advantage of electric

field control [21]. Quantum dots can now be readily coupled to microwave photon cavities, establishing the field of semiconductor hybrid QED [22], which provides a novel family of coherent quantum devices that combine electronic with photonic degrees of freedom on-chip [23, 24, 25, 26, 27, 28, 29, 30, 31, 32, 33]. The so-called strong coupling regime has been reached [34, 35, 36] as well as the full microwave control and readout of the quantum dot qubits [37].

Coupling quantum dots with quantum optical resonators adds a new dimension to cavity and circuit QED beyond the conventional paradigm of an atom coupled to a harmonic oscillator. This research line opens the path to exploring the correlations between charge transport and nonequilibrium, possibly quantum, regimes of localized electromagnetic radiation. The corresponding hybrid devices are also promising for implementing quantum transducers, in which single electrons control photonic quantum states in microwave cavities.

1.2 Light-Matter Interaction in Hybrid Systems: The Field of Cavity Quantum Electrodynamics

A fundamental physical topic that develops both in theory and experiment with huge effort is the interaction of light and matter. In the semi-classical theory the basic atom-field interaction of an electron, characterized by a charge e and mass m is described by the so-called minimal-coupling Hamiltonian, i.e. higher multipole moments are neglected. In terms of the canonical momentum $\boldsymbol{p}$, the vector potential $\boldsymbol{A}(\boldsymbol{r},t)$ and the scaler potential $U(\boldsymbol{r},t)$ of the external field as well the electrostatic potential $V(r)$ the Hamiltonian reads

$$H = \frac{1}{2m}\left[\boldsymbol{p} - e\boldsymbol{A}(\boldsymbol{r},t)\right]^2 + eU(\boldsymbol{r},t) + V(r)\,. \tag{1.1}$$

This Hamiltonian can be simplified using the dipole approximation. Latter is based on the fact that the characteristic length of an atom is much smaller than the wavelength of the external field [38], i.e. $\boldsymbol{k}\cdot\boldsymbol{r} \ll 1$. The field can be approximated by a plane electromagnetic wave with constant amplitude over the length scale of the atom, defined by the vector potential $\boldsymbol{A}(\boldsymbol{r_0}+\boldsymbol{r},t) = \boldsymbol{A}(t)e^{i\boldsymbol{k}(\boldsymbol{r_0}+\boldsymbol{r})} \approx \boldsymbol{A}(t)e^{i\boldsymbol{k}\boldsymbol{r_0}}$ and one obtains, after some transformation [39] the simplified Hamiltonian

$$H = \frac{\boldsymbol{p}^2}{2m} + V(\boldsymbol{r}) - e\boldsymbol{r}E(\boldsymbol{r_0},t)\,. \tag{1.2}$$

Moving from the semi-classical theory to the quantum description, writing momentum, position and therefore the fields in terms of the second quantization [40] we consider now a two-level system that is coupled to a multi-mode field, while each mode is indicated

by the index k. We can write the Hamiltonian in terms of the creation and annihilation operators as

$$H = \hbar \sum_k \nu_k \hat{a}_k^\dagger \hat{a}_k + \frac{1}{2}\hbar\omega\hat{\sigma}_z + \hbar \sum_k g_k(\hat{\sigma}_+ + \hat{\sigma}_-)(\hat{a}_k + \hat{a}_k^\dagger)\,. \tag{1.3}$$

The first term describes the modes with frequency ν_k, the second term the two-level system, described by the Pauli matrix $\hat{\sigma}_z$ with transition frequency ω and the third part is the interaction term with the coupling strength g_k between the atom and the kth mode. This coupling parameter is the electric dipole matrix element of the transition inside the atom multiplied with the cavity mode that is located at the atom [41]. $\hat{\sigma}_\pm$ are the raising and lowering operators

$$\sigma_z = \begin{pmatrix} 1 & 0 \\ 0 & -1 \end{pmatrix}\,, \quad \sigma_+ = \begin{pmatrix} 0 & 0 \\ 1 & 0 \end{pmatrix}\,, \quad \sigma_- = \begin{pmatrix} 0 & 1 \\ 0 & 0 \end{pmatrix}\,. \tag{1.4}$$

The interaction part contains four terms. Two of them conserve the quanta of excitations. These are $\hat{a}_k^\dagger\hat{\sigma}_-$ and $\hat{a}_k\hat{\sigma}_+$ where an atom decays from the upper to the lower state while a photon with mode k is created and vice versa. The other two terms lose or gain energy of $2\hbar\omega$. Neglecting these terms corresponds to the rotating-wave-approximation [39], that we will consider in more detail in the second part of this thesis. We focus in the following on a single two-level atom coupled to a single-mode so the index k drops, and we finally get the so-called Janes-Cummings Hamiltonian

$$H = \hbar\nu\hat{a}^\dagger\hat{a} + \frac{1}{2}\hbar\omega\hat{\sigma}_z + \hbar g(\hat{\sigma}_+\hat{a} + \hat{a}^\dagger\hat{\sigma_-})\,. \tag{1.5}$$

Compared to an atom in free space that is interacting with an electric field, the coupling properties and therefore the coupling strength can change remarkably if the atom is coupled to a "resonator-like" body, i.e. a cavity [41] as sketched in Fig. 1.1. Due to the

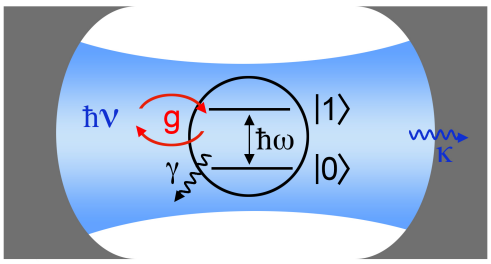

Fig. 1.1.: The basic idea of a two-level system is indicated here by the states $|0\rangle$ and $|1\rangle$ with a transition frequency ω and a decay rate γ. It is coupled to a cavity with resonance frequency ν and decay rate κ via a coupling constant/strength g.

cavity, the line spectrum of the field is well-defined, which increases the coupling for transitions in the two-level system adjusted to the resonance lines of the cavity. A photon

created by spontaneous emission is trapped inside the cavity for some time and can be reabsorbed by the atom. Induced emission by an external pumping source results in lasing effects. The coupling properties depend mainly on the geometric and optical properties of the cavity. A measure of the cavity's quality and, therefore, of the achievable coupling strength or lifetime of the photons is given by the quality factor Q. For a high Q-factor, one can achieve a strong coupling and long lifetime of the photons in the cavity, and if only photons of a single transition frequency, like in the two-level system, comes into play, this system can be described by the Janes-Cummings Hamiltonian [41]. A two-level system in the form of an atom is valid if the two levels, whose transition is in resonance with the cavity mode, are highly detuned from all other energy levels of the atom. Other possibilities are a double quantum dot with single levels, which have been interesting for quantum computation for a long time [42], or a superconducting qubit [22]. In addition to the mentioned properties of the cavity, its coupling to the environment influences the essential quantities of the coupled system, which are, besides the coupling strength, the spontaneous decay rate γ of the atom and κ of the cavity. This can be due to the coupling to a read-out cavity for the measurement, mesoscopic dissipation due to the contacts of a two-level system like a double quantum dot or other nano-conductors, effects due to the cavity drive, or just noise of the environment.

In general, one would like to have degrees of freedom with good coherence properties. This means for an artificial atom that, one tries to get a low coupling between the two-level system and the fermionic reservoirs to avoid decoherence. On the other hand, we want to give the side note that also systems with strong coupling show fascinating results since the transport effects are sizable, and one can study the effect of electron transport on a nano-circuit and the microwave resonator, yielding two qualitatively different signals providing different information. Also, dissipation of the reservoirs could modify the cavity states, and there are many more interesting physical quantities and effects of using electronic transport to manipulate or probe the state of a cavity, and it provides a powerful way to study condensed matter problems in a new way. In the last years, different coupling strengths were achieved experimentally, which can be classified into four different categories [43] and are summarized nicely in [44].

Weak coupling regime:
This regime is classified by the ratio $g \ll \gamma, \kappa$. The interaction between the electronic system and the cavity mode is incoherent, i.e. the damping rates γ and κ dominate in this process, and the energy dissipates from the system faster than the interaction can take place. Even if the time scale of the dissipation is small compared to the time scale of the interaction, the spontaneous emission rate is enhanced, which is the so-called Purcell effect [45]. Introducing two additional driving fields, one for the emitter and one for the cavity mode, enables new non-classical effects even in the weak coupling limit [46]. During the time, there have been lots of experiments, while the coupling is within the

range $30\,MHz < g < 50\,MHz$ with the damping within $350\,MHz < \gamma < GHz$ [47, 48, 49, 50].

Strong coupling regime:
This regime is classified by the ratio $\omega, \nu \gg g \gg \gamma, \kappa$. In this case, the dissipation plays a minor role, i.e. a photon can be coherently (re-)emitted and (re-) absorbed many times, and we can describe the interacting systems with the Janes-Cummings Hamiltonian [51]. The research field is immense, while the coupling to single or multiple atoms [52, 53] like Rdybger atoms[54] and now single or double quantum dots acting as qubits [35, 34, 36, 55, 56, 57, 58, 59] with normal or superconducting leads are of high interest. Recently the strong-coupling regime was reached with a THz-cavity coupled to just a single electronic level which is remarkable since the strong coupling to a THz-cavity was achieved so far only using collective modes to increase the coupling [60]. In the weak and strong coupling regime, ground state cooling, the excitation of mechanics, storage, and squeezing of mechanical states is possible [61].

Ultra strong coupling regime:
This regime is classified by the ratio $g/\nu \gtrsim 0.1$, i.e. the coupling is not stronger than the driving frequencies but is on a par with them. Mathematically spoken, the rotating-wave approximation does not hold any longer. For the coupling with a single electron [62] experiments reaches values for the ratio g/ν from 0.073 to 0.112. In this regime effects like photon blockade or non-gaussian and non-classical states appear [63, 64, 65, 66]. Note that the cooperativity $C = g^2/\gamma\kappa$ is the relevant quantity within this regime.

Deep strong coupling regime:
This regime is classified by the ratio $g/\nu \gtrsim 1$. Exceeding the limit from the ultra strong coupling regime, ratios g/ν up to 1.34 [67, 68] were achieved. The currently largest ratio of g/ν= 1.43 was obtained in [69]. An exciting effect in this regime is the decoupling of light and matter [70].

1.3 Entanglement in Hybrid Systems

Quantum entanglement is one of the most fascinating and, at the same time, one of the most difficult to understand topics in physics. Anyhow quantum entanglement is also an important property to differ between classical and quantum states. To transfer a quantum state, one needs to entangle the quantum memory with the transport or communication channel since a quantum state can not just be copied. By achieving this, the field of applications in the future is rather broad.

A more easy-to-understand example, as analogon in classical physics, is to take two coins that have either the value +1 or the value -1. Alice and Bob each get one of the coins without looking at them but receiving the information of the two different values. Then

the two separate from each other, like being in different places of the world or even on different planets. Now Alice checks her coin, and exactly at this moment, she also knows the value of Bob's coin [71]. Einstein called this "spooky action" since the information about Bob's coin was received by Alice even if they are spatially separated so far that the information would have to be traveled faster than light. Regarding the physics of entanglement behind this sketch, the idea is the following: Since the two coins have either one of the values, they are correlated in the classical way. When Alice is looking at her coin, i.e. she performs a measurement on her subsystem, she simultaneously determines the value of Bob's coin. So it is not possible to describe the quantum states of the subsystems independently from each other. A direct physical (particle) equivalent is the spin of an electron pair or the polarization of a pair of photons. As long as the measurement has not been done, the state of the system is a coherent superposition of the possible subsystem states.

Of course, this idea cannot easily be transferred to macroscopic systems. Here world's most famous example is the gedankenexperiment of Erwin Schrödinger. The rough idea is to put a cat, Schrödinger's cat, inside a box together with an unstable atom. The probability that the atom decays or not within a specific time is equal. If the atom decays, a poison is released, and the cat dies. Only if one opens the box, the measurement will occur, and the state of the atom - and the cat - is determined. Until this point, the atom is in the superposition of being decayed or not. However, also, the cat is in the superposition of being dead or alive until the box is opened for an indefinite time, which does, of course, not make sense.

The field of possible applications is rather broad, from quantum cryptography [72, 73, 74, 75], to quantum teleportation [76, 77] as basic part of the quantum internet [78], the overcome of noise in the entanglement distribution using not classical two-level qubits but systems with more levels [79], or exceptional applications like an entanglement-enhanced microscope [80].

We roughly scan the huge experimental field of entanglement involving photons starting with the entanglement of a single photon and an electronic counterpart as a single trapped atom [81, 82, 83], a single electron spin [84, 85, 86] or superconducting qubits [87, 88]. To exchange information coherently inside a quantum network is a fundamental request for quantum information processing. The electron spin has to be noted here since it has the longest coherence time, but problems occur with long-distance interaction. Photons are ideal candidates to carry and propagate the entanglement between spatially distant systems of which such a network is composed. In other words, entangling distant (superconducting) qubits, quantum dots, or spin-spin interaction mediated by cavities is an excellent and elegant way [22]. In an easy picture, the state of the qubit or else can be transferred to a photon and then be sent to another cavity-qubit system to be decoded [89, 90]. At least as interesting but experimentally much more challenging is the entanglement of distant photons. It offers possibilities for new platforms of quantum coherent devices,

quantum transport of nonequilibrium states, and quantum simulators [30]. Quantum entangled states of microwave photons have been realized in two spatially separated superconducting microwave resonator cavities [11], a single photon in two different "color" states, i.e. the coupling of the mode currents of two harmonics via a SQUID[12], two resonator modes of different frequency [13] as well as in propagating photons [14, 15, 16]. Beyond controlling photons one by one, superposition of more complex, multi-photon states have been reported as Schrödinger-cat states [91, 92] opening the route towards the encoding of continuous variable quantum computation [93, 94]. More recently, an entangled pair of two-mode cat states has been realized in two microwave cavities [17] that are coupled via a superconducting, artificial atom, and a dc-biased Josephson junction was used to create two continuous entangled microwave beams [18].

1.3.1 Entanglement Criteria

In general, a quantum mechanical state of a system can be characterized and described by its density matrix ρ. The measurement of an observable corresponds to the determination of the expectation value, defined as the trace of the density matrix and the related operator. Considering a bipartite system of two subsystems, denoted by (1) and (2), which can be, for instance, two electronic, two photonic, or a photonic and an electronic system, with commutating operators, the system is uncorrelated if the density matrix ρ of the combined system is a direct product of the two subsystem density matrices $\rho^{(1)}$ and $\rho^{(2)}$, so $\rho = \rho^{(1)} \otimes \rho^{(2)}$, i.e. the state is separable [95].

In this separable case, the measurement result of any observable $A^{(1)}$ of the first subsystem is entirely independent of the measurement result of any observable $B^{(2)}$ of the second subsystem. This means $\left\langle A^{(1)}B^{(2)} \right\rangle = \left\langle A^{(1)} \right\rangle \left\langle B^{(2)} \right\rangle$ for any A and B. If the system is not separable and the density matrix cannot be factorized, so $\rho \neq \rho^{(1)} \otimes \rho^{(2)}$, this equality is violated and concerning this matter we can define the covariance

$$C := \mathrm{cov}(A^{(1)}B^{(2)}) = \left\langle A^{(1)}B^{(2)} \right\rangle - \left\langle A^{(1)} \right\rangle \left\langle B^{(2)} \right\rangle , \tag{1.6}$$

which is nonzero in the case of a classical correlation between the two subsystems [95].

To prove if the system is not just classical correlated but quantum entangled, we need other (in)equalities. The most famous inequality that is violated in the case of quantum entanglement is Bell's inequality[96]. It contradicts the theory of Einstein, Podolsky, and Rosen that the quantum theory can be explained with hidden variables [97]. But there are several more criteria for which the general separability criterion is used [98, 99, 100, 101, 102]. There especially exists a class of inequalities which are applications of the Cauchy-Schwarz inequality $|\langle x, y\rangle|^2 \leq \langle x, x\rangle \langle y, y\rangle$ [103]. We focus on bipartite systems

with the expectation value $\langle A_1 A_2 B_1 B_2 \rangle$, whereby A_i and B_j belong to the two subsystems. The inequality

$$\left|\langle A_1 A_2 B_1 B_2 \rangle_{sep}\right|^2 \leq \left\langle A_1 A_1^\dagger B_2^\dagger B_2 \right\rangle_{sep} \left\langle A_2^\dagger A_2 B_1 B_1^\dagger \right\rangle_{sep} \tag{1.7}$$

is valid for separable states and can only be violated by entangled states, which depends on the choice of the operators A and B. For the special choice $A_2 = B_1 = 1$, $A_1 = A^\dagger = (a^m)^\dagger$ and $B_2 = B = b^n$, whereby a, b are the annihilation and $a^\dagger$, $b^\dagger$ the creation operators of system A and B, we obtain the criterion

$$\left|\left\langle a^m (b^\dagger)^n \right\rangle_{sep}\right|^2 \leq \left\langle (a^\dagger)^m a^m (b^\dagger)^n b^n \right\rangle_{sep} . \tag{1.8}$$

For $A_1 = B_1 = 1$, $A_2 = (a^m)^\dagger$ and $B_2 = B = b^n$ we obtain the criterion

$$\left|\langle a^m b^n \rangle_{sep}\right|^2 \leq \left\langle (a^\dagger)^m a^m \right\rangle_{sep} \left\langle (b^\dagger)^n b^n \right\rangle_{sep} .$$

Both criteria were also discussed by Hillery and Zubairy [98] and lead to an entanglement criterion based on the Cauchy-Schwarz inequality. In the special case of $m = n = 2$ we obtain

$$\left|\left\langle a^2 b^2 \right\rangle\right|^2 \leq \left\langle (a^\dagger)^2 a^2 \right\rangle \left\langle (b^\dagger)^2 b^2 \right\rangle . \tag{1.9}$$

After the first experimental observations, where the Cauchy-Schwarz inequality of the second-order correlation function was violated by a collection of ultracold bosons [104] there appeared also other experimental [105, 106, 107] and theoretical [108, 109, 110] paper showing that the violation of this inequality proves (particle) entanglement, also connecting photon antibunching and sub-Poisson photon statistics [111, 112].

1.4 Green's Functions and Nonequilibrium Keldysh Formalism

1.4.1 Equilibrium Green's Functions and Dyson Equation

"*In classical physics Green functions are used as a powerful method for solving inhomogeneous differential equations*" [113] so it is not surprising that a common used Green's function approach is the definition of the Green's function as the inverse of a differential operator [114]. In general, since the Schrödinger equation is a second-order differential equation,

it is possible to apply this approach in a perturbative way. For a free particle, it is given by

$$H_0(\boldsymbol{r})\Psi_E(\boldsymbol{r},t) = E\Psi_E(\boldsymbol{r},t)\,. \tag{1.10}$$

Here the eigenstates $\Psi_E(\boldsymbol{r})$ to a given energy of the "unperturbed" Hamiltonian $H_0(\boldsymbol{r})$ of the free particle are known and the corresponding Green's function of the unperturbed system is defined by the differential equation [114]

$$\left[E - H_0(\boldsymbol{r})\right] g(\boldsymbol{r},\boldsymbol{r}',E) = \delta(\boldsymbol{r}-\boldsymbol{r}')\,. \tag{1.11}$$

In the same way we can consider the time-dependent Schrödinger equation, where we also added a perturbation $V(\boldsymbol{r})$ acting on the particle, such that [115]

$$\left[i\partial_t - H_0(\boldsymbol{r}) - V(\boldsymbol{r})\right]\Psi(\boldsymbol{r},t) = 0\,, \tag{1.12}$$

and define the Green's functions via

$$\left[i\partial_t - H_0(\boldsymbol{r})\right] g(\boldsymbol{r}t,\boldsymbol{r}'t') = \delta(\boldsymbol{r}-\boldsymbol{r}')\delta(t-t')\,, \tag{1.13}$$

$$\left[i\partial_t - H_0(\boldsymbol{r}) - V(\boldsymbol{r})\right] G(\boldsymbol{r}t,\boldsymbol{r}'t') = \delta(\boldsymbol{r}-\boldsymbol{r}')\delta(t-t')\,. \tag{1.14}$$

This Green's function is nothing else as the non-interacting retarded single-particle Green's function. Besides the definition as the inverse of a differential operator it is also known as a propagator, namely the propagator of the wave function. If we know the wave function $\Psi(\boldsymbol{r}',t')$ at time t', the wave function $\Psi(\boldsymbol{r},t)$ for $t > t'$, is given by

$$\Psi(\boldsymbol{r},t) = \int d\boldsymbol{r}' G(\boldsymbol{r}t,\boldsymbol{r}'t')\Psi(\boldsymbol{r}',t')\,. \tag{1.15}$$

Note that the condition $t > t'$ for $\Psi(\boldsymbol{r},t)$ would be mathematically correct by adding the Heaviside step function $\Theta(t-t')$ on the left side of the latter equation. Comparing this equation now with

$$\langle \boldsymbol{r}|\Psi(t)\rangle = \int d\boldsymbol{r}' \left\langle \boldsymbol{r}\right| e^{-iH(t-t')} \left|\boldsymbol{r}'\right\rangle \left\langle \boldsymbol{r}'|\Psi(t')\right\rangle\,, \tag{1.16}$$

we can identify the so-called retarded Green's function that propagates forward in time

$$G^r(\boldsymbol{r}t,\boldsymbol{r}'t') = -i\Theta(t-t') \left\langle \boldsymbol{r}\right| e^{-iH(t-t')} \left|\boldsymbol{r}'\right\rangle\,. \tag{1.17}$$

Another possible solution is the so-called advanced Green's function, which propagates backward in time and therefore becomes

$$G^a(\boldsymbol{r}t,\boldsymbol{r}'t') = i\Theta(t'-t) \left\langle \boldsymbol{r}\right| e^{-iH(t-t')} \left|\boldsymbol{r}'\right\rangle\,. \tag{1.18}$$

Here $\Theta(t)$ is the Heaviside step function. If the system is in equilibrium, the Green's functions depend only on the time difference, i.e.

$$G^{r,a}(\boldsymbol{r}t, \boldsymbol{r'}t') = G^{r,a}(\boldsymbol{r}, \boldsymbol{r'}, t - t') \,. \tag{1.19}$$

Using the Fourier transformation of the Green's function

$$G^{r,a}(\boldsymbol{r}, \boldsymbol{r'}, t - t') = \int G^{r,a}(\boldsymbol{r}, \boldsymbol{r'}, E) e^{-iE(t-t')} dE \tag{1.20}$$

we can transform Eqs. (1.13) and Eq. (1.14) from time to energy domain and obtain

$$\lim_{\nu \to 0} \left[E^{r,a} - H_0(\boldsymbol{r}) - V(\boldsymbol{r})\right] G^{r,a}(\boldsymbol{r}, \boldsymbol{r'}, E) = \delta(\boldsymbol{r} - \boldsymbol{r'}) \,, \tag{1.21}$$

with $E^{r,a} = E \pm i\nu$. The retarded Green's function refers to $+i\nu$ and the advanced one to $-i\nu$. Note that we will suppress the expression $\lim_{\nu \to 0}$ in the following and imply the limit when the parameter $\pm i\nu$ appears. A typical ansatz to solve a differential equation like Eq. (1.21) is to consider a discrete lattice with lattice points i, j for the spatial coordinate and therefore transform the Green's function according to [113, p. 142 ff]

$$G^{r,a}(\boldsymbol{r}, \boldsymbol{r'}) \to G^{r,a}_{ij} \,. \tag{1.22}$$

In this way the latter equation changes from a differential equation to a matrix equation which depends on the discrete lattice. Now we can identify the energy-dependent Green's function as inverse of a matrix, i.e.

$$\boldsymbol{g^{r,a}}(E) = \left[E^{ra}\mathbf{1} - \boldsymbol{H_0}\right]^{-1} \,, \tag{1.23}$$

$$\boldsymbol{G^{r,a}}(E) = \left[E^{ra}\mathbf{1} - \boldsymbol{H_0} - \boldsymbol{V}\right]^{-1} \,. \tag{1.24}$$

$\boldsymbol{g^{r,a}}$ denotes the unperturbed Green's functions and we call $\boldsymbol{G^{r,a}}$ the full retarded and advanced Green's functions. Besides the possibility of determining the full retarded and advanced Green's function by the inverse of the matrix, we can also employ the perturbative Dyson equation to obtain the full solution for a given perturbation V. It can be derived iterating the integral solution for the differential equation or simply by inserting the inverse of the unperturbed Green's function from Eq. (1.23) inside Eq. (1.24) and multiply the inverse of this expression with $\boldsymbol{g^{ra}}$ from the left and $\boldsymbol{G^{ra}}$ from the right or vice versa . In the energy domain and matrix notation the Dyson equation reads

$$\boldsymbol{G^{r,a}}(E) = \boldsymbol{g^{r,a}}(E) + \boldsymbol{g^{r,a}}(E)\boldsymbol{V}\boldsymbol{G^{r,a}}(E) \,. \tag{1.25}$$

It was initially developed by Dyson [116] for single-particle Green's functions and a few years later generalized by Schwinger [117].

1.4.1.1. Minimal Example: Single Electronic Level Coupled to a Left and Right Lead

As a minimal example, which will guide us through the fundamentals section, we consider a single electronic level ε coupled, via a coupling parameter t, to a left and right lead which have the chemical potentials μ_L and μ_R. The Hamiltonian of this system reads

$$H_\varepsilon = \sum_{r=\mathrm{L,R}} \sum_k (\varepsilon_{kr} - \mu_r)\, \hat{c}^\dagger_{kr} \hat{c}_{kr} + \varepsilon \hat{d}^\dagger \hat{d} \; + t \sum_{r=\mathrm{L,R}} \sum_k \left(\hat{c}^\dagger_{kr} \hat{d} \; + \mathrm{h.c.} \right) , \tag{1.26}$$

where $\hat{c}^\dagger_{kr}$ and $\hat{d}^\dagger$ with $r = \mathrm{L,R}$ are the creation operators of the electrons in the left and right lead and of the single electronic level ε. The unperturbed or non-interacting Hamiltonian is described by the first part of $\hat{H}_\varepsilon$. The unperturbed retarded and advanced Green's functions are then determined by

$$\begin{aligned} \boldsymbol{g^{ra}}(E) &= \lim_{\nu \to 0} \left[(E \pm i\nu)\mathbf{1} - \boldsymbol{H_0} \right]^{-1} \\ &= \mathrm{diag}\left((E^{ra} - \varepsilon)^{-1}, (E^{ra} - \varepsilon_{kR})^{-1}, (E^{ra} - \varepsilon_{kL})^{-1} \right) \end{aligned}$$

with $E^{ra} = E \pm i\nu$. The tunnel coupling between the isolated electronic level and the leads is handled as perturbation V_{ij}, with $i, j \in \{1, L, R\}$, that is defined by

$$V_{1r} = V_{r1} = \begin{cases} t & \text{for } r \in \{R, L\} \\ 0 & \text{else} \end{cases} , \tag{1.27}$$

The full retarded and advanced Green's function can then be calculated with the Dyson equation

$$G^{ra}_{ij} = g^{ra}_{ij} + \sum_{lm} g^{ra}_{il} V_{lm} G^{ra}_{mj} \, , \tag{1.28}$$

which leads to the three coupled equations

$$G^{ra}_{11} = g^{ra}_{11} + g^{ra}_{11} V_{1L} G^{ra}_{L1} + g^{ra}_{11} V_{1R} G^{ra}_{R1} \, , \;\; G^{ra}_{R1} = g^{ra}_{RR} V_{R1} G^{ra}_{11} \, , \;\; G^{ra}_{L1} = g^{ra}_{LL} V_{L1} G^{ra}_{11} \, . \tag{1.29}$$

By inserting the latter two in the first one, we get

$$\begin{aligned} G^{ra}_{11} &= g^{ra}_{11}(1 + (V_{1L} g^{ra}_{LL} V_{L1} + V_{1R} g^{ra}_{RR} V_{R1}) G^{ra}_{11}) && (1.30) \\ &= g^{ra}_{11}(1 + t^2 (g^{ra}_{LL} + g^{ra}_{RR}) G^{ra}_{11}) && (1.31) \\ &= g^{ra}_{11}(1 \mp i\Gamma G^{ra}_{11}) && (1.32) \\ &= \frac{1}{E^{ra} - \varepsilon \pm i\Gamma} \, , && (1.33) \end{aligned}$$

To obtain Eq. (1.32) from Eq. (1.31) we used the wide-band approximation for the leads with $t^2 g^{ra}_{RR,LL} = \mp i \Gamma_{R,L}$ in the symmetric way $\Gamma_L = \Gamma_R = \Gamma/2$ [114]. Solving Eq. (1.32)

for G_{11}^{ra} gives the final result in Eq. (1.33) for the retarded and advanced Green's function of the isolated level.

1.4.1.2. Concept of Self-energy Illustrated at the Dyson Equation for the Retarded and Advanced Green's Function

Based on the minimal example, we would like to introduce, according to [114], a first concept of the self-energy. From Eqs. (1.30) and Eq. (1.31) one can determine the energy-dependent function

$$\Sigma_{11}^{r,a}(E) \equiv V_{1L} g_{LL}^{r,a}(E) V_{L1} + V_{1R} g_{RR}^{r,a}(E) V_{R1} \tag{1.34}$$

$$= t^2 g_{LL}^{r,a}(E) + t^2 g_{Rr}^{r,a}(E)\,. \tag{1.35}$$

Placing this new quantity in Eq. (1.30), we can cast the equation for the Green's function in the form

$$G_{11}^{ra} = \frac{1}{E^{ra} - \varepsilon - \Sigma_{11}^{ra}}\,. \tag{1.36}$$

Σ_{11}^{ra} is called the self-energy. In this setup, it is the self-energy of the dot due to the interaction with the fermionic leads, i.e. it contains the effects on the central region, here the single electronic level, due to interaction with the leads. The concrete form depends both on the coupling between dot and leads and on the electronic structure of the leads.

If we consider not just a single electronic level but a central region or conductor that is coupled to (semi-infinite) leads, Eq. (1.36) can be brought into the more general form [113, p. 151 ff]

$$G^{ra} = \frac{1}{E^{ra} - H_c - \Sigma^{ra}}\,, \tag{1.37}$$

where H_c is the Hamiltonian of the isolated conductor, and as introduced before, Σ^{ra} contains the effect of the leads on the conductor. In this way, it is possible to solve the issue of an open system with "infinite leads" and obtain a finite one, as shown in Fig. 1.2,

1.4.2 Keldysh Formalism

"*The real power of Green's functions is evident when we try to include the effect of interactions as electron-electron or electron-photon. Such interactions give rise to excitations within the conductor and cannot be described by simple S-matrices.*" [113].

To develop the perturbation formalism, we define the Green's functions in time domain. We will replace the real-time axis with a closed time contour and transform the Green's

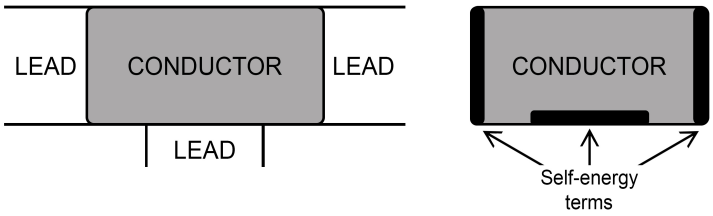

Fig. 1.2.: Left: A central region as a conductor coupled to several (semi-infinite) leads. Right: Equivalent semi-finite system where the self-energy terms describe the impact on the central region. This figure is redrawn from [113, p. 151].

functions from real-time arguments to contour-times introducing the so-called Keldysh contour and Keldysh Green's functions. Then we develop the perturbative expansion of the contour-ordered Green's functions and introduce Wick's theorem, which simplifies the calculation of a string of field operators while the occurring expressions can be represented in a graphical way using Feynman diagrams. The energy-dependent Green's functions can be obtained by a Fourier transformation of the time-dependent Green's functions. The following sections are mostly orientated in the notation and structure at [118].

1.4.2.1. General Introduction and Definition

The Hamiltonian of our system is composed by a non-interacting part H_0 and an interacting part $H^{(i)}$

$$H = H_0 + H^{(i)} \, . \tag{1.38}$$

We use the second quantization formalism to represent the time-ordered Green's function, whereby the time arguments correspond to the general real-time axis

$$G(x,t,x',t') = -i \left\langle T \left(\Psi_H(x,t) \Psi_H^\dagger(x',t') \right) \right\rangle \, . \tag{1.39}$$

The expectation value is evaluated for an arbitrary state described by the statistical operator

$$\rho(H) = \frac{e^{-H/k_B T}}{\mathrm{Tr}(e^{-H/k_B T})} \tag{1.40}$$

where k_B is the Boltzmann constant, T (only in the combination $k_B T$) is the temperature and the notation means $\langle ... \rangle = \mathrm{Tr}(\rho ...)$. The field operators $\psi_H(x,t)$ are defined in the Heisenberg picture with respect to the total Hamiltonian H. T is the time-ordering operator that orders the creation and annihilation operators according to their time arguments. The operator with the larger time argument is placed to the left. If we

effectively apply the time-ordering, i.e. we distinct the two cases $t' > t$ and $t' < t$, we can define the corresponding greater and lesser Green's function

$$G(x,t,x',t') = \begin{cases} G^{>}(x,t,x',t') = -i\langle \Psi_H(x,t)\Psi_H^\dagger(x',t')\rangle & ,t' < t \\ G^{<}(x,t,x',t') = \pm i\langle \Psi_H^\dagger(x',t')\Psi_H(x,t)\rangle & ,t' > t \end{cases} \tag{1.41}$$

whereby the upper sign of $G^{>}$ corresponds to Fermions and the lower one to Bosons. Furthermore we introduce the anti-time-ordered Green's function

$$\tilde{G}(x,t,x',t') = -i\langle \tilde{T}\left(\Psi_H(x,t)\Psi_H^\dagger(x',t')\right)\rangle\,. \tag{1.42}$$

whereby $\tilde{T}$ orders the arguments reverse to T.

Green's Functions of a System in Equilibrium

Starting with a system in thermal equilibrium, the statistical operator ρ becomes the Boltzman statistical operator $\rho(H_0)$ and the Green's functions read then

$$G(x,t,x',t') = -i\left\langle T\left(\Psi_{H_0}(x,t)\Psi_{H_0}^\dagger(x',t')\right)\right\rangle = \mathrm{Tr}\left(\frac{e^{-H_0/k_BT}\Psi_{H_0}(x,t)\Psi_{H_0}^\dagger(x',t')}{\mathrm{Tr}\left(e^{-H_0/k_BT}\right)}\right), \tag{1.43}$$

where $\Psi_{H_0}(x,t)$ is the field operator with respect to the unperturbed Hamiltonian H_0, which describes the system in equilibrium. The Green's functions depend then only on the difference of the time arguments $t - t'$. We can perform a Fourier transformation to pass from the time domain to the energy space with

$$G(x,t,x',t') = \int \frac{dp}{(2\pi)^3}\int \frac{dE}{2\pi} e^{i(p(x-x')-E(t-t'))}G(p,E)\,. \tag{1.44}$$

Extension of the System to Non-Equilibrium

Now we extend the system to non-equilibrium. To characterize the non-equilibrium state, we assume that the system was at a time $t < t_0$ in equilibrium at temperature T characterized by the Hamiltonian H_0. The state of the system at time t_0 is therefore described by the statistical operator $\rho(H_0)$. For times $t > t_0$ a perturbation H^i is applied to the system which is now described by the Hamiltonian $H = H_0 + H^i$. The new state can now be represented by

$$\rho(t) = U(t,t_0)\rho(H_0)U^\dagger(t,t_0)\,, \tag{1.45}$$

with the full time evolution operator

$$U(t,t_0) = Te^{-i\int_{t_0}^{t} d\bar{t}H(\bar{t})}\,. \tag{1.46}$$

1.4.2.2. Keldysh Contour - The Closed Time Path

One way to handle an interaction described by H^i is to consider it as a perturbation that is adiabatically operating on the non-interacting system, i.e. given by its ground state. Another possibility is to introduce a new time path that passes along the real time axis from t_0 to $t = \infty$ and then back to t_0. This formalism was developed in 1961 by Schwinger [119] and applied by Keldysh [120].

Ground State formalism and transformation to the interaction picture
At this point the field operators $\Psi_H(x,t)$ are in the Heisenberg picture with respect to H. We transform the field operators to the interaction picture, i.e. they are defined with respect to H_0. The corresponding time evolution operator in the interaction picture is defined as

$$U(t,t_r) = Te^{-i\int_{t_r}^{t} d\bar{t} H^{(i)}_{H_0}(\bar{t})} \text{ with } H^{(i)}_{H_0}(t) = e^{iH_0(t-t_r)} H^{(i)} e^{-iH_0(t-t_r)} . \tag{1.47}$$

The field operators are related by the unitary transformation

$$\psi_H(x,t) = U^\dagger(t,t_r)\psi_{H_0}(x,t)U(t,t_r) \text{ with } \psi_{H_0}(x,t) = e^{iH_0(t-t_r)}\psi_{H_0}(x)e^{-iH_0(t-t_r)} . \tag{1.48}$$

Based on these relations we can write the Green's function in terms of the new field operators

$$G(x,t,x',t') = -i\left\langle U^\dagger(\infty,-\infty)T\left(\psi_{H_0}(x,t)\psi^\dagger_{H_0}(x',t')U(\infty,-\infty)\right)\right\rangle , \tag{1.49}$$

while the average is evaluated in the ground state.

One way to handle the interaction is now to assume that it is turned on and off adiabatically. This can be achieved by replacing $H^{(i)}_{H_0}(t)$ with $e^{\epsilon|t|}H^{(i)}_{H_0}(t)$. The non-interacting ground state is transformed via $|G\rangle_\epsilon = U_\epsilon(0,\infty)|G_0\rangle$. In the limit $\lim \epsilon \to 0$ it can be shown perturbatively that the interacting ground state obtains a phase factor [118]

$$U_\epsilon(-\infty,\infty)|G_0\rangle = e^{i\Phi}|G_0\rangle \text{ and therefore } e^{i\Phi} = \langle G_0|U_\epsilon(\infty,-\infty)|G_0\rangle . \tag{1.50}$$

Now the the time-ordered Green's functions can be formulated in terms of the non-interacting ground state $|G_0\rangle$ and with the field operators in the interaction picture

$$G(x,t,x',t') = -i\frac{\langle G_0|T\left(\psi_{H_0}(x,t)\psi^\dagger_{H_0}(x',t')U_\epsilon(\infty,-\infty)\right)|G_0\rangle}{\langle G_0|U_\epsilon(\infty,-\infty)|G_0\rangle} .$$

Approach of a Closed Time Contour
Another, more elegant way is to calculate the propagation on a closed time contour. We introduce a closed time path C that passes along the real time axis from t_0 to $t = \infty$ and

then again back to t_0, as shown in Fig. 1.3. We denote the upper branch with C_+ and the lower one with C_-.

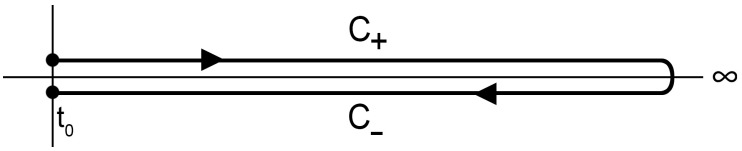

Fig. 1.3.: Basic idea of the Keldysh contour. Extension of the real time axis from $-\infty$ to ∞ while the Keldysh contour passes once in the forward and then in the backward direction. We denote the upper branch with C_+ and the lower branch with C_-

To find the unitary transformation that relates real times and contour times, one considers, as done in the latter part, the unitary transformation of an operator between the Heisenberg picture with respect to H and the Heisenberg picture with respect to H_0 and compares this to the transformation of operators from the Schrödinger picture to find for an arbitrary operator the relation

$$O_H(t) = U_H^\dagger(t,t_0)U_{H_0}(t,t_0)O_H(t)U_{H_0}^\dagger(t,t_0)U_H(t,t_0)\,, \tag{1.51}$$

while we define $V(t,t_0) = U_{H_0}^\dagger(t,t_0)U_H(t,t_0)$. The transformation between the Heisenberg and interaction picture on the closed time path shall be given by

$$O_H(t) = T_C\left(e^{-i\int_C d\tau H^i_{H_0}(\tau)}O_H(t)\right)\,, \tag{1.52}$$

where τ is a time on the contour and T_C orders the operators according to the position of τ. To show the equivalence of the transformation of operators with real-time arguments and those with contour times, one expands the exponential function of the latter equation

$$O_H(t) = \sum_{n=0}^{\infty}\frac{(-i)^n}{n!}\int_C d\tau_1\cdots\int_C d\tau_n T_{c_t}\left(H'_{H_0}(\tau_1)\ldots H'_{H_0}(\tau_n)O_{H_0}(t)\right)\,,$$

and splits the contour into a forward and a backward part $C = C_+ + C_-$. An additional transformation [118, p. 84 ff], and a parametrization of the forward and backward contour according to $\tau(t') = t$, for $t' \in [t_0, t]$ yields the two terms

$$T_{C_+}e^{-i\int_{C_+} d\tau H^i_{H_0}(\tau)} = Te^{-i\int_{t_0}^{t} dt' H^i_{H_0}(t')} = V(t,t_0)\,, \tag{1.53}$$

$$T_{C_-}e^{-i\int_{C_-} d\tau H^i_{H_0}(\tau)} = \tilde{T}e^{i\int_{t_0}^{t} dt' H^i_{H_0}(t')} = V^\dagger(t,t_0)\,. \tag{1.54}$$

The contour ordering operator corresponds to the normal time-ordering $T_{C_+} = T$, and the anti-time-ordering to $T_{C_-} = \tilde{T}$. Due to the equivalences in Eq. (1.54) one can conclude that the times in $V(t,t_0)$ corresponds to the contour times on the forward contour part

C_+ and $V^\dagger(t, t_0)$ corresponds to contour times on the backward part C_-.

Green's Functions on a Closed Time Path

We apply the unitary transformation given in Eq. (1.52) to the field operators of the time-ordered Green's functions and develop in this way the contour-ordered Keldysh Green's functions. The single-particle Green's function contains two field operators that depend, therefore, on two different real-time arguments t_1 and $t_{1'}$. Each of the corresponding contour times that we denote with τ_1 and $\tau_{1'}$ has two possibilities to be placed on the Keldysh contour, as it is shown in Fig. 1.4. We will call the contour-time dependent

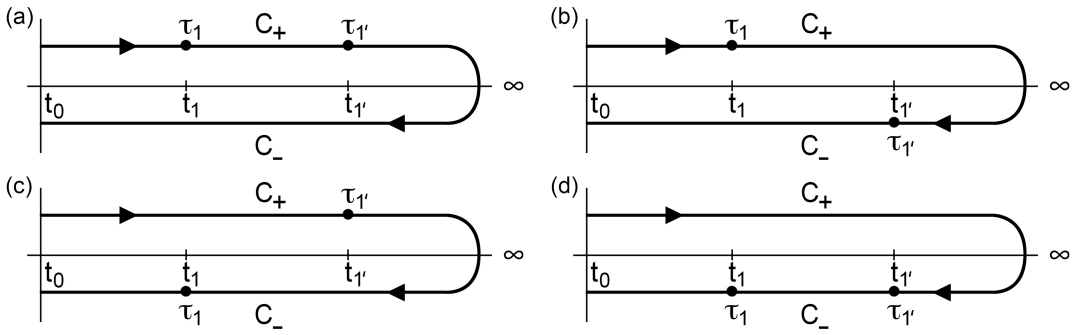

Fig. 1.4.: The real times t_1 and $t_{1'}$ correspond to the contour times τ_1 and $\tau_{1'}$. There are four different possibilities to distribute them on the contour $C = C_+ + C_-$ which belong to four different Keldysh Green's functions. (a): Time-ordered Green's function $G(\tau_1, \tau_{1'})$, (b): Lesser Green's function $G^<(\tau_1, \tau_{1'})$, (c): Greater Green's function $G^>(\tau_1, \tau_{1'})$, (d): Anti-time-ordered Green's function $\tilde{G}(\tau_1, \tau_{1'})$

Green's functions in the following Keldysh Green's functions [1] and define them by

$$G(x_1, \tau_1, x_{1'}, \tau_{1'}) = -i \frac{\mathrm{Tr}(e^{-H/k_BT} T_C(\psi_H(x_1, \tau_1)\psi_H^\dagger(x_{1'}, \tau_{1'})))}{\mathrm{Tr}(e^{-H/k_BT})} . \tag{1.55}$$

The contour ordering symbol T_C orders, as said before, the field operators according to their contour time argument. Therefore we can introduce the four different Keldysh Green's function as we did for those depending on real-times and shown in Fig. 1.4. The time-ordered Keldysh Green's function G, the lesser Keldysh Green's function $G^<$, the

[1] Note that there also exists "the" Keldysh Green's function defined as $G^K = G^> + G^<$. Since we do not use this function in the following, we will use the terminus "Keldysh" to abbreviate the large expression "contour-time-dependent w.r.t. the Keldysh-contour", i.e. in the following "Keldysh Green's functions" are contour-time-depending Green's functions where the contour-times are defined via the Keldysh-contour.

larger Keldysh Green's function $G^{>}$ and the anti-time-ordered Green's function $\tilde{G}$. They are defined as

$$\check{\boldsymbol{G}}(1,1') = \begin{pmatrix} G(1,1') & G^{<}(1,1') \\ G^{>}(1,1') & \tilde{G}(1,1') \end{pmatrix}, \tag{1.56}$$

$$= \begin{pmatrix} -i\left\langle T\left(\psi(1)\psi^{\dagger}(1')\right)\right\rangle & \pm i\left\langle \psi^{\dagger}(1')\psi(1)\right\rangle \\ -i\left\langle \psi(1)\psi^{\dagger}(1')\right\rangle & -i\left\langle \tilde{T}\left(\psi(1)\psi^{\dagger}(1')\right)\right\rangle \end{pmatrix}, \tag{1.57}$$

whereby we used the time-space coordinates $1 = x_1, \tau_1$ and $1' = x_{1'}, \tau_{1'}$. We can transform the field operators defining the Green's function in the interaction picture, i.e.

$$G(1,1') = -i\left\langle T_C\left(\psi_H(1)\psi_H^{\dagger}(1')\right)\right\rangle = -i\left\langle T_C\left(e^{-i\int_C d\tau H^i_{H_0}(\tau)}\psi_{H_0}(1)\psi^{\dagger}_{H_0}(1')\right)\right\rangle . \tag{1.58}$$

In this way, the interaction is captured in the exponential function while the field operators refer to the non-interacting system.

1.4.2.3. Perturbation Expansion

Now we can develop the perturbation theory for the contour-ordered Green's functions. Transforming the field operators in the interaction picture, one obtains the latter Eq. (1.58). With $\beta = 1/k_B T$ it reads in detail

$$G(1,1') = -i\frac{\mathrm{Tr}\left(e^{-\beta H}T_C\left(e^{-i\int_C d\tau\left(H^{(i)}_{H_0}(\tau)\right)}\psi_{H_0}(1)\psi^{\dagger}_{H_0}(1')\right)\right)}{\mathrm{Tr}(e^{-\beta H})} . \tag{1.59}$$

To transform the total expression to the interaction picture, we have to transform the statistical operator ρ as well. We need an imaginary time-evolution operator and therefore the contour has to be extended into to complex time plane from t_0 to $t_0 - i\beta$, that we denote by C_i, as shown in Fig. 1.5. The exponential function can then be written in the

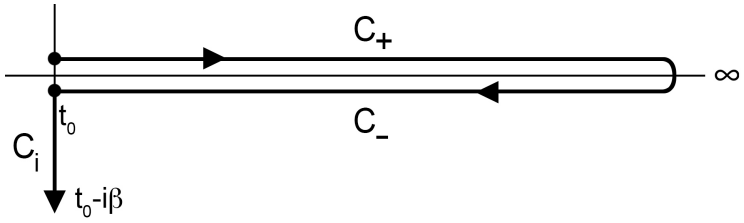

Fig. 1.5.: Extension of the Keldysh contour, see Fig. 1.4, into the complex time plane from t_0 to $t_0 - i\beta$, denoted by C_i.

form

$$e^{-\beta H} = e^{-\beta H_0} T_{C_i} e^{-i \int\limits_{C_i} d\tau H^{(i)}_{H_0}(\tau)} \,. \tag{1.60}$$

We insert the transformation of Eq. (1.60) in the contour-ordered Green's function (1.59) and extend the expression inserting the identity operator in terms of the closed contour contribution $T_C(e^{-i\int_C d\tau(H^i_{H_0}(\tau))}) = 1$ in the denominator and we obtain

$$G(1,1') = -i \frac{\mathrm{Tr}\left(e^{-\beta H_0}\left(T_{C_a} e^{-i\int\limits_{C_a} d\tau H^{(i)}_{H_0}(\tau)}\right) T_C\left(e^{-i\int\limits_{C} d\tau H^{(i)}_{H_0}(\tau)} \psi_{H_0}(1)\psi^\dagger_{H_0}(1')\right)\right)}{\mathrm{Tr}\left(e^{-\beta H_0} T_{C_a} e^{-i\int\limits_{C_a} d\tau H^{(i)}_{H_0}(\tau)} T_C\left(e^{-i\int\limits_{C} d\tau H^{(i)}_{H_0}(\tau)}\right)\right)} \,. \tag{1.61}$$

Since we do not consider transient phenomena, we can set t_0 in the far past to minus infinity, i.e. $t_0 = -\infty$. In this case, we can neglect the contribution of the imaginary contour part C_i compared to the whole contour $C + C_i$, and we can obtain the final expression [118, p. 92 ff]

$$G(1,1') = \mathrm{Tr}\left(\rho_0 T_C\left(e^{-i\int\limits_{C} d\tau H^{(i)}_{H_0}(\tau)} \psi_{H_0}(1)\psi^\dagger_{H_0}(1')\right)\right) \tag{1.62}$$

with $\rho_0 = e^{-H_0/k_BT}/\mathrm{Tr}\left(e^{-H_0/k_BT}\right)$. At this point, we are able to expand the Green's function, i.e. expand the exponential function containing the integral over the interaction Hamiltonian.

1.4.2.4. Wick's Theorem

The perturbation expansion of the exponential function in Eq. (1.62) leads to products of the interaction Hamiltonian and therefore to products of fermionic and/or bosonic field operators. The common trace over the bosonic and fermionic operators can be separated since they are independent of each other. To calculate the average of a long chain of field operators we use Wick's theorem, which allows us to decompose a contour-ordered string of creation and annihilation operators, derived from a quadratic Hamiltonian, into a sum over all possible pairwise products

$$\left\langle T_C\left(c(\tau_n)c(\tau_{(n-1)})\ldots c(\tau_2)c(\tau_1)\right)\right\rangle = \sum_{\text{a.p.p.}} \prod_{q,q'} \left\langle T_{c_t}\left(c_q(\tau)c_{q'}(\tau')\right)\right\rangle \,. \tag{1.63}$$

We sum over all possible ways of picking pairs (a.p.p.) of the n operators and neglect the ordering within a pair, while c_q represents either a creation or an annihilation operator.

Writing bosonic field operators ϕ and the fermionic field operators ψ, we specify Wick's theorem for the case of a fermionic or bosonic chain of operators.

Wick's theorem for bosonic operators:

$$\begin{aligned}&\langle T_C\left(\phi(x_{2n},\tau_{2n})\phi(x_{2n-1},\tau_{2n-1})\ldots\phi(x_2,\tau_2)\phi(x_1,\tau_1)\right)\rangle\\&=\sum_{a.p.p.}\prod_{i\neq j}\langle T_C\left(\phi(x_i,\tau_i)\phi(x_j,\tau_j)\right)\rangle=\sum_{a.p.p.}\prod_{i\neq j}i^N D_0(x_i,\tau_i;x_j,\tau_j)\end{aligned}\tag{1.64}$$

Wick's theorem of fermionic operators:

$$\begin{aligned}&\langle T_C\left(\psi(x_{2n},\tau_{2n})\psi(x_{2n-1},\tau_{2n-1})\ldots\psi(x_2,\tau_2)\psi(x_1,\tau_1)\right)\rangle\\&=\sum_{a.p.p.}\prod_{i\neq j}(-1)^{\zeta_P}\langle T_C\left(\psi(x_i,\tau_i)\psi(x_j,\tau_j)\right)\rangle=\sum_{a.p.p.}\prod_{i\neq j}(-1)^{\zeta_P}i^N G_0(x_i,\tau_i;x_j,\tau_j)\end{aligned}\tag{1.65}$$

For the bosonic and fermionic case, the last step is only valid if one operator is a creation and the other is an annihilation operator. If the expression contains an odd number of creation or annihilation operators, it is zero since the number of particles is not conserved. $(-1)^{\zeta_P}$ denotes the number of transpositions of operators since each swap of two fermionic operators adds a factor of (-1).

1.4.2.5. Feynman Diagrams and the Concept of Self-Energy

Performing the perturbative expansion and applying Wick's theorem leads to a huge, in principle infinite, amount of different combinations of Green's functions. In 1948, Richard Feynman introduced a method to represent these contributions graphically, the so-called Feynman diagrams [121]. On the one hand, the diagrams represent the perturbation theory in a (mathematical) exact way, while it is also an impressive possibility to decode the physical statement of long and messy expressions [115]. To use Feynman diagrams, we need some basic elements [122], as shown in Fig. 1.6

The structure of the Feynman diagrams depends directly on the kind of interaction in the system. The two standard examples given in most textbooks are interaction with an external static potential, and the electron-electron interaction [114, 115, 123]. Since we consider the electron-photon interaction in the minimal example in more detail at the end of this chapter, we just briefly show the results for the case of an external potential [114].

Feynman diagrams for an external potential
In this example we consider electrons that are interacting with an external potential

$$V^{(0)}=\sum_\sigma\int dr\Psi_\sigma^{(0)\dagger}(rt)V(r)\Psi_\sigma^{(0)}(rt)\,.\tag{1.66}$$

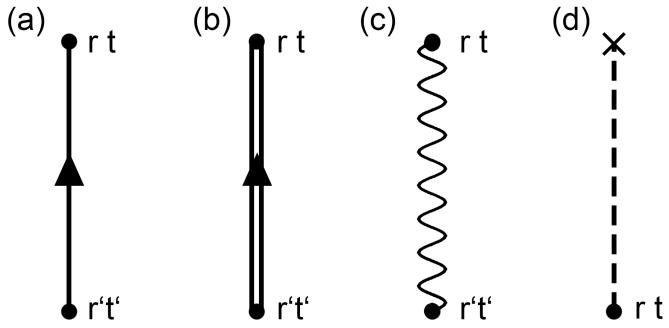

Fig. 1.6.: Basic elements of Feynman diagrams. (a) A straight line corresponds to the unperturbed propagator $G^{(0)}(r,t,r',t')$, (b) the double line represents the full propagator $G(r',t',r,t)$, (c) a wiggled line describes an interaction between the events $r't'$ and rt, (d) a dashed line represents an interaction with an external potential.

The expansion of the full Green's function in terms of the external potential is equivalent to the Feynman diagrams in Fig. 1.7. For the n-th perturbation order, one obtains n+1 propagators, i.e. the unperturbed Green's function and n interaction lines, i.e. the external potential, while one needs to integrate over the internal variables. Defining the "Feynman rules" [115, p. 228 ff] one can determine the perturbative expansion directly in terms of Feynman diagrams. The second-order diagram is then given my the mathematical

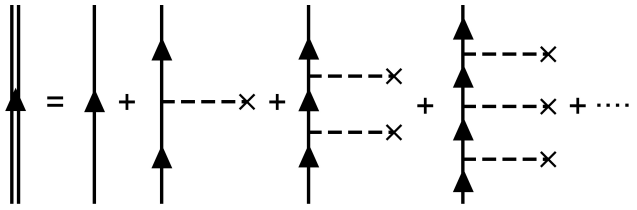

Fig. 1.7.: Perturbative series of the Green's function upon third order, graphically represented by Feynman diagrams, with an interaction given by an external potential.

expression

$$\int t_1 \int t_2 \; G^{(0)}(rt, r_1t_1)V(r_1)G^{(0)}(r_1t_1, r_2t_2)V(r_2)G^{(0)}(r_2t_2, r't') \,. \tag{1.67}$$

In this example we can easily see the concept of self-energy. As a first idea we consider the complete (infinite) expansion and summarize the occurring diagrams in the following way, compare Fig. 1.8. While we denote the gray area with Σ_I, we define a first idea of the self-energy and write the full propagator as

$$G = G^{(0)} + G^{(0)}\Sigma_I G^{(0)} \,. \tag{1.68}$$

We can see that the the diagrams defining Σ_I repeat the same sub-part several times. In detail, the n-th order diagrams contain n times exactly the same expression. Extending

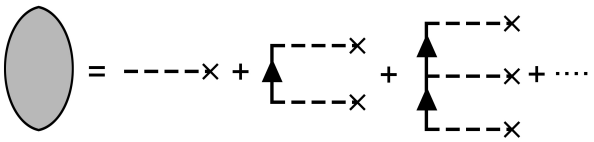

Fig. 1.8.: Perturbative series of the self-energy Σ_I.

and summarizing these contributions in a different way, we define the (proper) self-energy according to Fig. 1.9. In this way we finally recover again the Dyson equation in terms of

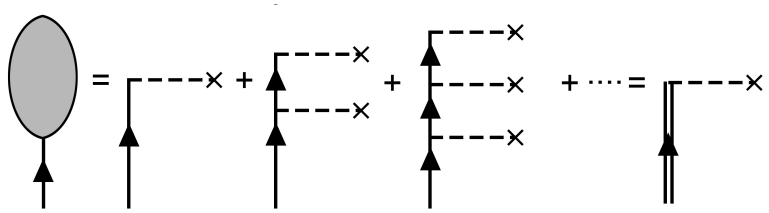

Fig. 1.9.: Perturbative series of the proper self-energy Σ.

the self-energy, i.e.

$$G = G^{(0)} + G^{(0)}\Sigma G\,. \tag{1.69}$$

1.4.2.6. Disconnected Diagrams

To develop the full propagator, we consider the numerator and denominator separately. It can then be shown that the denominator completely cancels all the "disconnected diagrams" and, therefore, only so-called "connected diagrams" remain. For the general derivation, we refer to textbooks but show the main principle in the example of pair interactions [115] .

The numerator contains the diagrams in Fig. 1.10. The free propagator belongs to the zeroth-order, the following diagrams to the first, and those of the second line to the second-order of the perturbative expansion. Of course, there are many more diagrams, but the main difference becomes clear already for this selection. In the first and fourth diagrams, all propagator and interaction lines are connected, and we refer to them as "connected diagrams". The second and third diagrams are examples of pure "disconnected diagrams" since the propagator between the reference points is not connected to the internal arguments. The last diagram in the second line is a combination of a connected and disconnected diagram. Diagrams that contribute to the denominator are shown in Fig. 1.11. As we can see, only disconnected diagrams contribute to it. If one considers all diagrams of the numerator, it can be separated into a part containing only completely connected diagrams, i.e. the first bracket in Fig. 1.12 and those terms that contribute to the diagrams that are combinations of connected and disconnected parts. This term

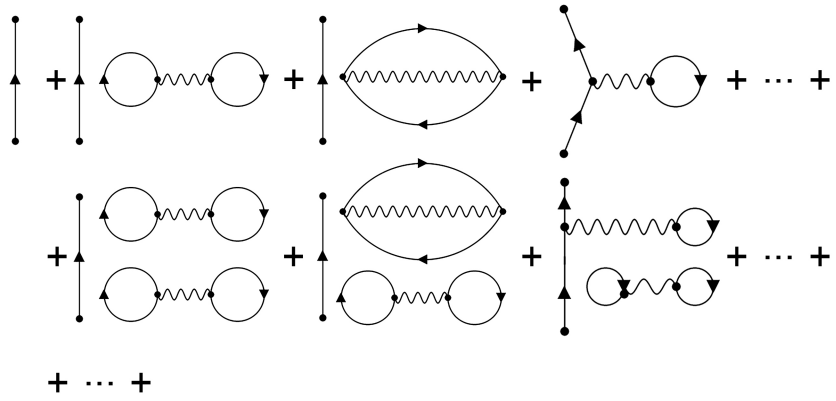

Fig. 1.10.: Feynman diagrams contributing to the numerator of the full propagator.

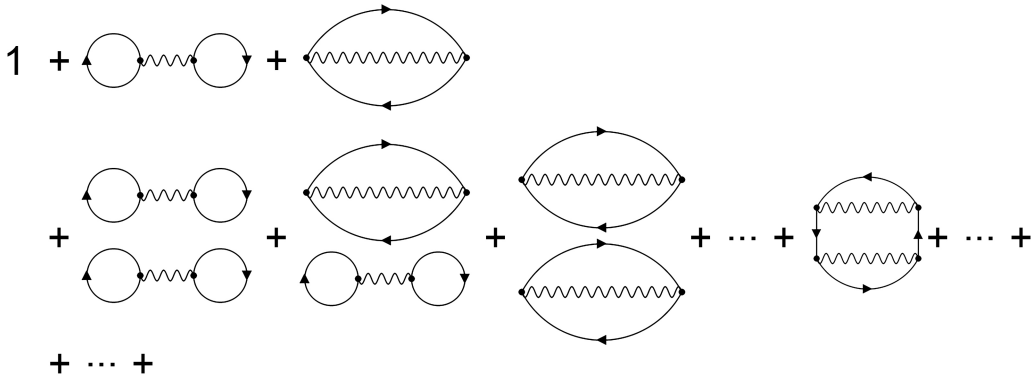

Fig. 1.11.: Feynman diagrams contributing to the denominator of the full propagator.

corresponds now exactly to the denominator and therefore cancels. Finally, one considers only the connected diagrams to determine the propagator in terms of Feynman diagrams.

1.4.2.7. Tadpole Diagrams

A so-called tadpole diagram is a Feynman diagram consisting of a loop and a single external leg. Therefore it can be disconnected by cutting just a single line. It is contributing to the vacuum expectation value of a field $\langle\Psi\rangle = \langle 0|\Psi(x,t)|0\rangle$. If the tadpoles of the given field are nonzero, one can redefine it via $\Phi(x) = \Psi(x) - \langle 0|\Psi(x)|0\rangle$ [@124, 125, 126]. Regarding a microwave cavity with the creation and annihilation operators $\hat{b}$, $\hat{b}^\dagger$, coupled to a quantum dot, this effect appears due to a shift of the resonator because of an average, nonzero force acting on it. Without such a shift, these tadpole diagrams would not appear in a system. To neglect the terms containing tadpoles, one can redefine the bosonic operator concerning this shift like $\hat{b}' = \hat{b} - \left\langle \hat{b} \right\rangle$. We show this in more detail in the minimal example in the next subsection.

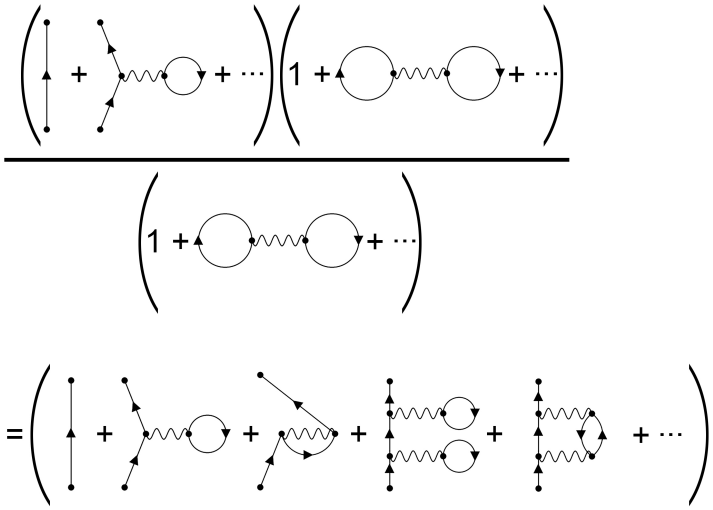

Fig. 1.12.: Feynman diagrams that did not cancel and finally determine the full propagator.

1.4.2.8. Minimal Example

In the latter section, we finished the minimal example by determining the retarded and advanced Green's function in Eq. (1.33) for a quantum dot with a single level coupled to left and right leads. We move on with this example in the following way: We first determine the Keldysh Green's functions. Then we couple this single level to a single microwave cavity. We perform the perturbative expansion on the single-particle Green's function and simplify it with Wick's theorem. Finally, we show the perturbative expansion in terms of Feynman diagrams and identify disconnected and tadpole diagrams.

Unperturbed Greater and Lesser Green's Function of the Leads

We use the Dyson equation to determine the full Keldysh Green's function. For this purpose, we will need the unperturbed Green's functions of the leads. The unperturbed Green's functions describe the isolated uncoupled subsystems, i.e. they are independent of the central region, and this result is valid both for a single and a double dot coupled to the leads. We first determine the unperturbed greater and lesser Green's functions, i.e. $g^{>}(E)$ and $g^{<}(E)$, [114, 127]. The lesser Green's function of a non-interacting system, that we denote with $\tilde{G}^{<}(E)$, can be expressed in terms of the electron distribution in equilibrium [2] and therefore with the local density of states $\rho_i(E)$ and the Fermi function $f(E)$ in the following way

$$\tilde{G}^{<}_{ii}(0) = i\langle c_i^{\dagger}(0)c_i(0)\rangle = i\langle n_i\rangle = \int \frac{dE}{2\pi}\tilde{G}^{<}_{ii}(E) = i\int \rho_i(E)f(E)dE\,. \tag{1.70}$$

[2] To be precise it is only the diagonal component. Since we consider the unperturbed, i.e. uncoupled system the offdiagonal elements vanish.

The greater Green's function of a non-interacting system can be found in an analogue way, while it is proportional to $1 - f(E)$. Together with the relation

$$G^a(E) - G^r(E) = G^<(E) - G^>(E)\,. \tag{1.71}$$

We can express the lesser and greater Green's functions in terms of the retarded and advanced Green's functions. The unperturbed system, i.e. the isolated dot(s) and leads, is a system in equilibrium without any interaction. The unperturbed greater and lesser Green's functions can therefore be defined in the same way as those of a non-interacting system and we end up with [114]

$$g^<_{ij}(E) = \left[g^a_{ij}(E) - g^r_{ij}(E)\right] f(E)\,, \tag{1.72}$$

$$g^>_{ij}(E) = -\left[g^a_{ij}(E) - g^r_{ij}(E)\right] [1 - f(E)]\,, \tag{1.73}$$

for $i = j$ and zero else. Since these functions are diagonal, the Green's functions are proportional to the density of states. For a quantum dot with a single energy level ε_i, this density of states is a delta function

$$\rho_i(E) = \delta(E - \varepsilon_i)\,. \tag{1.74}$$

We will see later that this fact will simplify the calculation of the full greater and lesser Green's functions, and it is not necessary to determine the unperturbed ones further. The voltage that is applied across the parallel double quantum dot is included in the unperturbed Hamiltonian by shifting the corresponding chemical potentials, which changes, in general, the energy-dependence of the unperturbed Green's functions. Since we still use the wide-band approximation for the (normal) leads, the Green's function becomes independent of the energy and the shift by the chemical potential. The energy shift is captured in the Fermi function describing the leads and we use the short notation $f_R = f(E + eV/2)$ and $f_L = f(E - eV/2)$.
The unperturbed Green's functions of the lead $r = L, R$ read

$$g^<_{rr}(E) = \quad [g^a_{rr}(E) - g^r_{rr}(E)]\, f_r(E)\,, \tag{1.75}$$

$$g^>_{rr}(E) = -\,[g^a_{rr}(E) - g^r_{rr}(E)]\, [1 - f_r(E)]\,. \tag{1.76}$$

Full greater and lesser Green's function
Now we can determine the greater and lesser Keldysh Green's functions via the Dyson equation. In the system of this minimal example, it can be simplified to the expression

$$G^<_{ij} = \sum_{lm} G^r_{il} \Sigma^<_{lm} G^a_{mj}\,. \tag{1.77}$$

The derivation of the latter equation needs a detailed explanation that we skip here but take care of it in the main part in Section 2.3.3.1. The self-energy of such a system consists only of the tunneling self-energy [128], which is defined as

$$\Sigma^{<}_{lm} = \sum_{r=L,R} V^{*}_{r,l} g^{<}_{rr} V_{r,m} \,. \tag{1.78}$$

Using the wide-band approximation, the lesser and greater self-energy become

$$\Sigma^{<}_{11} = i\Gamma(f_L + f_R)\,, \quad \Sigma^{>}_{11} = i\Gamma(f_L + f_R - 2)\,. \tag{1.79}$$

From this we can determine, together with the retarded and advanced Green's functions from Eq. (1.33), the greater and lesser Keldysh Green's functions in the high-voltage (h.v.) limit

$$G^{<}_{11} = G^{r}_{11}\Sigma^{<}_{11}G^{a}_{11} = \frac{i\Gamma(f_L + f_R)}{(E-\varepsilon)^2 + \Gamma^2} \overset{h.v.}{=} \frac{i\Gamma}{(E-\varepsilon)^2 + \Gamma^2}\,, \tag{1.80}$$

$$G^{>}_{11} = G^{r}_{11}\Sigma^{>}_{11}G^{a}_{11} = \frac{i\Gamma(f_L + f_R - 2)}{(E-\varepsilon)^2 + \Gamma^2} \overset{h.v.}{=} \frac{-i\Gamma}{(E-\varepsilon)^2 + \Gamma^2}\,. \tag{1.81}$$

For the time-ordered and anti-time-ordered Green's function, we use the relations

$$G_{11} = G^{<}_{11} + G^{r}_{11} = \frac{i\Gamma}{(E-\varepsilon)^2 + \Gamma^2} + \frac{1}{E - \varepsilon - i\Gamma} = \frac{E-\varepsilon}{(E-\varepsilon)^2 + \Gamma^2}\,, \tag{1.82}$$

$$\tilde{G}_{11} = G^{<}_{11} - G^{a}_{11} = \frac{i\Gamma}{(E-\varepsilon)^2 + \Gamma^2} - \frac{1}{E - \varepsilon + i\Gamma} = -\frac{E-\varepsilon}{(E-\varepsilon)^2 + \Gamma^2}\,. \tag{1.83}$$

In summary, we get the four Keldysh Green's functions in the high-voltage (h.v.) bias limit

$$\hat{\boldsymbol{G}}_{\mathbf{11}} = \begin{pmatrix} G_{11} & G^{<}_{11} \\ G^{>}_{11} & \tilde{G}_{11} \end{pmatrix} = \frac{1}{(E-\varepsilon)^2 + \Gamma^2} \begin{pmatrix} E-\varepsilon & i\Gamma \\ -i\Gamma & -(E-\varepsilon) \end{pmatrix}\,. \tag{1.84}$$

Perturbation expansion

As a next step, we couple a single microwave cavity to the quantum dot with the single electronic level. Therefore, the Hamiltonian will be extended by the photonic part, and the electron-photon interaction

$$H_{\text{total}} = H_{\varepsilon} + \omega_0 \hat{a}^{\dagger}\hat{a} + \lambda(\hat{a} + \hat{a}^{\dagger})\hat{d}^{\dagger}\hat{d}\,, \tag{1.85}$$

where H_{ε} given in Eq. (1.26) describes the electronic part, $\hat{a}$ are the bosonic operators, ω_0 the resonance frequency of the cavity and λ the dot-cavity coupling parameter. We want to determine the single-particle Green's function. To obtain this result we perform a perturbation expansion upon second order in the electron-photon interaction

$$\hat{H}_{\text{int}} = \lambda \left(\hat{a}^{\dagger} + \hat{a} \right) \hat{d}^{\dagger}\hat{d} \quad . \tag{1.86}$$

The first (and third) ordered term of the perturbative expansion become zero, because of the odd number of operators. However, the second-order perturbation expansion is nonzero and reads

$$\left\langle T_{\mathrm{C}}\left(\hat{a}(t)\hat{a}(t')^{\dagger}\right)\right\rangle \approx \left\langle T_{\mathrm{C}}\left(\hat{a}(t)\hat{a}(t')^{\dagger}\right)\right\rangle^{(0)} \tag{1.87}$$

$$+\frac{1}{2}\int_{C} dt_1 \int_{C} dt_2 (-i)^2 \left\langle T_{\mathrm{C}}\left(\hat{a}_t\hat{a}_{t'}^{\dagger}\left[\lambda(\hat{a}+\hat{a}^{\dagger})\right]_{t_1}\left[\lambda(\hat{a}+\hat{a}^{\dagger})\right]_{t_2}\right)\right\rangle . \tag{1.88}$$

Multiplying the terms of the interaction Hamiltonian, we can separate the string of bosonic and fermionic operators.

Wick's theorem

To simplify this expressions we then apply Wick's theorem and get four different contributions for the second order term:

$$\begin{aligned}
\left\langle T_{\mathrm{C}}\left(\hat{a}(t)\hat{a}(t')^{\dagger}\right)\right\rangle \approx \left\langle T_{\mathrm{C}}\left(\hat{a}(t)\hat{a}(t')^{\dagger}\right)\right\rangle^{(0)} \\
-\lambda^2 \int_{C} dt_1 \int_{C} dt_2 \left\langle T_{\mathrm{C}}\left(\hat{a}_t\hat{a}_{t'}^{\dagger}\right)\right\rangle \left\langle T_{\mathrm{C}}\left(\hat{a}_{t_1}\hat{a}_{t_2}^{\dagger}\right)\right\rangle \left\langle T_{\mathrm{C}}\left(\hat{d}_{t_1}^{\dagger}\hat{d}_{t_1}\right)\right\rangle \left\langle T_{\mathrm{C}}\left(\hat{d}_{t_2}^{\dagger}\hat{d}_{t_2}\right)\right\rangle \\
+\lambda^2 \int_{C} dt_1 \int_{C} dt_2 \left\langle T_{\mathrm{C}}\left(\hat{a}_t\hat{a}_{t'}^{\dagger}\right)\right\rangle \left\langle T_{\mathrm{C}}\left(\hat{a}_{t_1}\hat{a}_{t_2}^{\dagger}\right)\right\rangle \left\langle T_{\mathrm{C}}\left(\hat{d}_{t_1}^{\dagger}\hat{d}_{t_2}\right)\right\rangle \left\langle T_{\mathrm{C}}\left(\hat{d}_{t_2}^{\dagger}\hat{d}_{t_1}\right)\right\rangle \\
-\lambda^2 \int_{C} dt_1 \int_{C} dt_2 \left\langle T_{\mathrm{C}}\left(\hat{a}_t\hat{a}_{t_2}^{\dagger}\right)\right\rangle \left\langle T_{\mathrm{C}}\left(\hat{a}_{t_1}\hat{a}_{t'}^{\dagger}\right)\right\rangle \left\langle T_{\mathrm{C}}\left(\hat{d}_{t_1}^{\dagger}\hat{d}_{t_1}\right)\right\rangle \left\langle T_{\mathrm{C}}\left(\hat{d}_{t_2}^{\dagger}\hat{d}_{t_2}\right)\right\rangle \\
+\lambda^2 \int_{C} dt_1 \int_{C} dt_2 \left\langle T_{\mathrm{C}}\left(\hat{a}_t\hat{a}_{t_2}^{\dagger}\right)\right\rangle \left\langle T_{\mathrm{C}}\left(\hat{a}_{t_1}\hat{a}_{t'}^{\dagger}\right)\right\rangle \left\langle T_{\mathrm{C}}\left(\hat{d}_{t_1}^{\dagger}\hat{d}_{t_2}\right)\right\rangle \left\langle T_{\mathrm{C}}\left(\hat{d}_{t_2}^{\dagger}\hat{d}_{t_1}\right)\right\rangle .
\end{aligned} \tag{1.89}$$

Feynman diagrams

The occuring terms can now be represented as Feynman diagrams. Of course it would also have been possible to develop them directly. For the bosonic propagator we use the wiggled line while the arrow indicates the time-dependence. The straight line defines the fermionic ones. The diagrams are shown in Fig. 1.13 while they are given in the same

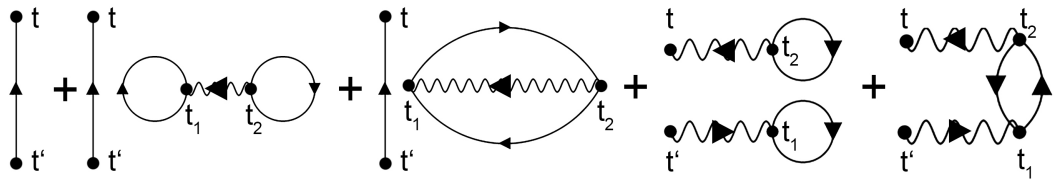

Fig. 1.13.: Feynman diagrams contributing to the numerator of the full propagator.

order as the contributions appear in Eq. (1.89). The first diagram corresponds to the zeroth-order. The other four diagrams correspond to the second-order while only the last

one is a connected diagram. In total, only the first and last diagrams contribute to the result. Furthermore, the third diagram of the second order is a tadpole diagram.

Tadpole diagrams

To explain it in more detail, we check the first-order perturbative expansion of $\langle b \rangle$

$$\langle b \rangle \approx \underbrace{\langle b \rangle_0}_{0} + \left\langle \lambda \int_C dt_1 (-i) b_t \left((b_{t_1} + b_{t_1}^\dagger) \tilde{d}_{t_1}^\dagger \tilde{d}_{t_1} \right) \right\rangle \tag{1.90}$$

$$= -i\lambda \int_C dt_1 \langle b_t b_{t_1} \rangle \left\langle \tilde{d}_{t_1}^\dagger \tilde{d}_{t_1} \right\rangle \tag{1.91}$$

$$= i\lambda \int_C dt_1 D(t, t_1) G_{22}(t_1, t_1) \tag{1.92}$$

and it is corresponding Feynman diagram. The first-order term represents the first-order

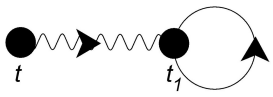

Fig. 1.14.: Tadpole diagram of order of λ, i.e. the first perturbative expansion of $\langle b \rangle$.

tadpole diagram. We can redefine the bosonic operator via $b' = b - \langle b \rangle_\lambda$ and obtain

$$\langle b' \rangle = \langle b \rangle - \langle b \rangle_\lambda = \underbrace{\langle b \rangle_0}_{0} + \langle b \rangle_\lambda + \underbrace{\langle b \rangle_{\lambda^2}}_{0} + \langle b \rangle_{\lambda^3} + \ldots - \langle b \rangle_\lambda \ . \tag{1.93}$$

Since the term $\langle b \rangle_\lambda$ is canceled in this way, diagrams containing tadpoles of the first order would vanish with the new bosonic operators $b' = b - \langle b \rangle$ and only a tadpole diagram of third-order or higher remain. If we proceed in this way and redefine the bosonic operator via $b' = b - \langle b \rangle$ with $\langle b \rangle = \langle b \rangle_\lambda + \langle b \rangle_{\lambda^2} + \ldots$, every tadpole-like diagram is canceled and results in a $\langle b' \rangle$, i.e. without tadpoles. Therefore, the diagrams containing tadpoles do not contribute to the result. Regarding a perturbative expansion up to the fourth order, only tadpole diagrams of first and third order appear. These tadpole diagrams are depicted in Fig. 1.15.

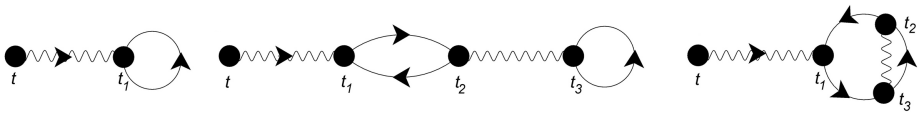

Fig. 1.15.: Perturbative expansion of $\langle b \rangle$ up to third order.

2 Quantum-Correlated Photons Generated by Nonlocal Electron Transport

F. Hellbach, F. Pauly, W. Belzig, G. Rastelli, *Quantum-correlated photons generated by nonlocal electron transport*, Phys. Rev. B **105**, L241407 (2022)

2.1 System and Main Idea

We analyze a parallel double quantum dot system, as shown in Fig. 2.1. Both dots are coupled to a common left and right lead with the chemical potential μ_{L} and μ_{R}, while electron transport between lead and dot is defined by the hopping constant t. Each dot is capacitively coupled to one of two separated microwave cavities of resonance frequencies ω_a and ω_b. We denote the coupling strength of the dot-cavity interaction by λ.

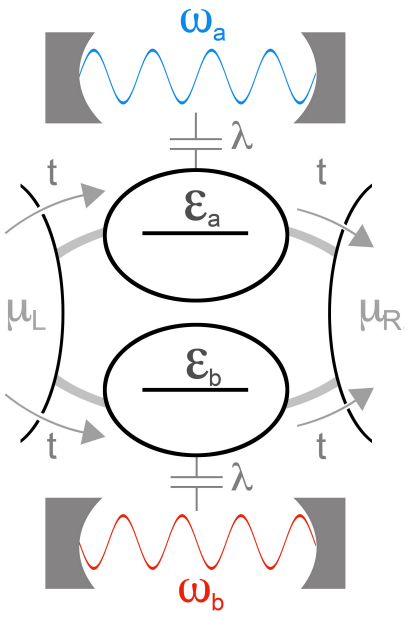

Fig. 2.1.: Main model: A parallel double quantum dot with a single electronic energy level in each quantum dot. Each dot is coupled to one of two separated microwave cavities and a common left and right lead.

We study a spinless model, consisting of a single electron state in each dot, whose energy level is given by $\varepsilon_{a,b} = \bar{\varepsilon} \pm \Delta\varepsilon$ for the upper and lower dot, respectively. There is no direct tunneling between the dots. A priori, we cannot exclude the possibility that both dots are occupied simultaneously. However, the tunneling of electrons into the double-dot system is an uncorrelated event in our model due to the lack of electron-electron interactions. Therefore, the process cannot generate quantum correlations between the two microwave cavities that go beyond the elementary single-electron tunneling process that we discuss in the following.

We explore how correlation and entanglement between the two cavities emerge by the coherent transport of a single electron passing simultaneously through the two different dots. Let us first assume that the energy levels of the dots are close to each other, in the sense that the energy difference is small compared to their broadening $|\Delta\varepsilon| = |\varepsilon_a - \varepsilon_b| \ll \Gamma$, i.e. the energy distributions overlap. In this regime the two paths are indistinguishable, and the electron flows through both branches simultaneously, causing quantum interference in the double quantum dot system. This means that the linear conductance associated with the levels of the double-dot system is different from the sum of the linear conductances of the two separate dots, i.e. different from the single level regime, see Chapter 2.3.2. If the difference between the two energy levels is increased, i.e. $|\Delta\varepsilon| \gg \Gamma$, the interference is destroyed, and the electron transfer occurs via the incoherent sum of the two possible paths, namely, the electron proceeds independently through the upper or through the lower branch, but not simultaneously through both. As we will see later, this mechanism allows or prevents entanglement. In Fig. 2.2 we sketch the idealized procedure of the entanglement process that we substantiate with the following equations.

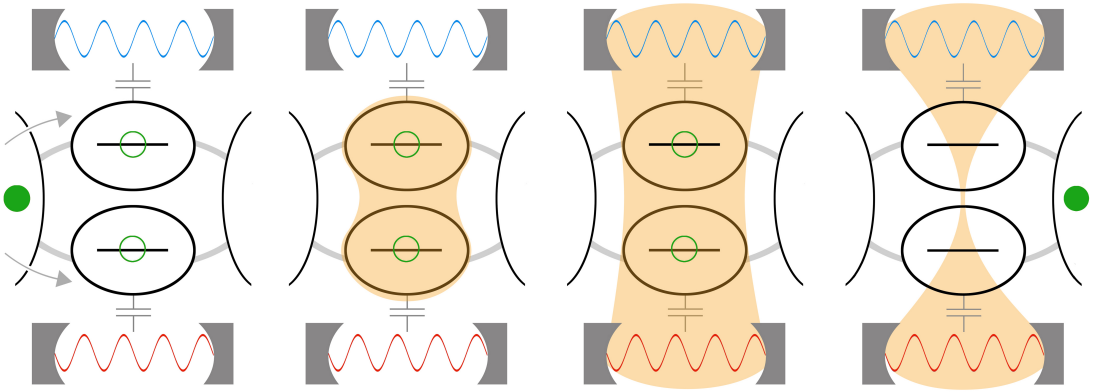

Fig. 2.2.: Sketch of the main idea: The electron travels inside the double-dot system and splits between the two branches. Therefore the electronic state is a coherent superposition of the electron occupying the upper or the lower quantum dot. Due to this superposition and after some dwell time, the dot-cavity interaction correlates the two cavities. Without knowledge of the path through that the electron has traveled, it is removed from the system in some kind of non-local measurement, creating an entangled state between the cavities that persists even if the dot state is empty.

When the electron travels inside the system, it splits. Therefore the electronic state is a coherent superposition of the electron occupying the upper dot or the lower dot, with the corresponding occupations $n_{\mathrm{a}}^{(\mathrm{el})}$ and $n_{\mathrm{b}}^{(\mathrm{el})}$. The state of the complete system is this superposed electron state coupled to the two ground states of the cavities $|\mathrm{GS}\rangle_{\mathrm{a}}$ and $|\mathrm{GS}\rangle_{\mathrm{b}}$

$$|\Psi\rangle_{\mathrm{in}} = \frac{1}{\sqrt{2}} \left(\left| n_{\mathrm{a}}^{(\mathrm{el})} = 1, n_{\mathrm{b}}^{(\mathrm{el})} = 0 \right\rangle + \left| n_{\mathrm{a}}^{(\mathrm{el})} = 0, n_{\mathrm{b}}^{(\mathrm{el})} = 1 \right\rangle \right) |\mathrm{GS}\rangle_{\mathrm{a}} \, |\mathrm{GS}\rangle_{\mathrm{b}} \, . \tag{2.1}$$

The interaction between an electron in a dot and the corresponding cavity ensures that a coherent state is created, depending on the position of the electron, described by the unitary time evolution operator

$$\hat{U}(\tau) = \hat{\mathcal{D}}_{\mathrm{a}}[\hat{n}_{\mathrm{a}}^{(\mathrm{el})} \rho(\tau)] \times \hat{\mathcal{D}}_{\mathrm{b}}[\hat{n}_{\mathrm{b}}^{(\mathrm{el})} \rho(\tau)] \, , \tag{2.2}$$

where $\hat{n}_{\mathrm{a}}^{(\mathrm{el})}$ and $\hat{n}_{\mathrm{b}}^{(\mathrm{el})}$ are the electron occupation operators of the two dots, $\hat{\mathcal{D}}_{\mathrm{a,b}}[\xi]$ are the coherent displacement operators with the associated parameter ξ, and $\rho(t) = -i\lambda t$. (We set $\hbar = 1$ here and in the following.) After some dwell time τ the state has evolved, and the dot-cavity interaction correlates the two cavities,

$$\hat{U}(\tau) \, |\Psi\rangle_{\mathrm{in}} = \frac{1}{\sqrt{2}} \Big(\left| n_{\mathrm{a}}^{(\mathrm{el})} = 1, n_{\mathrm{b}}^{(\mathrm{el})} = 0 \right\rangle |\rho(\tau)\rangle_{\mathrm{a}} \, |\mathrm{GS}\rangle_{\mathrm{b}} + \left| n_{\mathrm{a}}^{(\mathrm{el})} = 0, n_{\mathrm{b}}^{(\mathrm{el})} = 1 \right\rangle |\mathrm{GS}\rangle_{\mathrm{a}} \, |\rho(\tau)\rangle_{\mathrm{b}} \Big), \tag{2.3}$$

where $|\rho(\tau)\rangle_{\mathrm{a}}$ and $|\rho(\tau)\rangle_{\mathrm{b}}$ are coherent states of the cavities. The quantum delocalization of the single electron in the double-dot leads to a quantum correlation of the two cavities, which indicates the possibility of an entangled state. This state can persist even when the electron leaves the system, and the dot state is empty,

$$|\Psi\rangle_{\mathrm{out}} = \frac{1}{\sqrt{2}} \, |0,0\rangle \, (|\rho(\tau)\rangle_{\mathrm{a}} \, |\mathrm{GS}\rangle_{\mathrm{b}} + |\mathrm{GS}\rangle_{\mathrm{a}} \, |\rho(\tau)\rangle_{\mathrm{b}}). \tag{2.4}$$

Notice that in the last step the electron is removed without the knowledge of which path it passed through, and this operation corresponds to a kind of non-local measurement. When a second electron subsequently enters the double-dot, one can repeat a similar argument starting from the entangled photon state instead of the vacuum. However, for long times, the internal losses of the cavities should be included as well as their energy relaxation and dephasing due to the coupling with the conducting leads via the double-dot. In other words, Fig. 2.2 describes just the idealized argument of the entanglement generation process, where it is assumed that the interaction time of the electron and the cavity is short and that decoherence effects of the dots happen much later regarding the timescale of the interaction.

2.2 Hamiltonian and Correlators

To investigate the possibility of entanglement, we will evaluate two quantities: We prove correlation via the covariance of the Fock occupation numbers and quantum correlation via the violation of the classical Cauchy-Schwarz inequality [103] for the two cavities. We calculate these two quantities, and some more, by a perturbative expansion using the Keldysh Green's function formalism. For this reason, we determine the Keldysh Green's functions of the pure fermionic system, namely the parallel double-dot coupled to the left and right lead, as well as the Green's functions of the pure bosonic system, which consists of the two isolated microwave cavities. We write the covariance and classical Cauchy-Schwarz inequality in terms of single- and two-particle Green's functions. We then perform a perturbative expansion in the dot-cavity interaction Hamiltonian up to the fourth order.
The double quantum dot system with the attached cavities, shown in Fig. 2.1, is described by the following Hamiltonian including the electronic part $\hat{H}_{\text{el}}$, the photonic part $\hat{H}_{\text{ph}}$ as well as the electron-photon interaction $\hat{H}_{\text{int}}$:

$$\hat{H} = \hat{H}_{\text{el}} + \hat{H}_{\text{ph}} + \hat{H}_{\text{int}}\,, \tag{2.5}$$

$$\begin{aligned}\hat{H}_{\text{el}} = &\sum_{r=\text{L,R}} \sum_{k} (\varepsilon_{kr} - \mu_r)\, \hat{c}^\dagger_{kr} \hat{c}_{kr} + \sum_{\alpha=\text{a,b}} \varepsilon_\alpha \hat{d}^\dagger_\alpha \hat{d}_\alpha \\ &+ t \sum_{r=\text{L,R}} \sum_{\alpha=\text{a,b}} \sum_{k} \left(\hat{c}^\dagger_{kr} \hat{d}_\alpha + \text{h.c.} \right)\,,\end{aligned} \tag{2.6}$$

$$\hat{H}_{\text{ph}} = \sum_{\alpha=\text{a,b}} \omega_\alpha \hat{\alpha}^\dagger \hat{\alpha} \quad , \tag{2.7}$$

$$\hat{H}_{\text{int}} = \lambda \sum_{\alpha=\text{a,b}} \left(\hat{\alpha}^\dagger + \hat{\alpha} \right) \hat{d}^\dagger_\alpha \hat{d}_\alpha\,. \tag{2.8}$$

In this work we focus on the non-interacting, spinless model for the electronic system [129, 130]. We disregard the spin degree of freedom, as the interaction with the cavity is spin-independent. The electron spin is therefore not crucial for the entanglement generation process that we focus on here. $\hat{c}^\dagger_{kr}$ and $\hat{d}^\dagger_\alpha$ with $r = \text{L,R}$ and $\alpha = \text{a,b}$ are the creation operators of the electrons in the left and right lead and in the two quantum dots with energy levels $\varepsilon_{\text{a, b}} = \bar{\varepsilon} \pm \Delta\varepsilon$. $\hat{\alpha}^\dagger$ and $\hat{\alpha}$ are the creation and annihilation operators of photons with frequency ω_α in cavity α. $t \in \mathbb{R}$ is the hopping parameter describing the transport of an electron between dots and leads.

We focus on the regime of unidirectional transport. The voltage applied along the system shifts the electrochemical potential of the leads. We consider a symmetric shift in the high voltage limit

$$\mu_{\text{L}} = -\mu_{\text{R}} = \lim_{eV \to \infty} eV/2\,. \tag{2.9}$$

Therefore the Fermi functions of the left and right lead become $f_{\mathrm{L}}(E) = 1$ and $f_{\mathrm{R}}(E) = 0$. This approximation holds as long as the potential is the largest energy scale involved in our model, namely $|eV| \gg \max(k_{\mathrm{B}}T, \Gamma, \Delta\varepsilon, \omega_0, \eta)$. Here $k_{\mathrm{B}}T$ is the temperature of the leads and η is the damping parameter that characterizes the cavity losses, which we will describe in more detail in Chapter 2.5. The mean value of the dot energy levels is chosen to be in the middle of the electrochemical potentials of the two leads, i.e. $\bar{\varepsilon} = 0$. Dot energies are therefore specified only by the level difference, i.e. $\varepsilon_{\mathrm{a,b}} = \pm\Delta\varepsilon$.

To demonstrate the entanglement of photons in the two cavities, we calculate the covariance

$$C = \langle \hat{n}_{\mathrm{a}} \hat{n}_{\mathrm{b}} \rangle - \langle \hat{n}_{\mathrm{a}} \rangle \langle \hat{n}_{\mathrm{b}} \rangle \,, \tag{2.10}$$

which proves correlation if it is finite, i.e. $C \neq 0$, and test the classical Cauchy-Schwarz inequality

$$S = \frac{\left\langle \hat{a}^\dagger \hat{a} \hat{b}^\dagger \hat{b} \right\rangle}{\sqrt{\langle \hat{a}^\dagger \hat{a}^\dagger \hat{a} \hat{a} \rangle} \sqrt{\left\langle \hat{b}^\dagger \hat{b}^\dagger \hat{b} \hat{b} \right\rangle}} \leq 1, \tag{2.11}$$

which proves quantum correlation if it is violated. In the expressions, the cavity occupations are defined by the bosonic creation and annihilation operators $\hat{n}_{\mathrm{a}} = \hat{a}^\dagger \hat{a}$ and $\hat{n}_{\mathrm{b}} = \hat{b}^\dagger \hat{b}$, and S is the classical Cauchy-Schwarz parameter.

To evaluate Eqs. (2.10) and (2.11), we express the expectation values by Keldysh Green's functions and perform a diagrammatic perturbative expansion in the dot-cavity coupling λ up to fourth order, i.e. given by the interaction Hamiltonian in Eq. (2.8). For this reason, we define the bosonic two-particle Green's function

$$F_{\alpha\beta}(t, t') = -\, i \left\langle T_{\mathrm{C}} \left(\hat{\alpha}(t) \hat{\beta}(t) \hat{\alpha}^\dagger(t') \hat{\beta}^\dagger(t') \right) \right\rangle \,, \tag{2.12}$$

and the bosonic single-particle Green's function

$$D_{\alpha}(t, t') = -\, i \left\langle T_{\mathrm{C}} \left(\hat{\alpha}(t) \hat{\alpha}^\dagger(t') \right) \right\rangle \,. \tag{2.13}$$

Analog to the single-particle Keldysh Green's function, we obtain the four different Keldysh components for the two-particle Green's function, depending on the position of the time arguments on the Keldysh contour

$$F(t, t') = \begin{pmatrix} F(t, t') & F^{<}(t, t') \\ F^{>}(t, t') & \tilde{F}(t, t') \end{pmatrix} \,. \tag{2.14}$$

The expectation values of Eqa. (2.10) and (2.11) can now be represented in terms of the lesser component of Eq. (2.14), while the average occupation of a single cavity is given by the lesser component of the bosonic single-particle Green's function, i.e.

$$\langle \hat{n}_\alpha \rangle = D_\alpha^<(t,t), \tag{2.15}$$

$$C = \left(iF_{\mathrm{ab}}^<(t,t) + D_{\mathrm{a}}^<(t,t) D_{\mathrm{b}}^<(t,t) \right), \tag{2.16}$$

$$S = \frac{F_{\mathrm{ab}}^<(t,t)}{\sqrt{F_{\mathrm{aa}}^<(t,t) F_{\mathrm{bb}}^<(t,t)}}. \tag{2.17}$$

The conditions for entanglement are a nonzero covariance, $C \neq 0$, and a violated classical Cauchy-Schwarz inequality, i.e. $S > 1$. Both quantities have no finite contributions up to the third order, so we have to calculate them consistently up to the fourth order in λ.

2.3 Parallel Double Quantum Dot

To determine the electronic transport through the system in the absence of electron-photon interaction, we calculate the unperturbed electronic Green's functions associated with the electronic part $\hat{H}_{\mathrm{el}}$ of the Hamiltonian, using the diagrammatic Keldysh technique and applying the wide-band approximation for the leads [131, 132]. In this way, we obtain the broadening Γ of the electronic levels. These electronic Green's functions represent our bare propagators in the perturbative approach, where we expand in terms of the electron-photon interaction.

2.3.1 Retarded and Advanced Energy-Dependent Green's Functions

Recalling Section 1.4.1 the full retarded and advanced Green's functions can be calculated via the Dyson equation, that is given by Eq. (1.25). In our setup we define the single electronic levels of the parallel quantum dots and the continuum of electronic levels of the leads as unperturbed electronic system while the dot-lead interaction will be handled as the perturbation. The unperturbed fermionic Green's function can be determined via Eq. (1.23). With the Hamiltonian of the free levels

$$\boldsymbol{H_0} = \mathrm{diag}\left(\varepsilon_a, \varepsilon_b, \varepsilon_{kL}, \varepsilon_{kR}\right), \tag{2.18}$$

we get the unperturbed retarded and advanced Green's functions

$$\boldsymbol{g}^{r,a}(E) = \mathbf{diag}\left((E^{r,a} - \varepsilon_a)^{-1}, (E^{r,a} - \varepsilon_b)^{-1}, (E^{r,a} - \varepsilon_{kL})^{-1}, (E^{r,a} - \varepsilon_{kR})^{-1} \right). \tag{2.19}$$

If we know the self-energy of the system the Dyson equation allows us to directly calculate the full retarded and advanced Green's function in a similar way via Eq. (1.36), that we shortly recall

$$\boldsymbol{G}^{r,a}(E) = (E^{r,a}\mathbb{1} - \boldsymbol{H_0} - \boldsymbol{\Sigma}_{\boldsymbol{L}}^{r,a} - \boldsymbol{\Sigma}_{\boldsymbol{R}}^{r,a})^{-1} \,. \tag{2.20}$$

To justify the simplification regarding the equal tunnel couplings we start with a more general setup, where the tunneling of an electron from lead r to dot i is given by the hopping parameter t_{ri}, and the tunneling from dot i dot lead r by t_{ir}, with $r = L, R$ and $i = a, b$. We derive the Green's functions in the case of real, but four different couplings, described by Γ_i^r as shown in Fig. 2.3. In this system the self-energy consists only of the

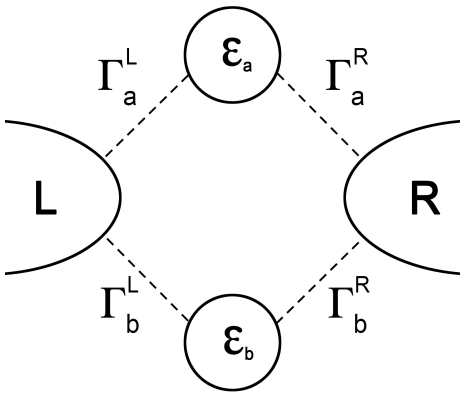

Fig. 2.3.: Parallel double quantum dot with levels $\varepsilon_{a,b}$, coupled to a common left and right lead, where $\Gamma_{a,b}^{R,L}$ describe the tunneling coupling of dots and leads.

tunneling self-energy [128], i.e.

$$\boldsymbol{\Sigma}_{\boldsymbol{X}}^{r,a} = \begin{pmatrix} t_{aX}\, g_{XX}^{r,a}\, t_{Xa} & t_{bX}\, g_{XX}^{r,a}\, t_{Xa} \\ t_{aX}\, g_{XX}^{r,a}\, t_{Xb} & t_{bX}\, g_{XX}^{r,a}\, t_{Xb} \end{pmatrix} \tag{2.21}$$

for $X = L, R$. Using the wide-band approximation we defined them via the finite linewidth of the electronic levels with $\Gamma_{a,b}^{L,R} = \pi(t_{a,b}^{L,R})^2 \rho_{L,R}(E_F)$ [114]. In terms of the four different tunnel couplings $\Gamma_{a,b}^{L,R}$ they become

$$\boldsymbol{\Sigma}_{\boldsymbol{L}}^{r,a} = \mp\, i\boldsymbol{\Gamma}^{\boldsymbol{L}} = \mp i \begin{pmatrix} \Gamma_{11}^L & \Gamma_{12}^L \\ \Gamma_{21}^L & \Gamma_{22}^L \end{pmatrix} = \mp i \begin{pmatrix} \Gamma_a^L & \sqrt{\Gamma_a^L \Gamma_b^L} \\ \sqrt{\Gamma_a^L \Gamma_b^L} & \Gamma_b^L \end{pmatrix} , \tag{2.22}$$

$$\boldsymbol{\Sigma}_{\boldsymbol{R}}^{r,a} = \mp\, i\boldsymbol{\Gamma}^{\boldsymbol{R}} = \mp i \begin{pmatrix} \Gamma_{11}^R & \Gamma_{12}^R \\ \Gamma_{21}^R & \Gamma_{22}^R \end{pmatrix} = \mp i \begin{pmatrix} \Gamma_a^R & \sqrt{\Gamma_a^R \Gamma_b^R} \\ \sqrt{\Gamma_a^R \Gamma_b^R} & \Gamma_b^R \end{pmatrix} . \tag{2.23}$$

With $\Gamma_{ij} = \Gamma_{ij}^L + \Gamma_{ij}^R$ Eq. (2.20) we get

$$\hat{\boldsymbol{G}}^{\boldsymbol{r,a}}(\omega) = \begin{pmatrix} \omega - \varepsilon_1 \pm i\Gamma_{11} & \pm i\Gamma_{12} \\ \pm i\Gamma_{21} & \omega - \varepsilon_2 \pm i\Gamma_{22} \end{pmatrix}^{-1} . \tag{2.24}$$

We introduce the average level energy and the level spacing

$$\bar{\varepsilon} = \frac{\varepsilon_a + \varepsilon_b}{2} , \quad \Delta = \varepsilon_a - \varepsilon_b , \tag{2.25}$$

so that the Green's function becomes

$$\hat{\boldsymbol{G}}^{\boldsymbol{r,a}}(\omega) = \frac{1}{\kappa^{r,a}(\omega)} \begin{pmatrix} \omega - \left(\bar{\varepsilon} - \frac{\Delta}{2}\right) \pm i\Gamma_{22} & \mp i\Gamma_{12} \\ \mp i\Gamma_{21} & \omega - \left(\bar{\varepsilon} + \frac{\Delta}{2}\right) \pm i\Gamma_{11} \end{pmatrix} , \tag{2.26}$$

$$\kappa^{r,a}(\omega) = \left(\omega - \bar{\varepsilon} - \frac{\Delta}{2} \pm i\Gamma_{11}\right)\left(\omega - \bar{\varepsilon} + \frac{\Delta}{2} \pm i\Gamma_{22}\right) + \Gamma_{12}\Gamma_{21} . \tag{2.27}$$

If we assume that all tunneling elements are equal with $\Gamma_{a,b}^L =: \Gamma^L$, $\Gamma_{a,b}^R =: \Gamma^R$, and $\Gamma^L = \Gamma^R =: \Gamma/2$ and the energy levels $\varepsilon_{a,b} = \pm\Delta\varepsilon$ the Green's function simplify to

$$\boldsymbol{G}^{\mathrm{r,\,a}}(E) = \frac{1}{\left(E^{\mathrm{r,\,a}} - \Delta\varepsilon \pm i\Gamma\right)\left(E^{\mathrm{r,\,a}} + \Delta\varepsilon \pm i\Gamma\right) + \Gamma^2} \begin{pmatrix} E^{\mathrm{r,\,a}} + \Delta\varepsilon \pm i\Gamma & \mp i\Gamma \\ \mp i\Gamma & E^{\mathrm{r,\,a}} - \Delta\varepsilon \pm i\Gamma \end{pmatrix} . \tag{2.28}$$

2.3.2 Transmission

The transmission through the system can be calculated via [133, 134]

$$T(E) = 4\mathrm{tr}\left\{\boldsymbol{G}^{\boldsymbol{a}}(E)\boldsymbol{\Gamma}^{\boldsymbol{R}}\boldsymbol{G}^{\boldsymbol{r}}(E)\boldsymbol{\Gamma}^{\boldsymbol{L}}\right\} , \tag{2.29}$$

where $\boldsymbol{G}^{\boldsymbol{r,a}}$ and $\boldsymbol{\Gamma}^{\boldsymbol{L,R}}$ are the 2x2 matrices defined above. With $\bar{E} = E - \bar{\varepsilon}$ the transmission for arbitrary tunnel couplings and finite level spacing becomes

$$T(\bar{E}) = \frac{4\left[2\bar{E}\Delta\left(\Gamma_a^L\Gamma_a^R - \Gamma_b^L\Gamma_b^R\right) + \bar{E}^2\left(\sqrt{\Gamma_a^L\Gamma_a^R} + \sqrt{\Gamma_b^L\Gamma_b^R}\right)^2 + \Delta^2\left(\sqrt{\Gamma_a^L\Gamma_a^R} - \sqrt{\Gamma_b^L\Gamma_b^R}\right)^2\right]}{\left[\bar{E}^2 - \Delta^2 - \left(\sqrt{\Gamma_a^L\Gamma_b^R} - \sqrt{\Gamma_a^R\Gamma_b^L}\right)^2\right]^2 + \left[\bar{E}\left(\Gamma_a^L + \Gamma_a^R + \Gamma_b^L + \Gamma_b^R\right) + \Delta\left(\Gamma_a^L + \Gamma_a^R - \Gamma_b^L - \Gamma_b^R\right)\right]^2} . \tag{2.30}$$

2.3.2.1. Equal tunnel couplings

In the case of equal tunnel couplings, with $\Gamma^L_{a,b} =: \Gamma^L$, $\Gamma^R_{a,b} =: \Gamma^R$, and $\Gamma^L = \Gamma^R =: \Gamma/2$ and the energy levels $\varepsilon_{a,b} = \pm\Delta\varepsilon$ the transmission reduces to

$$T_{DQD}(E) = \frac{4\Gamma^2(E-\bar{\varepsilon})^2}{\left((E-\bar{\varepsilon})^2 - \Delta\varepsilon^2\right)^2 + 4\Gamma^2(E-\bar{\varepsilon})^2}\,. \tag{2.31}$$

The transmission through a single quantum dot with a single electronic level ε, coupled to two leads with the same parameters as in the double-dot case, reads

$$T_{SQD}(E) = \frac{\Gamma^2}{(E-\varepsilon)^2 + \Gamma^2}\,. \tag{2.32}$$

Let us first assume that the energy levels of the two dots are close to each other, in the sense that the energy difference is small compared to their broadening $|\Delta\varepsilon| = |\varepsilon_a - \varepsilon_b| \ll \Gamma$, i.e. the energy distributions overlap. In this regime, the two paths are indistinguishable, and the electron flows through both branches simultaneously, causing quantum interference in the double quantum dot system. This means that the linear conductance, that is given by the transmission since we consider the whole system at zero temperature, associated with the levels of the double-dot system is different from the sum of the linear conductances of the two separate dots, i.e. different from the single level regime. This becomes more

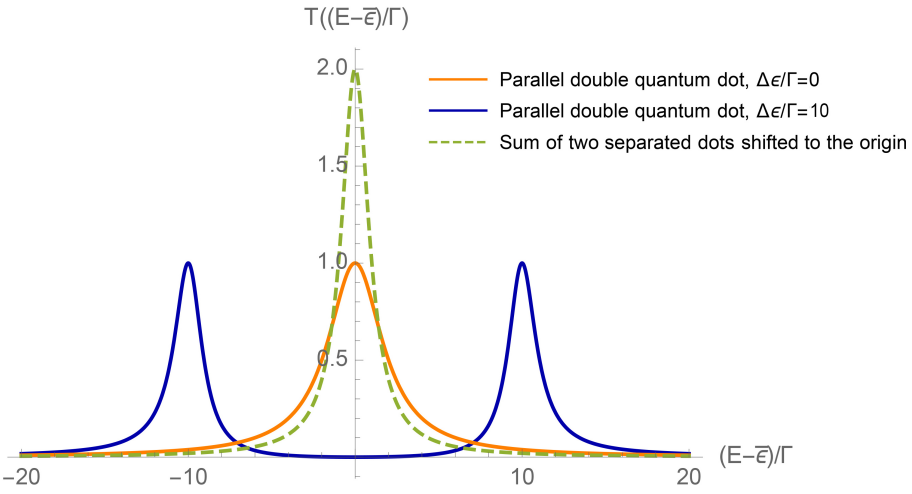

Fig. 2.4.: Transmission as a function of energy E for a parallel double quantum dot with equal dot levels, i.e. level spacing $\Delta\varepsilon/\Gamma = 0$ (orange), with different levels, i.e. a finite level spacing of $\Delta\varepsilon/\Gamma = 10$ (blue), and for the sum of the transmissions of two separated dots in the single level regime, with transmission peaks shifted to the origin (green dashed).

clear if we consider Fig. 2.4. The sum of the two transmissions of two identical separated quantum dots would reach the value $T = 2$, while the parallel double quantum dot just reaches $T = 1$. The total transmission can be viewed as the sum of incoherent

contributions reduced by interference, i.e. $2|T_1|^2 - |T_1|^2$ (incoherent + interference) with $T_1 = 1$ being the maximum transmission through a single quantum dot. This interference effect vanishes for an increased level spacing, and we get two separated peaks, each with a transmission of $T = 1$. The conductance is a continuous function of all our Hamiltonian parameters, particularly the level spacing and central level position. If the difference between the two energy levels is increased, i.e. $|\Delta\varepsilon| \gg \Gamma$, the interference is destroyed, and the electron transfer occurs via the incoherent sum of the two possible paths, namely, the electron proceeds independently through the upper or through the lower branch, but not simultaneously through both.

2.3.2.2. Arbitrary tunnel couplings

Since we consider the most simplified case for the tunnel coupling, i.e., all tunnel couplings are equal, we check the impact of arbitrary tunnel couplings on our proposal. For this we start with the transmission for arbitrary tunnel couplings and zero level spacing, i.e. given by

$$T(E)_{\Delta\varepsilon=0} = \frac{4\left(\sqrt{\Gamma_a^L\Gamma_a^R} + \sqrt{\Gamma_b^L\Gamma_b^R}\right)^2 (E-\bar{\tilde{\varepsilon}})^2}{\left[(E-\bar{\varepsilon})^2 - \left(\sqrt{\Gamma_a^L\Gamma_b^R} - \sqrt{\Gamma_a^R\Gamma_b^L}\right)^2\right]^2 + (E-\bar{\varepsilon})^2\left(\Gamma_a^L + \Gamma_a^R + \Gamma_b^L + \Gamma_b^R\right)^2} \tag{2.33}$$

We define $\delta := \sqrt{\Gamma_a^L\Gamma_b^R} - \sqrt{\Gamma_a^R\Gamma_b^L}$. At $E = \bar{\varepsilon}$ the transmission shows a different behaviour for zero or finite δ. If the tunnel couplings are arbitrary, the parameter δ is finite. In some special cases, this parameter vanishes, which can be, for instance, the case when all tunnel couplings are equal, which is the case that we consider in our study. For a finite δ the transmission vanishes at this point, forming a dip in the transmission curve. This dip discontinuously disappears as soon as $\delta = 0$ since, in this case, the term $(E-\bar{\varepsilon})^2$ in the numerator cancels, and we get a nonzero result for the transmission at $E = \bar{\varepsilon}$. An example for one arbitrary parameter set is shown in Fig. 2.5. This points out a singular dependence of the transmission function on the asymmetry and is important if (and only if) one considers the linear conductance. In other words, if we apply a "vanishing gate voltage" in our setup (with a symmetric bias voltage on the lead and $\bar{\varepsilon} = 0$) this singular behavior will strongly affect the final result as the current in such a linear regime strongly depends on the transmission. But, this critical dependence does not show up in all physical quantities and observables. For example, in the regime of the high voltage bias limit corresponding to the unilateral transport $f_{\mathrm{L}}(E) = 1$ and $f_{\mathrm{R}}(E) = 0$, that we consider in this work, the relevant quantity is the total current which is given by the integral over the transmission. To emphasize this we check the integral over the transmission depending

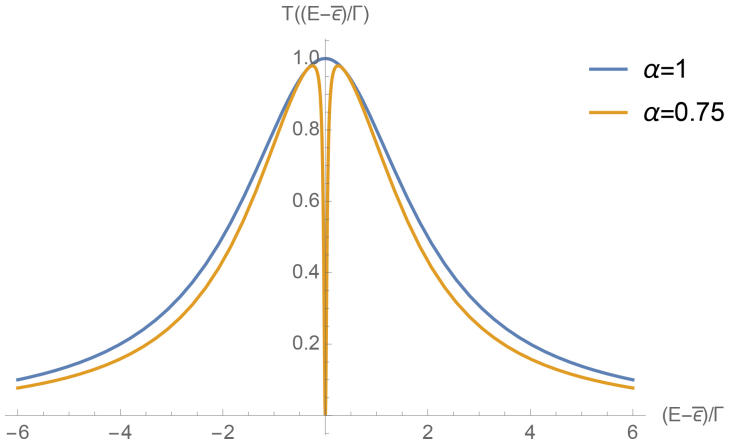

Fig. 2.5.: Transmission for equal ($\alpha = 1$) and arbitrary ($\alpha = 0.75$) tunneling couplings, for the choice $\Gamma_a^L = \Gamma_b^R = \Gamma/2$ and $\Gamma_b^L = \Gamma_a^R = \alpha\Gamma/2$.

on the parameter δ. Defining the three parameters

$$\delta = \sqrt{\Gamma_a^L \Gamma_b^R} - \sqrt{\Gamma_a^R \Gamma_b^L}\,, \tag{2.34}$$

$$\mathrm{I}_{sat} = \frac{\pi}{\bar{\Gamma}} \left(\sqrt{\Gamma_a^L \Gamma_a^R} + \sqrt{\Gamma_b^L \Gamma_b^R} \right)^2 , \tag{2.35}$$

$$\bar{\Gamma} = \frac{1}{4} \left(\Gamma_a^L + \Gamma_b^L + \Gamma_a^R + \Gamma_b^R \right) , \tag{2.36}$$

we can write the transmission in short form as

$$T(\bar{E}) = \mathrm{I}_{sat} \, \frac{4\bar{\Gamma}\bar{E}^2/\pi}{\left[\bar{E}^2 - \delta^2\right]^2 + 4\bar{\Gamma}^2\bar{E}^2} , \tag{2.37}$$

From Eq. (2.37) it is possible to show that the function of E that multiplies the constant I_{sat} is normalized independently of the parameter δ, since the integral over the transmission becomes [135]

$$\int_{-\infty}^{\infty} T(\bar{E}) d\bar{E} = \mathrm{I}_{sat} \, \frac{\sqrt{1 - \left(\frac{\delta}{\sqrt{8}\bar{\Gamma}}\right)^2} + \sqrt{1 - \left(\frac{\delta}{2\bar{\Gamma}}\right)^2} - \sqrt{1 - \left(\frac{\delta}{\sqrt{8}\bar{\Gamma}}\right)^2} - \sqrt{1 - \left(\frac{\delta}{2\bar{\Gamma}}\right)^2}}{\sqrt{2 - \frac{1}{2}\left(\frac{\delta}{\bar{\Gamma}}\right)^2}} \tag{2.38}$$

$$\approx \mathrm{I}_{sat} \tag{2.39}$$

corresponding to the saturation current, scaled in terms of $e/\hbar$. The result for the total current is, therefore a smooth function of the tunneling rates and has a continuous dependence on the asymmetry: it is given by Eq. (2.39), a kind of average of the tunneling rates. For an intuitive explanation, we illustrate this result in Fig. 2.6. In simple words, within the high voltage bias limit, the effective flux of electrons is confined by $\sim \bar{\Gamma}$, the average rate, and there is no reason why the electrons of a pretty small energy range, as

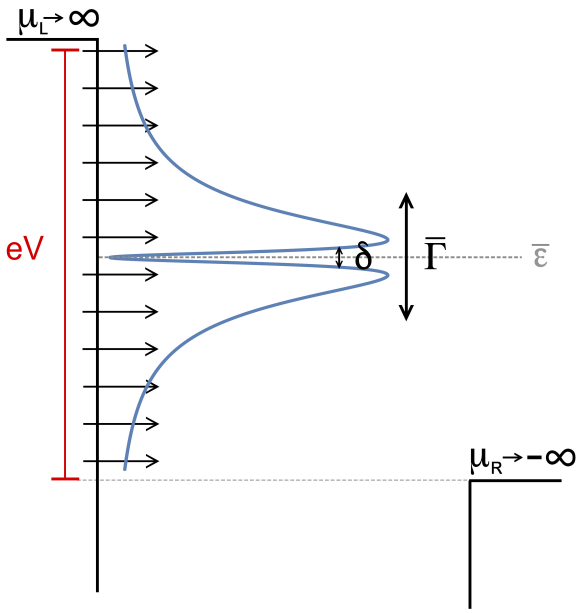

Fig. 2.6.: Transport of electrons (electron flux indicated by black arrows) in the high voltage bias limit, i.e. $\mu_{\rm L} = -\mu_{\rm R} = \lim_{eV\to\infty} eV/2$ through a parallel double quantum dot. The transmission function is described by the blue curve. The effective flux of electrons is confined by $\bar{\Gamma}$ while the dip associated to the asymmetry is related to an even smaller energy range $\delta \ll \bar{\Gamma}$ (see text).

given by the singularity $\delta \ll \bar{\Gamma}$, should contribute more to the current.

One can argue a similar conclusion if one takes into account only quantities for which we must integrate over the whole bias $\mu_{\rm L} = -\mu_{\rm R} = \lim_{eV\to\infty} eV/2$. Here the relevant mathematical quantities are the electronic Green's functions which are used to construct the diagrams in the perturbation theory to treat the parallel double-dot system with electron-photon interaction. For the degenerate case $\Delta\varepsilon = 0$, the denominator of the Green's function $G^{r,a}(E)$ simplifies and is reduced to

$$\kappa^{r,a}(\bar{E}) = \bar{E}^2 - \delta^2 \pm 4i\bar{\Gamma}\bar{E} \tag{2.40}$$

pointing out that a finite δ changes the position of the poles. However, the Green's functions are objects that have to be inserted inside the integrals defining the diagrams, and the small energy region associated to δ must give a small contribution to the full integral. Therefore we expect a smooth, continuous behavior of the diagrams as a function of the asymmetry. In other words, the electrons flowing in the small energy range associated with the region $\bar{E} \sim \delta$ with $\delta \ll \bar{\Gamma}$ are expected to give a small contribution to the entanglement when we compare them to the whole flux of electrons. Indeed, we have shown that the saturation current is proportional to the integral over the transmission, and it is independent of δ. Such small energy scale is also irrelevant when we consider inelastic

tunneling events as the resonance frequency of the microwave cavities is also a larger energy scale $\omega_0 \gg \bar{\Gamma}$. This justifies our approximation of setting all the tunneling rates equal to simplify the complex calculations of the perturbative diagrams largely. Overall we can conclude that the choice of equal tunnel couplings leads to a special transport property which is important for the linear conductance but not relevant for our proposal. The retarded and advanced Green's functions that we consider as bare electronic propagators are therefore given in Eq. (2.28).

2.3.3 Keldysh Green's Functions

As introduced in Section 1.4.2.2, a Green's function depending on two-time arguments t and t' there are four possibilities to distribute them on the two branches of the Keldysh contour leading to four different Keldysh Green's functions. Furthermore, we need to take into account the parallel double quantum dot coupled to the two leads, so for each Keldysh Green's function, we get again a matrix Green's function in the elements $i, j \in \{a, b, L, R\}$.

$$\hat{\boldsymbol{G}}_{\boldsymbol{ij}} = \begin{pmatrix} G_{ij} & G_{ij}^{<} \\ G_{ij}^{>} & \tilde{G}_{ij} \end{pmatrix} = -i \begin{pmatrix} \langle T_C(c_i(t)c_j^\dagger(t'))\rangle & -\langle c_j^\dagger(t')c_i(t)\rangle \\ \langle c_i(t)c_j^\dagger(t')\rangle & \langle \tilde{T}_C(c_i(t)c_j^\dagger(t'))\rangle \end{pmatrix} . \tag{2.41}$$

2.3.3.1. Dyson equation and full Green's functions

We recall the Dyson equation of the contour ordered Keldysh Green's functions, which reads for each matrix element

$$\hat{G}_{ij} = \hat{g}_{ij} + \sum_{lm} \hat{g}_{il}\hat{\Sigma}_{lm}\hat{G}_{mj} \, , \tag{2.42}$$

with the unperturbed Keldysh Green's function $\hat{\boldsymbol{g}}$, the self-energy $\hat{\boldsymbol{\Sigma}}$ and $i, j \in \{a, b, L, R\}$. To determine the lesser and greater Keldysh Green's function, we use the Langreth theorem [128, 136] and get the two equations

$$\begin{aligned} \boldsymbol{G}^{<} &= \boldsymbol{g}^{<} + \left(\hat{\boldsymbol{g}}\hat{\boldsymbol{\Sigma}}\hat{\boldsymbol{G}}\right)^{<} && (2.43)\\ &= \boldsymbol{g}^{<} + \boldsymbol{g}^{r}\boldsymbol{\Sigma}^{r}\boldsymbol{G}^{<} + \boldsymbol{g}^{r}\boldsymbol{\Sigma}^{<}\boldsymbol{G}^{a} + \boldsymbol{g}^{<}\boldsymbol{\Sigma}^{a}\boldsymbol{G}^{a} \, , && (2.44)\\ \boldsymbol{G}^{>} &= \boldsymbol{g}^{>} + \boldsymbol{g}^{r}\boldsymbol{\Sigma}^{r}\boldsymbol{G}^{>} + \boldsymbol{g}^{r}\boldsymbol{\Sigma}^{>}\boldsymbol{G}^{a} + \boldsymbol{g}^{>}\boldsymbol{\Sigma}^{a}\boldsymbol{G}^{a} \, . && (2.45) \end{aligned}$$

We transform Eq. (2.44) in the following way

$$\begin{aligned} (\mathbf{1} - \boldsymbol{g}^{r}\boldsymbol{\Sigma}^{r})\boldsymbol{G}^{<} &= \boldsymbol{g}^{<}(\mathbf{1} + \boldsymbol{\Sigma}^{a}\boldsymbol{G}^{a}) + \boldsymbol{g}^{r}\boldsymbol{\Sigma}^{<}\boldsymbol{G}^{a} && (2.46)\\ \boldsymbol{g}^{r}\left(\boldsymbol{G}^{r}\right)^{-1}\boldsymbol{G}^{<} &= \boldsymbol{g}^{<}\left(\boldsymbol{g}^{a}\right)^{-1}\boldsymbol{G}^{a} + \boldsymbol{g}^{r}\boldsymbol{\Sigma}^{<}\boldsymbol{G}^{a} && (2.47)\\ \boldsymbol{G}^{<} &= \boldsymbol{G}^{r}\left(\boldsymbol{g}^{r}\right)^{-1}\boldsymbol{g}^{<}\left(\boldsymbol{g}^{a}\right)^{-1}\boldsymbol{G}^{a} + \boldsymbol{G}^{r}\boldsymbol{\Sigma}^{<}\boldsymbol{G}^{a} \, , && (2.48) \end{aligned}$$

while we inserted a form of the Dyson equation for the retarded and advanced Green's function to obtain Eq. (2.47) from Eq. (2.46). We end up with an equation for $\boldsymbol{G}^<$ that depends only on the unperturbed, the retarded and advanced Green's functions as well as the lesser self-energy. Since the unperturbed Green's functions $\boldsymbol{g}^{r,a}$ and $\boldsymbol{g}^<$ are diagonal, the multiplication of the three unperturbed Green's functions is also a diagonal matrix. According to Eq. (2.19), the inverse of the retarded and advanced Green's functions are proportional to $E-\varepsilon_i$. In Eq. (1.74) we see, that the unperturbed lesser Green's functions of the dots are proportional to $\delta(E-\varepsilon_i)$. The product of the three unperturbed Green's functions for the first and second matrix element, 11 and 22, is proportional to

$$(g^r_{ii})^{-1} g^<_{ii} (g^a_{ii})^{-1} \propto \delta(E-\varepsilon_i)(E-\varepsilon_i)^2 = 0\,, \tag{2.49}$$

with $i=a,b$, and therefore vanishes. The third and fourth elements LL and RR contain the unperturbed Green's functions of the leads. The unperturbed lesser Green's function of the leads was determined in Eq. (1.75). We get

$$(g^r_{rr})^{-1} g^<_{rr} (g^a_{rr})^{-1} \propto \lim_{\nu\to 0} 2i\nu f_r(E) = 0\,. \tag{2.50}$$

Summarized, the first term of Eq. (2.48) vanishes since the multiplication of the unperturbed Green's functions vanishes. The same arguments hold for $\boldsymbol{G}^>$.

For the perturbative expansion we need only the greater and lesser Keldysh Green's functions of the dots, i.e. $i,j \in \{a,b\}$, and not of the leads. In this case, the equation for the fermionic lesser Green's function of the dots reduces to

$$G^<_{ij} = \sum_{l,m} G^r_{il} \Sigma^<_{lm} G^a_{mj}\,. \tag{2.51}$$

As already said, the self-energy of the parallel double quantum dot coupled to the two fermionic leads consists only of the tunneling self-energy, while the lesser self-energy, and the greater, respectively, are then in general determined by the equation [128].

$$\Sigma^<_{lm} = \sum_{k\alpha=L,R} V^*_{k\alpha,l} g^<_{k\alpha} V_{k\alpha,m}\,. \tag{2.52}$$

$V_{k\alpha,l}$ describes the coupling of the leads and the dots. Therefore $V_{k\alpha,l}=0$ if $k\alpha = l = L,R$ and $V_{k\alpha,l}=t$ else. With Eq. (1.75) for the unperturbed Keldysh Green's functions of the leads, we can determine the lesser self-energy and the greater self-energy, respectively

$$\boldsymbol{\Sigma}^< = i\Gamma\,(f_L+f_R)\begin{pmatrix}1 & 1\\ 1 & 1\end{pmatrix} \overset{\text{h.v.}}{=} i\Gamma\begin{pmatrix}1 & 1\\ 1 & 1\end{pmatrix}\,, \tag{2.53}$$

$$\boldsymbol{\Sigma}^> = i\Gamma\,(f_L+f_R-2)\begin{pmatrix}1 & 1\\ 1 & 1\end{pmatrix} \overset{\text{h.v.}}{=} -i\Gamma\begin{pmatrix}1 & 1\\ 1 & 1\end{pmatrix}\,. \tag{2.54}$$

The Fermi functions became $f_L(E) = 1$ and $f_R(E) = 0$ since we consider the electronic transport through the parallel double-dot system in the high voltage (h.v.) bias limit. When we have determined the greater and lesser Keldysh Green's functions, we can calculate the time-ordered and anti-time ordered Green's function with the relations

$$G(E) = G^{<}(E) + G^{\mathrm{r}}(E)\,, \tag{2.55}$$

$$\tilde{G}(E) = G^{>}(E) - G^{\mathrm{a}}(E)\,. \tag{2.56}$$

Finally, we get the four Keldysh Green's functions in the high voltage bias limit.

The greater and lesser Green's functions are

$$\boldsymbol{G}^{<}(E) = -\boldsymbol{G}^{>}(E) \tag{2.57}$$

$$= \frac{i\Gamma}{(E^2-\Delta\varepsilon^2)^2 + 4\Gamma^2E^2} \begin{pmatrix} (E+\Delta\varepsilon)^2 & (E^2-\Delta\varepsilon^2) \\ (E^2-\Delta\varepsilon^2) & (E-\Delta\varepsilon)^2 \end{pmatrix}, \tag{2.58}$$

and the time-ordered and anti-time-ordered Green's functions are

$$\boldsymbol{G}(E) = -\tilde{\boldsymbol{G}}(E) \tag{2.59}$$

$$= \frac{1}{(E^2-\Delta\varepsilon^2)^2 + 4\Gamma^2E^2} \begin{pmatrix} (E-\Delta\varepsilon)(E+\Delta\varepsilon)^2 + 2\Gamma^2E & -2\Gamma^2E \\ -2\Gamma^2E & (E-\Delta\varepsilon)^2(E+\Delta\varepsilon) + 2\Gamma^2E \end{pmatrix}. \tag{2.60}$$

2.4 Single Quantum Dot

We want to compare the transport through a double-dot coupled to two microwave cavities with the transport through a single dot, which is also coupled to separated microwave cavities. The system is shown in Fig. 2.7 while the Hamiltonian is the same as given by Eqs. (2.5) to (2.8), reduced by the terms of the second dot, i.e.

$$\hat{H} = \hat{H}_{\mathrm{el}} + \hat{H}_{\mathrm{ph}} + \hat{H}_{\mathrm{int}}\,, \tag{2.61}$$

$$\hat{H}_{\mathrm{el}} = \sum_{r=\mathrm{L,R}} \sum_{k} (\varepsilon_{kr} - \mu_r)\, \hat{c}^{\dagger}_{kr}\hat{c}_{kr} + \varepsilon \hat{d}^{\dagger}\hat{d} \; + \sqrt{2}t \sum_{r=\mathrm{L,R}} \sum_{k} \left(\hat{c}^{\dagger}_{kr}\hat{d} \; + \mathrm{h.c.}\right), \tag{2.62}$$

$$\hat{H}_{\mathrm{ph}} = \sum_{\alpha=\mathrm{a,b}} \omega_{\alpha}\hat{\alpha}^{\dagger}\hat{\alpha} \;\; , \tag{2.63}$$

$$\hat{H}_{\mathrm{int}} = \lambda \sum_{\alpha=\mathrm{a,b}} \left(\hat{\alpha}^{\dagger} + \hat{\alpha}\;\right) \hat{d}^{\dagger}\hat{d} \;\; . \tag{2.64}$$

The operators and parameters are defined in the same way as for the double-dot. If one considers the parallel double-dot at zero level spacing, the Hamiltonian of Eq. (2.6), i.e.

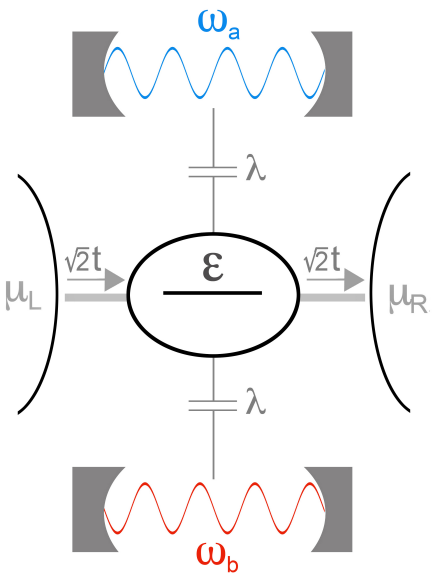

Fig. 2.7.: A single quantum dot with a single electronic energy level coupled simultaneously to two separated microwave cavities and a left and right lead.

the electronic part, can be transformed into an effective single-dot problem [132] while the dot-lead coupling is renormalized by a factor $\sqrt{2}$. To compare the results, in the end, we directly included this factor in the system with the single dot.

The Green's function of the electronic system does not depend on the coupling to the cavities, and we determined them already in the fundamentals part within the "minimal example". The retarded and advanced Green's functions were determined in Section 1.4.1.1 and given by Eq. (1.33), i.e.

$$G_{11}^{ra} = \frac{1}{E^{ra} - \varepsilon \pm 2i\Gamma} \,. \tag{2.65}$$

The corresponding Keldysh Green's function are determined in Section 1.4.1.1 and given by Eq. (1.33), i.e.

$$\hat{\boldsymbol{G}}(E) = \frac{1}{(E-\varepsilon)^2 + 4\Gamma^2} \begin{pmatrix} E-\varepsilon & 2i\Gamma \\ -2i\Gamma & -(E-\varepsilon) \end{pmatrix} . \tag{2.66}$$

2.5 Microwave Cavities

The calculation of the bosonic Green's functions of an (isolated) microwave cavity is well known in the literature. For completeness, we show the rough procedure also here. The Hamiltonian for the noninteracting microwave cavity, with time independent creation and annihilation operators $\hat{\alpha}^\dagger$ and $\hat{\alpha}$ for $\alpha = \mathrm{a}, \mathrm{b}$ reads

$$H_{\mathrm{ph},\alpha} = \omega_\alpha \hat{\alpha}^\dagger \hat{\alpha} \,. \tag{2.67}$$

The time-depended creation and annihilation operators can then be calculated as

$$\hat{\alpha}(t) = e^{-i\omega_\alpha t}\hat{\alpha}, \quad \hat{\alpha}^\dagger(t) = e^{i\omega_\alpha t}\hat{\alpha}^\dagger\,. \tag{2.68}$$

The four bosonic, time-depended Keldysh Green's functions become

$$D_\alpha^{<(0)}(t,t') = -i\left\langle \hat{\alpha}_{t'}^\dagger \hat{\alpha}_t \right\rangle_0 = -ie^{-i\omega_\alpha(t-t')}n_\alpha\,, \tag{2.69}$$

$$D_\alpha^{>(0)}(t,t') = -i\left\langle \hat{\alpha}_t \hat{\alpha}_{t'}^\dagger \right\rangle_0 = -ie^{-i\omega_\alpha(t-t')}(n_\alpha+1)\,, \tag{2.70}$$

$$D_\alpha{}^{(0)}(t,t') = -i\left\langle T_\mathsf{C}\left(\hat{\alpha}_{t'}^\dagger \hat{\alpha}_t\right)\right\rangle_0 = \Theta(t-t')D_\alpha^>(t,t') + \Theta(t'-t)D_\alpha^<(t,t')\,, \tag{2.71}$$

$$\tilde{D}_\alpha^{(0)}(t,t') = -i\left\langle T_\mathsf{C}\left(\hat{\alpha}_{t'}^\dagger \hat{\alpha}_t\right)\right\rangle_0 = \Theta(t'-t)D_\alpha^>(t,t') + \Theta(t-t')D_\alpha^<(t,t')\,, \tag{2.72}$$

with $n_\alpha = \left\langle \hat{\alpha}^\dagger\hat{\alpha}\right\rangle$. We calculate their Fourier transformations to obtain the bosonic Keldysh Green's functions in energy space. If the cavity is coupled to an external bath, as for instance a transmission line into which photons from the cavity escape, the bosonic Green's functions contain a finite imaginary part $\pm i\eta$, as used in the expressions below, which describes the damping of the cavity resonator. The energy-dependent free bosonic Green's functions are

$$D_\alpha^{<(0)}(E) = \frac{-in_\alpha\eta}{(E-\omega_\alpha)+\eta^2}\,, \tag{2.73}$$

$$D_\alpha^{>(0)}(E) = \frac{-i(n_\alpha+1)\eta}{(E-\omega_\alpha)+\eta^2}\,, \tag{2.74}$$

$$D_\alpha{}^{(0)}(E) = \frac{E-\omega_\alpha-i\eta(2n_\alpha+1)}{(E-\omega_\alpha)^2+\eta^2}\,, \tag{2.75}$$

$$\tilde{D}_\alpha^{(0)}(E) = \frac{-(E-\omega_\alpha)-i\eta(2n_\alpha+1)}{(E-\omega_\alpha)^2+\eta^2}\,. \tag{2.76}$$

We treat the cavities at zero temperature, such that the initial photon number n_α is zero. We will see later in the final formulas of the integrals that only the unperturbed time-ordered and anti-time-ordered bosonic Green's functions will contribute since we are interested only in the lesser functions, compare Eqs. (2.15) to (2.17). At zero temperature, these Green's functions simplify to

$$D_\alpha(E) = \frac{1}{E-\omega_\alpha+i\eta}\,, \tag{2.77}$$

$$\tilde{D}_\alpha(E) = \frac{1}{E-\omega_\alpha-i\eta}\,. \tag{2.78}$$

2.6 Perturbation Expansion

So far, we have introduced in Section 2.2 the correlators that can verify entanglement. We expressed them in terms of the lesser component of the bosonic single-particle and two-particle Keldysh Green's functions. In Section 2.3.3.1 and 2.5 we determined the unperturbed fermionic and bosonic Keldysh Green's functions. The next step is now to perform the perturbative expansion in the interaction Hamiltonian, i.e. the dot-cavity interaction given by Eq. (2.8).

Regarding Eqs. (2.15) to (2.17) we need to determine the single particle Green's functions $D_a^<(t,t')$ and $D_b^<(t,t')$ as well as the two-particle Green's functions $F_{\mathrm{aa}}^<(t,t')$, $F_{\mathrm{bb}}^<(t,t')$ and $F_{\mathrm{ab}}^<(t,t')$.

Before we start with the calculation we first clarify the notation. All operators depend on a time argument. To simplify the notation we place the time-dependence in the subscript.i.e. $\hat{\alpha}(t) \to \hat{\alpha}_t$. The bosonic operators of the two cavities are $\hat{\alpha}$. The fermionic operators of the two dots are $\hat{d}_\alpha$. With $\alpha = \mathrm{a}, \mathrm{b}$. To avoid a double subscript for the fermionic operators, i.e. the time argument and the index α, we distinguish the fermionic operators of the two quantum dots by a tilde. Therefore we use in the perturbative expansion the notation $\hat{d}_{\mathrm{a}}(t) \to \hat{d}_t$ and $\hat{d}_{\mathrm{b}}(t) \to \hat{\tilde{d}}_t$.

2.6.1 Single-Particle Green's Function of the Double-Dot

We start in detail with the perturbative expansion of the bosonic single-particle Green's function

$$iD_a(t,t') = \left\langle T_c\left(\hat{a}_t \hat{a}_{t'}^\dagger\right)\right\rangle = \mathrm{Tr}\left(\rho_0 T_c\left(e^{-i\int_C d\tau H^{(i)}(\tau)}\hat{a}_t\hat{a}_{t'}^\dagger\right)\right), \tag{2.79}$$

with the interaction Hamiltonian in the new notation

$$H^{(i)} = \lambda(\hat{a}+\hat{a}^\dagger)\hat{d}^\dagger\hat{d} + \lambda(\hat{b}+\hat{b}^\dagger)\hat{\tilde{d}}^\dagger\hat{\tilde{d}}\,.$$

The zeroth order corresponds to the unperturbed bosonic Green's function. In the end we need the lesser component

$$\left\langle T_{\mathrm{C}}\left(\hat{a}_t\hat{a}_{t'}^\dagger\right)\right\rangle^{<(0)} = iD_{\mathrm{a}}^{<(0)}(t,t') = 0\,, \tag{2.80}$$

which is zero at zero temperature. Since we calculate the correlators C and S upon fourth order and the single-particle Green's function appears only as product $D_{\mathrm{a}}^<(t,t')D_{\mathrm{b}}^<(t,t')$, we need the perturbation expansion of the single-particle Green's function only upon second order, since the product of the zeroth and fourth order contributions is zero. The

first order term of the perturbative expansion becomes zero, due to the odd number of operators. The second order can be calculated in the following way:

$$\left\langle T_{\mathrm{C}}\left(\hat{a}_t\hat{a}_{t'}^\dagger\right)\right\rangle^{(2)} = \frac{(-i)^2}{2!}\int_C dt_1\int_C dt_2\left\langle T_C\left(\hat{a}_t\hat{a}_{t'}^\dagger\left[\lambda(\hat{a}+\hat{a}^\dagger)\hat{d}^\dagger\hat{d}+\lambda(\hat{b}+\hat{b}^\dagger)\hat{\tilde{d}}^\dagger\hat{\tilde{d}}\right]_{t_1}\right.\right.$$
$$\left.\left.\times\left[\lambda(\hat{a}+\hat{a}^\dagger)\hat{d}^\dagger\hat{d}+\lambda(\hat{b}+\hat{b}^\dagger)\hat{\tilde{d}}^\dagger\hat{\tilde{d}}\right]_{t_2}\right)\right\rangle \tag{2.81}$$

$$= -\lambda^2\int_C dt_1\int_C dt_2\left\langle T_{\mathrm{C}}\left(\hat{a}_t\hat{a}_{t'}^\dagger\hat{a}_{t_1}\hat{a}_{t_2}^\dagger\right)\right\rangle\left\langle T_{\mathrm{C}}\left(\hat{d}_{t_1}^\dagger\hat{d}_{t_1}\hat{d}_{t_2}^\dagger\hat{d}_{t_2}\right)\right\rangle \tag{2.82}$$

$$= -\lambda^2\int_C dt_1\int_C dt_2\left\langle T_{\mathrm{C}}\left(\hat{a}_t\hat{a}_{t_2}^\dagger\right)\right\rangle_0\left\langle T_{\mathrm{C}}\left(\hat{a}_{t_1}\hat{a}_{t'}^\dagger\right)\right\rangle_0\left\langle T_{\mathrm{C}}\left(\hat{d}_{t_1}^\dagger\hat{d}_{t_2}\right)\right\rangle_0\left\langle T_{\mathrm{C}}\left(\hat{d}_{t_2}^\dagger\hat{d}_{t_1}\right)\right\rangle_0 \tag{2.83}$$

$$= \lambda^2\int_C dt_1\int_C dt_2 D_{\mathrm{a}}^{(0)}(t,t_2)D_{\mathrm{a}}^{(0)}(t_1,t')G_{aa}(t_1,t_2)G_{aa}(t_2,t_1)\,. \tag{2.84}$$

For the second-order perturbation term, we get the two-dimensional integral over the Keldysh contour written in Eq. (2.81). We can split the expectation value of the bosonic and the fermionic operators and summarize the full multiplication of the interaction Hamiltonians to the result in Eq. (2.82). We apply Wick's theorem to decompose the string of bosonic and fermionic operators separately. In Eq. (2.83) we already neglected disconnected or Tadpole diagrams as explained in Section 1.4.2.7. The last step is now to identify the unperturbed Keldyh Green's functions to finally get the expression in Eq. (2.84).

In the same way the expansion for the other microwave cavity is calculated and results in

$$\left\langle T_{\mathrm{C}}\left(\hat{b}_t\hat{b}_{t'}^\dagger\right)\right\rangle^{(2)} = \lambda^2\int_C dt_1\int_C dt_2 D_{\mathrm{b}}^{(0)}(t,t_2)D_{\mathrm{b}}^{(0)}(t_1,t')G_{bb}(t_1,t_2)G_{bb}(t_2,t_1) \tag{2.85}$$

A more pleasant way to consider the perturbative expansion and to compare the different terms for the calculation is the representation as Feynman diagrams. The wiggled lines correspond to bosonic, the straight lines to fermionic Keldysh Green's functions. The blue and red color correspond to the diagonal elements, i.e. blue for G_{aa} and $D_a^{(0)}$ and red for G_{bb} and $D_b^{(0)}$. Lines in green color, as used in the next part in Fig. (2.9), correspond to the off-diagonal fermionic Green's functions $G_{ab} = G_{ba}$.

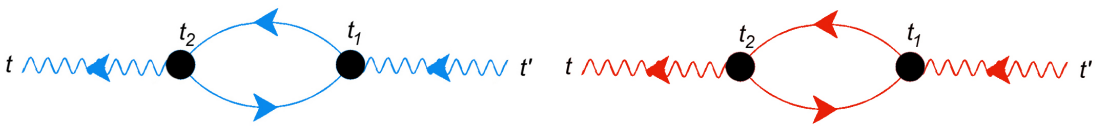

Fig. 2.8.: Nonzero Feynman diagrams of the second-order contribution of $D_a(t,t')$ in red and $D_b(t,t')$ in blue, depending on the contour times t_i, $i \in \{1,2\}$.

2.6.2 Two-particle Green's function of the Double-Dot

The correlators C and S contain two different two-particle Green's functions, i.e. $F_{\alpha\alpha}(t,t')$ with $\alpha = \mathrm{a}, \mathrm{b}$ and $F_{ab}(t,t')$ which we determine separately upon fourth order. The procedure to obtain the two-particle Green's function as contour-time integral over the unperturbed bosonic and fermionic Green's function is the same as explained for the single-particle Green's function. So in this section, we give just the final expression and show the more detailed calculation in the appendix. In the result shown here, we neglected all terms of the perturbation expansion that finally do not contribute to the integrals. These are disconnected and Tadpole diagrams, as also those terms that contains the unperturbed bosonic Green's function depending explicitly on t and t' in the way $D^{(0)}_{\mathrm{a,\,b}}(t,t')$. Since we consider in the end only the lesser component, these terms become zero since $D^{<(0)}_{\mathrm{a,\,b}}(t,t') = 0$.

2.6.2.1. Two-particle Green's function $F_{ab}(t,t')$

We start with the two-particle Green's function

$$F_{\mathrm{ab}}(t,t') = \left\langle T_{\mathrm{C}}\left(\hat{a}_t\hat{a}^\dagger_{t'}\hat{b}_t\hat{b}^\dagger_{t'}\right)\right\rangle .$$

The perturbative expansion's first and third-order term again becomes zero because of the odd number of operators. The perturbative expansion upon fourth order reads

$$\left\langle T_{\mathrm{C}}\left(\hat{a}_t\hat{a}^\dagger_{t'}\hat{b}_t\hat{b}^\dagger_{t'}\right)\right\rangle \approx \left\langle T_{\mathrm{C}}\left(\hat{a}_t\hat{a}^\dagger_{t'}\hat{b}_t\hat{b}^\dagger_{t'}\right)\right\rangle^{(0)} + \left\langle T_{\mathrm{C}}\left(\hat{a}_t\hat{a}^\dagger_{t'}\hat{b}_t\hat{b}^\dagger_{t'}\right)\right\rangle^{(2)} + \left\langle T_{\mathrm{C}}\left(\hat{a}_t\hat{a}^\dagger_{t'}\hat{b}_t\hat{b}^\dagger_{t'}\right)\right\rangle^{(4)} \tag{2.86}$$

$$\begin{aligned}
=&\frac{1}{2}\int_C dt_1\int_C dt_2(-i)^2\left\langle T_c\left(\hat{a}_t\hat{a}^\dagger_{t'}\hat{b}_t\hat{b}^\dagger_{t'}\left[\lambda(\hat{a}+\hat{a}^\dagger)d^\dagger d+\lambda(\hat{b}+\hat{b}^\dagger)\tilde{d}^\dagger\tilde{d}\right]_{t_1}\right.\right.\\
&\left.\left.\times\left[\lambda(\hat{a}+\hat{a}^\dagger)d^\dagger d+\lambda(\hat{b}+\hat{b}^\dagger)\tilde{d}^\dagger\tilde{d}\right]_{t_2}\right)\right\rangle\\
&+\frac{1}{24}\int_C dt_1\int_C dt_2\int_C dt_3\int_C dt_4(-i)^4\left\langle T_c\left(\hat{a}_t\hat{a}^\dagger_{t'}\hat{b}_t\hat{b}^\dagger_{t'}\right.\right.\\
&\times\left[\lambda(\hat{a}+\hat{a}^\dagger)d^\dagger d+\lambda(\hat{b}+\hat{b}^\dagger)\tilde{d}^\dagger\tilde{d}\right]_{t_1}\left[\lambda(\hat{a}+\hat{a}^\dagger)d^\dagger d+\lambda(\hat{b}+\hat{b}^\dagger)\tilde{d}^\dagger\tilde{d}\right]_{t_2}\\
&\left.\left.\times\left[\lambda(\hat{a}+\hat{a}^\dagger)d^\dagger d+\lambda(\hat{b}+\hat{b}^\dagger)\tilde{d}^\dagger\tilde{d}\right]_{t_3}\left[\lambda(\hat{a}+\hat{a}^\dagger)d^\dagger d+\lambda(\hat{b}+\hat{b}^\dagger)\tilde{d}^\dagger\tilde{d}\right]_{t_4}\right)\right\rangle
\end{aligned} \tag{2.87}$$

$$
\begin{aligned}
=&\lambda^4 \int_C dt_1 \int_C dt_2 \int_C dt_3 \int_C dt_4 \Big[\\
&+ D_a^{(0)}(t,t_2) D_a^{(0)}(t_1,t') D_b^{(0)}(t,t_4) D_b^{(0)}(t_3,t') G_{aa}(t_1,t_2) G_{aa}(t_2,t_1) G_{bb}(t_3,t_4) G_{bb}(t_4,t_3) \\
&- D_a^{(0)}(t,t_2) D_a^{(0)}(t_1,t') D_b^{(0)}(t,t_4) D_b^{(0)}(t_3,t') G_{aa}(t_1,t_2) G_{ab}(t_2,t_4) G_{ba}(t_3,t_1) G_{bb}(t_4,t_3) \\
&- D_a^{(0)}(t,t_2) D_a^{(0)}(t_1,t') D_b^{(0)}(t,t_4) D_b^{(0)}(t_3,t') G_{aa}(t_1,t_2) G_{ab}(t_2,t_3) G_{bb}(t_3,t_4) G_{ba}(t_4,t_1) \\
&- D_a^{(0)}(t,t_2) D_a^{(0)}(t_1,t') D_b^{(0)}(t,t_4) D_b^{(0)}(t_3,t') G_{ab}(t_1,t_3) G_{aa}(t_2,t_1) G_{bb}(t_3,t_4) G_{ba}(t_4,t_2) \\
&- D_a^{(0)}(t,t_2) D_a^{(0)}(t_1,t') D_b^{(0)}(t,t_4) D_b^{(0)}(t_3,t') G_{ab}(t_1,t_3) G_{ab}(t_2,t_4) G_{ba}(t_3,t_2) G_{ba}(t_4,t_1) \\
&- D_a^{(0)}(t,t_2) D_a^{(0)}(t_1,t') D_b^{(0)}(t,t_4) D_b^{(0)}(t_3,t') G_{ab}(t_1,t_4) G_{aa}(t_2,t_1) G_{ba}(t_3,t_2) G_{bb}(t_4,t_3) \\
&- D_a^{(0)}(t,t_2) D_a^{(0)}(t_1,t') D_b^{(0)}(t,t_4) D_b^{(0)}(t_3,t') G_{ab}(t_1,t_4) G_{ab}(t_2,t_3) G_{ba}(t_3,t_1) G_{ba}(t_4,t_2) \\
&+ D_a^{(0)}(t,t_2) D_a^{(0)}(t_3,t') D_b^{(0)}(t,t_4) D_b^{(0)}(t_1,t') G_{ab}(t_3,t_4) G_{ab}(t_2,t_1) G_{ba}(t_1,t_2) G_{ba}(t_4,t_3) \Big]
\end{aligned}
\tag{2.88}
$$

The large and complex expression of the latter equation can be represented again much easier as Feynman diagrams which we show in Fig. 2.9.

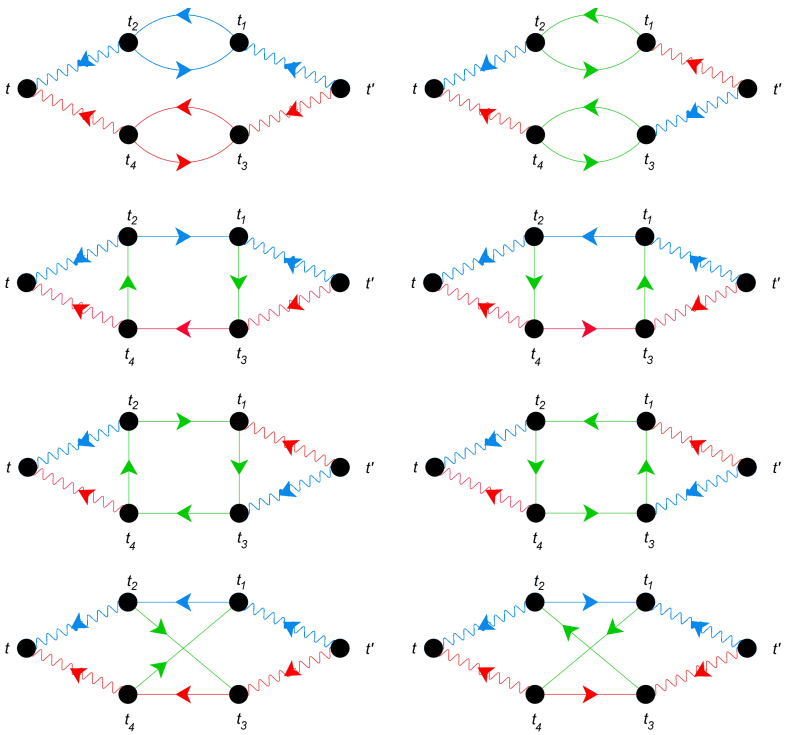

Fig. 2.9.: Nonzero Feynman diagrams of the fourth-order contribution of $F_{\mathrm{ab}}(t,t')$, depending on the contour times t_i, $i \in \{1,2,3,4\}$.

2.6.2.2. Two-particle Green's function $F_{\alpha\alpha}(t,t')$

The perturbation expansion of $F_{\mathrm{aa}}(t,t')$ and $F_{\mathrm{bb}}(t,t')$ leads to similar results as $F_{\mathrm{ab}}(t,t')$. The non-vanishing contributions are

$$\begin{aligned}
&\left\langle T_c\left(a_t a_t a_{t'}^\dagger a_{t'}^\dagger\right)\right\rangle \approx \\
&\lambda^4 \int_C dt_1 \int_C dt_2 \int_C dt_3 \int_C dt_4 \Big[\\
&\quad - D_a^{(0)}(t,t_2) D_a^{(0)}(t_1,t') D_b^{(0)}(t,t_4) D_b^{(0)}(t_3,t') G_{ab}(t_1,t_3) G_{ab}(t_2,t_4) G_{ba}(t_3,t_2) G_{ba}(t_4,t_1) \\
&\quad - D_a^{(0)}(t,t_2) D_a^{(0)}(t_1,t') D_b^{(0)}(t,t_4) D_b^{(0)}(t_3,t') G_{ab}(t_1,t_4) G_{aa}(t_2,t_1) G_{ba}(t_3,t_2) G_{bb}(t_4,t_3) \\
&\quad + D_a^{(0)}(t,t_2) D_a^{(0)}(t_3,t') D_b^{(0)}(t,t_4) D_b^{(0)}(t_1,t') G_{ab}(t_3,t_4) G_{ab}(t_2,t_1) G_{ba}(t_1,t_2) G_{ba}(t_4,t_3) \Big] ,
\end{aligned} \tag{2.89}$$

$$\begin{aligned}
&\left\langle T_c\left(b_t b_t b_{t'}^\dagger b_{t'}^\dagger\right)\right\rangle \approx \\
&\lambda^4 \int_C dt_1 \int_C dt_2 \int_C dt_3 \int_C dt_4 \Big[\\
&\quad - D_a^{(0)}(t,t_2) D_a^{(0)}(t_1,t') D_b^{(0)}(t,t_4) D_b^{(0)}(t_3,t') G_{ab}(t_1,t_3) G_{ab}(t_2,t_4) G_{ba}(t_3,t_2) G_{ba}(t_4,t_1) \\
&\quad - D_a^{(0)}(t,t_2) D_a^{(0)}(t_1,t') D_b^{(0)}(t,t_4) D_b^{(0)}(t_3,t') G_{ab}(t_1,t_4) G_{aa}(t_2,t_1) G_{ba}(t_3,t_2) G_{bb}(t_4,t_3) \\
&\quad + D_a^{(0)}(t,t_2) D_a^{(0)}(t_3,t') D_b^{(0)}(t,t_4) D_b^{(0)}(t_1,t') G_{ab}(t_3,t_4) G_{ab}(t_2,t_1) G_{ba}(t_1,t_2) G_{ba}(t_4,t_3) \Big] .
\end{aligned} \tag{2.90}$$

The Feynman diagrams of these equations are shown below in Fig. 2.10.

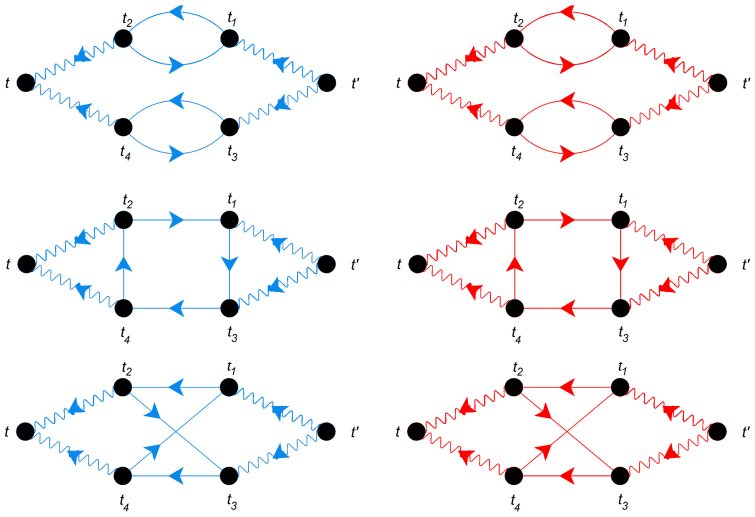

Fig. 2.10.: Nonzero Feynman diagrams of the fourth-order contribution of $F_{\mathrm{aa}}(t,t')$ in blue and $F_{\mathrm{bb}}(t,t')$ in red, depending on the contour times t_i, $i \in \{1,2,3,4\}$.

All diagrams have similar geometries and differ only in the composition of the matrix components of the Green's functions. The first analysis, compare Fig. 2.11, shows that due to the fourth order of the perturbative expansion, we get four interaction points

proportional to the dot-cavity coupling strength λ. The diagrams thus describe a two-photon process involving the emission and absorption of photons in both cavities with energies ω_a and ω_b, and different types of fermionic interaction in the double quantum dot system. The three basic geometries of the Feynman diagrams are shown in Fig. 2.11.

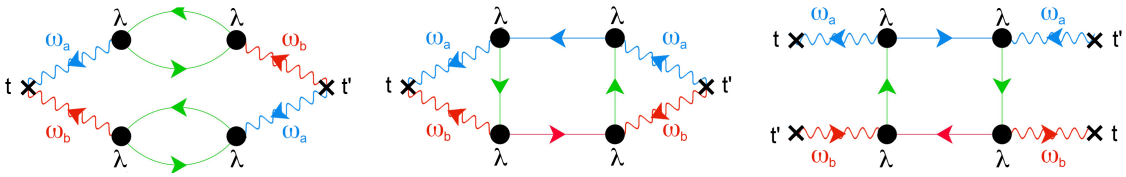

Fig. 2.11.: Examples of vertex diagrams, which correspond to the integrals of C and S. Black dots represent the electron-photon interaction proportional to λ. Wiggled lines correspond to bosonic Green's functions of the microwave cavities with resonance frequency $\omega_{a,b}$, distinguished by the colors red and blue. Straight lines signify fermionic Green's functions of the double quantum dot system. Diagonal ones are indicated by blue and red lines, offdiagonal Green's functions are represented in green.

2.6.3 Single- and Two-Particle Green's Function of the Single Dot

In the minimal example regarding the perturbative expansion, we considered a single dot coupled to a single microwave cavity. Since the interaction Hamiltonian differs for coupling to a single or two microwave cavities, the perturbative expansion becomes more complicated and similar to the expansion terms for the double-dot case since the bosonic part of the interaction is equivalent. Since we already determined the expansion of the single- and two-particle Green's function for the double-dot in detail, we directly give the results for the perturbative expansion. We show only nonzero contributions, i.e. we neglected disconnected diagrams, Tadpole diagrams, and contributions containing the term $D(t,t')$.

The result for the single-particle Green's function upon second-order reads

$$\left\langle a_t a_{t'}^\dagger \right\rangle^{(2)} = \lambda^2 \int_C dt_1 \int_C dt_2 D_a(t,t_2) D_a(t_1,t') G(t_1,t_2) G(t_2,t_1)\,, \tag{2.91}$$

$$\left\langle b_t b_{t'}^\dagger \right\rangle^{(2)} = \lambda^2 \int_C dt_1 \int_C dt_2 D_b(t,t_2) D_b(t_1,t') G(t_1,t_2) G(t_2,t_1)\,. \tag{2.92}$$

The fermionic parts of the two-particle Green's functions $F_{\alpha\alpha}(t,t')$ and $F_{\mathrm{ab}}(t,t')$ are equal and they differ only in the bosonic contribution. With the fermionic part

$$\begin{aligned} G_{\text{pert.SD}} = & G_{11}(t_2,t_1)G_{11}(t_3,t_2)G_{11}(t_4,t_3)G_{11}(t_1,t_4) \\ & + G_{11}(t_2,t_1)G_{11}(t_4,t_2)G_{11}(t_1,t_3)G_{11}(t_3,t_4) \\ & + G_{11}(t_3,t_1)G_{11}(t_1,t_2)G_{11}(t_4,t_3)G_{11}(t_2,t_4) \\ & + G_{11}(t_3,t_1)G_{11}(t_4,t_2)G_{11}(t_1,t_3)G_{11}(t_2,t_4) \\ & + G_{11}(t_3,t_1)G_{11}(t_4,t_2)G_{11}(t_2,t_3)G_{11}(t_1,t_4) \\ & + G_{11}(t_4,t_1)G_{11}(t_1,t_2)G_{11}(t_2,t_3)G_{11}(t_3,t_4) \\ & + G_{11}(t_4,t_1)G_{11}(t_3,t_2)G_{11}(t_1,t_3)G_{11}(t_2,t_4) \\ & + G_{11}(t_4,t_1)G_{11}(t_3,t_2)G_{11}(t_2,t_3)G_{11}(t_1,t_4)\,, \end{aligned} \tag{2.93}$$

the three two particle Green's functions upon fourth order read

$$\left\langle T_C\left(a_t a_t a_{t'}^\dagger a_{t'}^\dagger\right)\right\rangle = \lambda^4 \int_C dt_1 \int_C dt_2 \int_C dt_3 \int_C dt_4 D_a^{(0)}(t,t_3) D_a^{(0)}(t,t_4) D_a^{(0)}(t_1,t') D_a^{(0)}(t_2,t') G_{\text{pert.SD}}\,, \tag{2.94}$$

$$\left\langle T_C\left(b_t b_t b_{t'}^\dagger b_{t'}^\dagger\right)\right\rangle = \lambda^4 \int_C dt_1 \int_C dt_2 \int_C dt_3 \int_C dt_4 D_b^{(0)}(t,t_3) D_b^{(0)}(t,t_4) D_b^{(0)}(t_1,t') D_b^{(0)}(t_2,t') G_{\text{pert.SD}}\,, \tag{2.95}$$

$$\left\langle T_C\left(a_t b_t a_{t'}^\dagger b_{t'}^\dagger\right)\right\rangle = \lambda^4 \int_C dt_1 \int_C dt_2 \int_C dt_3 \int_C dt_4 D_a^{(0)}(t,t_3) D_b^{(0)}(t,t_4) D_a^{(0)}(t_1,t') D_b^{(0)}(t_2,t') G_{\text{pert.SD}}\,. \tag{2.96}$$

2.7 Integration

2.7.1 Real Time and Frequency Representation

Until now we have the integral representation over the unperturbed Keldysh Green's functions in contour times. Summarizing the multiplication of the fermionic Green's function by a quantity $P(t_1,t_2,t_3,t_4)$ all three types of diagrams, as shown in Fig. 2.11, read in this shorter notation

$$\int_C dt_1 \int_C dt_2 \int_C dt_3 \int_C dt_4 D(t,t_1) D(t,t_2) P(t_1,t_2,t_3,t_4) D(t_2,t') D(t_4,t')\,, \tag{2.97}$$

where $D(t_i,t_j)$ can be the bosonic Green's function of cavity a or b.

We parametrize the Keldysh contour through [118]

$$\int_{\mathrm{c}} d\tau = \int_{-\infty}^{\infty} dt^{+} + \int_{\infty}^{-\infty} dt^{-}\,, \tag{2.98}$$

where t^{+} are time arguments on the upper branch and t^{-} on the lower branch of the contour. We introduce a corresponding variable $s_i = \pm$ that denotes the position of the time argument t_i. We transform the integrals from contour time to real-time by subsequently summing up the integrand for all possible configurations of the integration variables t_1 to t_4 on the contour, which can be written as

$$\sum_{s_1,s_2,s_3,s_4=\pm} s_1 s_2 s_3 s_4 \int_{-\infty}^{\infty} dt_1^{s_1} \int_{-\infty}^{\infty} dt_2^{s_2} \int_{-\infty}^{\infty} dt_3^{s_3} \int_{-\infty}^{\infty} dt_4^{s_4} D^{s_t s_1}(t,t_1)\, D^{s_t s_3}(t,t_3)$$
$$P^{s_1 s_2 s_3 s_4}(t_1,t_2,t_3,t_4)\, D^{s_2 s_{t'}}(t_2,t')\, D^{s_3 s_{t'}}(t_3,t')\,. \tag{2.99}$$

Regarding Eqs. (2.15) to (2.17), the two time arguments t and t' are already fixed due to the choice of the lesser component. Regarding the latter equation we get only bosonic Green's function of the form $D^{+\ s_i}$ and $D^{s_i\ -}$. This and the fact that the bosonic lesser Green's function of Eq. (2.73) is zero reduces the number of possible configurations of time arguments on the contour to only a single one and we get the real time integral

$$\int_{-\infty}^{\infty} dt_1 \int_{-\infty}^{\infty} dt_2 \int_{-\infty}^{\infty} dt_3 \int_{-\infty}^{\infty} dt_4 D(t,t_1) D(t,t_2) P^{++--}(t_1,t_2,t_3,t_4) \tilde{D}(t_2,t') \tilde{D}(t_4,t'). \tag{2.100}$$

In Sections 2.3.3.1 and 2.5 we determined the unperturbed fermionic and bosonic Keldysh Green's functions depending on the energy. Via the Fourier transformation, we replace Green's functions with the integrals in energy space

$$G(t-t') = \mathcal{F}[G(\omega)](t-t') = \int_{-\infty}^{\infty} G(\omega) e^{-i\omega(t-t')} d\omega\,, \tag{2.101}$$

$$D(t-t') = \mathcal{F}[D(\omega)](t-t') = \int_{-\infty}^{\infty} D(\omega) e^{-i\omega(t-t')} d\omega\,. \tag{2.102}$$

In this way, we transform the integrals describing the diagrams from the real-time domain to the energy domain and can insert the energy-dependent Green's functions that we already obtained. To simplify the complex integration, we consider the limit of equal resonance frequencies of the microwave cavities, i.e. $\omega_a = \omega_b = \omega_0$ so that the bosonic Green's function of the two microwave cavities becomes equal, i.e. $\boldsymbol{D_a} = \boldsymbol{D_b} = \boldsymbol{D}$. The average occupations for the two cavities $\alpha =$ a,b upon second order, written in Eqs.

(2.84) and (2.85) dependent on contour times, reads in terms of the energy-dependent integrals

$$\bar{n}_\alpha = -\lambda^2 \iint d\omega_1\, d\omega_2\, D^{(0)}(\omega_2-\omega_1) G^<_{\alpha\alpha}(\omega_2) G^<_{\alpha\alpha}(\omega_1) \tilde{D}^{(0)}(\omega_2-\omega_1). \tag{2.103}$$

They become identical for zero level spacing, i.e. $\bar{n}_\mathrm{a} = \bar{n}_\mathrm{b}$, since then also the Green's functions of the two dots, the diagonal elements of Eq. (2.58), are equivalent. For a large level spacing the quantities have to be calculated separately.
The contour time integral of Eq. (2.88) reads in the energy domain

$$\begin{aligned}
\left\langle \hat{a}^\dagger \hat{a} \hat{b}^\dagger \hat{b} \right\rangle = \lambda^4 \iiiint & d\omega_1\, d\omega_2\, d\omega_3\, d\omega_4 \Big\{ \\
& D^{(0)}(\omega_1-\omega_2) D^{(0)}(\omega_3-\omega_4) \tilde{D}^{(0)}(\omega_1-\omega_2) \tilde{D}^{(0)}(\omega_3-\omega_4) G^<_{\mathrm{aa}}(\omega_1) G^<_{\mathrm{aa}}(\omega_2) G^<_{\mathrm{bb}}(\omega_3) G^<_{\mathrm{bb}}(\omega_4) \\
+ & D^{(0)}(\omega_1-\omega_2) D^{(0)}(\omega_3-\omega_4) \tilde{D}^{(0)}(\omega_1-\omega_2) \tilde{D}^{(0)}(\omega_3-\omega_4) G^<_{\mathrm{ab}}(\omega_3) G^<_{\mathrm{ab}}(\omega_2) G^<_{\mathrm{ab}}(\omega_1) G^<_{\mathrm{ab}}(\omega_4) \\
+ & D^{(0)}(\omega_1-\omega_2) D^{(0)}(\omega_3-\omega_4) \tilde{D}^{(0)}(\omega_1-\omega_4) \tilde{D}^{(0)}(\omega_3-\omega_2) G^<_{\mathrm{aa}}(\omega_1) G^<_{\mathrm{ab}}(\omega_2) G^<_{\mathrm{bb}}(\omega_3) G^<_{\mathrm{ab}}(\omega_4) \\
+ & D^{(0)}(\omega_1-\omega_2) D^{(0)}(\omega_3-\omega_4) \tilde{D}^{(0)}(\omega_1-\omega_4) \tilde{D}^{(0)}(\omega_3-\omega_2) G^<_{\mathrm{ab}}(\omega_3) G^<_{\mathrm{aa}}(\omega_2) G^<_{\mathrm{ab}}(\omega_1) G^<_{\mathrm{bb}}(\omega_4) \\
+ & D^{(0)}(\omega_1-\omega_2) D^{(0)}(\omega_2-\omega_4) \tilde{D}^{(0)}(\omega_1-\omega_3) \tilde{D}^{(0)}(\omega_3-\omega_4) G_{\mathrm{ab}}(\omega_2) G_{\mathrm{ab}}(\omega_3) G^<_{\mathrm{aa}}(\omega_1) G^<_{\mathrm{bb}}(\omega_4) \\
+ & D^{(0)}(\omega_1-\omega_2) D^{(0)}(\omega_2-\omega_4) \tilde{D}^{(0)}(\omega_1-\omega_3) \tilde{D}^{(0)}(\omega_3-\omega_4) G_{\mathrm{ab}}(\omega_2) G_{\mathrm{ab}}(\omega_3) G^<_{\mathrm{aa}}(\omega_4) G^<_{\mathrm{bb}}(\omega_1) \\
+ & D^{(0)}(\omega_1-\omega_2) D^{(0)}(\omega_2-\omega_4) \tilde{D}^{(0)}(\omega_1-\omega_3) \tilde{D}^{(0)}(\omega_3-\omega_4) G_{\mathrm{ab}}(\omega_2) G_{\mathrm{ab}}(\omega_3) 2\, G^<_{\mathrm{ab}}(\omega_1) G^<_{\mathrm{ab}}(\omega_4) \Big\}.
\end{aligned} \tag{2.104}$$

The real time integrals of Eqs. (2.89) and (2.89) becomes for $\alpha = a, b$

$$\begin{aligned}
\left\langle \hat{\alpha}^\dagger \hat{\alpha}^\dagger \hat{\alpha} \hat{\alpha} \right\rangle = 2\lambda^4 \iiiint & d\omega_1\, d\omega_2\, d\omega_3\, d\omega_4 \Big\{ \\
& 2 D^{(0)}(\omega_1-\omega_2) D^{(0)}(\omega_2-\omega_3) \tilde{D}^{(0)}(\omega_4-\omega_3) \tilde{D}^{(0)}(\omega_1-\omega_4) G_{\alpha\alpha}(\omega_4) G^<_{\alpha\alpha}(\omega_1) G_{\alpha\alpha}(\omega_2) G^<_{\alpha\alpha}(\omega_3) \\
+ & D^{(0)}(\omega_1-\omega_2) D^{(0)}(\omega_3-\omega_4) \tilde{D}^{(0)}(\omega_1-\omega_2) \tilde{D}^{(0)}(\omega_3-\omega_4) G^<_{\alpha\alpha}(\omega_1) G^<_{\alpha\alpha}(\omega_3) G^<_{\alpha\alpha}(\omega_2) G^<_{\alpha\alpha}(\omega_4) \\
+ & D^{(0)}(\omega_1-\omega_2) D^{(0)}(\omega_3-\omega_4) \tilde{D}^{(0)}(\omega_1-\omega_4) \tilde{D}^{(0)}(\omega_3-\omega_2) G^<_{\alpha\alpha}(\omega_1) G^<_{\alpha\alpha}(\omega_3) G^<_{\alpha\alpha}(\omega_2) G^<_{\alpha\alpha}(\omega_4) \Big\}
\end{aligned} \tag{2.105}$$

In the latter term, only diagonal elements of the fermionic Keldysh Green's function appear. In the case of zero level spacing, the integral result is equal for $\alpha = a$ and $\alpha = b$. Since we consider the limit of equal resonance frequencies, i.e. $\omega_a = \omega_b = \omega_0$, the bosonic Green's function are already the same while the fermionic Green's functions differ only in their dependence on $\Delta\varepsilon$. The fermionic Green's functions are different for a finite level spacing, and we have to calculate both cases independently. However, we will see that result will still be the same.

The bubble diagrams in the first line of Fig. 2.9 and Fig. 2.10, which correspond to the first summand in Eqs. (2.104) and (2.105), are factorizable and can be separated into

their upper and lower branches as in Fig. 2.8. This leads to two two-dimensional integrals, which are equal or similar to the integral of the average occupation of Eq. (2.103).

The real-time Green's functions for the single dot coupled to two microwave cavities transform similarly.

The two-dimensional integral over energy required for the average occupation in Eq. (2.103) and the separable terms of Eqs. (2.104) and (2.105) as well as the four-dimensional integrals of the eight Green's functions in Eqs. (2.104) and (2.105) are polynomial in the integration variables and thus in principal solvable. We consider the poles of the functions and perform energy integrations with the help of the residue theorem.

2.7.2 Results of the Single- and Two-Particle Green's Function for the Double-Dot

Due to the large number and complicated expressions for the poles, the algebraic results generally become pretty lengthy. To simplify the expressions, we decided to solve the integrals in the low damping limit, i.e. $\omega_0 \gg \Gamma \gg \eta$, as we also did in the minimal example. Due to the large effort, we directly determined the single- and two-particle Green's function, given by Eqs. (2.104) and (2.105) and determined not explicitly and separately the result for each diagram. While it would be manageable to show the results appearing after the first integration in this thesis already, the second integration leads to such lengthy expressions that it is not feasible to write them up in a helpful way. We, therefore, give the result directly for the single- and two-particle Green's function in the limits of zero and large level spacing.

Zero level spacing, i.e. $\Delta\varepsilon = 0$

The lesser single-particle Green's function upon second order becomes for $\alpha = a, b$

$$\left\langle \hat{\alpha}^\dagger \hat{\alpha} \right\rangle^< = \pi^2 \left(\frac{\lambda}{\omega_0}\right)^2 \left(\frac{\Gamma}{\eta}\right) . \tag{2.106}$$

The lesser two-particle Green's functions $F^<_{\mathrm{ab}}(t,t')$ and $F^<_{\alpha\alpha}(t,t')$, for $\alpha = a, b$, upon fourth order become

$$\left\langle \hat{a}^\dagger \hat{a} \hat{b}^\dagger \hat{b} \right\rangle = \frac{3}{2}\pi^4 \left(\frac{\lambda}{\omega_0}\right)^4 \left(\frac{\Gamma}{\eta}\right)^2 , \tag{2.107}$$

$$\left\langle \hat{\alpha}^\dagger \hat{\alpha}^\dagger \hat{\alpha} \hat{\alpha} \right\rangle = \frac{3}{4}\pi^4 \left(\frac{\lambda}{\omega_0}\right)^4 \left(\frac{\Gamma}{\eta}\right)^2 . \tag{2.108}$$

Large level spacing, i.e. $\Delta\varepsilon \gg \Gamma$

The lesser single-particle Green's function upon second order becomes for $\alpha = a, b$

$$\left\langle \hat{\alpha}^\dagger \hat{\alpha} \right\rangle^< = 2\pi^2 \left(\frac{\lambda}{\omega_0}\right)^2 \left(\frac{\Gamma}{\eta}\right) . \tag{2.109}$$

The lesser two-particle Green's functions $F_{\mathrm{ab}}(t,t')$ and $F_{\alpha\alpha}(t,t')$, for $\alpha = a, b$, upon fourth order become

$$\left\langle \hat{a}^\dagger \hat{a} \hat{b}^\dagger \hat{b} \right\rangle = (2\pi)^4 \left(\frac{\lambda}{\omega_0}\right)^4 \left(\frac{\Gamma}{\eta}\right)^2 , \tag{2.110}$$

$$\left\langle \hat{\alpha}^\dagger \hat{\alpha}^\dagger \hat{\alpha} \hat{\alpha} \right\rangle = 24\pi^4 \left(\frac{\lambda}{\omega_0}\right)^4 \left(\frac{\Gamma}{\eta}\right)^2 . \tag{2.111}$$

2.7.3 Results of the Single- and Two-Particle Green's Function for the Single Dot

The integral results for the single dot are obtained in the same way. For equal frequencies of the microwave cavities Eqs. (2.94) to (2.96) become equal. The Cauchy-Schwarz inequality parameter S, that is given by the ratio of these terms becomes then equal to one. Therefore we need to determine only the average occupation and the covariance for which we need two quantities

$$\left\langle \hat{\alpha}^\dagger \hat{\alpha} \right\rangle^< = 2\pi^2 \left(\frac{\lambda}{\omega_0}\right)^2 \left(\frac{\Gamma}{\eta}\right) , \tag{2.112}$$

$$\left\langle \hat{a}^\dagger \hat{a} \hat{b}^\dagger \hat{b} \right\rangle = 12\pi^4 \left(\frac{\lambda}{\omega_0}\right)^4 \left(\frac{\Gamma}{\eta}\right)^2 . \tag{2.113}$$

2.8 Results

In certain limits, we are able to calculate the relevant quantities analytically. We consider equal resonance frequencies $\omega_{\mathrm{a}} = \omega_{\mathrm{b}} \equiv \omega_0$ and zero temperature of the cavities. Furthermore, we focus on the regime of low damping inside the cavities, i.e. $\omega_0 \gg \Gamma \gg \eta$, and on the high voltage bias limit. Regarding the energy levels of the parallel quantum dots, we consider two different cases: First, we study the case of two almost equal energy levels, and second the case of two strongly differing levels. Finally, we compare these results with the case of a single dot coupled to two cavities at the same time, see Fig. 2.7.

We first determine the average photon number of the single cavities $\langle \hat{n}_{\mathrm{a}} \rangle = \langle \hat{n}_{\mathrm{b}} \rangle = \bar{n}$ up to second order and the corresponding fluctuations $\delta n^2 = \langle \hat{n}^2 \rangle - \bar{n}^2$ up to fourth order. The latter quantity can be computed from the knowledge of $\bar{n}$ and $\left\langle \hat{\alpha}^\dagger \hat{\alpha}^\dagger \hat{\alpha} \hat{\alpha} \right\rangle$ (viz. $F^<_{\alpha\alpha}(t,t)$).

Then one can analyze the behavior of the Fano factor, defined as $F = \delta n^2/\bar{n}$. Finally, we calculate the covariance C and the Cauchy-Schwarz parameter S both up to fourth order in λ. Due to the symmetries in the system, the results for both cavities are the same.

2.8.1 Average Photon Number, Fluctuation and Fano Factor

First, we show the results for the average occupation of the single cavities $\bar{n}$, their fluctuation δn^2, and the Fano factor F. Let us discuss them successively in the following.

The average occupation is directly given by the result of single-particle lesser Green's function, i.e. Eqs. (2.106) and (2.109) for the double-dot and Eq. (2.112) for the single dot coupled to two cavities. We define the average occupation for the double-dot coupled to the two cavities at zero level spacing as reference value $\bar{n}$ with

$$\bar{n} = \pi^2 \left(\frac{\lambda}{\omega_0}\right)^2 \left(\frac{\Gamma}{\eta}\right) . \tag{2.114}$$

The fluctuation can be expressed in terms of the average occupation and the two-particle Green's function of Eq. (2.108), and Eq. (2.111) respectively, via

$$\delta_n^2 = \left\langle n^2 \right\rangle - \langle n \rangle^2 = \left\langle \hat{a}^\dagger \hat{a}^\dagger \hat{a} \hat{a} \right\rangle - \langle n \rangle - \langle n \rangle^2 . \tag{2.115}$$

Finally the Fano factor is defined as

$$F = \frac{\delta n^2}{\langle n \rangle} . \tag{2.116}$$

The results for these three quantities are given in the Tab. 2.1. The first column describes the results for the parallel double-dot with equal energy levels, while the second column is the evaluation at large level spacing. The third column gives the result of Section 2.7.3, i.e. the single dot coupled to two cavities. The average occupation for the single and double-dot with large level spacing is equal since we calculate the average occupation only up to second order. The result of the double-dot with two almost equal energy levels, i.e. $\Delta\varepsilon \ll \Gamma$, acting as a single-electron splitter, is half the size of the case $\Delta\varepsilon \gg \Gamma$ and the single-dot system. This becomes clear when considering the electronic Hamiltonian of the parallel double-dot coupled to the two leads. In the case of zero or small level spacing, the Hamiltonian can be written in the form of an effective single-dot problem. Compared to the real single-dot case the dot-lead coupling parameter t is renormalized to $t \to t/\sqrt{2}$. With $\Gamma \propto |t|^2$, this renormalization enters as a factor of two in the bosonic occupation of the cavities [132]. Furthermore, we checked that the result for the single dot coupled simultaneously to two cavities coincides with previous results in the limit, in which the induced damping associated with the electron-boson interaction is smaller than the intrinsic damping of the cavities η [137, 138].

	DQD, $\Delta\varepsilon = 0$	DQD, $\Delta\varepsilon \gg \Gamma$	single dot
$\bar{n}$	n_0	$2n_0$	$2n_0$
δn^2	$n_0\,(1 - n_0/4)$	$2n_0\,(1 + n_0)$	$2n_0\,(1 + 4n_0)$
F	$1 - n_0/4$	$1 + n_0$	$1 + 4n_0$

Tab. 2.1.: Results for the average photon number of a single cavity $\bar{n}$, fluctuations δn^2, Fano factor F, for three different cases: the double quantum dot (DQD) coupled to two cavities with zero or large level spacing and a single quantum dot coupled to two cavities. Here $n_0 = \pi^2 \left(\frac{\lambda}{\omega_0}\right)^2 \left(\frac{\Gamma}{\eta}\right)$.

According to Tab. 2.1, for the fluctuations and the corresponding Fano factor of the double-dot system, we find a sub-Poissonian behavior in the regime, where we have quantum interference in transport through the double-dot, whereas we obtain a super-Poissonian behavior for the other two cases. The sub-Poissonian behavior corresponds to a photon anti-bunching in the local cavity. Let us emphasize that the nature of the interaction already appears at the level of a single-cavity quantity, namely the local fluctuations of the photons in a cavity. This fact can already be seen at two trivial examples, since the sub-Poissonian behavior occurs both for the entangled bosonic states in the Fock occupation

$$|\Psi\rangle_{pq} \propto |n_\mathrm{a} = p, n_\mathrm{b} = q\rangle + |n_\mathrm{a} = q, n_\mathrm{b} = p\rangle \ , \tag{2.117}$$

with $p, q \in \mathbb{N}$ or in the coherent state basis

$$|\Psi\rangle_{z_1 z_2} \propto |\xi_\mathrm{a} = z_1, \xi_\mathrm{b} = z_2\rangle + |\xi_\mathrm{a} = z_2, \xi_\mathrm{b} = z_1\rangle \ , \tag{2.118}$$

with $|\xi\rangle$ being a coherent state and $z_1, z_2 \in \mathbb{C}$.

2.8.2 Covariance and Cauchy-Schwarz Inequality Factor

The final aim was to calculate the covariance C and the Cauchy-Schwarz inequality factor S to prove classical and quantum correlation. We recall their equations

$$C = \left(iF^<_{\mathrm{ab}}(t,t) + D^<_\mathrm{a}(t,t) D^<_\mathrm{b}(t,t)\right) , \tag{2.119}$$

$$S = \frac{F^<_{\mathrm{ab}}(t,t)}{\sqrt{F^<_{\mathrm{aa}}(t,t) F^<_{\mathrm{bb}}(t,t)}} , \tag{2.120}$$

and use the results of Eqs. (2.106) to (2.111) to determine them. The final expressions are given in Tab. 2.2.

	DQD, $\Delta\varepsilon = 0$	DQD, $\Delta\varepsilon \gg \Gamma$	single dot
C	$n_0^2/2$	0	$8n_0^2$
S	2	$2/3$	1

Tab. 2.2.: Results for the covariance C and Cauchy-Schwarz inequality parameter S, for three different cases: the double quantum dot (DQD) coupled to two cavities with zero or large level spacing and a single quantum dot coupled to two cavities. Here $n_0 = \pi^2 \left(\frac{\lambda}{\omega_0}\right)^2 \left(\frac{\Gamma}{\eta}\right)$.

For the covariance C, we find a finite and positive value for the double quantum dot with two equal energy levels, verifying a correlation of the photons in the single cavities. The covariance for a large level spacing vanishes, meaning no correlation. This result is expected for the case of two separated electron pathways. Notice, however, that a finite covariance also arises in the case of a single dot simultaneously coupled to two cavities, see Fig. 2.7. This latter result can be interpreted as classical correlation, as we have a single photon emitter coupled to both cavities.

A finite covariance proves correlation but does not indicate quantum correlation (entanglement). To distinguish classical and quantum correlations, we calculated the classical Cauchy-Schwarz parameter S of Eq. (2.120), which we cast in the following form

$$S = \frac{\left|\bar{n}^2 + C\right|}{\left|\bar{n}\left(\bar{n} - 1\right) + \delta n^2\right|} = \frac{\left|\bar{n} + \frac{C}{\bar{n}}\right|}{\left|\bar{n} + F - 1\right|} \,. \tag{2.121}$$

The expression states that a violated Cauchy-Schwarz inequality ($S > 1$) occurs if a finite and positive covariance is combined with a sub-Poissonian ($F < 1$) behavior. As reported in Tab. 2.2, the Cauchy-Schwarz inequality for vanishing level spacing is clearly violated. This confirms the quantum entanglement of the photons in the two distant microwave cavities if the energy levels of the two dots are sufficiently close to each other, viz. the electron is delocalized over the two dots when it flows from one lead to the other. For strongly differing energy levels of the dots, the classical Cauchy-Schwarz inequality is no longer violated as $C = 0$ (uncorrelated systems). As a sanity check, for the single dot with $C > 0$ and $F > 1$ (super-Poissonian), we find that the classical Cauchy-Schwarz inequality is not violated but reaches the maximum classical value.

2.9 Limitations

Let us finally discuss the role of decoherence in the system.
Intrinsic contributions stem from losses in the cavities. Therefore, we assume high-quality cavities with intrinsic damping that is smaller than the broadening of the electronic levels $\eta \ll \Gamma \ll \omega_0$. We expect the photon production rate to be proportional to the flow of electrons through the dots. If the cavities lose energy at a rate that is faster than the rate at which photons are created, this will, of course, destroy entanglement.
Another source of decoherence arises from the stochastic nature of electron tunneling. The granular electron flow cannot generate a pure quantum state of the photons in the two cavities, but it will create an entangled mixed state.

We propose our setup as a proof of concept to realize bosonic quantum correlations mediated by single-electron transport. Although several parameters were assumed to be equal, we expect our results to be relevant for carefully chosen experimental settings. Since the covariance C and the Cauchy-Schwarz parameter S are continuous functions of the parameters of the Hamiltonian, we expect our idealized proposal to be robust to small variations and hence to be realizable. A long-term perspective may be the creation of pure entangled states. For this objective, a time-dependent control of the electron occupations of the dots may need to be implemented along the lines discussed in [9, 10].

2.10 Conclusion and Outlook

The theory of nonlocality is a fundamental property of quantum mechanics. The delocalization of a quantum particle in space according to its associated wave function, or its superposition and corresponding correlations between spatially separated parts of a quantum system are of huge interest in hybrid devices based on semiconducting quantum circuits with integrated microwave photonics. Our theoretical work suggested a realistic setup to generate entanglement between two spatially separated microwave cavities using quantum delocalized electrons that flow through a parallel double quantum dot connected between two electrodes. In Section 2.1 we gave a first heuristic argument. If the energy levels of the dots are close, the electron travels delocalized through the parallel double quantum dot. The occurring correlation in the electronic part of the system is extended to the coupled microwave cavities and remains even if the electron leaves the system, which corresponds to a nonlocal measurement since the electron is removed without knowing which path it passed through. In Section 2.2 we defined the covariance and the Cauchy-Schwarz inequality parameter based on terms of Keldysh Green's functions as verification for classical or quantum correlation. To determine these quantities, we considered the electronic subsystem separately in Section 2.3 and the bosonic in Section 2.5 to describe the interaction of both by a perturbation expansion in the dot-cavity

coupling. Before we analized this, we studied the electronic subsystem in more detail. Due to the significant simplification of equal couplings between the electronic levels of the dots and the fermionic leads, we obtained an unusual behavior in the transmission curve compared to the system with arbitrary tunnel couplings, i.e. we obtained a peak instead of a dip at energies in close vicinity to the origin of the dot levels. We demonstrated that this singularity does not affect our results. The essential argument is that, since we are assuming the high voltage limit, a local singularity of transport properties at $\bar{\varepsilon}$ is averaged out. The singularity thus neither leads to a discontinuous behavior of the integral of the total electron flux nor any other quantities, like Feynman diagrams, derived from integrals over energy. In Section 2.6 we then performed the perturbation expansion in the doty-cavity interaction Hamiltonian upon fourth-order leading to three different types of Feynman diagrams. Transforming the corresponding integrals to the energy domain and using the residue theorem, we calculated the results for the single and two-particle Green's function in Section 2.7 for the double-dot with zero and large level spacing, respectively, and also for a single dot coupled simultaneously to two cavities. Finally we showed the results in Section 2.8. We presented the average photon number, the fluctuation, and the Fano factor finding sub-Poissonian behavior for the case of zero level spacing, which corresponds to a photon anti-bunching in the local cavity, and super-Possonian behaviour else. It was remarkable that the nature of interaction already appeared at the level of a single cavity, namely the local fluctuations of the photons in a cavity. We determined the covariance, which is finite for zero level spacing, and the single dot proving classical correlation. However, the Cauchy-Schwarz inequality is only violated for the double quantum dot with zero level spacing, proving quantum correlation, i.e. entanglement. The Cauchy-Schwarz parameter can also be expressed in terms of the average occupation, the covariance, and the Fano factor and states that entanglement occurs if finite covariance is combined with a sub-Poissonian behavior. We propose this setup as proof of concept to realize bosonic quantum correlations mediated by single-electron transport.

Part II

Effects in Systems of Nonlinear Coupled and Linear or Parametrically Driven Duffing Resonators

3 Introduction and Theoretical Background

3.1 Nonlinear Resonances in Mechanical and Optical Resonators

Small nanomechanical oscillators can have atomic-scale dimensions like carbon nanotubes and graphene sheets [139, 140, 141, 142] and show therefore already at small amplitudes nonlinear behavior of their vibrations, like parametric oscillation [143, 144, 145, 146, 147] or bifurcation [148, 149, 150, 151, 152]. The applications for nanomechanical resonators are prominent in the field of sensors and molecular transport [153, 154]. There have been theoretical proposals [155] and successful experiments for the detection of mass [156, 157, 158] or the enhancement of the thermal responsibility [159], general signal enhancement [160] or the detection of noise [161, 162]. Enhancing significantly a weak signal by use of a vibrational force [163] or squeezing a weakly damped driven mode [164] can be used to reduce noise for signal processing in metrology. Already small changes in the driving force can lead to different amplitude due to the bistability of forced vibrations [165], and therefore nanomechanical resonators are, besides being used as force detectors [166], ideal candidates for logical gates [167, 143, 168]. A larger device, like a two-dimensional membrane resonator, has the advantage that the frequency range showing resonant behavior reaches from 100 kHz to several MHz, enabling to observe experimentally higher orders of the parametric resonance due to a broader frequency bandwidth [169]. The excitation of flexural modes passes the way for hybrid engineered systems since they can easily couple to other degrees of freedom like light or atoms. Coupling membranes to ultra-cold atoms [170] can be used for cooling the membrane [171] or successfully couple collective atomic spin strongly to a membrane over a distance of 1m [172].

Regarding photonic degrees of freedom, the field of cavity optomechanics is quite broad [173]. There exist different forms of optomechanical coupling, and it can, for example, be linear, quadratic, or quartic in the displacement of the membrane [174]. In this way, it can be used for position measurement [175], e.g. fluctuations in the radiation force are correlated temporal to the position of the resonator [176] or to improve microwave-to-optical converters [177]. The application as a sensor can also be extended to physics caused by internal resonances. Examples are the phononic frequency comb [178, 179], an arbitrary flexural mode can be used as a self-detector for the amplitude of another mode [180] or

the lack of frequency stability of an oscillator due to its small size can be restored [181]. In nano- and micromechanical systems, the coupling of modes with a frequency ratio close to 1:3 is often stronger than the coupling between modes close to 1:2 [182] and is therefore of great interest in current research [149, 148]. There exist several non-trivial aspects when an internal resonant condition between eigenfrequencies is matched [182]. Based on the coupling of only two internal modes [183], one proposed that the resonance amplitude is limited by nonlinear terms and therefore becomes independent of the driving level [184] and observed that the energy decay rate suddenly switches to a lower value if two modes hybridize [185]. The principal mode is driven, and the mechanical energy is stored in the vibrational mode. Turning off the external drive, the energy is coherently transferred back to the fundamental mode [186]. But also multimode coupling can be achieved [187].

As already said, nonlinear resonances occur if the frequencies of two vibrational modes have a rational proportion. If the proportion is small, in the way that one frequency is just twice or three times as large as the other one, the resonance effects are most present [182]. A classical analog is the coupling of two harmonic oscillators with similar frequencies that exchange energy due to their coupling. The same physical process occurs between different resonant modes that exchange energy due to internal nonlinear resonance. The advantage of microscopic resonators is the explicit frequency controlling [182, 188] and, therefore, the possibility to tune the modes in or out of resonance. Due to the coupling, the behavior of the resonator depends not only on its frequency but also on the amplitude of the modes. Therefore, one can generate an internal coupling of different modes and their overtones, changing the dynamics of the corresponding driven mode even if the drive is turned off.

3.2 Forced Duffing Resonators

The harmonic oscillator describes the simplest form of oscillation, which is valid if the amplitude is small enough. However, due to miniaturization, the systems differ from the harmonic oscillation already at small amplitudes, showing nonlinear behavior. The first correction is the Duffing nonlinearity, which is of cubic order. A system can be excited by a single force or pulse, acting as an initial perturbation on the equilibrium system, that responds without further excitation. On the other hand, one can apply a continuous drive to the system while we differentiate between two different types of excitation. The so-called *external excitation*, which is included by an inhomogeneous term in the equation of motion and the *parametric excitation* that appears as time-dependent variable [189]. In the example of the Duffing resonator, we consider its behavior under an external, linear drive in Section 3.2.1, while we consider the parametrically driven case in Section 3.2.2. Besides the amplitude of the drive, also its frequency is essential. If we drive close to

the eigenfrequency of the resonator, it is called primary or main resonance. Due to the overtones of the fundamental mode, one can also drive the system at larger frequencies, like twice or three times the eigenfrequency, to obtain resonance phenomena of the higher harmonics. Due to internal resonances, these higher-order modes can couple, similar to the coupling of two nonlinear resonators. A prominent example of optical higher-harmonics is a laser pulse interacting with an atomic gas [190, 191], while the non-linear interaction between a plane light wave and its second (or even higher) harmonic was initially described by Armstrong et al. [192]. The coupling of nonlinear oscillations leads to interesting effects like bifurcation, which we briefly describe in Section 3.2.3.

3.2.1 Duffing Resonator with Linear Driving Force

In which way a mode has to be described in theory depends on the strength of the excitation, i.e. its amplitude. If the force and amplitude of a driven resonator are weak and small enough, respectively, the dynamics of the resonator can be modeled by a simple harmonic oscillator with additional damping and driving terms, i.e. the equation of motion is linear in the amplitude. If the amplitude increases, the linear theory is no longer sufficient to capture all occurring features. The first correction to the harmonic oscillator is a cubic nonlinearity, also known as Duffing nonlinearity [193]. The dynamics of the Duffing resonator, named after Georg Duffing [194], is described by the equation for the amplitude $q(t)$, which reads

$$\ddot{q} = -\omega_0^2 q - 2\Gamma\dot{q} - \gamma q^3 + \frac{F}{m}\cos(\omega_d t)\,. \tag{3.1}$$

Note that we set the mass $m = 1$ here and in the following. The system is characterized by the eigenfrequency ω_0, the linear damping constant Γ, the Duffing nonlinearity γ, and the linear driving force F with driving frequency ω_d. If the system is driven in this way, the driving frequency needs to be on primary resonance, i.e. the driving frequency needs to be close to eigenfrequency $\omega_d \approx \omega_0$ to respond with sufficiently large amplitudes. We use a canonical transformation for $q(t)$ to switch to the rotating frame

$$u = \left(q - \frac{i}{\omega_d}\dot{q}\right) e^{-i\omega_d t}\,, \qquad u^* = \left(q + \frac{i}{\omega_d}\dot{q}\right) e^{i\omega_d t}\,. \tag{3.2}$$

The corresponding equation for the new variable $u(t)$ reads then

$$\frac{du}{dt} = -\frac{i}{\omega_d} e^{-i\omega_d t}\left((\omega_d^2 - \omega_0^2)q - 2\Gamma\dot{q} - \gamma q^3 + F\cos(\omega_d t)\right)\,. \tag{3.3}$$

We apply the rotating wave approximation (RWA), i.e. we neglect the fast oscillating terms while we are within small detuning, i.e. $|\omega_d - \omega_0| \ll \omega_d\,, \omega_0$. Regarding Eq. (3.3), the individual terms approximate to

$$e^{-i\omega_d t} q \approxeq \frac{u}{2}, \quad e^{-i\omega_d t}\dot{q} \approxeq i\frac{\omega_d}{2}u, \quad e^{-i\omega_d t}q^3 = \frac{3}{8}|u|^2 u, \quad e^{-i\omega_d t}F\cos(\omega_d t) \approxeq \frac{F}{2}\,. \tag{3.4}$$

Introducing the detuning $\delta\omega_d = \omega_d - \omega_0$, the first term of the latter equation can be approximated by

$$\frac{\omega_d^2 - \omega_0^2}{2\omega_d} = \frac{\omega_d^2 - [\omega_d - \delta\omega_d]^2}{2\omega_d} \approxeq \delta\omega_d\,.$$

In this way, we get the final expression for the variable $u(t)$ in the RWA:

$$\frac{du}{dt} = -i\delta\omega_d u - \Gamma u + i\frac{3\gamma}{8\omega_d}|u|^2 u - i\frac{F}{2\omega_d}\,. \tag{3.5}$$

To simplify the expression of Eq. (3.5) and plot the numerical solution, we introduce new, scaled variables, i.e. the amplitude $z(t)$, detuning δ and force $\sqrt{\beta}$

$$u = \sqrt{\frac{8\omega_d\Gamma}{3\gamma}}z\,, \qquad \delta = \frac{\delta\omega_d}{\Gamma}\,, \qquad \sqrt{\beta} = \sqrt{\frac{3\gamma F^2}{32\omega_d^3\Gamma^3}}\,, \tag{3.6}$$

and finally obtain the equation for the scaled amplitude in the RWA, which now depends, besides the detuning, only on the parameter $\sqrt{\beta}$, which is proportional to the driving force

$$\frac{1}{\Gamma}\frac{dz}{dt} = \left(-i\delta - 1 + i|z|^2\right)z - i\sqrt{\beta}\,. \tag{3.7}$$

We consider the steady-state solution $\bar{z}$, which can be derived by $d\bar{z}/dt = 0$, and take the square modulus of both sides, obtaining the equation

$$\beta = \left[1 + \left(\delta - |\bar{z}|^2\right)^2\right]|\bar{z}|^2\,, \tag{3.8}$$

that we solve numerically. Equation. (3.8) has either one or three solutions, which we plotted for different forces $\sqrt{\beta}$ in Fig. 3.1. If the force is small, we obtain only a single stable solution. With increasing force, we obtain three steady-state solutions, of which two are stable, and one is unstable. In contrast to the linear system, the state in which the system responds to the drive depends on the initial conditions. If the detuning is small, i.e. the driving frequency is below the eigenfrequency, the system shows the high-amplitude solution. Increasing the driving frequency and, therefore, the detuning, the amplitude follows the curve indicated by the red arrows. At some point, the solution breaks down, the amplitude shows a jump, and continues in the low amplitude solution. If the initial driving has a large detuning, the amplitude corresponds to the low amplitude state and follows the curve indicated by the green arrows with decreasing detuning. If the

detuning has decreased enough, a jump appears upwards to the high amplitude solution. The maximum amplitude value can be obtained only with increasing detuning. The dashed line is also a steady-state solution but belongs to a saddle point that is unstable and therefore cannot be reached in the experiment [189]. We show the same curve for different strong driving forces in the right panel of Fig. 3.1. With increasing force, the curve bends stronger to the right. Note that we assumed that the Duffing nonlinearity is positive, i.e. $\gamma > 0$, otherwise the curve would have been bent to the left. If one plots the maximum amplitude value for all possible forces in between, one gets the so-called backbone curve, which is the gray dashed line in Fig. 3.1.

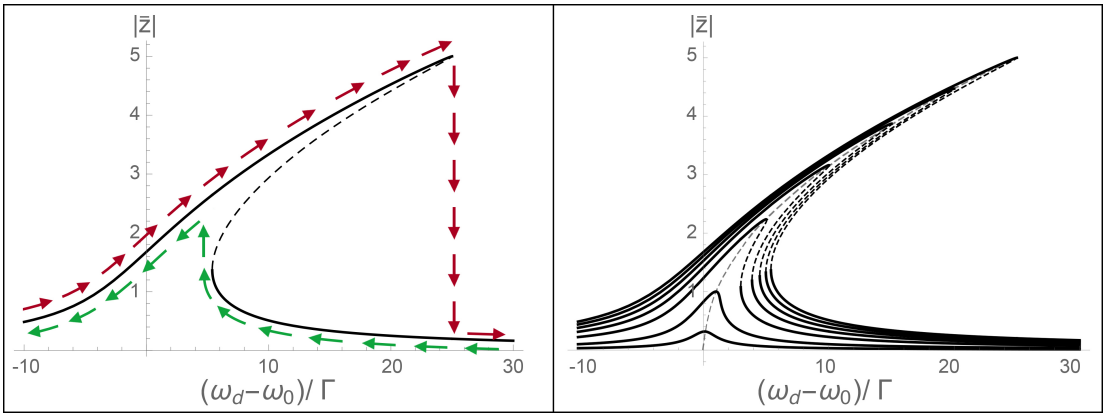

Fig. 3.1.: Numerical solutions for the Duffing equation. Bold lines represent stable solutions and dashed lines the unstable solutions. Left plot: Duffing solutions for a force characterized by the parameter $\beta = 25$. The red arrows indicate the amplitude for increasing detuning while the green arrows indicate the amplitude for measurements with decreasing detuning. Right plot: Duffing solutions for different forces characterized by the parameter $\beta = 0.1,\ 1,\ 5,\ 10,\ 15,\ 20,\ 25$. Gray dashed line represents the backbone function.

3.2.2 Duffing Resonator with Parametric Force

The Duffing resonator in the previous section was driven by an external force that occurred in the equation of motions as an inhomogeneous extension. We still consider a Duffing resonator but with a driving force that occurs as a coefficient. The (time-dependent) excitation appears then as a parameter in the equation of motion, which is the reason why this excitation is called parametric excitation [189]. Contrary to the external force, which needs a primary resonance to initiate finite amplitudes, the parametric excitation produces a significant amplitude response if it drives close to twice the system's eigenfrequencies.

The parametric drive is mathematically described by $\mu\cos(2\omega_d t + \varphi)$. μ is the modulation amplitude, and we modulate close to twice the eigenfrequency, i.e. $|\omega_0 - \omega_d| \ll \omega_d,\ \omega_0$

while the drive varies over time. The equation of motion describing the dynamics of this system reads then

$$\ddot{q} = -\left[\omega_0^2 + 2\mu\cos\left(2\omega_d t + \varphi\right)\right] q - \gamma q^3 - 2\Gamma\dot{q}\,. \tag{3.9}$$

We choose the same canonical transformation, as defined in Eq. (3.2), to switch to the rotating frame. The driving term becomes in the RWA $e^{-i\omega_d t}\cos(\omega_d t + \varphi)q \approx u^*/4 \cdot e^{i\varphi}$. The equation of motion transforms then to

$$\frac{\dot{u}}{\Gamma} = -i\delta u + i\frac{\mu}{2\omega_d\Gamma}e^{i\varphi}u^* + i\frac{3\gamma}{8\omega_d\Gamma}|u|^2 u - u\,. \tag{3.10}$$

We introduce the scaled parameters

$$u = \sqrt{\frac{8\omega_d\Gamma}{3\gamma}}z\,, \quad \delta = \frac{\delta\omega}{\Gamma}\,, \quad \tilde{\mu} = \frac{\mu}{2\omega_d\Gamma}\,, \tag{3.11}$$

and obtain finally the equation of motion of the scaled amplitude depending on the scaled parameters

$$\frac{\dot{z}}{\Gamma} = \left[-1 + i(|z|^2 - \delta)\right] z + i\tilde{\mu}e^{i\varphi}z^*\,. \tag{3.12}$$

We consider the steady-state solution $d\bar{z}/dt = 0$ and take the square modulus of both sides. Besides the trivial solution $\bar{z} = 0$ we also get the finite-amplitude solution

$$|\bar{z}|_\pm = \sqrt{\delta \pm \sqrt{\tilde{\mu}^2 - 1}}\,, \tag{3.13}$$

which is only valid if $\mu > 1$ and $\delta > \sqrt{\tilde{\mu}^2 - 1}$. To determine the phase, we use the general phase representation of the steady-state $\bar{z}_\pm = |\bar{z}_\pm|e^{i\arg(\bar{z}_\pm)}$ with the amplitude of Eq. (3.13). Inserting them into the steady-state equation we obtain the phase, with $n \in \mathbb{N}$

$$\arg(\bar{z}_{+-}) = -\arctan\left(\mp\sqrt{\tilde{\mu}^2 - 1} + \tilde{\mu}\right) + \frac{\varphi}{2} + \pi n\,. \tag{3.14}$$

Stability analysis

To investigate the stability of the possible steady-state solutions, we consider a small fluctuation $\delta z(t)$ around the steady-state $\bar{z}$, i.e. $z(t) = \bar{z} + \delta z(t)$. In this way, we can analyze if a small perturbation of the oscillation in the steady-state decays or rises, which illustrates the stability of the steady-state solution. In other words; after some time the so called dynamical state solution should approach the steady-state solution, i.e. $\lim_{t\to\infty} z(t) = \bar{z}$. Hence, the fluctuations must be small, so that occurring higher orders of δz can be neglected.

We expand the scaled equation of motion in the RWA to first order in $\delta z(t)$, i.e. we neglect higher-order terms and obtain

$$\frac{\dot{\bar{z}} + \dot{\delta z}(t)}{\Gamma} \approx \Big[-1 + i(|\bar{z}|^2 - \delta)\Big]\, \bar{z} + i\tilde{\mu} e^{i\varphi} \bar{z}^* + \Big[-1 + i(2|\bar{z}^2| - \delta)\Big]\, \delta z(t) + i(\bar{z}^2 + \tilde{\mu} e^{i\varphi}) \delta z(t)^* \,. \tag{3.15}$$

Identifying the steady-state equation as the first and second addend of the latter equation, we can isolate the differential equation for the fluctuation

$$\frac{\dot{\delta z}(t)}{\Gamma} = \Big[-1 + i(2|\bar{z}^2| - \delta)\Big] \delta z(t) + i(\bar{z}^2 + \tilde{\mu} e^{i\varphi}) \delta z(t)^* \,. \tag{3.16}$$

With $\alpha = \left[-1 + i(2|\bar{z}^2| - \delta)\right]$ and $\beta = i(\bar{z}^2 + \tilde{\mu} e^{i\varphi})$, we write the latter equation and its conjugated version in matrix form

$$\frac{1}{\Gamma} \begin{pmatrix} \dot{\delta z} \\ \dot{\delta z}^* \end{pmatrix} = \begin{pmatrix} \alpha & \beta \\ \beta^* & \alpha^* \end{pmatrix} \begin{pmatrix} \delta z \\ \delta z^* \end{pmatrix} , \tag{3.17}$$

and determine the eigenvalues

$$\nu_\pm = \frac{\alpha + \alpha^*}{2} \pm \sqrt{\left(\frac{\alpha + \alpha^*}{2}\right)^2 - (|\alpha|^2 - |\beta|^2)} = \mathrm{Re}(\alpha) \pm \sqrt{|\beta|^2 - \mathrm{Im}^2(\alpha)} \,, \tag{3.18}$$

and the eigenvectors

$$x_\pm = \begin{pmatrix} \frac{\nu_\pm - \alpha^*}{\beta^*} \\ 1 \end{pmatrix} . \tag{3.19}$$

The general solution of the fluctuation is then given by the expression

$$\delta z(t) = c_+ \frac{\nu_+ - \alpha^*}{\beta^*} e^{\nu_+ t} + c_- \frac{\nu_- - \alpha^*}{\beta^*} e^{\nu_- t} \,. \tag{3.20}$$

Only if the real part of both eigenvalues $\nu_\pm$ is negative, the exponential function of the latter equation tends to zero for large times and the fluctuation converges, which is necessary to reach a stable steady-state. It is trivial that real part of the eigenvalue ν_- is negative since $\mathrm{Re}(\alpha) = -1$. For the second eigenvalue, the following condition has to hold:

$$\sqrt{|\beta|^2 - \mathrm{Im}^2(\alpha)} < 1 \rightarrow \quad |\beta|^2 - |\alpha|^2 < 0 \,. \tag{3.21}$$

For the trivial amplitude solution $\bar{z} = 0$, the condition implies that $|\delta| > \sqrt{\tilde{\mu}^2 - 1}$. The non-trivial steady-state solution $\bar{z}_+$ is valid if $\mu > 1$ while the solution $\bar{z}_-$ requires the additional limit $\delta > \sqrt{\tilde{\mu}^2 - 1}$. The stability condition of the latter becomes $\delta > -\sqrt{\tilde{\mu}^2 - 1}$ which are mutually exclusive. Therefore, $\bar{z}_+$ describes a stable solution while $\bar{z}_-$ is

unstable. Exemplary, we show the absolute value for $\mu = \sqrt{2}$ depending on the detuning in Fig. 3.2(a). To delimit the different kinds of stable and unstable solutions in the field of parametric oscillators, we emphasize again that we have considered so far a parametrically driven Duffing oscillator in the R.W.A. and studied if the occurring dynamical solutions are stable or unstable within the R.W.A. Furthermore, a harmonic, i.e., non-Duffing, the parametric oscillator has "unstable" solutions in the sense that they diverge. Physically speaking, the fluctuations make these solutions unstable, and the stable solution has no finite lifetime. Exemplary shown in Fig. 3.2(b), the colored regions, the so-called Arnolds tongue, correspond to parametric oscillations that diverge in time, while in the white region, only zero-amplitude solutions exist. With increasing linear damping, these regions deform. By introducing a nonlinearity, one can pass from a diverging and, therefore, unstable solution to a metastable solution with a finite amplitude.

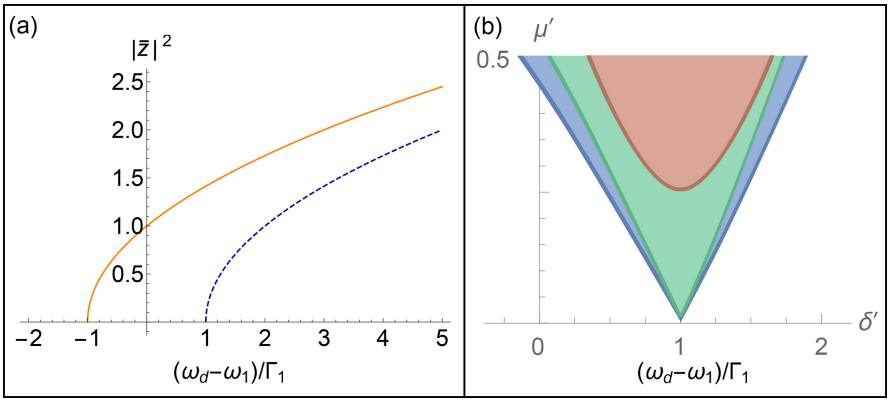

Fig. 3.2.: Numerical solutions for the parametrically driven Duffing resonator. (a) shows the solution of the amplitude. Orange line represents a stable solution, the dashed blue line the unstable solution. Due to RWA the breakdown has to be taken by hand. (b) shows the so-called Arnolds tongue for increasing damping. Blue parts correspond to zero damping while it is finite for the green and even larger for the red areas.

3.2.3 Bifurcation as Effect of Coupled Nonlinear Resonators

They dynamics of a system, described by the equation of motion, can show interesting behavior in certain ranges of parameter regimes. One example is to consider a fixed point which can be created, destroyed or its stability is changed due to a varying parameter. These changes in the dynamics are so-called bifurcations [198] and the values of the parameters at which these changes appear are called bifurcation points. A basic and simple mechanism is the saddle-node bifurcation. We consider a first-order system, depending on a parameter r described by the equation

$$\dot{x} = r + x^2 \,. \tag{3.22}$$

Depending on the value of r we get different curves, plotted in Fig. 3.3. Regarding the steady-state solution we are interested in the poles of the latter equation. If $r < 0$ two fixed points are visible. With decreasing r the curve moves upwards while the two points move closer until they merge at $r = 0$ to only one point that vanishes for $r > 0$. In this case the bifurcation appears at $r = 0$. If we now plot the possible solutions for $\dot{x} = 0$ depending on the parameter r we obtain the right panel of Fig. 3.3, the bifurcation diagram, visualizing that the solutions can appear simultaneously.

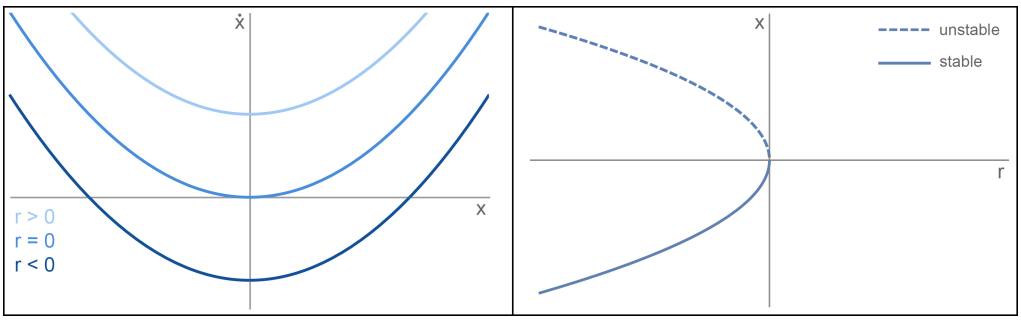

Fig. 3.3.: Saddle-node bifurcation. The left panel shows Eq. (3.22) for different values of r. The dark blue curve corresponds to $r < 0$, medium blue to $r = 0$ and light blue to $r > 0$. The right panel shows stable and by a dashed line the unstable solutions depending on the parameter r.

If the system has a symmetry, the fixed points seem to appear and vanish in pairs and the so-called pitchfork bifurcation occurs. There are two different types, the super- and the subcritical pitchfork bifurcation, while we focus only on the first one. The corresponding equation reads

$$\dot{x} = rx - x^3 \,, \tag{3.23}$$

and is plotted for different values of r in the right panel of Fig. 3.4. For $r < 0$, which is the dark blue curve, we get a single fixed point that is stable. At $r = 0$ it becomes a saddle point and decreasing further it becomes unstable. However two additional stable fixed points appear. If we plot these solutions over the parameter r we obtain in the right panel of Fig. 3.4 the occurring bifurcation diagram.

If the symmetry is lifted and we get at least minor differences between the left and right side, described for example by an additional parameter h

$$\dot{x} = h + rx - x^3 \,, \tag{3.24}$$

also the bifurcation diagram changes. The parameter h shifts the curve along the vertical axes indicating a left-right asymmetry regarding the fixed points. The case of one or three intersection corresponds to the pitchfork bifurcation, shown the light and dark blue curve in Fig. 3.5. But if the axis is tangential to the curve, like the medium blue curve, a saddle-node bifurcation occure. If we now consider the stable and unstable solutions in

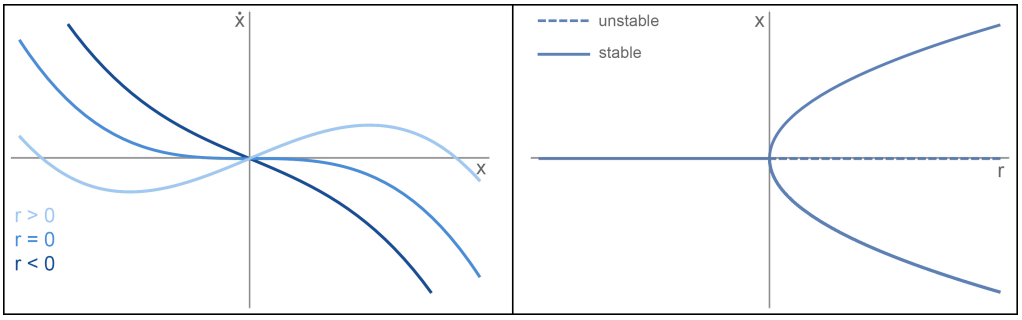

Fig. 3.4.: Supercritical pitch-fork bifurcation. The left panel shows Eq. (3.23) for different values of r. The dark blue curve corresponds to $r < 0$, medium blue to $r = 0$ and light blue to $r > 0$. The right panel shows stable and unstable solutions depending on the parameter r.

the right panel of Fig 3.5 we see that the pitchfork of Fig. 3.4 is now disconnected into two pieces.

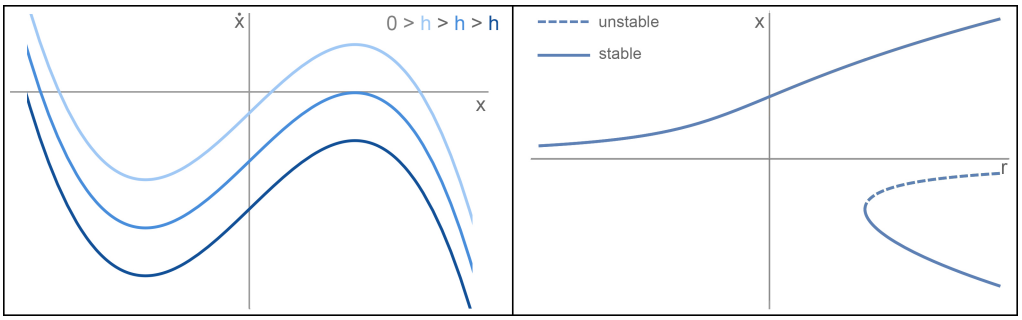

Fig. 3.5.: Imperfect bifurcation. The left panel shows Eq. (3.24) for a fixed value of r and different values of h which are chosen to be negative. The right panel shows stable and unstable solutions depending on the parameter r for a fixed value of h.

4

Persistent Response in Ultra-Strongly Driven Mechanical Membrane Resonators

F. Yang, F. Hellbach, F. Rochau, W. Belzig, E. M. Weig, G. Rastelli, and E. Scheer, *Persistent Response in an Ultrastrongly Driven Mechanical Membrane Resonator*, Phys. Rev. Lett. **127**, 014304 (2021)

In the last decades, mechanical resonators were driven mainly through small driving forces while one studied their feedback, i.e. the (weakly) linear response. Just in the last years, the strongly nonlinear regime received more attention. Mechanical resonators have the great advantage of directly visualizing effects due to nonlinear dynamics in the system, which can then be transferred to other resonating systems. In the experiment of Yang et al. [199] a membrane resonator with an ultra-strong drive is studied, i.e. in the regime of extremely nonlinear response. A vibrating state of the membrane with nearly constant and high amplitude over an extremely wide frequency range is explored, which is now designated as *persistent response*. This effect is pioneering in avoiding a breakdown since it establishes a self-limitation of the maximum amplitude due to nonlinear self-interactions. This novel phenomenon is based on two different kinds of parametric couplings between different flexural modes and their overtones, which has not been described anywhere else before.

This part of the work was done in close collaboration with Dr. F. Yang and Prof. Dr. Elke Scheer from the University of Konstanz. Yang and other coauthors set up the remarkable experiment and obtained fascinating and novel nonlinear phenomena. In intense discussions, we developed the theory to explain and substantiate the occurring physics. The figures taken from the original paper were also produced by F. Yang, while content not indicated by a reference was done by myself.

4.1 Experimental Setup

A schematic of the experimental setup is shown in Fig. 4.1. A SiN membrane that is 478 nm thick and 413.5 $\times$ 393.5 μm^2 wide is carried by a silicon chip. This chip is connected to a piezoelectric ring, to which a sinusoidal AC voltage $V_{\text{exc}} \sin(2\pi f_d t)$ is applied. Due to the voltage, the height of the actuator of the piezoelectric ring changes, which excites then the membrane. The different modes are denoted as (m,n) modes, i.e. they are specified by the integers m and n, which correspond to the number of deflection nodes in two spatial directions. The characterizing parameters for the fundamental (1,1) mode are among others the eigenfrequency $\omega_{11}/2\pi = 323.5$ kHz and the mechanical Q factor $Q_{11} = 20.000$. The membrane is driven close to the eigenfrequency of the fundamental mode. The resonance frequency of the (2,2) mode is with $\omega_{22}/2\pi = 646$ kHz not exactly twice of the (1,1) mode. The reason is a non-zero bending rigidity and and the small rectangular deviation from a quadratic shape of the membrane. To visualize the vibrational states of the different modes of the membrane, the imaging white light interferometry is used. In this way, one can spatially resolve the deflection profile of the membrane and can determine the average mean amplitude response. Furthermore, a Michelson interferometer is used, focusing on a single membrane position. Other parameters and further details for the fabrication and measurement are given in [200].

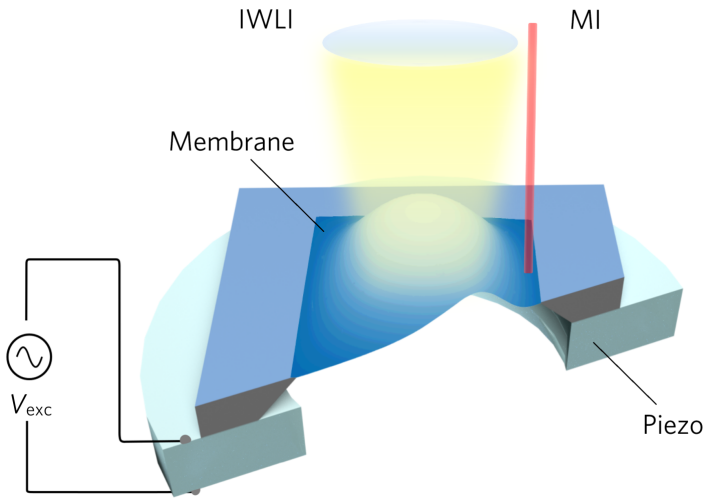

Fig. 4.1.: Sketch of the experimental setup: A free-standing SiN membrane is carried on a piezoelectric ring that is driven by an AC Voltage. The measurements are taken by imaging white light interferometer (IWLI) and a laser beam of the Michelson interferometer (MI). Figure taken from [200]

4.2 Theoretical Introduction

The entire theoretical description of the nonlinear coupling between different types of tones and modes and the complex superposition of these internal resonances is quite challenging. To explain the experimental observations qualitatively, we focus on the underlying process of each feature and show, solving the theoretical models for three individual cases, that each model explains one of the observations.

We first develop a model for the nonlinearly excited fundamental mode (1,1) of the membrane with eigenfrequency ω_{11}. The goal is to explain qualitatively the experimental observation of the "persistent response", namely the two central facts that first, the average vibration amplitude of the membrane is almost flat by increasing the detuning, and second, the maximum frequency detuning at which the resonator switches from the high amplitude state to the low amplitude state is much larger with respect to the Duffing model. A consistent theoretical scenario can explain these two facts.

In a second step, we consider the interaction of the fundamental mode and one specific higher-frequency mode, where we focus on one example for each of two different coupling cases. This is either an indirect parametric nonlinear interaction moderated by the overtones of the fundamental mode, where we study the case of the third harmonic of the (1,1) mode with eigenfrequency $3\,\omega_{11}$ which drives indirectly the (2,2) mode with $\omega_{22} \simeq 2\,\omega_{11}$. Or it is a direct parametric nonlinear interaction with a fractional resonance, where we study the interaction of the fundamental mode (1,1) with the (1,2) mode with $\omega_{12} \simeq \frac{3}{2}\,\omega_{11}$.

4.3 Persistent Response

4.3.1 Interaction of the Fundamental Mode (1,1) with the Harmonic Modes (2,2), (3,3) and (4,4)

Driving the system in the ultra-strong regime and measuring the mean amplitude response of the (1,1) mode for varying drive frequency, one observes a flattening response curve as shown in Fig. 4.2(a). In the range of small detuning above the linear eigenfrequency, the flattening can be explained by the spatial modulation of localized overtones [201]. At larger detuning, the amplitude becomes almost independent of the driving frequency, and one can detect small steps and kinks, i.e. peculiarities that deviate from the smooth response curve. This almost constant amplitude over the extremely wide frequency range is denoted as *persistent response*. Besides the spatial modulation of overtones, a second interaction mechanism occurs, i.e. a nonlinear coupling between different flexural modes that becomes dominant with increasing detuning.

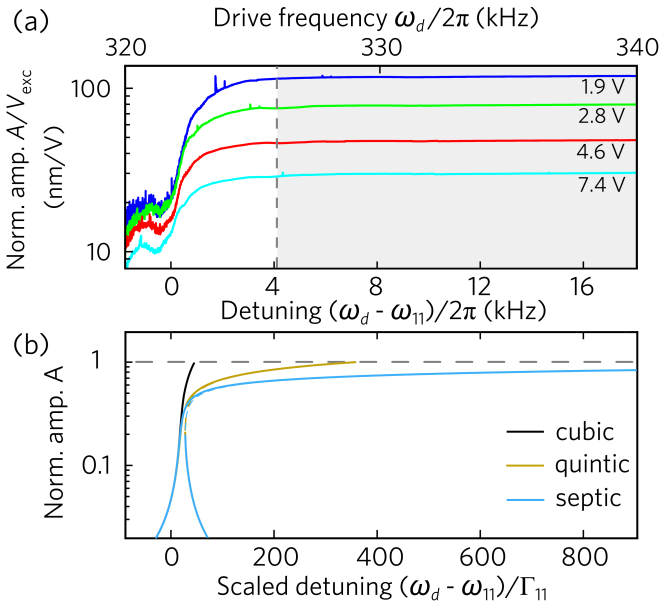

Fig. 4.2.: (a) Response function, i.e. the normalized mean amplitude response of the (1,1) mode with eigenfrequency around 321 kHz, measured for four different driving voltages. In the gray area the amplitude is almost independent of the driving frequency. (b) Theoretical curves for the amplitude of the (1,1) mode with different higher-order nonlinear forces. Original figure of [199].

By expanding the complex elastic energy potential of the membrane in terms of the normal modes, one generates all possible nonlinear interactions between the different modes. The generic term reads

$$V^{(kh)}_{(n\,m\,|\,\ell\,p)} \;=\; \lambda^{(kh)}_{(n\,m\,|\,\ell\,p)}\; q^{k}_{n\,m}\;\; q^{h}_{\ell\,p}\,, \tag{4.1}$$

with the coupling strength $\lambda^{(kh)}_{(n\,m\,|\,\ell\,p)}$ where k, h are integers and $q_{n\,m}$ and $q_{\ell\,p}$ the amplitudes of the two modes (n, m) and (ℓ, p). Except for some frequency ranges, where we observe features that deviate from the smooth curve of the persistent response, we assume the higher-order modes and/or the overtones are weakly excited due to nonlinear interaction with the fundamental mode $(1, 1)$ such that they oscillate in their linear or Duffing state.

However, the dynamics of the activated high frequency modes affects the response of the mode $(1, 1)$. To illustrate this idea, we discuss as example a minimal (toy) model to qualitatively capture the experimental findings. In this model we consider the fundamental mode $(1, 1)$ with eigenfrequency $\omega_{11} \simeq \omega_d$ only coupled to the three modes (n, n) with $n = 2, 3, 4$ and eigenfrequencies $\omega_{nn} \simeq n\,\omega_{11}$ through the potential

$$\sum_{n=2}^{4} V^{(n1)}_{(1\,1\,|\,n\,n)} = \sum_{n=2}^{4} \lambda^{(n1)}_{(1\,1\,|\,n\,n)}\;\; q^{n}_{11} q_{nn}\,. \tag{4.2}$$

Then the dynamical equations read

$$\ddot{q}_{11} = -\omega_{11}^2 q_{11}(t) - 2\Gamma_{11}\dot{q}_{11}(t) - \gamma_1 q_{11}^3(t) + F_d\cos(\omega_d t) - \sum_{n=2}^{4} n\ \lambda^{(n1)}_{(1\,1\,|\,n\,n)}\ q_{11}^{n-1} q_{nn}\,, \tag{4.3}$$

$$\ddot{q}_{nn} = -\omega_{nn}^2 q_{nn}(t) - 2\Gamma_{nn}\dot{q}_{nn}(t) - \lambda^{(n1)}_{(1\,1\,|\,n\,n)}\ q_{11}^n\,, \quad (n \geq 2)\,. \tag{4.4}$$

As already noted, the modes are described by effective resonators with frequencies ω_{nn} and damping constant Γ_{nn} for n=1,2,3,4. The fundamental mode (1,1) is driven by a linear force F and can be described by a Duffing nonlinearity strength γ_1 while the higher harmonics are assumed to behave linearly. The fundamental mode is described as a Duffing resonator, with Duffing nonlinearity strength γ_1 and driven by the force F, while the higher harmonics are assumed to be linear. Using the canonical transformations

$$u_n(t) = \frac{e^{-in\omega_d t}}{2}\left(q_{nn}(t) - \frac{i}{n\omega_d}\dot{q}_{nn}(t)\right)\,, \tag{4.5}$$

$$u_n^*(t) = \frac{e^{in\omega_d t}}{2}\left(q_{nn}(t) + \frac{i}{n\omega_d}\dot{q}_{nn}(t)\right)\,, \tag{4.6}$$

and applying the rotating wave approximation (RWA), we get the equations

$$\dot{u}_1(t) = -\left(\Gamma_{11} + i\delta\omega_1 - i\frac{3\gamma_1}{2\omega_d}|u_1(t)|^2\right)u_1(t) - i\frac{F}{4\omega_d} + \sum_{n=2}^{4}\frac{in}{2\omega_d}\ \lambda^{(n1)}_{(1\,1\,|\,n\,n)}\ u_n(t)(u_1^*(t))^{n-1}\,, \tag{4.7}$$

$$\dot{u}_n(t) = -\left(\Gamma_{nn} + in\delta\omega_n\right)u_n(t) + i\frac{\lambda^{(n1)}_{(1\,1\,|\,n\,n)}}{2n\omega_d}u_1^n(t)\,, \quad (n \geq 2)\,, \tag{4.8}$$

with the detuning $\delta\omega_n = \omega_d - \omega_{nn}$. $u(t)$ describes the vibration amplitude in the rotating frame at the driving frequency ω_d. We scale the amplitude like

$$u_n(t) = \sqrt{\frac{2\omega_d\Gamma_{11}}{3\gamma_1}}z_n(t)\,, \tag{4.9}$$

and introduce new parameters: the scaled detuning, the scaled damping and the scaled force

$$\Omega_n = \frac{\delta\omega_n}{\Gamma_{11}}, \quad \kappa_n = \frac{\Gamma_{nn}}{\Gamma_{11}}, \quad \beta = \frac{3F^2\gamma_1}{32\omega_d^3\Gamma_{11}^3}\,. \tag{4.10}$$

With these parameters we get the scaled equations

$$\dot{z}_1(t) = -\left(\Gamma_{11} + i\delta\omega_1 - i\Gamma_{11}|z_1(t)|^2\right) z_1(t) - i\Gamma_{11}\sqrt{\beta}$$
$$+ \sum_{n=2}^{4} \frac{in}{2\omega_d}\, \lambda^{(n1)}_{(1\,1\,|\,n\,n)} \left(\sqrt{\frac{2\omega_d\Gamma_{11}}{3\gamma_1}}\right)^{n-1} z_n(t)(z_1^*(t))^{n-1}\,, \tag{4.11}$$

$$\dot{z}_n(t) = -\left(\Gamma_{nn} + in\delta\omega_n\right) z_n(t) + i\frac{\lambda^{(n1)}_{(1\,1\,|\,n\,n)}}{2n\omega_d} \left(\sqrt{\frac{2\omega_d\Gamma_{11}}{3\gamma_1}}\right)^{n-1} z_1^n(t)\,. \tag{4.12}$$

In the steady state, $\dot{z}_n(t) = 0$ one can obtain a closed equation from Eq. (4.11) and (4.12) for the the stationary solution $\bar{z}_1$. With the abbreviation

$$g_n = \frac{\left(\lambda^{(n1)}_{(1\,1\,|\,n\,n)}\right)^2}{4\omega_d^2\Gamma_{11}^2} \left(\frac{2\omega_d\Gamma_{11}}{3\gamma_1}\right)^{n-1}\,, \tag{4.13}$$

we finally get

$$-i\sqrt{\beta} = \left[1 + i\Omega_1 - \left(i - \frac{g_2}{(\kappa_2 + 2i\Omega_2)}\right)|z_1|^2 + \frac{g_3}{(\kappa_3 + 3i\Omega_3)}\,|z_1|^4 + \frac{g_4}{(\kappa_4 + 4i\Omega_4)}\,|z_1|^6\right] z_1$$
$$\simeq \left[1 + i\Omega_1 - i\left(1 + \frac{g_2}{2\Omega_2}\right)|z_1|^2 - i\frac{g_3}{3\Omega_3}|z_1|^4 - i\frac{g_4}{4\Omega_4}|z_1|^6\right] z_1\,, \tag{4.14}$$

where we used the condition $\kappa_n \ll \Omega_n$. The latter result corresponds to an effective septic force for the fundamental mode in the RWA.

4.3.2 Theoretical Description of Fundamental Mode as Nonlinear Resonator with an Effective Septic Potential

From the previous section, we argue that the dynamics of the fundamental mode (1,1) of the membrane with eigenfrequency ω_{11} driven by a force, can be modeled by an effective septic force if the higher-order modes are in the harmonic regime. Therefore, with the drive $\omega_d \simeq \omega_{11}$ we assume the following equation for the dynamics of the (1,1) mode

$$\ddot{q}_{11}(t) = -\omega_{11}^2 q_{11}(t) - 2\Gamma_{11}\dot{q}_{11}(t) + F\cos(\omega_d t) - \gamma_1 q_{11}^3(t) - \mu_1 q_{11}^5(t) - \nu_1 q_{11}^7(t)\,, \tag{4.15}$$

which corresponds to an effective resonator, driven by a linear force, the Duffing nonlinearity with parameter γ_1, a quintic nonlinearity with parameter $\mu_1 > 0$ and a septic nonlinearity with parameter $\nu_1 > 0$.

One expects a priori that the vibration amplitude is large for a sufficiently strong drive, and the nonlinear higher-order terms become more and more important. In particular, the Duffing nonlinearity is insufficient to explain the dynamics, and we need to include

these higher-order nonlinearities. The crucial effect of the latter terms is to produce a deflection of the Duffing response curve as a function of the drive frequency. It is also important to note that the inclusion of the quintic (or other higher-order terms) does not necessarily imply that the resonator has more stable solutions than the ones in the Duffing model. As will be shown below, in the regime of parameters that describe the experimental observations of this work, the nonlinear resonator of Eq. (4.15) still has three possible real solutions, out of which two are stable and one unstable, as in the Duffing case.

Using the canonical transformations

$$u(t) = \left(q_{11}(t) - \frac{i}{\omega_d}\dot{q}_{11}(t)\right) e^{-i\omega_d t}\,, \tag{4.16}$$

$$u^*(t) = \left(q_{11}(t) + \frac{i}{\omega_d}\dot{q}_{11}(t)\right) e^{i\omega_d t}\,, \tag{4.17}$$

and applying the RWA we get the equation

$$\dot{u}(t) = \left[-i\delta\omega_d - \Gamma_{11} + i\frac{3\gamma_1}{8\omega_d}|u(t)|^2 + i\frac{5\mu_1}{16\omega_d}|u(t)|^4 + i\frac{35\nu_1}{128\omega_d}|u(t)|^6\right] u(t) - i\frac{F}{2\omega_d}\,, \tag{4.18}$$

with the detuning $\delta\omega_d = \omega_d - \omega_{11}$. The variable $u(t)$ describes the vibration amplitude in the rotating frame at the driving frequency ω_d. We scale the amplitude like

$$u(t) = \sqrt{\frac{8\omega_d\Gamma_{11}}{3\gamma_1}}z(t)\,, \tag{4.19}$$

and introduce the new parameters: the scaled detuning, the scaled quintic and septic nonlinearity parameters and the scaled force, provided by an external drive,

$$\Omega = \frac{\delta\omega_d}{\Gamma_{11}}\,, \qquad \tilde{\mu}_1 = \frac{20}{9}\mu_1\frac{\omega_d\Gamma_{11}}{\gamma_1^2}\,, \qquad \tilde{\nu}_1 = \frac{140}{27}\nu_1\frac{\omega_d^2\Gamma_{11}^2}{\gamma_1^3}\,, \qquad \beta = \frac{3\gamma_1 F^2}{32\omega_d^3\Gamma_{11}^3}\,. \tag{4.20}$$

With these, we get the short equation for the scaled amplitude in the RWA

$$\frac{1}{\Gamma_{11}}\dot{z}(t) = \left(-i\Omega - 1 + i|z(t)|^2 + i\tilde{\mu}_1|z(t)|^4 + i\tilde{\nu}_1|z(t)|^6\right) z(t) - i\sqrt{\beta}\,. \tag{4.21}$$

In the steady state, $\dot{z}(t) = 0$, the stationary solution $\bar{z}$ is given by the equation

$$\beta = \left[1 + \left(\Omega - |\bar{z}|^2 - \tilde{\mu}_1|\bar{z}|^4 - \tilde{\nu}_1|\bar{z}|^6\right)^2\right]|\bar{z}|^2\,. \tag{4.22}$$

If the external driving force is fixed, the parameter β is fixed. One can then plot the solutions of Eq. (4.22) as a function of the scaled detuning Ω. With the scaling proposed above, the solutions then depend only on two parameters, namely $\tilde{\nu}_1$ and $\tilde{\mu}_1$, as evident from Eq. (4.22). The Duffing resonator is recovered if $\mu_1 = \nu_1 = 0$. As shown in Fig.

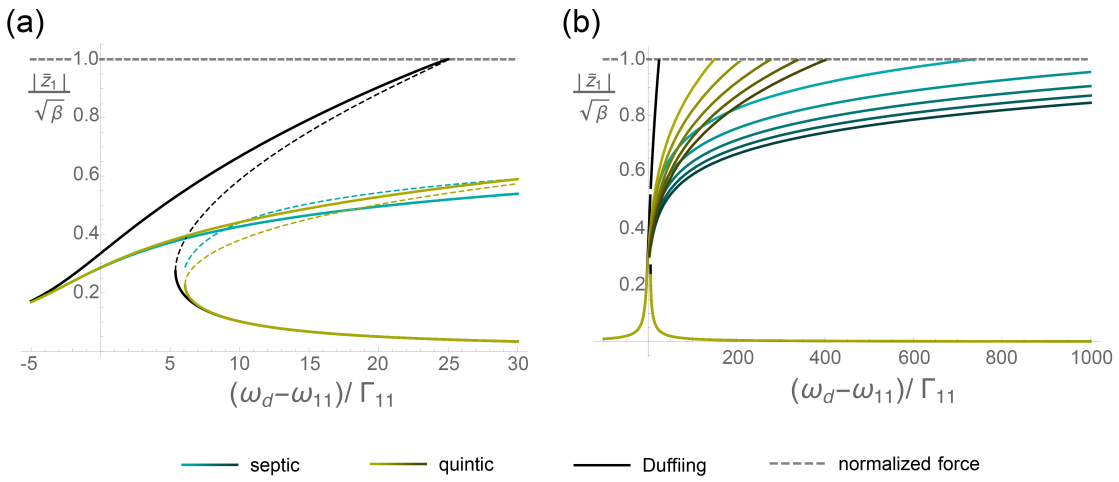

Fig. 4.3.: Theoretical curves for the amplitude of the fundamental (1,1) mode including different nonlinearities, i.e. the black curve includes only the Duffing nonlinearity, yellow includes, in addition, the quintic, and blue also the septic nonlinearity. (a) Shows how the amplitude is bent in a small frequency range. Bold lines represent stable solutions and dashed lines the unstable solutions. (b) Only stable solutions over a wide frequency range for different strong nonlinearities. The values for ν, the quintic nonlinearity, pass from 0.2 to 0.6 with a step size of 0.1 and μ, the septic nonlinearity, from 0.0015 to 0.0075 with a step size of 0.0015. As larger the nonlinearities as darker the yellow or blue curve.

4.3(a), at small frequency range, the quintic nonlinearity already bends down the curve largely while adding the septic nonlinearity does not show a great effect. The important impact of the septic order can be seen at a wide frequency range, see Fig. 4.3(b). The concrete profile depends on the choice of the parameters, while larger nonlinearities imply greater bending. Compared to the experimental results, the corresponding theoretical curve, both shown in Fig. 4.2, was generated by using the parameters $\beta = 25$, $\tilde{\nu}_1 = 0.5$ and $\tilde{\mu}_1 = 0.0075$. Besides the impact of the concrete choice of the nonlinearities ν and μ, it is evident that already the septic order is sufficient to describe the persistent response. If one would compare the solutions of the RWA, so Eq. (4.22), for the amplitude with a complete numerical simulation of a version of Eq. (4.15) that is scaled in the same way, deviations between the complete numerical solution and the RWA solution appear at large detuning beyond the validity of the RWA which is given by

$$|\omega_d - \omega_{11}| \ll \omega_d, \, \omega_{11} \, . \tag{4.23}$$

The RWA breaks down when the detuning is comparable to ω_{11}.

Solving Eq. (4.22) for the detuning Ω, we assume that we have either 1 or 3 real solutions for $|\bar{z}|^2$. Then the condition $\beta \,/\, |\bar{z}|^2 - 1 = 0$ set the maximum amplitude $|z_{\text{max}}|^2 = \beta$ leads to the maximum detuning of

$$\Omega_{\text{max}} = |\bar{z}|^2_{\text{max}} + \tilde{\mu}_1(|\bar{z}|^2_{\text{max}})^2 + \tilde{\nu}_1(|\bar{z}|^2_{\text{max}})^3 = \beta + \tilde{\mu}_1\beta^2 + \tilde{\nu}_1\beta^3 \,. \tag{4.24}$$

Without the scaling, the maximum amplitude and maximum detuning become

$$|u_{\text{max}}|^2 = \frac{F^2}{4\omega_d^2\Gamma_{11}^2} \,, \tag{4.25}$$

$$\frac{\delta\omega_d}{\Gamma_{11}} = \frac{3\gamma_1 F^2}{32\omega_d^3\Gamma_{11}^3} + \frac{5\mu_1 F^4}{256\omega_d^5\Gamma_{11}^5} + \frac{35\nu_1 F^6}{2^{13}\omega_d^7\Gamma_{11}^7} \,. \tag{4.26}$$

As shown in Fig. 4.2(b), the curve of the amplitude vs. detuning becomes flattered by adding nonlinear self-interaction terms in the equation. This explains the observed saturation qualitatively in the measurements.

4.4 Nonlinear Parametric Interaction

Zooming in the mostly smooth and flat response curve, nanometer-scale variations appear in the form of small steps and kinks, compare Fig. 4.4(a). Considering the deflection profile in this detuning area, which is shown in the inset of Fig. 4.4(a) , higher-order modes (m, n) appear. This is a signature of nonlinear mode coupling. Since it is also possible to excite overtones of the individual (m,n) modes [201]; one can argue that the complex superposition of several modes is generated by an effective nonlinear coupling between different types of modes and overtones. Small continuous deviations from a smooth response curve can qualitatively be described in terms of nonlinear coupling with overtones [201], but here we focus on and discuss the discontinuous steps. They can be explained by an *indirect parametric nonlinear interaction* mediated by the overtones of the fundamental mode $(m = n)$ or *direct parametric nonlinear interaction* between the modes $(m \neq n)$. We discuss two examples to illustrate this idea.

4.4.1 Indirect Parametric Nonlinear Interaction Activated by the Second Overtone of the Fundamental Mode

For the first coupling mechanism, the indirect parametric nonlinear interaction activated by the overtones of the fundamental mode, we study the specific case of the second overtone of the (1,1) mode with eigenfrequency $3\,\omega_{11}$ which drives indirectly the (2,2)

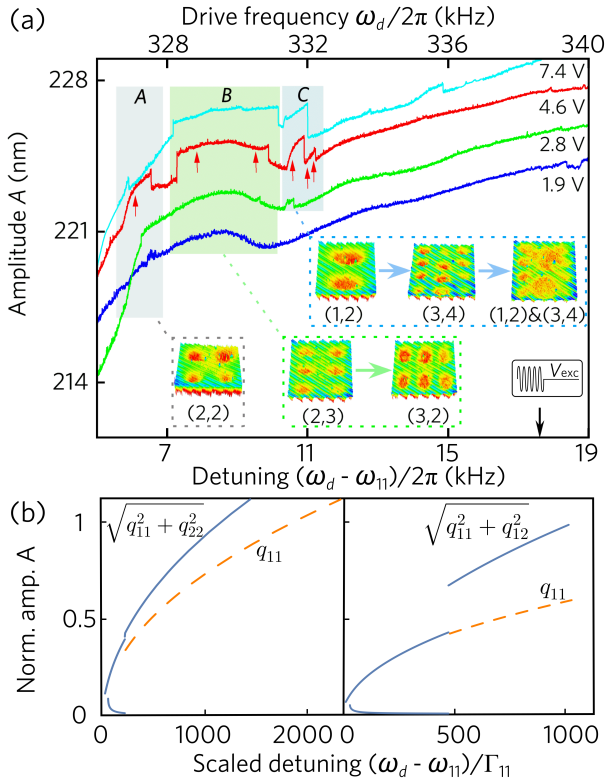

Fig. 4.4.: (a) Close-up of the large detuning range in Fig. 1(a), indicated by the gray background. Along the mostly constant plateau, we see small steps and kinks. The red arrows indicate the positions where one captured the deflection patterns for $V_{exc} = 4.6V$ shown in the insets. (b) Numerical solutions of the amplitudes of the nonlinear coupling models (solid lines: common amplitude of the coupled modes, dashed lines: driven modes without interaction). Left: indirect interaction between the mode (1, 1), i.e. its second overtone, and the mode (2, 2); Right: direct interaction between the mode (1, 1) and the mode (1, 2). Original figure of [199].

mode with $\omega_{22} \simeq 2\,\omega_{11}$. We consider the nonlinear interaction term, described by the potential

$$V^{(22)}_{(1\,1\,|\,2\,2)} \;=\; \frac{1}{2}\,\lambda^{(22)}_{(1\,1\,|\,2\,2)}\; q_{11}^2\; q_{22}^2 \tag{4.27}$$

between the two Duffing resonators q_{11} and q_{22}, with interaction strength $\lambda \equiv \lambda^{(22)}_{(11|22)}$. For simplicity and qualitative analysis, we neglect high order nonlinearities of the fundamental mode since the main features are captured already at this order. Therefore, we set the following coupled equations for the amplitudes $q_{11}(t)$ and q_{22}(t)

$$\ddot{q}_{11}(t) = -\omega_{11}^2 q_{11}(t) - 2\Gamma_{11}\dot{q}_{11}(t) + F\cos(\omega_d t) - \gamma_1(t) q_{11}^3(t) - \lambda q_{11}(t) q_{22}^2(t)\,, \tag{4.28}$$

$$\ddot{q}_{22}(t) = -\omega_{22}^2 q_{22}(t) - 2\Gamma_{22}\dot{q}_{22}(t) - \gamma_2 q_{22}^3(t) - \lambda q_{11}^2(t) q_{22}(t)\,. \tag{4.29}$$

Both effective resonators of Eq. (4.28) and (4.29) are characterized by a Duffing nonlinearity with strength γ_1 or γ_2, the eigenfrequencies ω_{11} and ω_{22}, and a damping constant

Γ_{11} or Γ_{22}. The first resonator is linearly driven by the force F. We use the following ansatz to include also the presence of the overtone of the fundamental mode

$$q_{11}(t) = \frac{1}{2}\left(u_1(t)e^{i\omega_d t} + u_1^*(t)e^{-i\omega_d t}\right) + \frac{1}{2}\left(u_3(t)e^{3i\omega_d t} + u_3^*(t)e^{-3i\omega_d t}\right), \tag{4.30}$$

$$q_{22}(t) = \frac{1}{2}\left(v(t)e^{2i\omega_d t} + v^*(t)e^{-2i\omega_d t}\right). \tag{4.31}$$

Note that the first overtone at $2\omega_2$ is also present but couples to another higher-order mode. Then, the mixing term $q_{11}^2 \propto u_1 u_3 e^{i4\omega_d t}$ in Eq. (4.27) represents the parametric excitation for the high frequency mode $(2,2)$, which becomes resonant and relevant as soon as $4\,\omega_d \approx 2\,\omega_{22}$. To obtain three coupled equations for $u_i(t)$ with $i = 1,2,3$ we check the RWA for $\ddot{q}_1$ separately for the order $n = 1$ and $n = 3$, i.e. we consider only rotating terms with either ω_d or $3\omega_d$. More details are shown in the Appendix in Section B.3. In combination with the RWA for $\ddot{q}_2$ we get then the three coupled equations

$$\begin{aligned} 0 = &\left(\left(\omega_d^2 - \omega_1^2\right) - 2i\omega_d\Gamma_{11} - \frac{3}{4}\gamma_1|u_1(t)|^2 - \frac{3}{2}\gamma_1|u_3(t)|^2 - \frac{\lambda}{2}|v^2(t)|\right)u_1(t) + F \\ &- \frac{3}{4}\gamma_1(u_1^*(t))^2 u_3(t) - \frac{\lambda}{4}u_3^*(t)v^2(t), \end{aligned} \tag{4.32}$$

$$\begin{aligned} 0 = &\left(\left(9\omega_d^2 - \omega_1^2\right) - 6i\omega_d\Gamma_{11} - \frac{3}{4}\gamma_1|u_3(t)|^2 - \frac{3}{2}\gamma_1|u_1(t)|^2 - \frac{\lambda}{2}|v(t)|^2\right)u_3(t) \\ &- \frac{\gamma_1}{4}u_1^3(t) - \frac{\lambda}{4}u_1^*(t)v^2(t), \end{aligned} \tag{4.33}$$

$$\begin{aligned} 0 = &\left(\left(4\omega_d^2 - \omega_2^2\right) - 4i\omega_d\Gamma_{22} - \frac{3}{4}\gamma_2|v^2(t)| - \frac{\lambda}{2}\left(|u_1(t)|^2 + |u_3(t)|^2\right)\right)v(t) \\ &- \frac{\lambda}{2}u_1(t)u_3(t)v^*(t). \end{aligned} \tag{4.34}$$

With the detunings of the two resonators $\delta\omega_1 = \omega_d - \omega_{11}$ and $\delta\omega_2 = 2\omega_d - \omega_{12}$. The detuning of the second resonators can be expressed in terms of the first one via $\delta\omega_2 = 2\delta\omega_{11} - \Delta\omega$ with $\Delta\omega = 2\omega_{11} - \omega_{12}$. Dividing Eqs. (4.32) and (4.33) by $2i\omega_d$ and Eq. (4.34) by $4i\omega_d$ we applied the following approximations to express the equations in terms of the detuning $\delta\omega_1$

$$\frac{\omega_d^2 - \omega_1^2}{2\omega_d} = \frac{\omega_d^2 - (\omega_d - \delta\omega_1)^2}{2\omega_d} = \frac{\omega_d^2 - \left(\omega_d^2 - 2\omega_d\delta\omega_1 - \delta\omega_1^2\right)}{2\omega_d} \approx \delta\omega_1, \tag{4.35}$$

$$9\omega_d^2 - \omega_1^2 = 9\omega_d^2 - (\omega_d - \delta\omega_1)^2 = 9\omega_d^2 - \omega_d^2 + 2\omega_d\delta\omega_1 - \delta\omega_1^2 \approx 8\omega_d^2 \approx 8\omega_1^2, \tag{4.36}$$

$$\frac{4\omega_d^2 - \omega_2^2}{4\omega_d} = \frac{4\omega_d^2 - (2\omega_d - \delta\omega_2)^2}{4\omega_d} = \frac{4\omega_d^2 - \left(4\omega_d^2 - 4\omega_d\delta\omega_2 + \delta\omega_2^2\right)}{4\omega_d} \approx \delta\omega_2. \tag{4.37}$$

To simplify the expressions, we use the following scaling for the amplitudes

$$z_1(t) = \sqrt{\frac{3\gamma_1}{8\omega_d\Gamma_{11}}}u_1(t)\,,\quad z_3(t) = \sqrt{\frac{3\gamma_1}{8\omega_d\Gamma_{11}}}u_3(t)\,,\quad w(t) = \sqrt{\frac{3\gamma_2}{8\omega_d\Gamma_{22}}}v(t)\,, \tag{4.38}$$

and the parameters for the difference between the resonance frequencies scaled by Γ_{11}, the scaled force, the detuning of the first resonator scaled by Γ_{11} and the detuning of the second resonator scaled by Γ_{22}, a coupling parameter and an asymmetry factor

$$\Delta = \frac{\Delta\omega}{\Gamma_{11}}\,,\quad \sqrt{\beta} = \sqrt{\frac{3\gamma_1 F^2}{32\omega_d^3\Gamma_{11}^3}}\,,\quad \Omega_1 = \frac{\delta\omega_1}{\Gamma_{11}}\,,\quad \Omega_2 = \frac{\delta\omega_2}{\Gamma_{22}} = \frac{\Gamma_{11}}{\Gamma_{22}}(2\Omega_1 - \Delta)\,, \tag{4.39}$$

$$g = \frac{\lambda}{\sqrt{\gamma_1\gamma_2}}\,,\quad \alpha = \sqrt{\frac{\gamma_1}{\gamma_2}}\left(\frac{\Gamma_{22}}{\Gamma_{11}}\right)\,. \tag{4.40}$$

The scaled coupled equations read as follows:

$$\begin{aligned} 0 = &\left(-1 - i\Omega_1 + i|z_1(t)|^2 + 2i|z_3(t)|^2 + i\frac{2}{3}g\alpha|w(t)|^2\right)z_1(t) - i\sqrt{\beta} + i(z_1^*(t))^2 z_3(t) \\ &+ i\frac{g}{3}\alpha z_3^*(t)w^2(t)\,, \end{aligned} \tag{4.41}$$

$$\begin{aligned} 0 = &\left(4 - \frac{\Gamma_{11}}{\omega_d}|z_3(t)|^2 - 2\frac{\Gamma_{11}}{\omega_d}|z_1(t)|^2 - \frac{2}{3}g\alpha\frac{\Gamma_{11}}{\omega_d}|w(t)|^2\right)z_3(t) - \frac{\Gamma_{11}}{3\omega_d}z_1^3(t) \\ &- \frac{1}{3}\frac{\Gamma_{11}}{\omega_d}g\alpha z_1^*(t)w^2(t)\,, \end{aligned} \tag{4.42}$$

$$0 = \left(-1 - i\frac{\Gamma_{11}}{\Gamma_{22}}(2\Omega_1 - \Delta) + \frac{i}{2}|w(t)|^2 + \frac{i}{3}\frac{g}{\alpha}\left(|z_1(t)|^2 + |z_3(t)|^2\right)\right)w(t) + \frac{i}{3}\frac{g}{\alpha}z_1(t)z_3w^*(t)\,. \tag{4.43}$$

For $w(t) \neq 0$ the last equation can be transformed to a direct expression for $|w(t)|$ depending on $z_1(t)$ and $z_3(t)$. Assuming $\frac{\Gamma_{11}}{\omega_d}|z_1|^2 \ll 1$, $\frac{\Gamma_{11}}{\omega_d}|z_3|^2 \ll 1$, $\frac{\Gamma_{11}}{\omega_d}|w|^2 \ll 1$ and $\alpha \ll 1$ we can simplify the equations to

$$0 = \left(-1 - i\Omega_1 + i|z_1|^2 + 2i|z_3|^2 + i\frac{2}{3}g\alpha|w|^2\right)z_1 - i\sqrt{\beta} + i(z_1^*)^2 z_3\,, \tag{4.44}$$

$$z_3 = \frac{\Gamma_{11}}{12\omega_d}z_1^3\,, \tag{4.45}$$

$$|w|^2 = 2\frac{\Gamma_{11}}{\Gamma_{22}}(2\Omega_1 - \Delta) - \frac{2g}{3\alpha}\left(|z_1|^2 + |z_3|^2\right) \pm 2\sqrt{\frac{1}{9}\left(\frac{g}{\alpha}\right)^2|z_1|^2|z_3|^2 - 1}\,. \tag{4.46}$$

Inserting Eq. (4.45) in Eq. (4.44) yields a closed equation for $|z_1|$. Inserting Eq. (4.45) in Eq. (4.46) we obtain an equation for $|w|$ depending only on $|z_1|$ that has been determined by the closed equation before. We solved this problem numerically. The result is shown in the right panel of Fig. 4.4(b). Notice that the result for z_1 has effective high-order nonlinearities.

4.4.2 Direct Parametric Nonlinear Interaction Caused by Fractional Resonance

For the direct parametric nonlinear interaction with higher flexural modes ($m \neq n$), so caused by a fractional resonance, we consider the interaction of the fundamental mode (1,1) with eigenfrequency ω_{11}, with the (1,2) mode with frequency $\omega_{12} \approx 3/2\,\omega_{11}$. To this end, we treat both modes as individual resonators and consider a nonlinear coupling between the two. An essential ingredient is the nonlinear interaction of the two resonators, described by the potential

$$V^{(32)}_{(11|12)} = \frac{1}{2}\,\lambda^{(32)}_{(11|12)}\,q_{11}^3\,q_{12}^2\,, \tag{4.47}$$

with interaction strength $\lambda \equiv \lambda^{(32)}_{(11|12)}$. Therefore, we can set the following coupled equations for the amplitudes $q_{11}(t)$ and $q_{12}(t)$:

$$\ddot{q}_{11}(t) = -\omega_{11}^2 q_1(t) - 2\Gamma_{11}\dot{q}_{11}(t) + F\cos(\omega_d t) - \gamma_1 q_{11}^3(t) - \frac{3}{2}\lambda q_{11}^2(t) q_{12}^2(t)\,, \tag{4.48}$$

$$\ddot{q}_{12}(t) = -\omega_{12}^2 q_{12}(t) - 2\Gamma_{12}\dot{q}_{12}(t) - \gamma_2 q_{12}^3(t) - \lambda q_{11}^3(t) q_{12}(t)\,. \tag{4.49}$$

Both effective resonators of Eqs. (4.48) and (4.49) are characterized by a Duffing nonlinearity with strength γ_1 or γ_2, the eigenfrequencies ω_{11} and ω_{12}, and a damping constant Γ_{11} or Γ_{12}. The first resonator is linearly driven by the force F. We use the canonical transformations

$$u_1(t) = \left(q_{11}(t) - \frac{i}{\omega_d}\dot{q}_{11}(t)\right) e^{-i\omega_d t}, \qquad u_1(t)^* = \left(q_{11}(t) + \frac{i}{\omega_d}\dot{q}_{11}(t)\right) e^{i\omega_d t}\,, \tag{4.50}$$

$$u_2(t) = \left(q_{12}(t) - \frac{i2}{(3\omega_d)}\dot{q}_{12}(t)\right) e^{-i\frac{3}{2}\omega_d t}, \quad u_2(t)^* = \left(q_{12}(t) + \frac{i2}{(3\omega_d)}\dot{q}_{12}(t)\right) e^{i\frac{3}{2}\omega_d t}\,. \tag{4.51}$$

The parametric interaction becomes resonant and relevant when $3\,\omega_d \approx 2\,\omega_{12}$: In the nonlinear interaction Eq. (4.47) the term $q_{11}^3 \propto u_1^3 e^{i3\omega_d t}$ represents the parametric excitation for the mode $(1,2)$. Applying the RWA we obtain two coupled equations

$$\dot{u}_1(t) = \left(-i\delta\omega_1 - \Gamma_{11} + i\frac{3\gamma_1}{8\omega_d}|u_1(t)|^2\right) u_1(t) - i\frac{F}{2\omega_d} + i\frac{3}{32}\frac{\lambda}{\omega_d}\,(u_1^*(t))^2\,u_2^2(t)\,, \tag{4.52}$$

$$\dot{u}_2(t) = \left(-i\frac{3}{2}\delta\omega_2 - \Gamma_{12} + i\frac{\gamma_2}{4\omega_d}|u_2(t)|^2\right) u_2(t) + i\frac{\lambda}{24\omega_d}u_1^3(t)u_2^*(t)\,, \tag{4.53}$$

with the detunings $\delta\omega_1 = \omega_d - \omega_{11}$ and $\delta\omega_2 = \omega_d - 2/3\,\omega_{12}$. The variables $u_1(t)$ and $u_2(t)$ describe the vibration amplitude of the two effective resonators. To obtain the detunings in the latter equations we made the approximations

$$\frac{\omega_d^2 - \omega_1^2}{2\omega_d} = \frac{\omega_d^2 - [\omega_d - \delta\omega_1]^2}{2\omega_d} \approx \delta\omega_1\,, \tag{4.54}$$

$$\frac{\left(\frac{3}{2}\omega_d\right)^2 - \omega_2^2}{\frac{3}{2}\omega_d} = \frac{\left(\frac{3}{2}\omega_d\right)^2 - \left(\frac{3}{2}\omega_d - \frac{3}{2}\delta\omega_2\right)^2}{\frac{3}{2}\omega_d} \approx 3\delta\omega_2\,. \tag{4.55}$$

We use the following scaling for the two amplitudes

$$u_1(t) = \sqrt{\frac{8\omega_d\Gamma_{11}}{3\gamma_1}}z_1(t), \quad u_2(t) = \sqrt{\frac{4\omega_d\Gamma_{12}}{\gamma_2}}z_2(t)\,. \tag{4.56}$$

To simplify the the coupled equations of the scaled amplitudes we directly introduce the parameter $\sqrt{\beta}$ for the scaled force and the abbreviations g and h

$$\beta = \frac{3\gamma_1 F^2}{32\omega_d^3\Gamma_{11}^3}\,, \quad g = \frac{27}{8}\left(\frac{\Gamma_{12}}{\Gamma_{11}}\right)^2\left(\frac{\gamma_1}{\gamma_2}\right)h\,, \quad h = \frac{\lambda}{9}\left(\frac{\Gamma_{11}}{\Gamma_{12}}\right)\sqrt{\frac{8\omega_d\Gamma_{11}}{3\gamma_1^3}}\,. \tag{4.57}$$

In the steady state $\dot{z}_1 = \dot{z}_2 = 0$, the stationary solutions $\bar{z}_1$ and $\bar{z}_2$ are given by the two coupled equations

$$0 = \left(-i\frac{\delta\omega_1}{\Gamma_{11}} - 1 + i|\bar{z}_1|^2\right)\bar{z}_1 - i\sqrt{\beta} + ig(\bar{z}_1^*)^2\bar{z}_2^2\,, \tag{4.58}$$

$$0 = \left(-i\frac{\frac{3}{2}\delta\omega_2}{\Gamma_{12}} - 1 + i|\bar{z}_2|^2\right)\bar{z}_2 + ih\bar{z}_1^3(t)\bar{z}_2^*\,. \tag{4.59}$$

Transforming Eq. (4.59) and taking the square modulus of both sides yields an expression for $|\bar{z}_2| \neq 0$ depending only on $|\bar{z}_1|$

$$|\bar{z}_2|^2 = \frac{3\delta\omega_2}{2\Gamma_{12}} + \sqrt{h^2|\bar{z}_1|^6 - 1}\,, \tag{4.60}$$

which is valid only if $h^2|\bar{z}_1|^6 \geq 1$. To transform Eq. (4.58) we need to take the phase into account, i.e. we use the phase representation $\bar{z}_i = |\bar{z}_i|e^{i\Theta_i}$ for the two amplitudes and Eq. (4.60). In this way we achieve the phase relation between Θ_1 and Θ_2 in the long amplitude limit, i.e.

$$e^{2i\Theta_2} = \frac{-h\bar{z}_1^3}{\sqrt{h^2|\bar{z}_1|^6 - 1} + i} \approx \frac{-h\bar{z}_1^3}{\sqrt{h^2|\bar{z}_1|^6}} = \frac{-\bar{z}_1^3}{|\bar{z}_1|^3} = \frac{-|\bar{z}_1|^3 e^{3i\Theta_1}}{|\bar{z}_1|^3} = -e^{3i\Theta_1}\,. \tag{4.61}$$

Therefore, the phase relation reads $\Theta_2 = 3/2\Theta_1$. With this phase relation Eq. (4.58) can be transformed into a phase-independent equation

$$\beta = \left[1 + \left(\frac{\delta\omega_1}{\Gamma_{11}} - |\bar{z}_1|^2 - g|\bar{z}_1||\bar{z}_2|^2\right)\right]|\bar{z}_1|^2 \,. \tag{4.62}$$

If $|\bar{z}_2| \neq 0$ we can replace $|\bar{z}_2|$ by Eq. (4.60), which is valid only if $h^2|\bar{z}_1|^6 \geq 1$. In this case we get a closed equation for $|\bar{z}_1|$ and can solve the problem numerically for.

$$\left[1 + \left(\frac{\delta\omega_1}{\Gamma_{11}} - |\bar{z}_1|^2 - g|\bar{z}_1|\left[\frac{3\delta\omega_2}{2\Gamma_{12}} + \sqrt{h^2|\bar{z}_1|^6 - 1}\right]\right)^2\right]|\bar{z}_1|^2 = \beta \,. \tag{4.63}$$

If $|\bar{z}_2| = 0$, which is the case if $h^2|\bar{z}_1|^6 < 1$ we solve Eq. (4.58) for $|\bar{z}_1|$ while setting $|\bar{z}_2| = 0$. The threshold value depends on the amplitude $|\bar{z}_1|$ which itself depends on the detuning. Therefore we get a jump at the point were the solution merge. The result is shown in the left panel of Fig. 4.4(b).

5 Nonlinear Coupled Parametrically Driven Duffing Resonators

In 1956, the experiment of Hanbury Brown and Twiss demonstrated that photons of a light beam with a narrow spectral width tend to arrive in correlated pairs [202]. In 1962, Glauber developed the quantum mechanical theory of correlated photons to explain this effect and derived the distribution of the photon number in an incoherent beam [203]. He extended the previous ansatz of Mandel and Wolf, that classical Gaussian stochastic processes can describe an electric field of such a beam [204, 205, 206]. In 1989, it was shown theoretically by Yuen that optical radiation, prepared in a minimum-uncertainty state, may significantly improve the performance in an optical communication system [207] compared to correlated photons [208]. Already 12 years earlier, Yuen derived that the radiation state of ideal two-photon lasers, which perform far above the threshold [209], can produce such states, which are called two-photon coherent states.

Two-photon coherent states are essential in quantum optics and, as a possible minimum-uncertainty state, of enormous interest for applications in quantum communication. Mathematically, a unitary operator associated with quadratic Hamiltonians applied to a coherent state can obtain such a state. Coherent states can be generated from ideal single-photon sources, while a two-photon coherent state needs a two-photon process for two photons of the same mode. Their noise properties are close to those of a minimum-uncertainty state, i.e. a squeezed state. This can be achieved in systems with parametric processes, while a first success was obtained in 1985 by Slusher et al. [210] and others followed soon [211]. Hence, parametric oscillators are present in the field of quantum communication using entangled pairs of photons or as sensors due to their ability to create squeezed states [212, 213]. A prominent example is the enhancement of the sensitivity in the famous LIGO gravitational wave detector [214]. Further, recently, a parametric oscillator for phonons was successfully obtained in an experiment [215] paving the way for entangled or squeezed phonon states.

Motivated by the large field of applications for two-photon states and the significance of entangled and squeezed states for various domains, we will consider the nonlinear interaction of two parametrically driven Duffing resonators. We derive and solve the equation of motion in the classical regime and obtain the steady-state amplitudes of both resonators. Investigating different parameter regimes, we find the most interesting case, which is when a bifurcation occurs. We analyze this in more detail by determining the

ideal setup. With the amplitudes derived in the classical regime, we find the effective Hamiltonian for the quantum fluctuations and check some first quantities that can indicate squeezed states. Finally, we give an outlook on the steps that still need to be taken and the results that still need to be calculated.

This work was initiated as a Bachelor thesis *Nonlinear interacting quantum Duffing resonators* of Michael Saur, submitted in 2020 to obtain the degree Bachelor of Science (B.Sc.). Although there exists some double content, calculation, figures, and plots have been done by myself.

5.1 Classical Regime

5.1.1 Derivation of the Steady-State Solution and Fluctuations as Stability Criteria

We consider two nonlinear interacting Duffing resonators, while the interaction is described by the potential

$$V_{(1|2)}^{(22)} = \frac{1}{2}\lambda_{(1|2)}^{(22)} q_1^2 q_2^2 \,, \tag{5.1}$$

with the interaction strength $\lambda \equiv \lambda_{(1|2)}^{(22)}$. Both resonators with amplitudes $q_i(t)$ are characterized by their eigenfrequencies ω_i, the Duffing nonlinearities with strength γ_i and the damping constant Γ_i, with i=1,2. Both resonators can be modulated by a parametric drive $\tilde{\mu}_i \cos(2\omega_d t + \varphi_i)$, where $\tilde{\mu}_i$ is the modulation amplitude and we drive each resonator close to twice of the eigenfrequency. Therefore, $|\omega_i - \omega_d| \ll \omega_d,\, \omega_0$. The Hamiltonian of this system reads

$$H = \sum_{i=1}^{2} \left[\frac{p_i^2}{2} + \left(\frac{\omega_i^2}{2} + \tilde{\mu}_i \cos\left(2\omega_d t + \varphi_i\right) \right) q_i^2 + \frac{\gamma_i}{4} q_i^4 \right] + \frac{\lambda}{2} q_1^2 q_2^2 \,. \tag{5.2}$$

By introducing (phenomenologically) the damping Γ_i, the equations of motion of the two oscillators become

$$\ddot{q}_i = -\left[\omega_i^2 + 2\tilde{\mu}_i \cos\left(2\omega_d t + \varphi_i\right) \right] q_i - \gamma_i q_i^3 - 2\Gamma_i \dot{q}_i - \lambda q_i q_j^2 \,. \tag{5.3}$$

We use the same canonical transformation as for the single Duffing to switch into the rotating frame

$$u_i = \left(q_i - \frac{i}{\omega_d} \dot{q}_i \right) e^{-i\omega_d t} \,, \qquad u_i^* = \left(q_i + \frac{i}{\omega_d} \dot{q}_i \right) e^{i\omega_d t} \,. \tag{5.4}$$

Except for the coupling term, whose RWA reads

$$e^{i\omega_d t} q_i q_j^2 \approx \frac{1}{8}\left(2u_i|u_j|^2 + u_i^* u_j^2\right) , \tag{5.5}$$

the other terms were already derived in Section 3.2.2 and we obtain

$$\frac{\dot{u}_i}{\Gamma_i} = -i\delta_i u_i + i\frac{\tilde{\mu}_i}{2\omega_d\Gamma_i}e^{i\varphi_i}u_i^* + i\frac{3\gamma_i}{8\omega_d\Gamma_i}|u_i|^2 u_i - u_i + i\frac{\lambda}{8\omega_d\Gamma_i}\left(2u_i|u_j|^2 + u_i^* u_j^2\right) . \tag{5.6}$$

We introduce the scaled parameters

$$u_i = \sqrt{\frac{8\omega_d\Gamma_i}{3\gamma_i}}z_i , \quad \delta_i = \frac{\delta\omega_i}{\Gamma_i} \quad \mu_i = \frac{\tilde{\mu}_i}{2\omega_d\Gamma_i} , \quad \lambda_i = \frac{\lambda}{3\gamma_j}\frac{\Gamma_i}{\Gamma_j} , \tag{5.7}$$

yielding the two coupled equations in the scaled representation (for i, j =1, 2, with i ≠j)

$$\frac{\dot{z}_1}{\Gamma_1} = \left[-1 + i(|z_1|^2 - \delta_1)\right] z_1 + i\mu_1 e^{i\varphi_1} z_1^* + i\lambda_1\left(2z_1|z_2|^2 + z_1^* z_2^2\right) , \tag{5.8}$$

$$\frac{\dot{z}_2}{\Gamma_2} = \left[-1 + i(|z_2|^2 - \delta_2)\right] z_2 + i\mu_2 e^{i\varphi_2} z_2^* + i\lambda_2\left(2z_2|z_1|^2 + z_2^* z_1^2\right) . \tag{5.9}$$

We assume that the resonance frequencies of the two resonators are close, and define their difference by $\Delta\omega = \omega_1 - \omega_2$ with the scaled analog $\Delta = \Delta\omega/\Gamma_1$. Hence the detunings are not independent of each other, we express δ_2 in terms of δ_1:

$$\delta_2 = \frac{\delta\omega_2}{\Gamma_2} = \frac{\omega_d - \omega_2}{\Gamma_2} = \frac{\omega_d - \omega_1}{\Gamma_2} + \frac{\Delta\omega}{\Gamma_2} = \frac{\Gamma_1}{\Gamma_2}\left(\frac{\delta\omega_1}{\Gamma_1} + \frac{\Delta\omega}{\Gamma_1}\right) = \frac{\Gamma_1}{\Gamma_2}\left(\delta_1 + \Delta\right) . \tag{5.10}$$

The equation for the steady-state solution, i.e. $\dot{\bar{z}}_i = 0$, reads

$$0 = \left[-1 + i(|\bar{z}_i|^2 - \delta_i)\right] \bar{z}_i + i\mu_i e^{i\varphi_i}\bar{z}_i^* + i\lambda_i\left(2\bar{z}_i|\bar{z}_j|^2 + \bar{z}_i^*\bar{z}_j^2\right) . \tag{5.11}$$

To investigate the stability, we consider again a small fluctuation around the steady-states, i.e. $z_i(t) = \bar{z}_i + \delta z_i(t)$. We expand the RWA equation to first order in $\delta z_i(t)$ and neglect all higher contributions of $\delta z_i(t)$.

$$\begin{aligned}\frac{\dot{\bar{z}}_i + \dot{\delta z}_i(t)}{\Gamma_i} \approx & i\Big[i + (|\bar{z}_i|^2 - \delta_i)\Big]\bar{z}_i + \mu_i e^{i\varphi_i}\bar{z}_i^* + \lambda\left(2\bar{z}_i|\bar{z}_j|^2 + \bar{z}_i^*\bar{z}_j^2\right) \\ & + i(2|\bar{z}_i{}^2| - \delta_i + 2\lambda_i|\bar{z}_j|^2)\delta z_i(t) + i(\bar{z}_i^2 + \mu_i e^{i\varphi_i} + \lambda_i\bar{z}_j^2)\delta z_i(t)^* \\ & + i2\lambda_i\Big((\bar{z}_i\bar{z}_j^* + \bar{z}_i^*\bar{z}_j)\Big)\delta z_j(t) + i2\lambda_i\bar{z}_i\bar{z}_j\delta z_j^*(t) .\end{aligned} \tag{5.12}$$

The first line of the latter equation can be identified as the steady-state solution. Furthermore, we define

$$a_{ij} = (2|\bar{z}_i{}^2| - \delta_i + 2\lambda_i|\bar{z}_j|^2)\,, \tag{5.13}$$

$$b_{ij} = (\bar{z}_i^2 + \mu_i e^{i\varphi_i} + \lambda_i \bar{z}_j^2)\,, \tag{5.14}$$

$$c_{ij} = 2\lambda_i \left((\bar{z}_i \bar{z}_j^* + \bar{z}_i^* \bar{z}_j)\right), \tag{5.15}$$

$$d_{ij} = 2\lambda_i \bar{z}_i \bar{z}_j\,, \tag{5.16}$$

and write this system of equations in matrix form:

$$\begin{pmatrix} \dot{\delta z}_1 \\ \dot{\delta z}_1^* \\ \dot{\delta z}_2 \\ \dot{\delta z}_2^* \end{pmatrix} = i \begin{pmatrix} a_{12} & b_{12} & c_{12} & d_{12} \\ b_{12}^* & a_{12}^* & d_{12}^* & c_{12}^* \\ c_{21} & d_{21} & a_{21} & b_{21} \\ d_{21}^* & c_{21}^* & b_{21}^* & a_{21}^* \end{pmatrix} \begin{pmatrix} \delta z_1 \\ \delta z_1^* \\ \delta z_2 \\ \delta z_2^* \end{pmatrix} - \begin{pmatrix} 1 & 0 & 0 & 0 \\ 0 & 1 & 0 & 0 \\ 0 & 0 & 1 & 0 \\ 0 & 0 & 0 & 1 \end{pmatrix} \begin{pmatrix} \delta z_1 \\ \delta z_1^* \\ \delta z_2 \\ \delta z_2^* \end{pmatrix}, \tag{5.17}$$

where we isolated the damping. Based on this eigenvalue problem, we obtain a condition for a stable solution that the real part of the eigenvalues has to be negative, i.e. $\mathrm{Re}(\nu) < 0$. We solve the coupled system of equations in Eq. (5.11) for $i, j = 1, 2$ with $i \neq j$ to obtain the possible solutions and the eigenvalue problem to distinguish stable and unstable solutions numerically.

5.1.2 Trivial and Non-Trivial Solutions and Their Instabilities

Solving the nonlinear coupled resonators equations, we always obtain pairs of solutions of the two amplitudes $|z_1|$ and $|z_2|$. Several trivial solutions exist, i.e. the amplitude of one or both resonators is zero, and the corresponding nonzero amplitude behaves like an uncoupled parametrically driven resonator. However, the coupling between the resonators changes the stability condition even for zero amplitude compared to the real noninteracting parametric driven oscillator. We compare the trivial and non-trivial solutions and analyze the coupling effect for either one or both resonators driven by a parametric force.

To compare the case with indeed zero coupling to those with a zero amplitude solution pair, we plot the stable solutions of both cases in Fig. 5.1. We drive the first resonator by a force with amplitude $\mu_1 = 10$ while the second resonator is not affected by any external force. Furthermore, we set symmetric parameters $\varphi_i = 0$, $\Gamma_1 = \Gamma_2$ and $\gamma_1 = \gamma_2$ and the coupling constant either zero or finite as $\lambda = \frac{33}{80}\gamma_1$, such that $\lambda_i = \frac{\lambda}{3\gamma_i}\frac{\Gamma_i}{\Gamma_j} = \frac{11}{80}$. Regarding Fig. 5.1, the red and green solutions correspond to the uncoupled system. Since the second resonator is not driven, its amplitude is zero, while the first resonator shows the classic behavior of a parametric driven oscillator. For a finite coupling, we obtain two stable solution pairs: the yellow and blue lines. Here we show only the pair where one

solution is zero. Comparing the uncoupled and coupled system, i.e. the red/green solution to blue/yellow, a gap appears. This gap results from an instability. The uncoupled solution

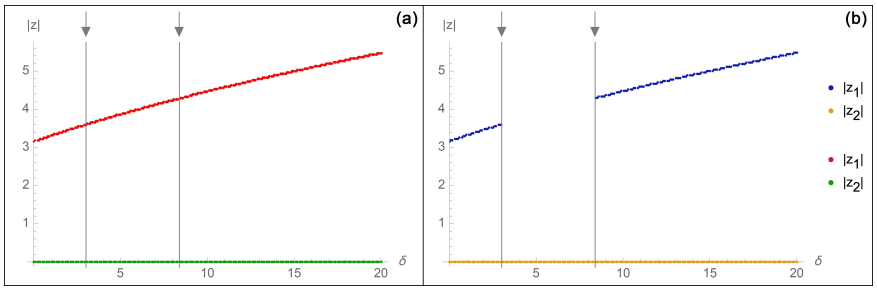

Fig. 5.1.: Plot of the stable numerical solutions for two coupled oscillators. The first resonator is driven parametrically by a force with amplitude $\mu_1 = 10$. The second resonator is not driven, i.e. $\mu_2 = 0$. Further parameters are $\varphi_i = 0$, $\Gamma_1 = \Gamma_2$ and $\gamma_1 = \gamma_2$. (a) Red and green solutions belong to the uncoupled system. (b) Blue and orange solutions correspond to a finite coupling with $\lambda = \frac{33}{80}\gamma_1$ and therefore $\lambda_i = \frac{\lambda}{3\gamma_i}\frac{\Gamma_i}{\Gamma_j} = \frac{11}{80}$. In the area indicated by the gray lines, the solution pair with one zero solution but corresponding to finite coupling shows a gap.

exists, but due to the finite coupling to the second resonator, it is unstable, even when the amplitude of the second resonator is zero. Considering Eq. (5.16) and in detail the elements a_{ij} and b_{ij}, we note that even if the amplitude z_i is zero, the terms $\lambda_i|\bar{z}_j|^2\delta z_i(t)$ and $\lambda_i\bar{z}_j^2\delta z_i(t)^*$ couple the fluctuations of the zero amplitude via λ_i to the finite amplitude z_j. Due to this coupling, there is a parameter regime in which some solutions become unstable, which are stable in the uncoupled case.

This can be visualized, plotting the real part of the eigenvalues from Eq. (5.17) depending on the coupling parameter $\lambda_1 = \lambda_2$. We show this in Fig. 5.2 for the amplitude $z_1(\delta_1)$ at two different values of the detuning, i.e. $\delta_1 = 5$ and $\delta_1 = 10$. The coupling parameter used in Fig. 5.1, i.e. $\lambda_1 = \lambda_2 = 11/80$ is denoted by the gray line. The solution of z_i is stable if the real part of all eigenvalues is negative. For a specific range of the coupling constant, the real part of one eigenvalue becomes positive, and in this region, the solution becomes unstable.

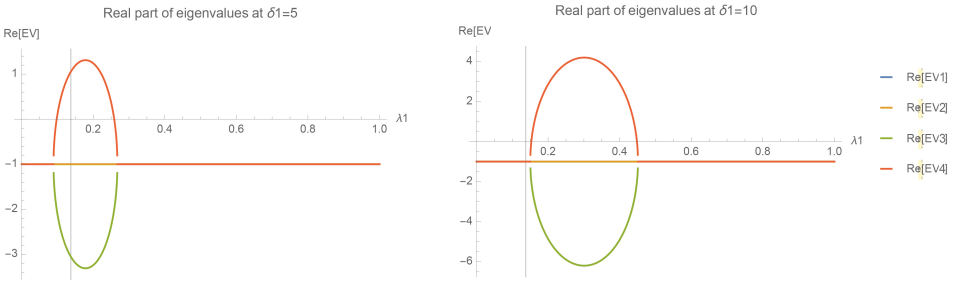

Fig. 5.2.: Real part of the four eigenvalues of solutions for the two different detuning values, i.e. $\delta = 5$ and $\delta = 10$ depending on the coupling constant $\lambda_1 = \lambda_2$. In a certain range of the coupling constant, the real part of one eigenvalue becomes positive, leading to an unstable solution. The gray line indicates the coupling constant $11/80$ that is used in Fig. 5.1. For an amplitude for $\delta = 5$, i.e. the left plot, the solution is unstable while it is stable for $\delta = 10$, i.e. the right plot.

The same observation can be made considering two nonlinear coupled Duffing oscillators where now both resonators are driven by a parametric force that differs slightly, i.e. $\mu_1 = 2.5$ and $\mu_2 = 2.25$, while the other parameters are the same as in the example before. In Fig. 5.3, we plotted the stable solutions of the uncoupled system in red and green, while the stable solutions of the system with finite coupling are shown in yellow and blue. Again we plot only the solution pairs with one zero-amplitude solution, differing slightly due to the different driving forces. It seems that there occurs a jump in the amplitude, indicated by the gray arrows in Fig. 5.3 (b), which contradicts the behavior of the uncoupled driven system. The reason is still the instability of the solution due to the coupling of the fluctuations. Therefore, this jump does not occur because a sufficient strong detuning is needed, which implies a sufficiently large amplitude to activate the oscillation of the second resonator. Plotting the real part of the eigenvalues shows similar results as in Fig. 5.2.

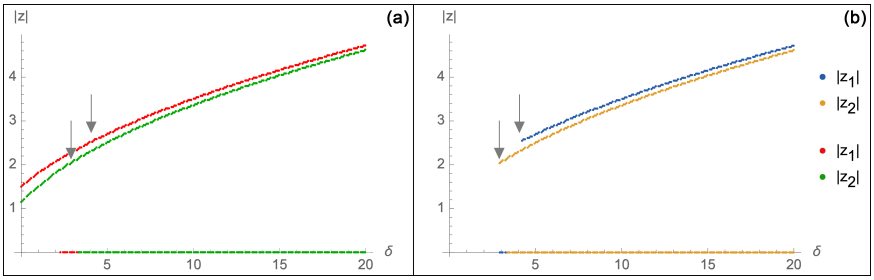

Fig. 5.3.: Plot of the stable numerical solutions for two coupled oscillators. The first resonator is driven parametrically by a force with amplitude $\mu_1 = 2.5$. The second resonator is driven parametrically by a force with amplitude $\mu_1 = 2.25$. Further parameters are $\varphi_i = 0$, $\Gamma_1 = \Gamma_2$ and $\gamma_1 = \gamma_2$. (a) Red and green solutions belong to the uncoupled system. (b) Blue and orange solutions correspond to a finite coupling with $\lambda = \frac{33}{80}\gamma_1$ and therefore $\lambda_i = \frac{\lambda}{3\gamma_i}\frac{\Gamma_i}{\Gamma_j} = \frac{11}{80}$. In the area indicated by the gray arrows, the solution pair with one zero solution but corresponding to finite coupling shows a gap.

5.1.3 Bifurcation Effect for a Parametric Drive with Equal Driving Strengths

After we did the consistency check of the zero-amplitude solution pairs and clarified the reason for the occurring gaps as instabilities we focus now on the solution pairs, where both solutions are finite. As a first indication we show both zero and nonzero solution pairs in Fig. 5.4. Both for a single and two driven resonators. These solutions have a lower amplitude compared to the uncoupled/zero amplitude solutions.

It was already found in [216] that for a sufficiently strong and equal drive, the coupled system with two drives shows additional solutions in the form of a bifurcation. We will extend these studies and investigate this behavior further. For this purpose, we first consider the coupled system with equal driving forces applied to the two resonators.

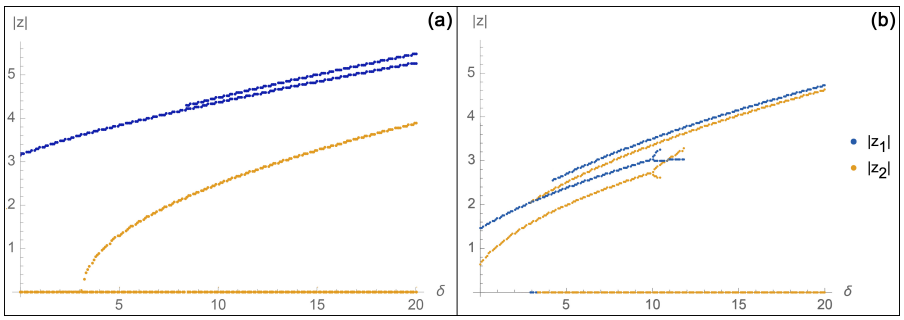

Fig. 5.4.: Plot of the stable numerical solutions for two coupled oscillators. The first resonator is driven parametrically by a force with amplitude $\mu_1 = 2.5$. (a) The second resonator is not affected by an external force. (b) The second resonator is driven parametrically by a force with amplitude $\mu_1 = 2.25$. Further parameters are $\varphi_i = 0$, $\Gamma_1 = \Gamma_2$ and $\gamma_1 = \gamma_2$. We consider a finite coupling with $\lambda = \frac{33}{80}\gamma_1$ and therefore $\lambda_i = \frac{\lambda}{3\gamma_i}\frac{\Gamma_i}{\Gamma_j} = \frac{11}{80}$. Compared to the latter chapter the nonzero solution pairs are the lower blue and yellow lines. The bifurcation in (b) will be explained in the following.

We investigate the impact of the driving strength, the strength of the coupling, how asymmetry in the system affects the amplitudes and if a similar effect occurs if only a single resonator is driven. Since the interesting effects happen if both resonators oscillate simultaneously, we will show only solutions where both amplitudes are finite in the following. We start with the impact of the driving strength. The parameters for the

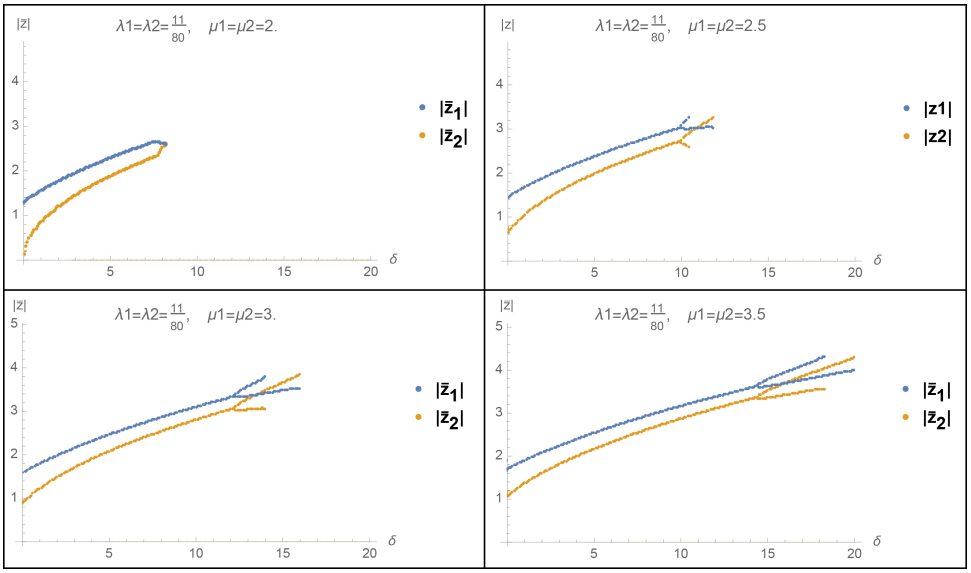

Fig. 5.5.: Effect of equal, increasing driving forces on the amplitudes of nonlinear coupled parametrically driven Duffing resonators. The other parameters are $\varphi_i = 0$, $\Gamma_1 = \Gamma_2$ and $\gamma_1 = \gamma_2$,$\lambda = \frac{33}{80}\gamma_1$ and therefore $\lambda_i = \frac{\lambda}{3\gamma_i}\frac{\Gamma_i}{\Gamma_j} = \frac{11}{80}$. Plots of the nontrivial, stable solutions. We consider equal forces acting on the two resonators while we increase the strength from $\mu_1 = \mu_2 = 2$ to $\mu_1 = \mu_2 = 4$.

plots in Fig. 5.5 are $\varphi_i = 0$, $\Gamma_1 = \Gamma_2$ and $\gamma_1 = \gamma_2$. We consider a finite coupling for which we set $\lambda = \frac{33}{80}\gamma_1$ and therefore $\lambda_i = \frac{\lambda}{3\gamma_i}\frac{\Gamma_i}{\Gamma_j} = \frac{11}{80}$. We drive both resonators with the same driving strength given by the parameters $\mu_1 = \mu_2$. The curves cross, i.e. the

resonator oscillates with the same amplitude, and it exists only a single solution for the coupled equations. They build additional branches in terms of a bifurcation. As the force increases, the amplitudes increase because more energy is pumped into the system. The arms of the bifurcation become more pronounced and the two new branches evolve even more symmetric concerning the initial curve. Furthermore, the range of detuning in which the nontrivial solution exists is extended with increasing force. The analysis of the stability condition shows that the real solution does not become unstable but disappears. To study the consequences of an increasing coupling strength λ, we fix the

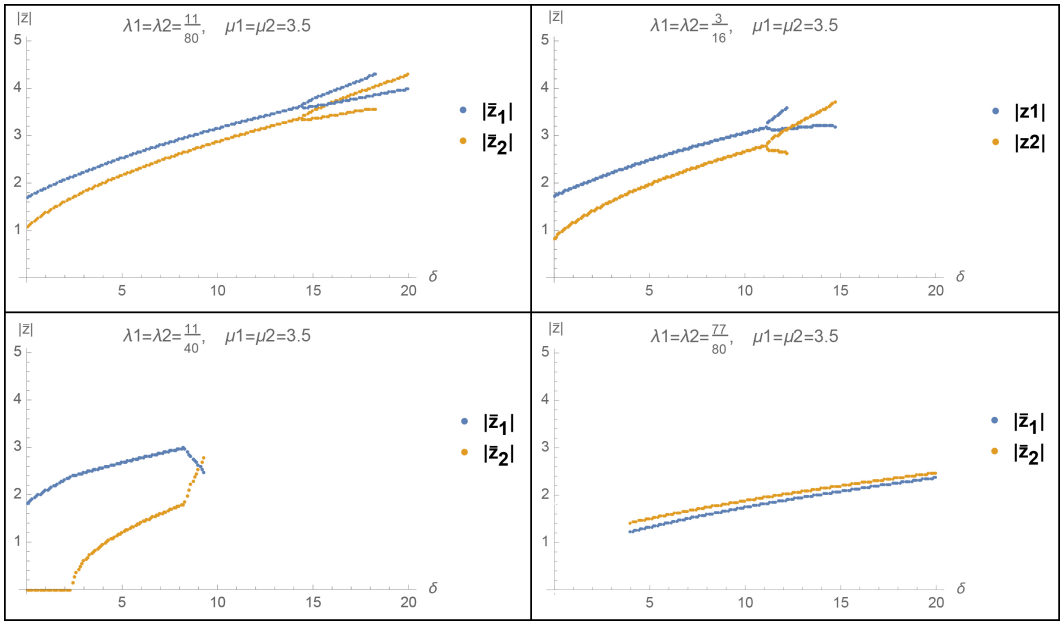

Fig. 5.6.: Effect of the coupling strength on the amplitudes of nonlinear coupled parametrically driven Duffing resonators. The other parameters are $\varphi_i = 0$, $\Gamma_1 = \Gamma_2$, $\gamma_1 = \gamma_2$ and $\mu_1 = \mu_2 = 3.5$. Plots of the nontrivial, stable solutions for different coupling strength. Due to the scaling $\lambda_i = \frac{\lambda}{3\gamma_i}\frac{\Gamma_i}{\Gamma_j}$, we define the coupling constant λ_i always in terms of γ_i.

force of the two resonators at equal values $\mu_1 = \mu_2 = 3.5$. Due to the scaling $\lambda_i = \frac{\lambda}{3\gamma_i}\frac{\Gamma_i}{\Gamma_j}$, we define λ always in terms of γ_i. In Fig. 5.6, we notice that increasing the coupling strength has the inverse effect of increasing the driving force. The range of detuning in which a real solution exists decreases. The additional arms become less symmetric and pronounced until they finally regress completely. The amplitude of one resonator remains almost constant while the other amplitude decreases significantly. For really strong coupling, i.e. if the coupling parameter is larger than the Duffing nonlinearity, we get a solution comparable with two independent oscillations, where the breakdown cannot be seen due to the RWA. So far, we assumed a symmetric setup, i.e. equal Duffing nonlinearities, damping coefficients, and driving forces. We still keep the latter two but evaluate the influence of different Duffing nonlinearities. Note that this also affects the scaling of the amplitudes. We consider the case where $\lambda_2 = 1.2\,\lambda_1$ which corresponds to $\gamma_2 = 10/12\,\gamma_1 \approx 0.83\,\gamma_1$. In the first two plots of Fig. 5.7, we compared the symmetric and asymmetric system at $\mu_i = 3.5$. While the branching effect is well pronounced

in the symmetric case, in the left plot, the additional arms disappear entirely in the asymmetric case. Analyzing the stability conditions, we notice again that this is not due to instability, but the solutions disappear completely. The curves drift away, and the detuning

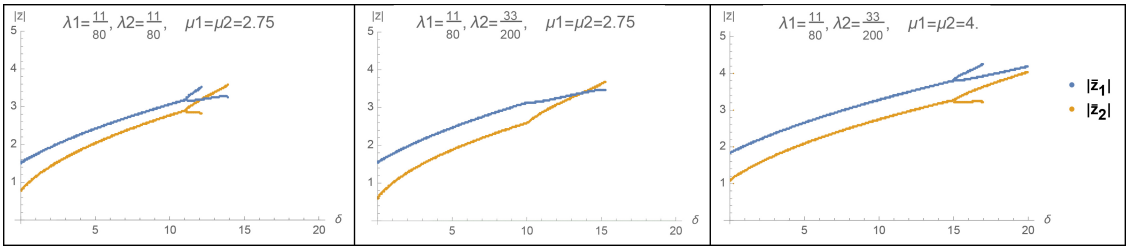

Fig. 5.7.: Effect of different Duffing nonlinearities on the amplitude of nonlinear coupled parametrically driven Duffing resonators. We fixed $\varphi_i = 0$, $\Gamma_1 = \Gamma_2$ and $\gamma_1 = \gamma_2$. Plots of the nontrivial, stable solutions. In the left plot and middle plot, we set $\mu_1 = \mu_2 = 2.75$. We compare the effect for either equal nonlinearities on the left, and different nonlinearities at the middle, where we set $\lambda_2 = 1.2\,\lambda_1$ which corresponds to $\gamma_2 = 10/12\gamma_1 \approx 0.83\gamma_1$. We kept the different Duffing nonlinearities in the right plot but increased the driving force to $\mu_1 = \mu_2 = 4$.

range for a finite solution slightly increases. Thus, the crossing point shifts to a larger detuning. We already noticed this effect varying the coupling strength. Due to our scaling, increasing the coupling strength has the same effect as a symmetric decrease of both Duffing nonlinearities. With increasing force, shown in the right panel of Fig. 5.7, we can reproduce the bifurcation, i.e. when the force is large enough to overcome the asymmetry induced by different Duffing constants. The extra branches of each solution reappear, and the curves cross, although at larger detuning than in the symmetric system. This indicates that the two resonators need to be affected by a similar force to show the special behavior.

One estimated reason for the bifurcation is the frequency change of the resonators due to the interaction, i.e. if one resonator starts to oscillate in the predicted way, its frequency is shifted at that moment when the second oscillator starts to move. To check the effect of the coupling, we consider the case where only one of the two resonators is driven parametrically while the second one is not affected by any external force, i.e. it oscillates just due to the coupling. In Fig. 5.8, we show the solutions for two different forces acting on the first resonator. Here, we also plotted the trivial solution, where the amplitude of the second resonator is zero, and the corresponding (high) blue curve represents the uncoupled solution of resonator one. The nontrivial solution pair does not show any additional branches and does not cross, even for large detunings. We notice just the well-known behavior, i.e. if the detuning is large enough, the amplitude of the first resonator is sufficiently strong, such that the second resonator can oscillate then with a stable amplitude. The amplitudes are close to each other, but less than the uncorrelated solutions since the same total energy is distributed at two oscillators. Increasing the force also raises the amplitude of the first resonator. Therefore, a stable oscillation of the second resonator is obtained already at smaller detuning. The effective frequency also

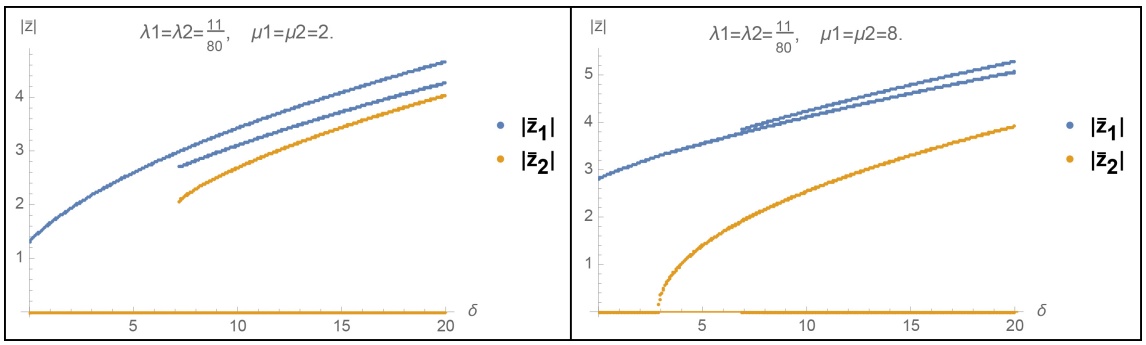

Fig. 5.8.: Stable solutions of two nonlinear coupled Duffing resonators while a parametric force drives only one of them. We check two different driving strengths and compare the trivial with the nontrivial solutions. The other parameters are $\varphi_i = 0$, $\Gamma_1 = \Gamma_2$ and $\gamma_1 = \gamma_2$,$\lambda = \frac{33}{80}\gamma_1$ and therefore $\lambda_i = \frac{\lambda}{3\gamma_i}\frac{\Gamma_i}{\Gamma_j} = \frac{11}{80}$.

depends on the amplitude of the coupled resonator. Therefore, the amplitudes of both resonators differ stronger than at smaller forces. However, this effect does not explain the bifurcation.

5.1.4 Bifurcation Effect for a Parametric Drive with Different Driving Strengths

So far, we figured out that the bifurcation, and even the crossing, is not simply caused by the frequency shift due to the coupling and both resonators need to be driven parametrically. Increasing the driving force causes a more pronounced and symmetric bifurcation. An asymmetry in the Duffing nonlinearities can suppress the bifurcation entirely while the crossing still occurs. Nevertheless, a sufficiently large force can overcome this effect. In the following, we still drive both resonators but investigate the consequence of different driving amplitudes $\mu_1 \neq \mu_2$. To give more insight, we show in Fig. 5.9, not only the stable but also the unstable solutions. The bold curves represent the stable solutions while the other curves correspond to the unstable ones. We still show only nontrivial solution pairs. We fix the force driving the second resonator at $\mu_2 = 3.5$ while we sweep the amplitude of the force proportional to μ_1. More details are shown in the appendix, Section C.2, where we give the plots with a stepsize of $\Delta\mu_1 = 0.05$. In Fig. 5.9, we show the solution of four different force combination. We obtain two different solution pairs for the amplitude. The first one, denoted *inner solution* in the following, starting at zero detuning and the second, denoted *outer solution* in the following, which appears around $\delta_1 = 15$. The inner solution pair increases in amplitude and detuning range with increasing force. The curves drift slightly away from each other. Hence, the crossing point also drifts to larger detuning values, and the tails approach each other. The outer solutions show just minor changes. The length almost does not change, but they move slightly to the left overall. In this way, the inner solutions squeeze in between the outer ones, and at equal forces, they finally connect. Verifying the unstable solutions shows that the gap is not just due to instability,

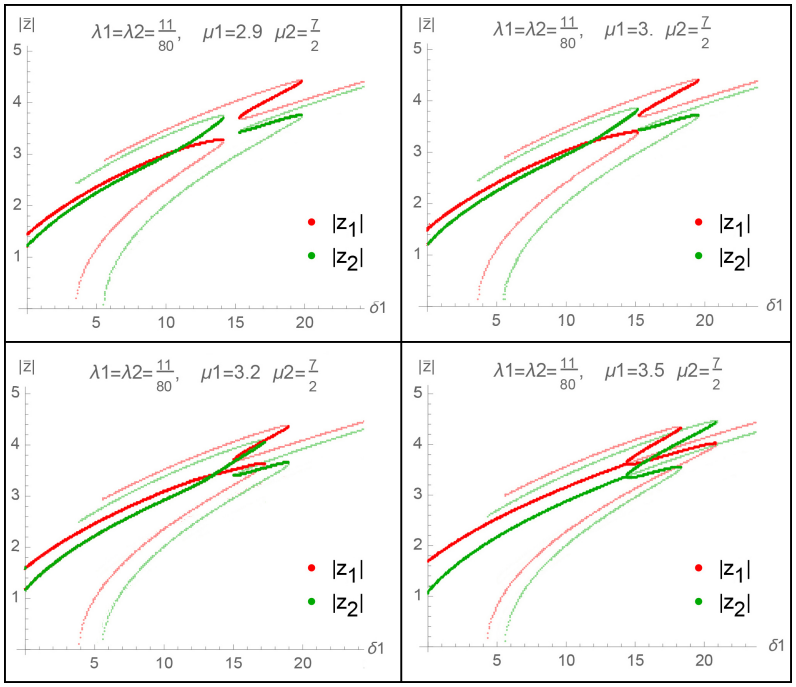

Fig. 5.9.: Nontrivial solutions for nonlinear coupled, parametrically driven Duffing resonators for different driving forces. Both stable (bold lines) and unstable solutions are shown. The parameters are $\varphi_i = 0$, $\Gamma_1 = \Gamma_2$ and $\gamma_1 = \gamma_2$,$\lambda = \frac{33}{80}\gamma_1$ and therefore $\lambda_i = \frac{\lambda}{3\gamma_i}\frac{\Gamma_i}{\Gamma_j} = \frac{11}{80}$. The driving force of the second resonator is fixed at $\mu_2 = 3.5$. We check four different strength for the driving force of the first resonator.

but no solution exists. Regarding Fig. 5.10, we see that the bifurcation, i.e. the connected branches, occurs if and only if the two driving forces are equal. A slight change of the forces leads directly to disconnected arms, i.e. an imperfect bifurcation. Considering the insets of Fig. 5.10, it is visible that if one force approaches from below towards the fixed force, the inner solution squeezes between the outer. When the force exceeds the fixed force, the inner branches detach in the region where the solutions overlap, and the new outer solutions retreat.

At this point, we cannot explain the classical physics behind this behavior. However, it seems that something exciting happens in this parameter regime. To investigate this further, we will transform the nonlinear coupled resonators to the quantum regime and consider the quadratures of the two resonators in the parameter regime obtained from the classical approach. We have four quadratures, two for each resonator. Since we cannot plot a four-dimensional surface, we will fix two quadratures of one resonator, using the steady-state solutions we obtained in the classical case, and plot a two-dimensional surface of only one resonator. For this purpose, we vary the detuning and extract the steady-state solutions for one of the resonators in the classical regime. We can verify our calculations, checking if the occurring surface has a minimum at the steady-state solution pair of both resonators. Furthermore, we investigate how the surface evolves with different parameters. Moreover, similar to the classical case, we will derive the stability conditions by introducing quantum fluctuations. The occurring equation gives

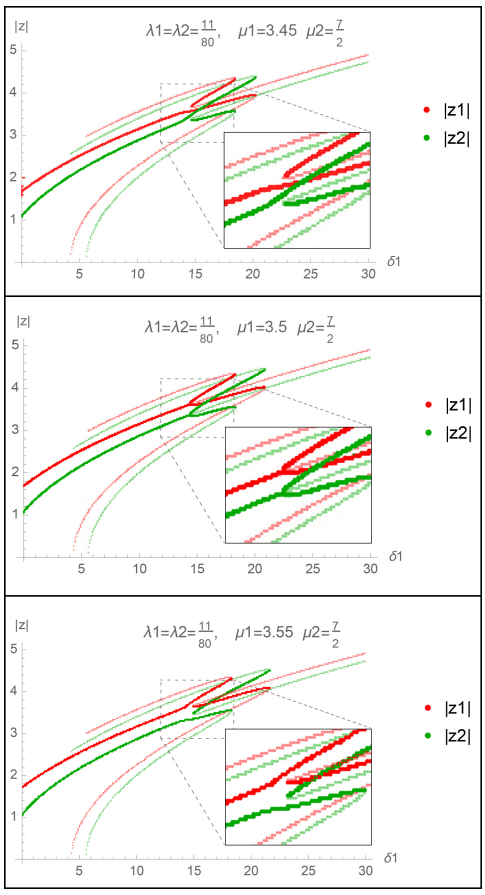

Fig. 5.10.: Closeup for solutions for nonlinear coupled, parametrically driven Duffing resonators for different driving forces. Only nontrivial solutions are plotted while both stable (bold lines) and unstable solutions are shown. The parameters are $\varphi_i = 0$, $\Gamma_1 = \Gamma_2$ and $\gamma_1 = \gamma_2$,$\lambda = \frac{33}{80}\gamma_1$ and therefore $\lambda_i = \frac{\lambda}{3\gamma_i}\frac{\Gamma_i}{\Gamma_j} = \frac{11}{80}$. The driving force of the second resonator is fixed at $\mu_2 = 3.5$. We check three different strengths for the driving force of the first resonator that is slightly below, equal and slightly above the second resonator. The inset shows a zoom of the crossing area.

direct access to squeezing and stability information, allowing us to determine possible entangled states. However, we have to extract the steady-state solutions for this approach, i.e. the full solution defined by amplitude and phase. So far, we spoke about only one solution pair for each visible pair of amplitude curves until now. To be precise, we obtain four solution pairs with equal absolute values that differ in the phase. Consequently, we study how the phase of the stable solution pairs behaves. For this purpose, we check two cases, i.e. $\mu_1 = 3.3$ with $\mu_2 = 3.5$ and $\mu_1 = \mu_2 = 3.5$.

In Fig. 5.11, we plotted the occurring phases. Red and orange dots represent the phases of the solutions for the first resonator, while blue and cyan dots correspond to the second resonator. Lighter colors correspond to the inner branches, while darker colors correspond to the outer branches. Both resonators have one solution with the positive and one with the negative phase. The four solution pairs correspond, therefore, to all possible combinations.

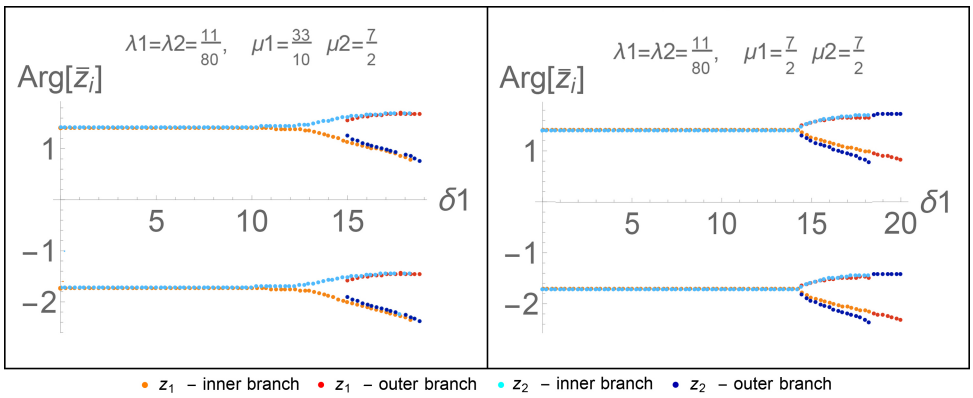

Fig. 5.11.: Phase of the four nontrivial solutions for nonlinear coupled, parametrically driven Duffing resonators for two different driving forces. The parameters are $\varphi_i = 0$, $\Gamma_1 = \Gamma_2$ and $\gamma_1 = \gamma_2$,$\lambda = \frac{33}{80}\gamma_1$ and therefore $\lambda_i = \frac{\lambda}{3\gamma_i}\frac{\Gamma_i}{\Gamma_j} = \frac{11}{80}$. The driving force of the second resonator is fixed at $\mu_2 = 3.5$. We check two different strengths for the driving force of the first resonator. Red and orange dots correspond two the first, and blue and cyan dots to the second resonator.

In the detuning range, where both solutions behave almost like uncoupled resonators, the phases are close to $\pm\pi/2$. The exact value $\pm\pi/2$ is reached in the limit of large forces. Therefore, the discrepancy originates from the parametric forces used in the numerical calculations are not very strong. When the interaction between the resonators influences the behavior of the amplitude, the phase also starts to vary. However, the difference between the positive and negative phases is always equal to π, which will become important in the following section.

5.2 Quantum Regime

This aim of this chapter is to derive the effective Hamiltonian of the quantum fluctuations. For this purpose, we write the Hamiltonian of Eq. (5.2) in terms of the bosonic creation and annihilation operators, i.e. $\hat{a}_i^\dagger$, $\hat{a}_i$ for $m = 1$ via

$$q_i \to \hat{q}_i = \sqrt{\frac{\hbar}{2\omega_i}}\left(\hat{a}_i + \hat{a}_i^\dagger\right), \tag{5.18}$$

$$p_i \to \hat{p}_i = -i\sqrt{\frac{\hbar\omega_i}{2}}\left(\hat{a}_i - \hat{a}_i^\dagger\right), \tag{5.19}$$

whereby the operators fulfill the bosonic commutator relation

$$[\hat{a}_i, \hat{a}_j] = [\hat{a}_i^\dagger, \hat{a}_j^\dagger] = 0, \tag{5.20}$$

$$[\hat{a}_i, \hat{a}_j^\dagger] = \hat{a}_i\hat{a}_j^\dagger - \hat{a}_j^\dagger\hat{a}_i = \delta_{ij}. \tag{5.21}$$

This leads to a lengthy expression, including quadratic and quartic terms in the bosonic operators.

The Hamiltonian can be transformed into the rotating frame by the unitary transformation

$$\hat{H} \to \hat{U}\hat{H}\hat{U}^\dagger + i\hbar\dot{\hat{U}}\hat{U}^\dagger\,, \tag{5.22}$$

with the unitary operator

$$U(t) = e^{i\omega_d t\sum_{i=1}^{2}\hat{a}_i^\dagger\hat{a}_i}\,. \tag{5.23}$$

The detuning is still defined as $\delta\omega_i := \omega_d - \omega_i$. Neglecting the fast oscillating terms, we obtain the Hamiltonian in the RWA

$$\begin{aligned}\hat{H}_{\text{RWA}} = \sum_{i=1}^{2}\left[\frac{\hbar\omega_i}{2} - \hbar\delta\omega_i\hat{a}_i^\dagger\hat{a}_i + \frac{\tilde{\mu}_i\hbar}{4\omega_i}\left(\hat{a}_i^2 e^{i\varphi_i} + (\hat{a}_i^\dagger)^2 e^{-i\varphi_i}\right) + \frac{3\gamma_i\hbar^2}{8\omega_i^2}\left((\hat{a}_i^\dagger)^2\hat{a}_i^2 + 2\hat{a}_i^\dagger\hat{a}_i + \frac{1}{2}\right)\right] \\ + \frac{\tilde{\lambda}\hbar^2}{8\omega_1\omega_2}\left(\hat{a}_1^2(\hat{a}_2^\dagger)^2 + 4\hat{a}_1^\dagger\hat{a}_1\hat{a}_2^\dagger\hat{a}_2 + 2\hat{a}_1^\dagger\hat{a}_1 + (\hat{a}_1^\dagger)^2\hat{a}_2^2 + 2\hat{a}_2^\dagger\hat{a}_2 + 1\right).\end{aligned} \tag{5.24}$$

From this expression we derive the Heisenberg equation of motion

$$\dot{\hat{a}}_i = \frac{\mathrm{d}\hat{a}_i}{\mathrm{dt}} = i[\hat{H}_{\text{RWA}}, \hat{a}_i] + \frac{\partial a_i}{\partial t} = i[\hat{H}_{\text{RWA}}\hat{a}_i - \hat{a}_i\hat{H}_{\text{RWA}}]\,, \tag{5.25}$$

and add (heuristically) the damping, i.e. $-\Gamma_i\hat{a}_i$ to obtain finally, with $i, j \in \{1, 2\}$ but $i \neq j$, the equation of motion

$$\dot{\hat{a}}_i = \left[i\left(\hbar\delta\omega_i - \frac{3\gamma_i\hbar^2}{4\omega_i^2}\left(1 + \hat{a}_i^\dagger\hat{a}_i\right) - \frac{\tilde{\lambda}\hbar^2}{4\omega_1\omega_2}\right) - \Gamma_i\right]\hat{a}_i - i\frac{\tilde{\mu}_i\hbar}{2\omega_i}e^{-i\varphi_i}\hat{a}_i^\dagger - i\frac{\tilde{\lambda}\hbar^2}{4\omega_1\omega_2}\left(2\hat{a}_i\hat{a}_j^\dagger\hat{a}_j + \hat{a}_i^\dagger\hat{a}_j^2\right). \tag{5.26}$$

A classical wave package describes the quantum dynamics of the oscillator. Its center is characterized by classical physics, which we considered in the latter chapter, and the fluctuations around this stable state of oscillation are of quantum nature. To investigate this in more detail, we use the so-called semiclassical approximation, i.e. $\hat{a}_i(t) = c_i + \delta\hat{a}_i$. Here $\delta\hat{a}_i$ are the quantum fluctuations. We insert these approximations in the equation of motion and receive

$$\begin{aligned}\dot{\delta\hat{a}}_i = &\left[i\left(\hbar\delta\omega_i - \frac{3\gamma_i\hbar^2}{4\omega_i^2}\left(1+\left(c_i^*+\delta\hat{a}_i^\dagger\right)\left(c_i+\delta\hat{a}_i\right)\right) - \frac{\tilde{\lambda}\hbar^2}{4\omega_1\omega_2}\right) - \Gamma_i\right]\left(c_i+\delta\hat{a}_i\right)\\ &- i\frac{\tilde{\mu}_i\hbar}{2\omega_i}e^{-i\varphi_i}\left(c_i^*+\delta\hat{a}_i^\dagger\right)\\ &- i\frac{\tilde{\lambda}\hbar^2}{4\omega_1\omega_2}\Big(2\left(c_i+\delta\hat{a}_i\right)\left(c_j^*+\delta\hat{a}_j^\dagger\right)\left(c_j+\delta\hat{a}_j\right)+\left(c_i^*+\delta\hat{a}_i^\dagger\right)\left(c_j+\delta\hat{a}_j\right)^2\Big)\,. \end{aligned} \tag{5.27}$$

As a first step, we do a consistency check. If we study the stable solutions, neglecting the fluctuation, we should receive an equation similar to the classical limit. We obtain

$$0 = \left[i\left(\hbar\delta\omega_i - \frac{3\gamma_i\hbar^2}{4\omega_i^2}\left(1+|c_i|^2\right) - \frac{\tilde{\lambda}\hbar^2}{4\omega_1\omega_2}\right) - \Gamma_i\right]c_i - i\frac{\tilde{\mu}_i\hbar}{2\omega_i}e^{-i\varphi_i}c_i^* - i\frac{\tilde{\lambda}\hbar^2}{4\omega_1\omega_2}\Big(2c_i|c_j|^2 + c_i^*c_j^2\Big)\,. \tag{5.28}$$

Compared to the steady equation in the classical limit, given by Eq. (5.11), the only difference is the renormalization of the detuning by the factor $-\frac{3\gamma_i\hbar^2}{4\omega_i^2}-\frac{\tilde{\lambda}\hbar^2}{4\omega_i\omega_j}$. To investigate the fluctuations, we consider the whole expression in Eq. (5.27) and keep terms only up to the first order in the fluctuations, as we assume that the fluctuations are small. Similar to the derivation in the classical limit, we can identify the steady-state equation, which is zero, and obtain the equation of motion of the quantum fluctuations:

$$\begin{aligned}\dot{\delta\hat{a}}_i = &-i\left(-\hbar\delta\omega_i + \frac{3\gamma_i\hbar^2}{4\omega_i^2}\left(1+2|c_i|^2\right) + \frac{\tilde{\lambda}\hbar^2}{4\omega_1\omega_2}\left(1+2|c_j|^2\right)\right)\delta\hat{a}_i - \Gamma_i\delta\hat{a}_i\\ &- i\left(\frac{\tilde{\mu}_i\hbar}{2\omega_i}e^{-i\varphi_i} + \frac{3\gamma_i}{4\omega_i^2}c_i^2 + \frac{\tilde{\lambda}}{4\omega_1\omega_2}c_j^2\right)\delta\hat{a}_i^\dagger - i\frac{2\tilde{\lambda}\hbar^2}{4\omega_1\omega_2}c_ic_j\delta\hat{a}_j^\dagger - i\frac{2\tilde{\lambda}\hbar^2}{4\omega_1\omega_2}\left(c_i^*c_j + c_ic_j^*\right)\delta\hat{a}_j\,. \end{aligned} \tag{5.29}$$

In terms of the parameters

$$A_{ij} = \left(-\hbar\delta\omega_i + \frac{3\gamma_i\hbar^2}{4\omega_i^2}\left(1+2|c_i|^2\right) + \frac{\tilde{\lambda}\hbar^2}{4\omega_1\omega_2}\left(1+2|c_j|^2\right)\right)\,, \tag{5.30}$$

$$B_{ij} = \left(\frac{\tilde{\mu}_i\hbar}{2\omega_i}e^{-i\varphi_i} + \frac{3\gamma_i}{4\omega_i^2}c_i^2 + \frac{\tilde{\lambda}}{4\omega_1\omega_2}c_j^2\right)\,, \tag{5.31}$$

$$C_{ij} = \frac{2\tilde{\lambda}\hbar^2}{4\omega_1\omega_2}c_ic_j\,, \tag{5.32}$$

$$D_{ij} = \frac{2\tilde{\lambda}\hbar^2}{4\omega_1\omega_2}\left(c_i^*c_j + c_ic_j^*\right)\,, \tag{5.33}$$

we can write the equations of motion for the fluctuation operators in matrix form. Note that $C_{ij} = C_{ji} \equiv C$ and $D_{ij} = D_{ji} \equiv D$ and, therefore,

$$\begin{pmatrix} \delta\dot{\hat{\tilde{a}}}_1 \\ \delta\dot{\hat{\tilde{a}}}_1^\dagger \\ \delta\dot{\hat{\tilde{a}}}_2 \\ \delta\dot{\hat{\tilde{a}}}_2^\dagger \end{pmatrix} = -i \begin{pmatrix} \tilde{A}_{12} & \tilde{B}_{12} & \tilde{C} & \tilde{D} \\ -\tilde{B}_{12}^* & -\tilde{A}_{12}^* & -\tilde{D}^* & -\tilde{C}^* \\ \tilde{C} & \tilde{D} & \tilde{A}_{21} & \tilde{B}_{21} \\ -\tilde{D}^* & -\tilde{C}^* & -\tilde{B}_{21}^* & -\tilde{A}_{21}^* \end{pmatrix} \begin{pmatrix} \delta\hat{\tilde{a}}_1 \\ \delta\hat{\tilde{a}}_1^\dagger \\ \delta\hat{\tilde{a}}_2 \\ \delta\hat{\tilde{a}}_2^\dagger \end{pmatrix} - \begin{pmatrix} \Gamma & 0 & 0 & 0 \\ 0 & \Gamma & 0 & 0 \\ 0 & 0 & \Gamma & 0 \\ 0 & 0 & 0 & \Gamma \end{pmatrix} \begin{pmatrix} \delta\hat{\tilde{a}}_1 \\ \delta\hat{\tilde{a}}_1^\dagger \\ \delta\hat{\tilde{a}}_2 \\ \delta\hat{\tilde{a}}_2^\dagger \end{pmatrix}, \quad (5.34)$$

while the last term describes the damping. Like in the steady-state equation, the matrix element A_{ij} contains a shift in the detuning, but the structure and the matrix elements are similar to the classical case. Therefore the steady-state solution that we derived in the classical regime can also be used for the quantum regime equations, while we have to keep in mind the renormalization of the detuning.

The elements A_{ji} and B_{ij} just renormalize the detuning and the parametric force, while C and D contain information about a possible squeezing of the quadrature of the quantum fluctuations. If these elements vanish, the quadratures of the fluctuations about the stable-state would be equal [164, 217], i.e. no squeezing effect occurs. The quadratures are determined by the real and imaginary parts, respectively. Hence, we consider how the real and imaginary part of the matrix elements C and D of Eq. (5.34) evolve for two different parameter sets. The elements depend on two multiplied amplitudes of the resonator or its complex conjugated. The four possible solution pairs, that we derived in the classical regime, show a phase difference between within a pair of zero or exactly π. The additional phase factors of the products either compensate or sum up to 2π. Hence, the phase does not affect the matrix elements. Since the four solution pairs differ only in the phase and not in the amplitude, we need to analyze and evaluate other quantities for only one solution pair. We fix the force of the second resonator to $\mu_2 = 3.5$. For the first resonator, we consider the three different forces $\mu_1 = 2.9$, $\mu_1 = 3.3$ and $\mu_1 = 3.5$. The other parameters are $\varphi_i = 0$, $\Gamma_1 = \Gamma_2$ and $\gamma_1 = \gamma_2$. We consider a finite coupling and set $\tilde{\lambda} = \frac{33}{80}\gamma_1$ and therefore $\lambda_i = \frac{\tilde{\lambda}}{3\gamma_i}\frac{\Gamma_i}{\Gamma_j} = \frac{11}{80}$, which are the parameters that we used in the classical regime. In this way, we plug in the amplitudes of the classical steady-state equation and determine the real and imaginary part of C and D which we show in Fig. 5.12. In all three setups, we find an interesting behavior of both matrix elements. While the real part of element C vanishes, the imaginary part is finite. For the element D, both real and imaginary parts are finite. This indicates that the quadratures of the fluctuations are not equal, i.e. there is a squeezing effect. To prove this, we derive the effective Hamiltonian of the quantum fluctuations. This Hamiltonian has in general the following form:

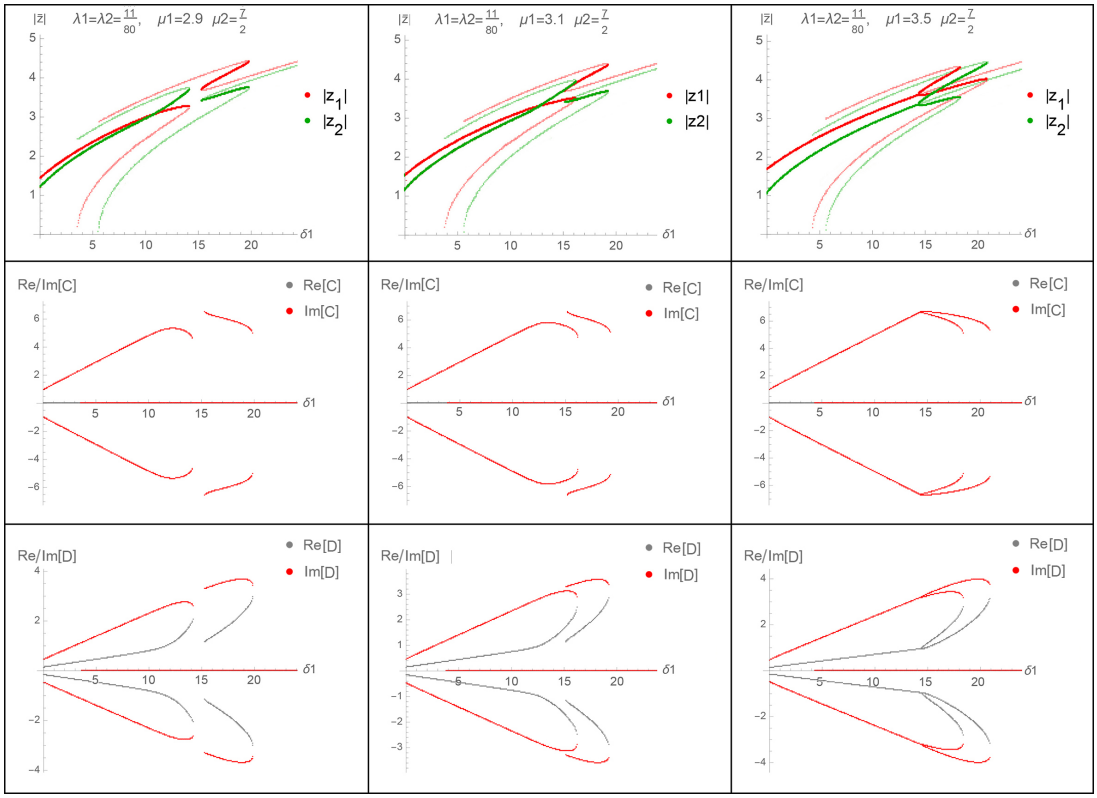

Fig. 5.12.: In the first row, we plotted again the nontrivial solution pairs for the coupled resonator, where the bold lines correspond to the stable solutions. The second and third rows show the real and imaginary part of the matrix elements C_{ij} and D_{ij}, respectively, for the stable nontrivial solutions. We consider the evolution from a smaller force of the first resonator towards equal forces, i.e. $\mu_1 = 2.9$, $\mu_1 = 3.3$ and $\mu_1 = 3.5$ for $\mu_2 = 3.5$. The other parameters are $\varphi_i = 0$, $\Gamma_1 = \Gamma_2$ and $\gamma_1 = \gamma_2$. We consider a finite coupling and set $\tilde{\lambda} = \frac{33}{80}\gamma_1$ and therefore $\lambda_i = \frac{\tilde{\lambda}}{3\gamma_i}\frac{\Gamma_i}{\Gamma_j} = \frac{11}{80}$

$$\begin{aligned} H_{\text{ex}} =& \omega_1^{\text{eff}} \delta a_1^\dagger \delta a_1 + X_1 \left[\delta a_1^\dagger \delta a_1^\dagger + \text{h.c.}\right] + \omega_2^{\text{eff}} \delta a_2^\dagger \delta a_2 + X_2 \left[\delta a_2^\dagger \delta a_2^\dagger + \text{h.c.}\right] \\ &+ X_3 \left[\delta a_1 \delta a_2^\dagger + \text{h.c.}\right] + X_4 \left[\delta a_1^\dagger \delta a_2^\dagger + \text{h.c.}\right] . \end{aligned} \tag{5.35}$$

To find the exact coefficients, we determine the equation of motion from this exemplary Hamiltonian and compare the result with Eq. (5.34). By comparison, we can identify the coefficients

$$\omega_1^{\text{eff}} = A_{12} = -\hbar\delta\omega_1 + \frac{3\gamma_1\hbar^2}{4\omega_1^2}\left(1+2|c_1|^2\right) + \frac{\tilde{\lambda}\hbar^2}{4\omega_1\omega_2}\left(1+2|c_2|^2\right), \tag{5.36}$$

$$\omega_2^{\text{eff}} = A_{21} = -\hbar\delta\omega_2 + \frac{3\gamma_2\hbar^2}{4\omega_2^2}\left(1+2|c_2|^2\right) + \frac{\tilde{\lambda}\hbar^2}{4\omega_1\omega_2}\left(1+2|c_1|^2\right), \tag{5.37}$$

$$X_1 = \frac{1}{2}B_{12} = \left(\frac{\mu_1\hbar}{2\omega_1}e^{-i\varphi_1} + \frac{3\gamma_1\hbar^2}{4\omega_1^2}c_1^2 + \frac{\tilde{\lambda}\hbar^2}{4\omega_1\omega_2}c_2^2\right), \tag{5.38}$$

$$X_2 = \frac{1}{2}B_{21} = \left(\frac{\mu_2\hbar}{2\omega_2}e^{-i\varphi_2} + \frac{3\gamma_2\hbar^2}{4\omega_2^2}c_2^2 + \frac{\tilde{\lambda}\hbar^2}{4\omega_1\omega_2}c_1^2\right), \tag{5.39}$$

$$X_3 = C = \frac{2\tilde{\lambda}\hbar^2}{4\omega_1\omega_2}c_1c_2\,, \tag{5.40}$$

$$X_4 = D = \frac{2\tilde{\lambda}\hbar^2}{4\omega_1\omega_2}\left(c_1^*c_2 + c_1c_2^*\right). \tag{5.41}$$

The effective Hamiltonian for the fluctuation reads therefore

$$\begin{aligned} H_{\text{ex}} =& A_{12}\delta a_1^\dagger\delta a_1 + \frac{1}{2}B_{12}\left[\delta a_1^\dagger\delta a_1^\dagger + \text{h.c.}\right] + A_{21}\delta a_2^\dagger\delta a_2 + \frac{1}{2}B_{21}\left[\delta a_2^\dagger\delta a_2^\dagger + \text{h.c.}\right] \\ &+ C\left[\delta a_1\delta a_2^\dagger + \text{h.c.}\right] + D\left[\delta a_1^\dagger\delta a_2^\dagger + \text{h.c.}\right]. \end{aligned} \tag{5.42}$$

This part of the work is still in preparation. Using a Bogoliubov transformation, the Hamiltonian of Eq. (5.42) can be diagonalized. Then, we can evaluate the quadratures of the two resonators in the parameter regime obtained from the classical approach. As already explained we will use the steady-state solutions of the classical regime to plot the quadrature of one resonator depending on the detuning. Furthermore we have access to non-classical quantities indicated by squeezed states. In this way, we will investigate entanglement criteria for different parameter sets in the bifurcation regime.

6 Summary and Outlook

Small nanomechanical oscillators can have atomic-scale dimensions and show, therefore, already at small amplitudes nonlinear behavior of their vibrations, like parametric oscillation or bifurcation. The field of applications is huge since the excitation of flexural modes paves the way for hybrid engineered systems because they can easily be coupled to other degrees of freedom like light or atoms. Internal resonances like the 1:3 resonance lead to non-trivial aspects, like the self-limitation of the amplitude. In this context, the Scheer group of the University Konstanz and, in particular, F. Yang developed an experiment of a vibrating membrane resonator under ultra-strong drive. Deriving the theory for this experiment, we were able to show that the persistent response, which denotes a vibrating state that has a nearly constant, high amplitude over a frequency range of more than 50% of the eigenfrequency, is caused by a previously undescribed parametric coupling between different flexural modes and their overtones. In Section 4.3.1, we demonstrated that the dynamics of the fundamental (1,1) mode with its higher harmonics, where we limited ourselves to the second, third, and fourth harmonics, can be modeled by an effective septic force if the higher-order modes are in the harmonic regime. Under this point of view, we derived in Section 4.3.2 a scaled expression of the amplitude that demonstrated the flat response obtained in the experiment. Furthermore, we determined the maximum amplitude and detuning. However, the overall smooth response showed special features on the nanometer scale in terms of small steps and kinks. Evaluating the deflection profile, the experimental group had identified these as a signature of nonlinear mode coupling. In Section 4.4 we confirmed that two different nonlinear coupling mechanisms cause these variations. In Section 4.4.1, we demonstrated an indirect parametric nonlinear interaction, activated by the overtones of the fundamental mode ($m = n$). In detail, we studied the coupling of the second overtone of the fundamental mode with the (2,2) mode. In Section 4.4.2, we considered a direct parametric interaction with higher flexural modes ($m \neq n$). The resonance is fractional, and we studied in detail the interaction of the (1,1) mode with the (1,2) mode. A comparison to the experiment proved that both coupling mechanisms could be associated with the features in the measurement.

Furthermore, parametric processes can produce two-photon coherent states. These states are essential in quantum optics and quantum communication. Motivated by the large field of applications and the significance of entangled and squeezed states for various domains, we studied the nonlinear interaction of two parametrically driven Duffing resonators. In Section 5.1.2, we analyzed the stability of the trivial solutions and obtained that the coupling led to unstable regions even if the amplitude of one resonator is zero. Obtaining

the steady-state solution of the amplitude, we ascertained a bifurcation if the driving forces are equal, which we analyzed in Section 5.1.3. The larger the forces, the more pronounced the bifurcation. If the coupling increases, this has the reverse effect of an increasing driving force. If the Duffing nonlinearities of the two resonators differ, the bifurcation can be suppressed while the amplitudes still cross. Increasing the force overcomes this effect. If the forces are equal, the two branches are connected to the initial curve before the bifurcation. If the forces differ slightly, the solution in some detuning range vanishes and a gap appears in one of the two branches, i.e. only an imperfect bifurcation appears, what we showed in Section 5.1.4. If we consider not only the amplitude but also the phase of the possible solutions, we obtain four different solution pairs with different combinations of a positive or negative phase value. The relevant information is the constant phase difference of π. To investigate the presence of possibly squeezed states and apply other entanglement criteria, we studied in Section 5.2 the system in the quantum regime. Deriving the equation of motion for the quantum fluctuations, we performed a first analysis of the matrix elements using the steady-state solutions of the classical regime that gave rise to the presence of squeezed states. We derived the effective Hamiltonian of the quantum fluctuations. Further steps will be the diagonalization of this Hamiltonian using a Bogoliubov transformation. Then, we evaluate the quadratures of the two resonators in the parameter regime obtained from the classical approach. We will fix the quadratures of one resonator using the classical solutions and study the two-dimensional surface of the other resonator for different values of the detuning. In this way, we will investigate entanglement criteria for different parameter sets in the bifurcation regime.

List of Figures

List of Tables

A Detailed Calculation of the Perturbation Expansion

A.1 Perturbation Expansion of the Two-Particle Green's Function $F_{\mathrm{ab}}(t,t')$

A.1.1 Zeroth Order

At zeroth order the application of Wick's theorem leads to mixed terms of $\hat{a}$ and $\hat{b}$ that vanish since the particle number of each resonator is not conserved and there is no direct interaction between the resonators. We end up with the multiplication of the bosonic Keldysh Green's function of each resonator,

$$\left\langle T_{\mathrm{C}}\left(\left(a_t a_{t'}^\dagger b_t b_{t'}^\dagger\right)\right)\right\rangle^{(0)} = \left\langle T_C\left(a(t)a^\dagger(t')\right)\right\rangle \left\langle T_C\left(b(t)b^\dagger(t')\right)\right\rangle = -D_a^{(0)}(t,t')D_b^{(0)}(t,t')\,. \tag{A.1}$$

A.1.2 Second Order

The second order term is the two-dimensional integral over contour times written in Eq. (A.2). Since mixed terms, i.e. terms with an odd number of operators $\hat{a}$ or $\hat{b}$, become zero the only nonzero contributions of the two multiplied interaction Hamiltonians are given in Eq. (A.3). We separate the string of bosonic and fermionic operators and summarize the different contributions in Eq. (A.4). In the next step we apply Wicks theorem to decompose the strings of bosonic and fermionic operators separately. We already neglected disconnected and Tadpole diagrams and end up with Eq. (A.5) Finally we identify the Keldysh Green's functions and receive the contour-time integral over fermionic and bosonic unperturbed Keldysh Green's functions in Eq. (A.6).

$$\begin{aligned}\left\langle T_{\mathrm{C}}\left(\hat{a}_t\hat{a}_{t'}^\dagger\hat{b}_t\hat{b}_{t'}^\dagger\right)\right\rangle^{(2)} =& \frac{(-i)^2}{2!}\int_C dt_1\int_C dt_2\left\langle T_C\left(a_t a_{t'}^\dagger b_t b_{t'}^\dagger\ \left[\lambda(a+a^\dagger)d^\dagger d+\lambda(b+b^\dagger)\tilde{d}^\dagger\tilde{d}\right]_{t_1}\right.\right.\\ &\left.\left.\times\ \left[\lambda(a+a^\dagger)d^\dagger d+\lambda(b+b^\dagger)\tilde{d}^\dagger\tilde{d}\right]_{t_2}\right)\right\rangle\end{aligned} \tag{A.2}$$

$$
\begin{aligned}
=&\frac{-1}{2}\int_C dt_1 \int_C dt_2 \left\langle T_C \left(a_t a_{t'}^\dagger b_t b_{t'}^\dagger \left[\lambda(a_{t_1} + a_{t_1}^\dagger) d_{t_1}^\dagger d_{t_1}\right] \left[\lambda(a_{t_2} + a_{t_2}^\dagger) d_{t_2}^\dagger d_{t_2}\right]\right)\right\rangle \\
+&\frac{-1}{2}\int_C dt_1 \int_C dt_2 \left\langle T_C \left(a_t a_{t'}^\dagger b_t b_{t'}^\dagger \left[\lambda(b_{t_1} + b_{t_1}^\dagger) \tilde{d}_{t_1}^\dagger \tilde{d}_{t_1}\right] \left[\lambda(b_{t_2} + b_{t_2}^\dagger) \tilde{d}_{t_2}^\dagger \tilde{d}_{t_2}\right]\right)\right\rangle
\end{aligned} \tag{A.3}
$$

$$
\begin{aligned}
=&-\lambda^2 \int_C dt_1 \int_C dt_2 \left\langle T_C \left(a_t a_{t'}^\dagger b_t b_{t'}^\dagger a_{t_1} a_{t_2}^\dagger \right)\right\rangle \left\langle T_C \left(d_{t_1}^\dagger d_{t_1} d_{t_2}^\dagger d_{t_2}\right)\right\rangle \\
&-\lambda^2 \int_C dt_1 \int_C dt_2 \left\langle T_C \left(a_t a_{t'}^\dagger b_t b_{t'}^\dagger b_{t_1} b_{t_2}^\dagger \right)\right\rangle \left\langle T_C \left(\tilde{d}_{t_1}^\dagger \tilde{d}_{t_1} \tilde{d}_{t_2}^\dagger \tilde{d}_{t_2}\right)\right\rangle
\end{aligned} \tag{A.4}
$$

$$
\begin{aligned}
=&\lambda^2 \int_C dt_1 \int_C dt_2 \left\langle T_C \left(a_t a_{t_2}^\dagger \right)\right\rangle \left\langle T_C \left(b_t b_{t'}^\dagger \right)\right\rangle \left\langle T_C \left(a_{t_1} a_{t'}^\dagger \right)\right\rangle \times \left\langle T_C \left(d_{t_1}^\dagger d_{t_2}\right)\right\rangle \left\langle T_C \left(d_{t_2}^\dagger d_{t_1}\right)\right\rangle \\
+&\lambda^2 \int_C dt_1 \int_C dt_2 \left\langle T_C \left(a_t a_{t'}^\dagger \right)\right\rangle \left\langle T_C \left(b_t b_{t_2}^\dagger \right)\right\rangle \left\langle T_C \left(b_{t_1} b_{t'}^\dagger \right)\right\rangle \times \left\langle T_C \left(\tilde{d}_{t_1}^\dagger \tilde{d}_{t_2}\right)\right\rangle \left\langle T_C \left(\tilde{d}_{t_2}^\dagger \tilde{d}_{t_1}\right)\right\rangle
\end{aligned} \tag{A.5}
$$

$$
\begin{aligned}
=&i\lambda^2 \int_C dt_1 \int_C dt_2 D_a^{(0)}(t,t_2) D_a^{(0)}(t_1,t') D_b^{(0)}(t,t') G_{aa}(t_1,t_2) G_{aa}(t_2,t_1) \\
+&i\lambda^2 \int_C dt_1 \int_C dt_2 D_a^{(0)}(t,t') D_b^{(0)}(t,t_2) D_b^{(0)}(t_1,t') G_{bb}(t_1,t_2) G_{bb}(t_2,t_1)
\end{aligned} \tag{A.6}
$$

A.1.3 Fourth Order

For the fourth order term we now get the four-dimensional integral over contour times, shown in Eq. (A.8). The multiplication of the four interaction Hamiltonians can be summarized and decomposed in the same way as before to obtain Eq. (A.10). In a first step we apply Wick's theorem only to the string of bosonic operators and end up with Eq. (A.10). Next we apply Wick's theorem to the string of fermionic operators. To short the occurring expression we summarize the sum of two antisymmetric bosonic Green's functions as $\tilde{D}^{(0)}(t_i,t_j) = D^{(0)}(t_i,t_j) + D^{(0)}(t_j,t_i)$. We again neglect disconnected and Tadpole diagrams and end up with the final expression of the perturbative expansion upon fourth order in Eq. (A.10). To improve the readability we use the color code of the Feynman diagrams exceptionally also for the equation. Blue and red corresponds to the diagonal elements, i.e. the bosonic Green's function $D_{\mathrm{a}}^{(0)}$ and the fermionic Green's function G_{aa} in blue and the bosonic Green's function $D_{\mathrm{b}}^{(0)}$ and the fermionic Green's function G_{bb} in red. Green belongs to the offdiagonal fermionic Green's functions, i.e. G_{ab} and G_{ba}.

$$\left\langle T_{\mathsf{C}}\left(\hat{a}_t\hat{a}^\dagger_{t'}\hat{b}_t\hat{b}^\dagger_{t'}\right)\right\rangle^{(4)} \tag{A.7}$$

$$= \frac{(-i)^4}{24}\int_C dt_1\int_C dt_2\int_C dt_3\int_C dt_4 \left\langle T_C\left(a_t a^\dagger_{t'} b_t b^\dagger_{t'}\left[\lambda(a+a^\dagger)d^\dagger d+\lambda(b+b^\dagger)\tilde{d}^\dagger\tilde{d}\right]_{t_1}\left[\lambda(a+a^\dagger)d^\dagger d+\lambda(b+b^\dagger)\tilde{d}^\dagger\tilde{d}\right]_{t_2}\right.\right.$$
$$\left.\left.\times\left[\lambda(a+a^\dagger)d^\dagger d+\lambda(b+b^\dagger)\tilde{d}^\dagger\tilde{d}\right]_{t_3}\left[\lambda(a+a^\dagger)d^\dagger d+\lambda(b+b^\dagger)\tilde{d}^\dagger\tilde{d}\right]_{t_4}\right)\right\rangle \tag{A.8}$$

$$\begin{aligned}=&\frac{\lambda^4}{24}\int_C dt_1\int_C dt_2\int_C dt_3\int_C dt_4\\ &\Big[\quad 6\left\langle T_{\mathsf{C}}\left(a_t a^\dagger_{t'} b_t b^\dagger_{t'} a_{t_1} a_{t_2} a^\dagger_{t_3} a^\dagger_{t_4}\right)\right\rangle\left\langle T_{\mathsf{C}}\left(d^\dagger_{t_1} d_{t_1} d^\dagger_{t_2} d_{t_2} d^\dagger_{t_3} d_{t_3} d^\dagger_{t_4} d_{t_4}\right)\right\rangle\\ &+\ 6\left\langle T_{\mathsf{C}}\left(a_t a^\dagger_{t'} b_t b^\dagger_{t'} b_{t_1} b_{t_2} b^\dagger_{t_3} b^\dagger_{t_4}\right)\right\rangle\left\langle T_{\mathsf{C}}\left(\tilde{d}^\dagger_{t_1}\tilde{d}_{t_1}\tilde{d}^\dagger_{t_2}\tilde{d}_{t_2}\tilde{d}^\dagger_{t_3}\tilde{d}_{t_3}\tilde{d}^\dagger_{t_4}\tilde{d}_{t_4}\right)\right\rangle\\ &+24\left\langle T_{\mathsf{C}}\left(a_t a^\dagger_{t'} b_t b^\dagger_{t'} a_{t_1} a^\dagger_{t_2} b_{t_3} b^\dagger_{t_4}\right)\right\rangle\left\langle T_{\mathsf{C}}\left(d^\dagger_{t_1} d_{t_1} d^\dagger_{t_2} d_{t_2}\tilde{d}^\dagger_{t_3}\tilde{d}_{t_3}\tilde{d}^\dagger_{t_4}\tilde{d}_{t_4}\right)\right\rangle\Big]\end{aligned} \tag{A.9}$$

$$\begin{aligned}=&\frac{\lambda^4}{24}\int_C dt_1\int_C dt_2\int_C dt_3\int_C dt_4\\ &\Big[\ D^{(0)}_{\mathsf{b}}(t,t')D^{(0)}_{\mathsf{a}}(t,t_3)D^{(0)}_{\mathsf{a}}(t_1,t')D^{(0)}_{\mathsf{a}}(t_2,t_4)\left\langle T_{\mathsf{C}}\left(d^\dagger_{t_1} d_{t_1} d^\dagger_{t_2} d_{t_2} d^\dagger_{t_3} d_{t_3} d^\dagger_{t_4} d_{t_4}\right)\right\rangle\\ &+D^{(0)}_{\mathsf{a}}(t,t')D^{(0)}_{\mathsf{b}}(t,t_3)D^{(0)}_{\mathsf{b}}(t_1,t')D^{(0)}_{\mathsf{b}}(t_2,t_4)\left\langle T_{\mathsf{C}}\left(\tilde{d}^\dagger_{t_1}\tilde{d}_{t_1}\tilde{d}^\dagger_{t_2}\tilde{d}_{t_2}\tilde{d}^\dagger_{t_3}\tilde{d}_{t_3}\tilde{d}^\dagger_{t_4}\tilde{d}_{t_4}\right)\right\rangle\\ &+\Big(D^{(0)}_{\mathsf{a}}(t,t')D^{(0)}_{\mathsf{a}}(t_1,t_2)D^{(0)}_{\mathsf{b}}(t,t_4)D^{(0)}_{\mathsf{b}}(t_3,t')\\ &+\ D^{(0)}_{\mathsf{a}}(t,t_2)D^{(0)}_{\mathsf{a}}(t_1,t')D^{(0)}_{\mathsf{b}}(t,t')D^{(0)}_{\mathsf{b}}(t_3,t_4)\\ &+\ D^{(0)}_{\mathsf{a}}(t,t_2)D^{(0)}_{\mathsf{a}}(t_1,t')D^{(0)}_{\mathsf{b}}(t,t_4)D^{(0)}_{\mathsf{b}}(t_3,t')\Big)\left\langle T_{\mathsf{C}}\left(d^\dagger_{t_1} d_{t_1} d^\dagger_{t_2} d_{t_2}\tilde{d}^\dagger_{t_3}\tilde{d}_{t_3}\tilde{d}^\dagger_{t_4}\tilde{d}_{t_4}\right)\right\rangle\Big]\end{aligned} \tag{A.10}$$

$$\left\langle T_C\left(a_t b_t a_{t'}^\dagger b_{t'}^\dagger\right)\right\rangle \approx \left\langle T_C\left(a_t a_t b_{t'}^\dagger b_{t'}^\dagger\right)\right\rangle^{(0)} + \left\langle T_C\left(a_t a_t b_{t'}^\dagger b_{t'}^\dagger\right)\right\rangle^{(2)} + \left\langle T_C\left(a_t a_t b_{t'}^\dagger b_{t'}^\dagger\right)\right\rangle^{(4)} \tag{A.11}$$

$$\begin{aligned}
&= - D_a^{(0)}(t,t')D_b^{(0)}(t,t') \\
&\quad + i\lambda^2 \int_C dt_1 \int_C dt_2 D_a^{(0)}(t,t_2)D_a^{(0)}(t_1,t')D_b^{(0)}(t,t')G_{aa}(t_1,t_2)G_{aa}(t_2,t_1) \\
&\quad + i\lambda^2 \int_C dt_1 \int_C dt_2 D_a^{(0)}(t,t')D_b^{(0)}(t,t_2)D_b^{(0)}(t_1,t')G_{bb}(t_1,t_2)G_{bb}(t_2,t_1) \\
&\quad + \lambda^4 \int_C dt_1 \int_C dt_2 \int_C dt_3 \int_C dt_4 \Big[\\
&\qquad 2D_b^{(0)}(t,t')D_a^{(0)}(t,t_2)D_a^{(0)}(t_1,t')\tilde{D}_a^{(0)}(t_3,t_4)G_{aa}(t_1,t_3)G_{aa}(t_3,t_1)G_{aa}(t_2,t_4)G_{aa}(t_4,t_2) \\
&\qquad - 2D_b^{(0)}(t,t')D_a^{(0)}(t,t_2)D_a^{(0)}(t_1,t')\tilde{D}_a^{(0)}(t_3,t_4)G_{aa}(t_1,t_3)G_{aa}(t_3,t_4)G_{aa}(t_2,t_1)G_{aa}(t_4,t_2) \\
&\qquad - 2D_b^{(0)}(t,t')D_a^{(0)}(t,t_2)D_a^{(0)}(t_1,t')\tilde{D}_a^{(0)}(t_3,t_4)G_{aa}(t_1,t_3)G_{aa}(t_3,t_2)G_{aa}(t_2,t_4)G_{aa}(t_4,t_1) \\
&\qquad - 2D_b^{(0)}(t,t')D_a^{(0)}(t,t_2)D_a^{(0)}(t_1,t')\tilde{D}_a^{(0)}(t_3,t_4)G_{aa}(t_1,t_2)G_{aa}(t_3,t_1)G_{aa}(t_2,t_4)G_{aa}(t_4,t_3) \\
&\qquad + 2D_a^{(0)}(t,t')D_b^{(0)}(t,t_2)D_b^{(0)}(t_1,t')\tilde{D}_b^{(0)}(t_3,t_4)G_{bb}(t_1,t_3)G_{bb}(t_3,t_1)G_{bb}(t_2,t_4)G_{bb}(t_4,t_2) \\
&\qquad - 2D_a^{(0)}(t,t')D_b^{(0)}(t,t_2)D_b^{(0)}(t_1,t')\tilde{D}_b^{(0)}(t_3,t_4)G_{bb}(t_1,t_3)G_{bb}(t_3,t_4)G_{bb}(t_2,t_1)G_{bb}(t_4,t_2) \\
&\qquad - 2D_a^{(0)}(t,t')D_b^{(0)}(t,t_2)D_b^{(0)}(t_1,t')\tilde{D}_b^{(0)}(t_3,t_4)G_{bb}(t_1,t_3)G_{bb}(t_3,t_2)G_{bb}(t_2,t_4)G_{bb}(t_4,t_1) \\
&\qquad - 2D_a^{(0)}(t,t')D_b^{(0)}(t,t_2)D_b^{(0)}(t_1,t')\tilde{D}_b^{(0)}(t_3,t_4)G_{bb}(t_1,t_2)G_{bb}(t_3,t_1)G_{bb}(t_2,t_4)G_{bb}(t_4,t_3) \\
&\qquad - 2D_a^{(0)}(t,t')\tilde{D}_a^{(0)}(t_3,t_4)D_b^{(0)}(t,t_2)D_b^{(0)}(t_1,t')G_{aa}(t_3,t_4)G_{ab}(t_4,t_2)G_{ba}(t_1,t_3)G_{bb}(t_2,t_1) \\
&\qquad - 2D_a^{(0)}(t,t')\tilde{D}_a^{(0)}(t_3,t_4)D_b^{(0)}(t,t_2)D_b^{(0)}(t_1,t')G_{aa}(t_3,t_4)G_{ab}(t_4,t_1)G_{bb}(t_1,t_2)G_{ba}(t_2,t_3) \\
&\qquad + 2D_a^{(0)}(t,t')\tilde{D}_a^{(0)}(t_3,t_4)D_b^{(0)}(t,t_2)D_b^{(0)}(t_1,t')G_{ab}(t_3,t_1)G_{ab}(t_4,t_2)G_{ba}(t_1,t_3)G_{ba}(t_2,t_4) \\
&\qquad - 2D_a^{(0)}(t,t')\tilde{D}_a^{(0)}(t_3,t_4)D_b^{(0)}(t,t_2)D_b^{(0)}(t_1,t')G_{ab}(t_3,t_1)G_{ab}(t_4,t_2)G_{ba}(t_1,t_4)G_{ba}(t_2,t_3) \\
&\qquad - 2D_a^{(0)}(t,t_2)D_a^{(0)}(t_1,t')D_b^{(0)}(t,t')\tilde{D}_b^{(0)}(t_3,t_4)G_{aa}(t_1,t_2)G_{ab}(t_2,t_4)G_{ba}(t_3,t_1)G_{bb}(t_4,t_3) \\
&\qquad - 2D_a^{(0)}(t,t_2)D_a^{(0)}(t_1,t')D_b^{(0)}(t,t')\tilde{D}_b^{(0)}(t_3,t_4)G_{ab}(t_1,t_3)G_{aa}(t_2,t_1)G_{bb}(t_3,t_4)G_{ba}(t_4,t_2) \\
&\qquad + 2D_a^{(0)}(t,t_2)D_a^{(0)}(t_1,t')D_b^{(0)}(t,t')\tilde{D}_b^{(0)}(t_3,t_4)G_{ab}(t_1,t_3)G_{ab}(t_2,t_4)G_{ba}(t_3,t_1)G_{ba}(t_4,t_2) \\
&\qquad - 2D_a^{(0)}(t,t_2)D_a^{(0)}(t_1,t')D_b^{(0)}(t,t')\tilde{D}_b^{(0)}(t_3,t_4)G_{ab}(t_1,t_3)G_{ab}(t_2,t_4)G_{ba}(t_3,t_2)G_{ba}(t_4,t_1) \\
&\qquad + D_a^{(0)}(t,t_2)D_a^{(0)}(t_1,t')D_b^{(0)}(t,t_4)D_b^{(0)}(t_3,t')G_{aa}(t_1,t_2)G_{aa}(t_2,t_1)G_{bb}(t_3,t_4)G_{bb}(t_4,t_3) \\
&\qquad - D_a^{(0)}(t,t_2)D_a^{(0)}(t_1,t')D_b^{(0)}(t,t_4)D_b^{(0)}(t_3,t')G_{aa}(t_1,t_2)G_{ab}(t_2,t_4)G_{ba}(t_3,t_1)G_{bb}(t_4,t_3) \\
&\qquad - D_a^{(0)}(t,t_2)D_a^{(0)}(t_1,t')D_b^{(0)}(t,t_4)D_b^{(0)}(t_3,t')G_{aa}(t_1,t_2)G_{ab}(t_2,t_3)G_{bb}(t_3,t_4)G_{ba}(t_4,t_1) \\
&\qquad - D_a^{(0)}(t,t_2)D_a^{(0)}(t_1,t')D_b^{(0)}(t,t_4)D_b^{(0)}(t_3,t')G_{ab}(t_1,t_3)G_{aa}(t_2,t_1)G_{bb}(t_3,t_4)G_{ba}(t_4,t_2) \\
&\qquad - D_a^{(0)}(t,t_2)D_a^{(0)}(t_1,t')D_b^{(0)}(t,t_4)D_b^{(0)}(t_3,t')G_{ab}(t_1,t_3)G_{ab}(t_2,t_4)G_{ba}(t_3,t_2)G_{ba}(t_4,t_1) \\
&\qquad - D_a^{(0)}(t,t_2)D_a^{(0)}(t_1,t')D_b^{(0)}(t,t_4)D_b^{(0)}(t_3,t')G_{ab}(t_1,t_4)G_{aa}(t_2,t_1)G_{ba}(t_3,t_2)G_{bb}(t_4,t_3) \\
&\qquad - D_a^{(0)}(t,t_2)D_a^{(0)}(t_1,t')D_b^{(0)}(t,t_4)D_b^{(0)}(t_3,t')G_{ab}(t_1,t_4)G_{ab}(t_2,t_3)G_{ba}(t_3,t_1)G_{ba}(t_4,t_2) \\
&\qquad + D_a^{(0)}(t,t_2)D_a^{(0)}(t_3,t')D_b^{(0)}(t,t_4)D_b^{(0)}(t_1,t')G_{ab}(t_3,t_4)G_{ab}(t_2,t_1)G_{ba}(t_1,t_2)G_{ba}(t_4,t_3)\Big]
\end{aligned} \tag{A.12}$$

A.1.4 Perturbation Expansion of the Two-Particle Green's Function $F_{\mathrm{aa}}(t,t')$ and $F_{\mathrm{bb}}(t,t')$

The perturbation expansion of $F_{\mathrm{aa}}(t,t')$ and $F_{\mathrm{bb}}(t,t')$ leads to similar results as $F_{\mathrm{ab}}(t,t')$. As already explained in the main text, we finally consider the lesser component and therefore all terms containing the quantity $D^{(0)}_{a,b}(t,t')$ vanish. The non-vanishing contributions are

$$\left\langle T_C\left(a_t a_t a^\dagger_{t'} a^\dagger_{t'}\right)\right\rangle \approx \tag{A.13}$$

$$\begin{aligned}
&+\lambda^4 \int_C dt_1 \int_C dt_2 \int_C dt_3 \int_C dt_4 \Big[\\
&\quad - D^{(0)}_a(t,t_2) D^{(0)}_a(t_1,t') D^{(0)}_b(t,t_4) D^{(0)}_b(t_3,t') G_{ab}(t_1,t_3) G_{ab}(t_2,t_4) G_{ba}(t_3,t_2) G_{ba}(t_4,t_1) \\
&\quad - D^{(0)}_a(t,t_2) D^{(0)}_a(t_1,t') D^{(0)}_b(t,t_4) D^{(0)}_b(t_3,t') G_{ab}(t_1,t_4) G_{aa}(t_2,t_1) G_{ba}(t_3,t_2) G_{bb}(t_4,t_3) \\
&\quad + D^{(0)}_a(t,t_2) D^{(0)}_a(t_3,t') D^{(0)}_b(t,t_4) D^{(0)}_b(t_1,t') G_{ab}(t_3,t_4) G_{ab}(t_2,t_1) G_{ba}(t_1,t_2) G_{ba}(t_4,t_3) \Big]
\end{aligned} \tag{A.14}$$

$$\left\langle T_C\left(b_t b_t b^\dagger_{t'} b^\dagger_{t'}\right)\right\rangle \approx \tag{A.15}$$

$$\begin{aligned}
&+\lambda^4 \int_C dt_1 \int_C dt_2 \int_C dt_3 \int_C dt_4 \Big[\\
&\quad - D^{(0)}_a(t,t_2) D^{(0)}_a(t_1,t') D^{(0)}_b(t,t_4) D^{(0)}_b(t_3,t') G_{ab}(t_1,t_3) G_{ab}(t_2,t_4) G_{ba}(t_3,t_2) G_{ba}(t_4,t_1) \\
&\quad - D^{(0)}_a(t,t_2) D^{(0)}_a(t_1,t') D^{(0)}_b(t,t_4) D^{(0)}_b(t_3,t') G_{ab}(t_1,t_4) G_{aa}(t_2,t_1) G_{ba}(t_3,t_2) G_{bb}(t_4,t_3) \\
&\quad + D^{(0)}_a(t,t_2) D^{(0)}_a(t_3,t') D^{(0)}_b(t,t_4) D^{(0)}_b(t_1,t') G_{ab}(t_3,t_4) G_{ab}(t_2,t_1) G_{ba}(t_1,t_2) G_{ba}(t_4,t_3) \Big]
\end{aligned} \tag{A.16}$$

A.2 Feynman Diagrams

A more pleasant way to consider the perturbative expansion and to compare the different terms is the representation in Feynman diagrams. They Feynman diagrams, that finally contribute to the correlators have been shown in the main text. For completeness and a better overview, we show in the appendix the Feynman diagrams upon second-order contributions of the single-particle Green's function and the contribution upon fourth order of the two-particle Green's function as written in Eq. (A.12). The legend for

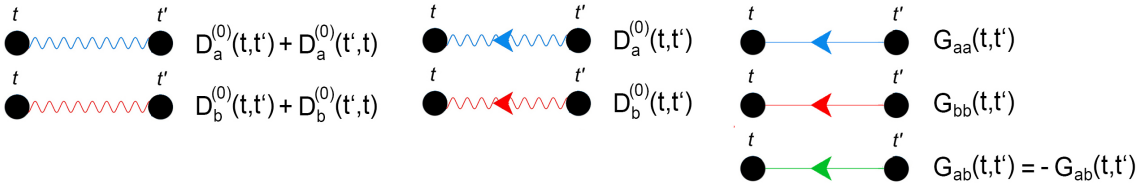

Fig. A.1.: Legend of the Feynman diagrams

the elements used in the Feynman diagrams is shown in Fig. (A.1). The wiggled lines correspond to bosonic and the straight lines to fermionic Green's functions. The color indicates the matrix element of the corresponding Green's function. Blue belongs to the bosonic a and fermionic aa element, red to the bosonic b and fermionic bb element and green to the offdiagonal elements, i.e. the fermionic ab and ba element.

A.2.1 Perturbative Expansion of the Zeroth Order

The zeroth order of the single-particle Green's function, written in Eq. (2.80) and of the two-particle Green's function, which is the first line of Eq. (A.12) becomes in terms of Feynman diagrams

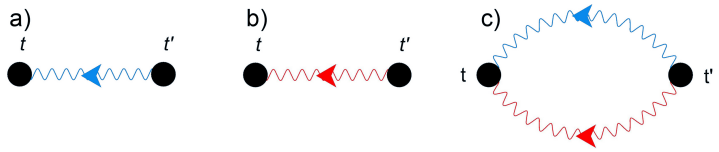

Fig. A.2.: Feynman diagrams of the zeroth order perturbative expansion. a) $\left\langle T_{\mathrm{C}}\left(a_t a_{t'}^{\dagger}\right)\right\rangle^{(0)}$, b) $\left\langle T_{\mathrm{C}}\left(b_t b_{t'}^{\dagger}\right)\right\rangle^{(0)}$ and c) $\left\langle T_{\mathrm{C}}\left(a_t a_{t'}^{\dagger} b_t b_{t'}^{\dagger}\right)\right\rangle^{(0)}$

A.2.2 Perturbative Expansion of the Second Order

The second order contribution of the single-particle Green's function, written in Eq. (2.84) and of the two-particle Green's function, which is shown in the second and third line of Eq. (A.12) becomes in terms of Feynman diagrams

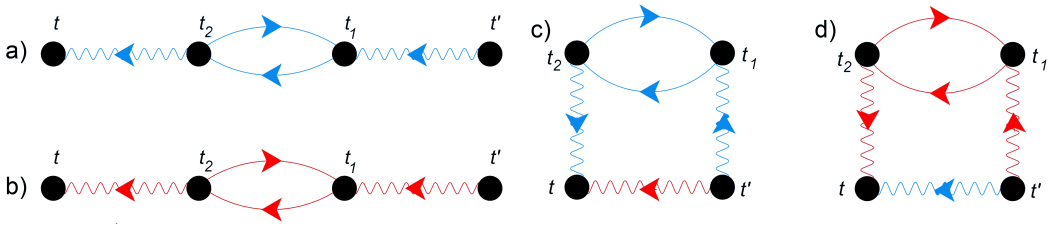

Fig. A.3.: Feynman diagrams of the second order perturbative expansion. a) $\left\langle T_{\mathrm{C}}\left(a_t a_{t'}^{\dagger}\right)\right\rangle^{(2)}$, b) $\left\langle T_{\mathrm{C}}\left(b_t b_{t'}^{\dagger}\right)\right\rangle^{(2)}$ and c), d) $\left\langle T_{\mathrm{C}}\left(a_t a_{t'}^{\dagger} b_t b_{t'}^{\dagger}\right)\right\rangle^{(2)}$

A.2.3 Perturbative Expansion of the Fourth Order of $\left\langle T_{\mathrm{C}}\left(a_t a_{t'}^{\dagger} b_t b_{t'}^{\dagger}\right)\right\rangle$

Regarding the fourth-order contributions of Eq. (A.12) the geometry of the Feynman diagrams representing the first until fourth paragraph are equal. Only the "color", i.e. the corresponding matrix element ij with $i, j \in \{a, b\}$, of the Green's function changes. We show the first and third paragraph as first and second line in Fig. (A.4). To obtain the second and fourth paragraph red and blue color have to change. The last eight integral of the last paragraph are also shown in Fig. (A.4)

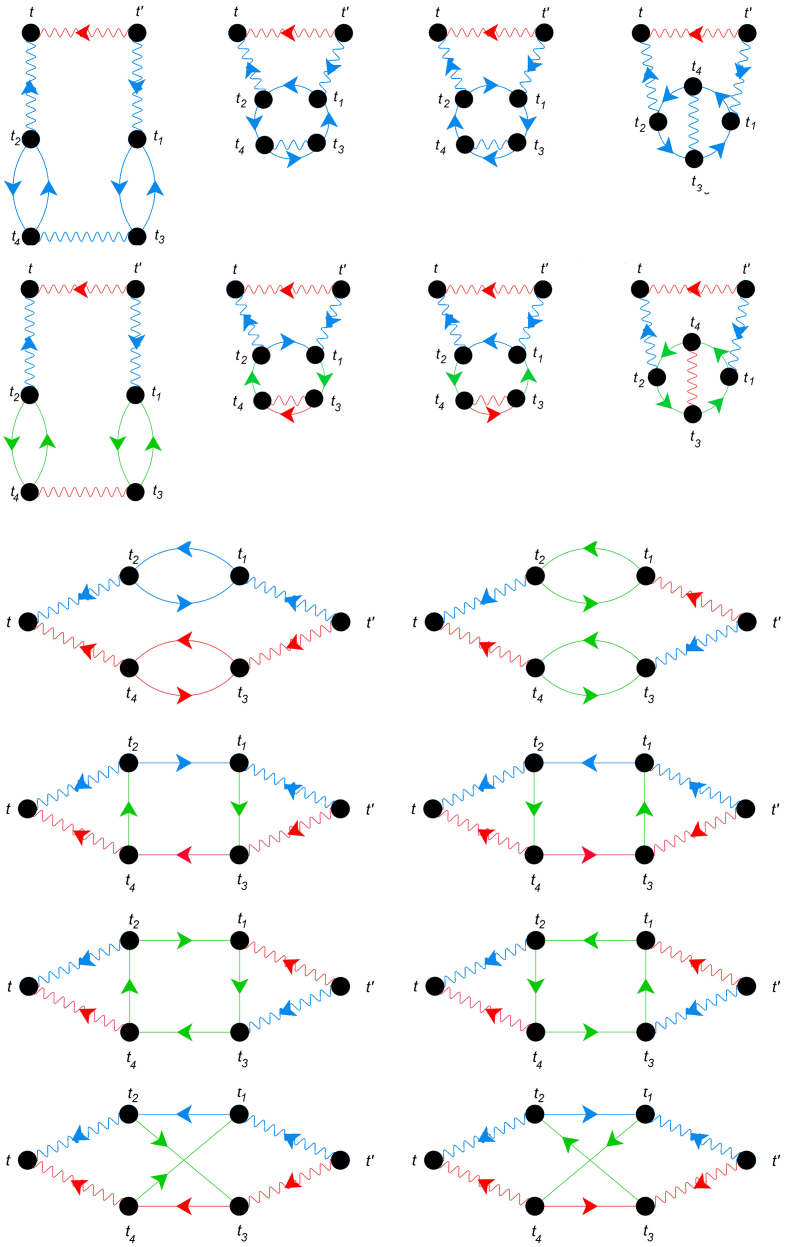

Fig. A.4.: Feynman diagrams of the fourth order perturbative expansion of the two-particle Green's function $\left\langle T_{\mathrm{C}}\left(a_t a_{t'}^{\dagger} b_t b_{t'}^{\dagger}\right)\right\rangle^{(4)}$.

A.2.4 Perturbative Expansion of the Fourth Order of $\left\langle T_{\mathrm{C}}\left(a_t a_t a_{t'}^{\dagger} a_{t'}^{\dagger}\right)\right\rangle$ and $\left\langle T_{\mathrm{C}}\left(b_t b_t b_{t'}^{\dagger} b_{t'}^{\dagger}\right)\right\rangle$

The non-zero contributions written in Eq. (A.14) and Eq. (A.16) have in Feynman diagrams the form shown in Fig. (A.5)

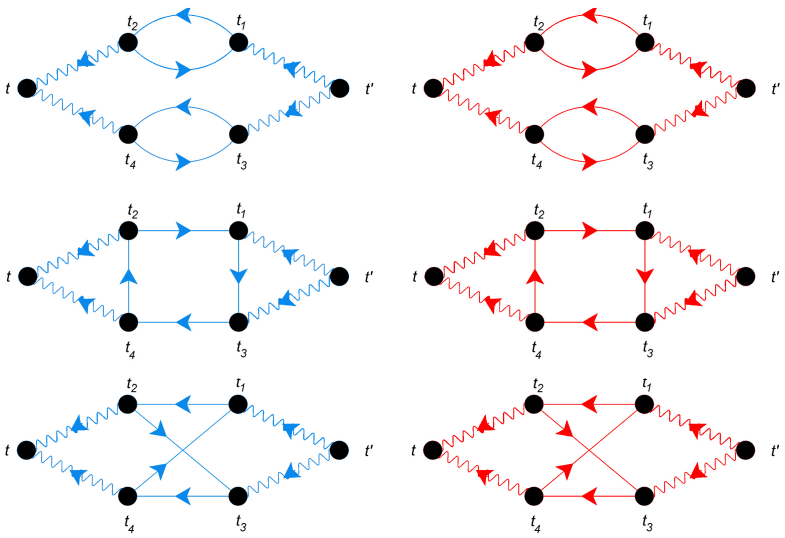

Fig. A.5.: Feynman diagrams nonzero contributions of the fourth order perturbative expansion of the two-particle Green's function $\left\langle T_{\mathrm{C}}\left(a_t a_t a_{t'}^{\dagger} a_{t'}^{\dagger}\right)\right\rangle$, left blue diagrams, and $\left\langle T_{\mathrm{C}}\left(b_t b_t b_{t'}^{\dagger} b_{t'}^{\dagger}\right)\right\rangle$, right red diagrams.

B RWA for Nonlinear Coupled Resonators

B.1 RWA for the Fundamental (1,1) Mode Interacting with Higher Harmonics

Regarding the interaction of the fundamental mode (1,1) with higher harmonics, or the description of the (1,1) mode in an effective septic potential, the equation of motion contains terms proportional to q^n from $n = 1$ up to $n = 7$. Using the canonical transformation of Eqs. (4.5) and (4.6) the RWA of these terms reads

$$e^{-i\omega_d t} q_1^n = e^{-i\omega_d t} \frac{1}{2^n} \left(u_1(t) e^{i\omega_d t} + u_1^*(t) e^{-i\omega_d t} \right)^n \tag{B.1}$$

$$= \frac{1}{2^n} e^{-i\omega_d t} \sum_{k=0}^{n} \binom{n}{k} \left(u_1 e^{i\omega_d t} \right)^k \left(u_1^* e^{-i\omega_d t} \right)^{n-k} \tag{B.2}$$

$$= \frac{1}{2^n} e^{-i\omega_d t} \sum_{k=0}^{n} \frac{n!}{k!(n-k)!} u_1^k (u_1^*)^{n-k} e^{i\omega_d t(k+k-n)} \qquad \text{(with n odd)} \tag{B.3}$$

Condition: $2k - n - 1 = 0 \rightarrow k = \dfrac{n+1}{2}$ (n odd $\rightarrow$ n-1 even)

$$\approx \frac{1}{2^n} \frac{n!}{\left(\frac{n+1}{2}\right)! \left(n - \frac{n+1}{2}\right)!} u^{\frac{n+1}{2}} (u^*)^{n - \frac{n+1}{2}} \tag{B.4}$$

$$= \frac{1}{2^n} \frac{n!}{\left(\frac{n-1}{2}\right)! \left(\frac{n+1}{2}\right)!} u^{\frac{n+1}{2}} (u^*)^{\frac{n-1}{2}} \tag{B.5}$$

$$= \frac{1}{2^n} \frac{n!}{\left(\frac{n-1}{2}\right)! \left(\frac{n+1}{2}\right)!} \left(|u|^2 \right)^{\frac{n-1}{2}} u \,. \tag{B.6}$$

The three occuring terms become then

$$n = 3 \;\rightarrow\; \frac{3}{8} |u|^2 u \tag{B.7}$$

$$n = 5 \;\rightarrow\; \frac{5}{16} |u|^4 u \tag{B.8}$$

$$n = 7 \;\rightarrow\; \frac{35}{128} |u|^6 u \tag{B.9}$$

B.2 RWA for the Direct Nonlinear Interaction

B.2.1 Derivation for the RWA of Higher Order q_1:

Besides the terms equivalent to those of the fundamental mode coupled to higher harmonics we get in addition the the mixed terms for $u_1(t)$

$$e^{i\omega_d t} q_1^2 q_2^2 = \frac{1}{16}\left(u_1^2 e^{i\omega_d t} + 2|u_1|^2 e^{-i\omega_d t} + (u_1^*)^2 e^{-3i\omega_d t}\right)\left(u_2^2 e^{3i\omega_d t} + 2|u_2|^2 + (u_2^*)^2 e^{-3i\omega_d t}\right) \tag{B.10}$$

$$\approx \frac{1}{16}(u_1^*)^2 u_2^2 \,. \tag{B.11}$$

Besides the terms similar to those of the fundamental mode coupled to higher harmonics we get in addition also mixed terms for $u_2(t)$

$$e^{-i\frac{3}{2}\omega_d t} q_1^3 q_2 = \frac{1}{16}\left(u_1^3 e^{3i\omega_d t} + 3|u_1|^2 u_1 e^{i\omega_d t} + 3|u_1|^2 u_1^* e^{-i\omega_d t} + (u_1^*)^3 e^{-3i\omega_d t}\right)\left(u_2 + u_2^* e^{-3i\omega_d t}\right) \tag{B.12}$$

$$\approx \frac{1}{16} u_1^3 u_2^* \tag{B.13}$$

Summarized all terms in the RWA transform

$$e^{-i\omega_d t} F\cos(\omega_d t) \approx \frac{F}{2}\,, \tag{B.14}$$

$$e^{-i\omega_d t} q_1 \approx \frac{u_1}{2}\,, \qquad e^{-i\omega_d t}\dot{q}_1 \approx i\frac{\omega_d}{2} u_1\,, \tag{B.15}$$

$$e^{-i\omega_d t} q_1^3 \approx \frac{3}{8}|u_1|^2 u_1\,, \qquad e^{i\omega_d t} q_1^2 q_2^2 \approx \frac{1}{16}(u_1^*)^2 u_2^2 \tag{B.16}$$

$$e^{-i\frac{3}{2}\omega_d t} q_2 \approx \frac{u_2}{2}\,, \qquad e^{-i\frac{3}{2}\omega_d t}\dot{q}_2 \approx i\frac{3}{4}\omega_d u_2 \tag{B.17}$$

$$e^{-i\frac{3}{2}\omega_d t} q_2^3 \approx \frac{3}{8}|u_2| u_2\,, \qquad e^{-i\frac{3}{2}\omega_d t} q_1^3 q_2 \approx \frac{1}{16} u_1^3 u_2^* \tag{B.18}$$

$$\tag{B.19}$$

B.3 RWA for Indirect Nonlinear Interaction

Canonical transformation and RWA for first resonator

The canonical transformation for q_1 has contributions $\propto u_1 e^{i\omega_d t}$ and $\propto u_3 e^{3i\omega_d t}$. Inserting the canonical transformation we get

$$\begin{aligned}\frac{dq_1^2}{dt} = &-\omega_1\left(\frac{u_1}{2}e^{i\omega_d t}+\frac{u_3}{2}e^{3i\omega_d t}+\text{c.c.}\right)-2\Gamma_1\left(i\omega_d\frac{u_1}{2}e^{i\omega_d t}+3i\omega_d\frac{u_3}{2}e^{3i\omega_d t}+\text{c.c.}\right)\\&+\frac{F}{2}\left(e^{i\omega_d t}+\text{c.c.}\right)-\gamma_1 q_1^3-\lambda q_1 q_2^2\end{aligned} \tag{B.20}$$

with the cubic term

$$\begin{aligned}q_1^3 =&\frac{1}{8}\Big[\left(u_1^3e^{3i\omega_d t}+3|u_1|^2u_1e^{i\omega_d t}+u_3^3e^{9i\omega_d t}+3|u_3|^2u_3e^{3i\omega_d t}+\text{c.c.}\right)\\&+3\left(u_1^2u_3e^{5i\omega_d t}+u_1^2u_3^*e^{-i\omega_d t}+2|u_1|^2u_3e^{3i\omega_d t}+2|u_1|^2u_3^*e^{-3i\omega_d t}\right.\\&\left.+(u_1^*)^2u_3e^{i\omega_d t}+(u_1^*)^2u_3^*e^{-5i\omega_d t}\right)\\&+3\left(u_1u_3^2e^{7i\omega_d t}+u_1^*u_3^2e^{5i\omega_d t}+2u_1|u_3|^2e^{i\omega_d t}+2u_1^*|u_3|^2e^{-i\omega_d t}\right.\\&\left.+u_1(u_3^*)^2e^{-5i\omega_d t}+u_1^*(u_3^*)^2e^{-7i\omega_d t}\right)\Big].\end{aligned} \tag{B.21}$$

Considering only terms rotating with ω_d or $3\omega_d$ this expression approximates to

$$\begin{aligned}q_1^3 \approxeq &\frac{1}{8}\left[u_1^3e^{3i\omega_d t}+3|u_1|^2u_1e^{i\omega_d t}+3|u_3|^2u_3e^{3i\omega_d t}+\text{c.c.}\right]\\&+\frac{3}{8}\left[(u_1^*)^2u_3e^{i\omega_d t}+2|u_1|^2u_3e^{3i\omega_d t}+2u_1|u_3|^2e^{i\omega_d t}+\text{c.c.}\right].\end{aligned} \tag{B.22}$$

The mixed cubic term reads

$$\begin{aligned}q_1q_2^2 =&\frac{1}{8}\Big[u_1v^2e^{5i\omega_d t}+u_1^*v^2e^{3i\omega_d t}+u_3v^2e^{7i\omega_d t}+u_3^*v^2e^{i\omega_d t}\\&+2u_1|v|^2e^{i\omega_d t}+2u_1^*|v|^2e^{-i\omega_d t}+2u_3|v|^2e^{3i\omega_d t}+2u_3^*|v|^2e^{-3i\omega_d t}\\&+u_1(v^*)^2e^{-3i\omega_d t}+u_1^*(v^*)^2e^{-5i\omega_d t}+u_3(v^*)^2e^{-i\omega_d t}+u_3^*(v^*)^2e^{-7i\omega_d t}\Big].\end{aligned} \tag{B.23}$$

Considering only terms rotating with ω_d or $3\omega_d$ this expression approximates to

$$q_1q_2^2 \approxeq \frac{1}{8}\left[2u_1|v|^2e^{i\omega_d t}+2u_3|v^2|e^{3i\omega_d t}+u_3^*v^2e^{i\omega_d t}+u_1^*v^2e^{3i\omega_d t}+\text{c.c.}\right]. \tag{B.24}$$

For the order $n=1$ we get for $\ddot{q}_1$

$$-\omega_d^2\frac{u_1}{2} = -\omega_1^2\frac{u_1}{2}-2i\omega_d\Gamma_1\frac{u_1}{2}+\frac{F}{2}-\frac{\gamma_1}{8}\left[3|u_1|^2u_1+3(u_1^*)^2u_3+6u_1|u_3|^2\right]-\frac{\lambda}{8}\left[u_3^*v^2+2u_1|v|^2\right] \tag{B.25}$$

$$0 = \left(\left(\omega_d^2-\omega_1^2\right)-2i\omega_d\Gamma_1\right)u_1+F-\frac{3}{4}\gamma_1\left[|u_1|^2u_1+(u_1^*)^2u_3+2u_1|u_3|^2\right]-\frac{\lambda}{4}\left[u_3^*v^2+2u_1|v|^2\right] \tag{B.26}$$

For the order $n = 3$ we get for $\ddot{q}_1$

$$-9\omega_d^2\frac{u_3}{2} = -\omega_1^2\frac{u_3}{2} - 6i\omega_d\Gamma_1\frac{u_3}{2} - \frac{\gamma_1}{8}\left[u_1^3 + 3|u_3|^2u_3 + 6|u_1|^2u_3\right] - \frac{\lambda}{8}\left[u_1^*v^2 + 2|v^2|u_3\right] \tag{B.27}$$

$$0 = \left(\left(9\omega_d^2 - \omega_1^2\right) - 6i\omega_d\Gamma_1\right)u_3 - \frac{\gamma_1}{4}\left[u_1^3 + 3|u_3|^2u_3 + 6|u_1|^2u_3\right] - \frac{\lambda}{4}\left[u_1^*v^2 + 2|v^2|u_3\right] \tag{B.28}$$

Canonical transformation and RWA for second resonator

The canonical transformation for q_2 leads to

$$\begin{aligned}\ddot{q}_2 = &-\omega_2^2\left(\frac{v}{2}e^{2i\omega_d t} + \text{c.c.}\right) - 4i\omega_d\Gamma_2\left(\frac{v}{2}e^{2i\omega_d t} + \text{c.c.}\right)\\ &-\frac{\gamma_2}{8}\left[v^3e^{6i\omega_d t} + 3|v|^2ve^{2i\omega_d t} + \text{c.c.}\right] - \lambda q_1^2q_2\end{aligned} \tag{B.29}$$

where the cubic term becomes

$$\begin{aligned}q_1^2q_2 = &\frac{1}{8}\Big[\left(u_1^2e^{4i\omega_d t} + 2|u_1|^2e^{2i\omega_d t} + (u_1^*)^2\right)v + \left(u_3^2e^{8i\omega_d t} + 2|u_3|^2e^{2i\omega_d t} + (u_3^*)^2e^{-4i\omega_d t}\right)v\\ &+\left(u_1^2 + 2|u_1|^2e^{-2i\omega_d t} + (u_1^*)^2e^{-4i\omega_d t}\right)v^* + \left(u_3^2e^{4i\omega_d t} + 2|u_3|^2e^{-2i\omega_d t} + (u_3^*)^2e^{-8i\omega_d t}\right)v^*\\ &+2\left(u_1u_3e^{6i\omega_d t} + u_1^*u_3e^{4i\omega_d t} + u_1u_3^* + u_1^*u_3^*e^{-2i\omega_d t}\right)v\\ &+2\left(u_1u_3e^{2i\omega_d t} + u_1^*u_3 + u_1u_3^*e^{-4i\omega_d t} + u_1^*u_3^*e^{-6i\omega_d t}\right)v^*\Big]\end{aligned} \tag{B.30}$$

Considering only terms rotating with $2\omega_d$ this expression approximates to

$$q_1^2q_2 = \frac{1}{8}\left(2|u_1|^2v + 2|u_3|^2v + u_1u_3v^* + \text{c.c.}\right)e^{2i\omega_d t} \tag{B.31}$$

For the order $n = 2$ we get for $\ddot{q}_2$

$$-4\omega_d^2\frac{v}{2} = -\omega_2^2\frac{v}{2} - 4i\omega_d\Gamma_2\frac{v}{2} - \frac{3}{8}\gamma_2|v^2|v - \frac{\lambda}{8}\left[2\left(|u_1|^2 + |u_3|^2\right)v + 2u_1u_3v^*\right] \tag{B.32}$$

$$0 = \left(\left(4\omega_d^2 - \omega_2^2\right) - 4i\omega_d\Gamma_2\right)v - \frac{3\gamma_2}{4}|v^2|v - \frac{\lambda}{2}\left[\left(|u_1|^2 + |u_3|^2\right)v + u_1u_3v^*\right] \tag{B.33}$$

C

Detailed Figures for the Nonlinear Coupled, Parametrically Driven Duffing Resonators

C.1 Solution Pairs Two Driven Resonators

Solving the coupled equations we obtain always pairs of solutions. We show exemplary, for one set of parameters, which pairs, i.e. which branches belong together. We check stable and unstable solutions, but only those, where both amplitude are finite. We get five different solution pairs, that we color in red, green, cyan, blue and magenta. The lighter color belongs to the amplitude $\bar{z}_1$ of the first resonator while the darker color belong to the amplitude $\bar{z}_2$ of the second resonator.

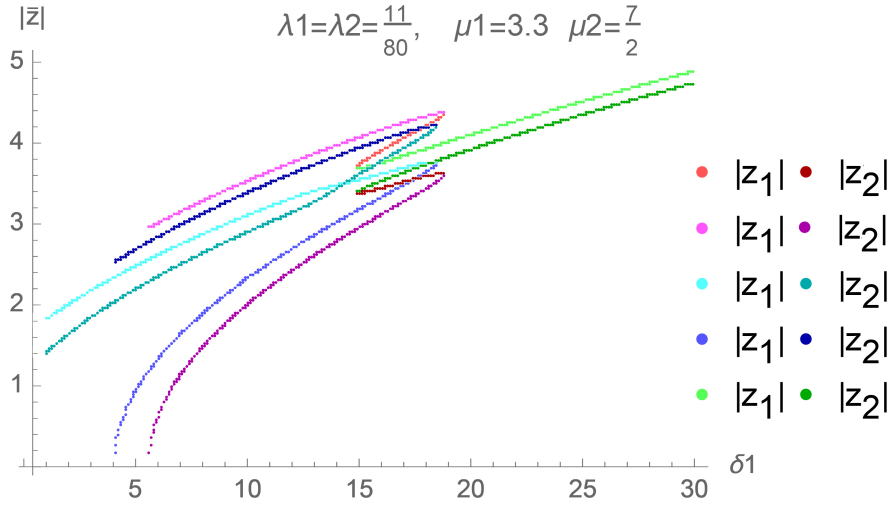

Fig. C.1.: Solution pairs of the resonators. We have five different solution pairs, i.e. red, green, cyan, blue and magenta. The lighter color belongs to the amplitude of the first resonator $\bar{z}_1$, the darker color belongs to the amplitude of the second resonator $\bar{z}_2$

C.2 Evolution of the Bifurcation

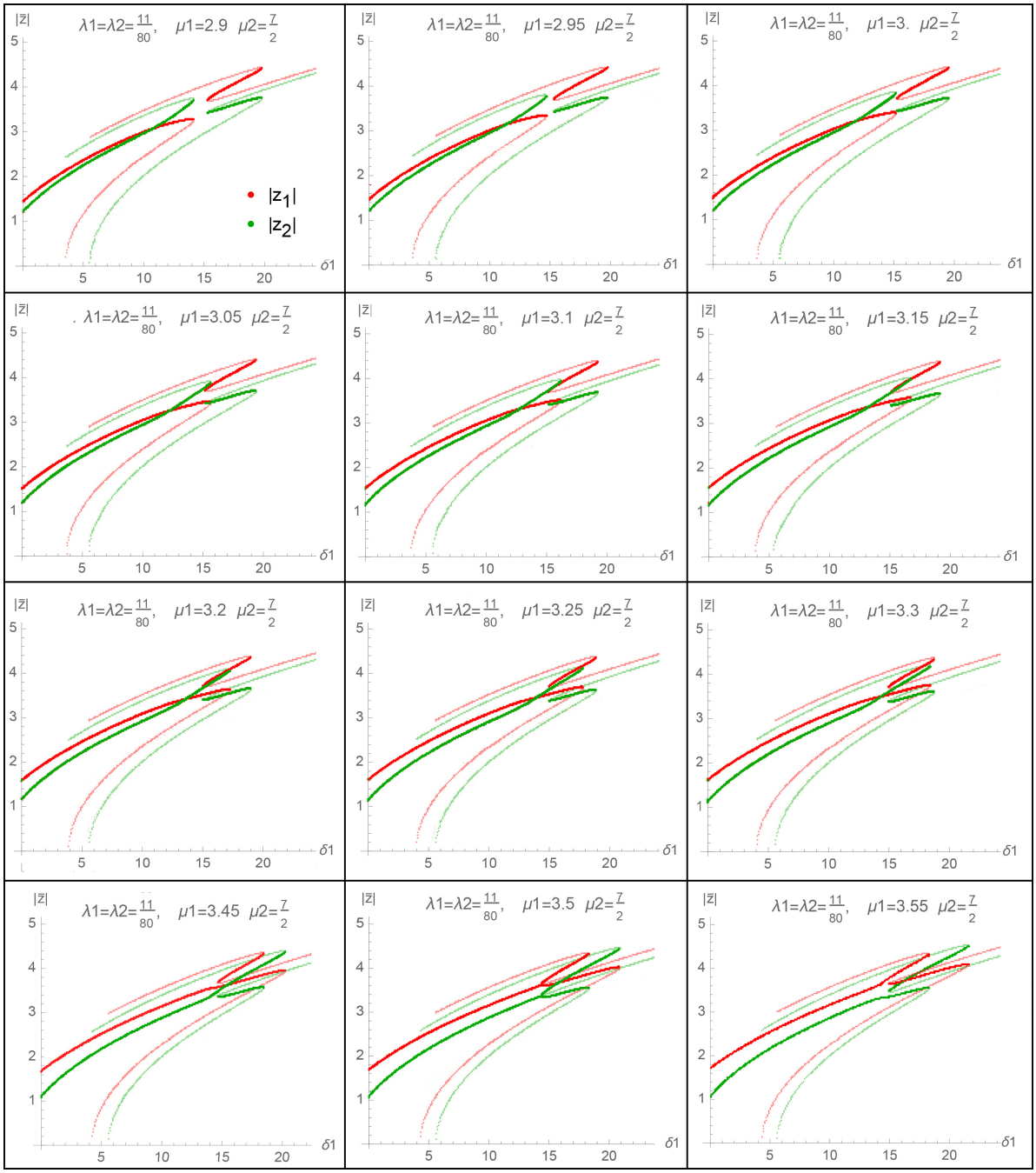

Fig. C.2.: Detailed evolution how the bifurcation is built. We fixed the parameters $\mu_2 = 3.5$, $\Gamma_1 = \Gamma_2$, $\gamma_1 = \gamma_2$, $\lambda = \frac{33}{80}\gamma_1$ and therefore $\lambda_i = \frac{\lambda}{3\gamma_i}\frac{\Gamma_i}{\Gamma_j} = \frac{11}{80}$. Then we increased the force of the first resonator with a step size of 0.05 until the bifurcation appear and slightly above. Bold curves correspond to stable solutions while the other ones are unstable.

Bibliography

[1]A. W. Holleitner, C. R. Decker, H. Qin, K. Eberl, and R. H. Blick. “Coherent Coupling of Two Quantum Dots Embedded in an Aharonov-Bohm Interferometer”. In: *Phys. Rev. Lett.* 87 (25 Nov. 2001), p. 256802.

[2]Martin Sigrist, Thomas Ihn, Klaus Ensslin, Matthias Reinwald, and Werner Wegscheider. “Coherent Probing of Excited Quantum Dot States in an Interferometer”. In: *Phys. Rev. Lett.* 98 (3 Jan. 2007), p. 036805.

[3]T Hatano, T Kubo, Y Tokura, et al. “Aharonov-Bohm Oscillations Changed by Indirect Interdot Tunneling via Electrodes in Parallel-Coupled Vertical Double Quantum Dots”. In: *Phys. Rev. Lett.* 106.7 (Feb. 2011), p. 076801.

[4]Géraldine Haack, Heidi Förster, and Markus Büttiker. “Parity detection and entanglement with a Mach-Zehnder interferometer”. In: *Phys. Rev. B* 82 (15 Oct. 2010), p. 155303.

[5]Yang Ji, Yunchul Chung, D Sprinzak, et al. “An electronic Mach–Zehnder interferometer”. In: *Nature* 422.6930 (Mar. 2003), pp. 415–418.

[6]R Schuster, E Buks, M Heiblum, et al. “Phase measurement in a quantum dot via a double-slit interference experiment”. In: *Nature* 385.6615 (Jan. 1997), pp. 417–420.

[7]E Bocquillon, V Freulon, J M Berroir, et al. “Coherence and Indistinguishability of Single Electrons Emitted by Independent Sources”. In: *Science* 339.6123 (Mar. 2013), pp. 1054–1057.

[8]Alexandre Blais, Arne L Grimsmo, S M Girvin, and Andreas Wallraff. “Circuit quantum electrodynamics”. In: *Rev. Mod. Phys.* 93.2 (May 2021), p. 025005.

[9]Max Hofheinz, E M Weig, M Ansmann, et al. “Generation of Fock states in a superconducting quantum circuit”. In: *Nature* 454.7202 (July 2008), pp. 310–314.

[10]Max Hofheinz, H Wang, M Ansmann, et al. “Synthesizing arbitrary quantum states in a superconducting resonator”. In: *Nature* 459.7246 (May 2009), pp. 546–549.

[11]H. Wang, Matteo Mariantoni, Radoslaw C. Bialczak, et al. “Deterministic Entanglement of Photons in Two Superconducting Microwave Resonators”. In: *Phys. Rev. Lett.* 106 (6 Feb. 2011), p. 060401.

[12]Eva Zakka-Bajjani, François Nguyen, Minhyea Lee, et al. “Quantum superposition of a single microwave photon in two different ’colour’ states”. In: *Nat. Phys.* 7.8 (Aug. 2011), pp. 599–603.

[13]François Nguyen, Eva Zakka-Bajjani, Raymond W. Simmonds, and José Aumentado. “Quantum Interference between Two Single Photons of Different Microwave Frequencies”. In: *Phys. Rev. Lett.* 108 (16 Apr. 2012), p. 163602.

[14]C. Eichler, D. Bozyigit, C. Lang, et al. “Observation of Two-Mode Squeezing in the Microwave Frequency Domain”. In: *Phys. Rev. Lett.* 107 (11 Sept. 2011), p. 113601.

[15]E. Flurin, N. Roch, F. Mallet, M. H. Devoret, and B. Huard. “Generating Entangled Microwave Radiation Over Two Transmission Lines”. In: *Phys. Rev. Lett.* 109 (18 Oct. 2012), p. 183901.

[16]C Lang, C Eichler, L Steffen, et al. “Correlations, indistinguishability and entanglement in Hong–Ou–Mandel experiments at microwave frequencies”. In: *Nat. Phys.* 9.6 (June 2013), pp. 345–348.

[17]Chen Wang, Yvonne Y Gao, Philip Reinhold, et al. “A Schrödinger cat living in two boxes”. In: *Science* 352.6289 (May 2016), pp. 1087–1091.

[18]A. Peugeot, G. Ménard, S. Dambach, et al. “Generating Two Continuous Entangled Microwave Beams Using a dc-Biased Josephson Junction”. In: *Phys. Rev. X* 11 (3 July 2021), p. 031008.

[19]J R Petta, A C Johnson, J M Taylor, et al. “Coherent Manipulation of Coupled Electron Spins in Semiconductor Quantum Dots”. In: *Science* 309.5744 (Sept. 2005), pp. 2180–2184.

[20]F H L Koppens, C Buizert, K J Tielrooij, et al. “Driven coherent oscillations of a single electron spin in a quantum dot”. In: *Nature* 442.7104 (Aug. 2006), pp. 766–771.

[21]K C Nowack, F H L Koppens, Yu V Nazarov, and L M K Vandersypen. “Coherent Control of a Single Electron Spin with Electric Fields”. In: *Science* 318.5855 (Nov. 2007), pp. 1430–1433.

[22]Guido Burkard, Michael J Gullans, Xiao Mi, and Jason R Petta. “Superconductor–semiconductor hybrid-circuit quantum electrodynamics”. In: *Nat. Rev. Phys.* 2.3 (Mar. 2020), pp. 129–140.

[23]K D Petersson, L W McFaul, M D Schroer, et al. “Circuit quantum electrodynamics with a spin qubit”. In: *Nature* 490.7420 (Nov. 2012), pp. 380–383.

[24]C. Rössler, D. Oehri, O. Zilberberg, et al. “Transport Spectroscopy of a Spin-Coherent Dot-Cavity System”. In: *Phys. Rev. Lett.* 115 (16 Nov. 2015), p. 166603.

[25]J J Viennot, M C Dartiailh, A Cottet, and T Kontos. “Coherent coupling of a single spin to microwave cavity photons.” In: *Science* 349.6246 (July 2015), pp. 408–411.

[26]L E Bruhat, J J Viennot, M C Dartiailh, et al. “Cavity Photons as a Probe for Charge Relaxation Resistance and Photon Emission in a Quantum Dot Coupled to Normal and Superconducting Continua”. In: *Phys. Rev. X* 6.2 (May 2016), p. 021014.

[27]David Hagenmüller, Stefan Schütz, Johannes Schachenmayer, Claudiu Genes, and Guido Pupillo. “Cavity-assisted mesoscopic transport of fermions: Coherent and dissipative dynamics”. In: *Phys. Rev. B* 97.20 (May 2018), p. 205303.

[28]Mircea Trif and Pascal Simon. “Braiding of Majorana Fermions in a Cavity”. In: *Phys. Rev. Lett.* 122 (23 June 2019), p. 236803.

[29]W. Khan, P.P. Potts, S. Lehmann, et al. “Efficient and continuous microwave photoconversion in hybrid cavity-semiconductor nanowire double quantum dot diodes”. In: *Nat. Commun.* 12 (2021), p. 5130.

[30]Audrey Cottet, Zaki Leghtas, and Takis Kontos. “Theory of interactions between cavity photons induced by a mesoscopic circuit”. In: *Phys. Rev. B* 102 (15 Nov. 2020), p. 155105.

[31]Olesia Dmytruk, Mircea Trif, Christophe Mora, and Pascal Simon. “Out-of-equilibrium quantum dot coupled to a microwave cavity”. In: *Phys. Rev. B* 93 (7 Feb. 2016), p. 075425.

[32]Jincheng Lu, Rongqian Wang, Jie Ren, Manas Kulkarni, and Jian-Hua Jiang. “Quantum-dot circuit-QED thermoelectric diodes and transistors”. In: *Phys. Rev. B* 99 (3 Jan. 2019), p. 035129.

[33]Bibek Bhandari, Paolo Andrea Erdman, Rosario Fazio, Elisabetta Paladino, and Fabio Taddei. “Thermal rectification through a nonlinear quantum resonator”. In: *Phys. Rev. B* 103 (15 Apr. 2021), p. 155434.

[34]X Mi, J V Cady, D M Zajac, P W Deelman, and J R Petta. “Strong coupling of a single electron in silicon to a microwave photon”. In: *Science* 355.6321 (Dec. 2016), aal2469–158.

[35]A Stockklauser, P Scarlino, J V Koski, et al. “Strong Coupling Cavity QED with Gate-Defined Double Quantum Dots Enabled by a High Impedance Resonator”. In: *Phys. Rev. X* 7.1 (Mar. 2017), p. 011030.

[36]X Mi, M Benito, S Putz, et al. “A coherent spin–photon interface in silicon”. In: *Nature* 555.7698 (Mar. 2018), pp. 599–603.

[37]P. Scarlino, D. J. van Woerkom, A. Stockklauser, et al. “All-Microwave Control and Dispersive Readout of Gate-Defined Quantum Dot Qubits in Circuit Quantum Electrodynamics”. In: *Phys. Rev. Lett.* 122 (20 May 2019), p. 206802.

[38]J. Weiner and P.-T. Ho. *Light-Matter Interaction Volume 1 Fundamentals and Applications*. 1st ed. Wiley, 2003.

[39]M. O. Scully and M. S. Zubairy. *Quantum Optics*. 2nd ed. Cambridge University Press, 1997.

[40]M. Kira and S. W. Koch. *Semiconductor Quantum Optics*. 1st ed. Cambridge University Press, 2012.

[41]W. Vogel and D.-G. Welsch. *Quantum Optics*. 3rd ed. Wiley-VCH verlag, 2006.

[42]Daniel Loss and David P. DiVincenzo. “Quantum computation with quantum dots”. In: *Phys. Rev. A* 57 (1 Jan. 1998), pp. 120–126.

[43]Alberto Mercurio, Vincenzo Macri, Chris Gustin, et al. “Regimes of cavity QED under incoherent excitation: From weak to deep strong coupling”. In: *Phys. Rev. Research* 4 (2 Apr. 2022), p. 023048.

[44]Yimin Wang and ing Yan Haw. “Bridging the gap between the Jaynes–Cummings and Rabi models using an intermediate rotating wave approximation”. In: *Physics Letters A* 370 (8 2015), pp. 779–786.

[45]E. M Purcell. “Spontaneous Emission Probabilities at Radio Frequencies”. In: *Confined Electrons and Photons: New Physics and Applications*. Ed. by Elias Burstein and Claude Weisbuch. Boston, MA: Springer US, 1995, pp. 839–839.

[46]Changsuk Noh. “Emission of single photons in the weak coupling regime of the Jaynes Cummings model”. In: *Scientific Reports* 10 (1 Sept. 2020), p. 16076.

[47]T. Frey, P. J. Leek, M. Beck, et al. “Dipole Coupling of a Double Quantum Dot to a Microwave Resonator”. In: *Phys. Rev. Lett.* 108 (4 Jan. 2012), p. 046807.

[48]K. D. Petersson L. W. McFaul M. D. Schroer M. Jung J. M. Taylor A. A. Houck J. R. Petta. "Circuit quantum electrodynamics with a spin qubit". In: *Nature* 490 (2012), pp. 380–383.

[49]Guang-Wei Deng, Da Wei, Shu-Xiao Li, et al. "Coupling Two Distant Double Quantum Dots with a Microwave Resonator". In: *Nano Letters* 15.10 (2015), pp. 6620–6625.

[50]T. Kontos J. J. Viennot M. C. Dartiailh A. Cottet. "Coherent coupling of a single spin to microwave cavity photons". In: *Science* 349 (6246 2015), pp. 408–411.

[51]P. Meystre and M. Sargent III. *Elements of Quantum Optics*. 3rd ed. Springer-Verlag, 1998.

[52]Y. Kaluzny, P. Goy, M. Gross, J. M. Raimond, and S. Haroche. "Observation of Self-Induced Rabi Oscillations in Two-Level Atoms Excited Inside a Resonant Cavity: The Ringing Regime of Superradiance". In: *Phys. Rev. Lett.* 51 (13 Sept. 1983), pp. 1175–1178.

[53]M. Brune, F. Schmidt-Kaler, A. Maali, et al. "Quantum Rabi Oscillation: A Direct Test of Field Quantization in a Cavity". In: *Phys. Rev. Lett.* 76 (11 Mar. 1996), pp. 1800–1803.

[54]J. M. Raimond, M. Brune, and S. Haroche. "Manipulating quantum entanglement with atoms and photons in a cavity". In: *Rev. Mod. Phys.* 73 (3 Aug. 2001), pp. 565–582.

[55]Alexandre Blais, Ren-Shou Huang, Andreas Wallraff, S. M. Girvin, and R. J. Schoelkopf. "Cavity quantum electrodynamics for superconducting electrical circuits: An architecture for quantum computation". In: *Phys. Rev. A* 69 (6 June 2004), p. 062320.

[56]L. E Bruhat, T. Cubaynes, J. J. Viennot, et al. "Circuit QED with a quantum-dot charge qubit dressed by Cooper pairs". In: *Phys. Rev. B* 98 (15 Oct. 2018), p. 155313.

[57]N. Samkharadze, G. Zheng, N. Kalhor, et al. "Strong spin-photon coupling in silicon". In: *Science* 359 (6380 2018), pp. 1123–1127.

[58]A. J. Landig, J. V. Koski, P. Scarlino, et al. "Coherent spin–photon coupling using a resonant exchange qubit". In: *Nature* 560 (2018), pp. 179–184.

[59]P. Scarlino, D. J. van Woerkom, U. C. Mendes, et al. "Coherent microwave-photon-mediated coupling between a semiconductor and a superconducting qubit". In: *Nature Commucations* 10 (2019), p. 3011.

[60]F. Valmorra, K. Yoshida, L. C. Contamin, et al. "Vacuum-field-induced THz transport gap in a carbon nanotube quantum dot". In: *Nature Communications* 12 (2021), p. 5490.

[61]W. P. Bowen and G. J. Milburn. *Quantum Opotomechanics*. 1st ed. CRC Press, 2016.

[62]T. Niemczyk, F. Deppe, H. Huebl, et al. "Circuit quantum electrodynamics in the ultrastrong-coupling regime". In: *Nature Phys.* 6 (10 2010), pp. 772–776.

[63]Markus Aspelmeyer, Tobias J. Kippenberg, and Florian Marquardt. "Cavity optomechanics". In: *Rev. Mod. Phys.* 86 (4 Dec. 2014), pp. 1391–1452.

[64]Xin-You Lü, Ying Wu, J. R. Johansson, et al. "Squeezed Optomechanics with Phase-Matched Amplification and Dissipation". In: *Phys. Rev. Lett.* 114 (9 Mar. 2015), p. 093602.

[65]P. Rabl. "Photon Blockade Effect in Optomechanical Systems". In: *Phys. Rev. Lett.* 107 (6 Aug. 2011), p. 063601.

[66]A. Nunnenkamp, K. Børkje, and S. M. Girvin. "Single-Photon Optomechanics". In: *Phys. Rev. Lett.* 107 (6 Aug. 2011), p. 063602.

[67]Fumiki Yoshihara, Tomoko Fuse, Sahel Ashhab, et al. “Superconducting qubit–oscillator circuit beyond the ultrastrong-coupling regime”. In: *Nature Physics* 13 (2017), pp. 44–47.

[68]M. Halbhuber, J. Mornhinweg, V. Zeller, et al. “Non-adiabatic stripping of a cavity field from electrons in the deep-strong coupling regime”. In: *Nature Photonics* 14 (2020), pp. 675–679.

[69]Andreas Bayer, Marcel Pozimski, Simon Schambeck, et al. “Terahertz Light–Matter Interaction beyond Unity Coupling Strength”. In: *Nano Letters* 17.10 (2017), pp. 6340–6344.

[70]Yuto Ashida, Ataç Imamoglu, and Eugene Demler. “Cavity Quantum Electrodynamics at Arbitrary Light-Matter Coupling Strengths”. In: *Phys. Rev. Lett.* 126 (15 Apr. 2021), p. 153603.

[71]Yuying Guo. “Introduction to quantum entanglement”. In: *AIP Conference Proceedings* 2066.1 (2019), p. 020009.

[72]Charles H. Bennett and Gilles Brassard. “Quantum cryptography: Public key distribution and coin tossing”. In: *Theoretical Computer Science* 560 (2014). Theoretical Aspects of Quantum Cryptography – celebrating 30 years of BB84, pp. 7–11.

[73]Artur K. Ekert. “Quantum cryptography based on Bell’s theorem”. In: *Phys. Rev. Lett.* 67 (6 Aug. 1991), pp. 661–663.

[74]Charles H. Bennett, Gilles Brassard, and N. David Mermin. “Quantum cryptography without Bell’s theorem”. In: *Phys. Rev. Lett.* 68 (5 Feb. 1992), pp. 557–559.

[75]Juan Yin, Yu-Huai Li, Sheng-Kai Liao, et al. “Entanglement-based secure quantum cryptography over 1,120 kilometres”. In: *Nature* 582.7813 (June 2020), pp. 501–505.

[76]Charles H. Bennett, Gilles Brassard, Claude Crépeau, et al. “Teleporting an unknown quantum state via dual classical and Einstein-Podolsky-Rosen channels”. In: *Phys. Rev. Lett.* 70 (13 Mar. 1993), pp. 1895–1899.

[77]Abhishek Parakh. “Quantum teleportation with one classical bit”. In: *Scientific Reports* 12.1 (Mar. 2022), p. 3392.

[78]H. J. Kimble. “The quantum internet”. In: *Nature* 453.7198 (June 2008), pp. 1023–1030.

[79]Sebastian Ecker, Frédéric Bouchard, Lukas Bulla, et al. “Overcoming Noise in Entanglement Distribution”. In: *Phys. Rev. X* 9 (4 Nov. 2019), p. 041042.

[80]Takafumi Ono, Ryo Okamoto, and Shigeki Takeuchi. “An entanglement-enhanced microscope”. In: *Nature Communications* 4.1 (Sept. 2013), p. 2426.

[81]B. B. Blinov, D. L. Moehring, L.-. M. Duan, and C. Monroe. “Observation of entanglement between a single trapped atom and a single photon”. In: *Nature* 428.6979 (Mar. 2004), pp. 153–157.

[82]Jürgen Volz, Markus Weber, Daniel Schlenk, et al. “Observation of Entanglement of a Single Photon with a Trapped Atom”. In: *Phys. Rev. Lett.* 96 (3 Jan. 2006), p. 030404.

[83]A. Stute, B. Casabone, P. Schindler, et al. “Tunable ion–photon entanglement in an optical cavity”. In: *Nature* 485.7399 (May 2012), pp. 482–485.

[84]E. Togan, Y. Chu, A. S. Trifonov, et al. “Quantum entanglement between an optical photon and a solid-state spin qubit”. In: *Nature* 466.7307 (Aug. 2010), pp. 730–734.

[85]Kristiaan De Greve, Leo Yu, Peter L. McMahon, et al. “Quantum-dot spin–photon entanglement via frequency downconversion to telecom wavelength”. In: *Nature* 491.7424 (Nov. 2012), pp. 421–425.

[86]W. B. Gao, P. Fallahi, E. Togan, J. Miguel-Sanchez, and A. Imamoglu. “Observation of entanglement between a quantum dot spin and a single photon”. In: *Nature* 491.7424 (Nov. 2012), pp. 426–430.

[87]Jens Koch, Terri M. Yu, Jay Gambetta, et al. “Charge-insensitive qubit design derived from the Cooper pair box”. In: *Phys. Rev. A* 76 (4 Oct. 2007), p. 042319.

[88]C. Eichler, C. Lang, J. M. Fink, et al. “Observation of Entanglement between Itinerant Microwave Photons and a Superconducting Qubit”. In: *Phys. Rev. Lett.* 109 (24 Dec. 2012), p. 240501.

[89]P. Kurpiers, P. Magnard, T. Walter, et al. “Deterministic quantum state transfer and remote entanglement using microwave photons”. In: *Nature* 558.7709 (May 2018), pp. 264–267.

[90]M. R. Delbecq, L. E. Bruhat, J. J. Viennot, et al. “Photon-mediated interaction between distant quantum dot circuits”. In: *Nature Communications* 4.1 (Jan. 2013), p. 1400.

[91]Brian Vlastakis, Gerhard Kirchmair, Zaki Leghtas, et al. “Deterministically Encoding Quantum Information Using 100-Photon Schrödinger Cat States”. In: *Science* 342.6158 (2013), pp. 607–610. eprint: `https://www.science.org/doi/pdf/10.1126/science.1243289`.

[92]Z. Leghtas, S. Touzard, I. M. Pop, et al. “Confining the state of light to a quantum manifold by engineered two-photon loss”. In: *Science* 347.6224 (2015), pp. 853–857. eprint: `https://www.science.org/doi/pdf/10.1126/science.aaa2085`.

[93]Samuel L. Braunstein and Peter van Loock. “Quantum information with continuous variables”. In: *Rev. Mod. Phys.* 77 (2 June 2005), pp. 513–577.

[94]Christian Weedbrook, Stefano Pirandola, Raúl Garcia-Patrón, et al. “Gaussian quantum information”. In: *Rev. Mod. Phys.* 84 (2 May 2012), pp. 621–669.

[95]R I A Davis, R Delbourgo, and P D Jarvis. “Covariance, correlation and entanglement”. In: *Journal of Physics A: Mathematical and General* 33.9 (Feb. 2000), pp. 1895–1914.

[96]J. S. Bell. “On the Einstein Podolsky Rosen paradox”. In: *Physics Physique Fizika* 1 (3 Nov. 1964), pp. 195–200.

[97]A. Einstein, B. Podolsky, and N. Rosen. “Can Quantum-Mechanical Description of Physical Reality Be Considered Complete?” In: *Phys. Rev.* 47 (10 May 1935), pp. 777–780.

[98]Mark Hillery and M. Suhail Zubairy. “Entanglement Conditions for Two-Mode States”. In: *Phys. Rev. Lett.* 96 (5 Feb. 2006), p. 050503.

[99]Lu-Ming Duan, G. Giedke, J. I. Cirac, and P. Zoller. “Inseparability Criterion for Continuous Variable Systems”. In: *Phys. Rev. Lett.* 84 (12 Mar. 2000), pp. 2722–2725.

[100]Stefano Mancini, Vittorio Giovannetti, David Vitali, and Paolo Tombesi. “Entangling Macroscopic Oscillators Exploiting Radiation Pressure”. In: *Phys. Rev. Lett.* 88 (12 Mar. 2002), p. 120401.

[101]Vittorio Giovannetti, Stefano Mancini, David Vitali, and Paolo Tombesi. “Characterizing the entanglement of bipartite quantum systems”. In: *Phys. Rev. A* 67 (2 Feb. 2003), p. 022320.

[102]M. G. Raymer, A. C. Funk, B. C. Sanders, and H. de Guise. “Separability criterion for separate quantum systems”. In: *Phys. Rev. A* 67 (5 May 2003), p. 052104.

[103]S. Wölk, M. Huber, and O. Gühne. “Unified approach to entanglement criteria using the Cauchy-Schwarz and Hölder inequalities”. In: *Phys. Rev. A* 90.2 (Aug. 2014), p. 022315.

[104]K. V. Kheruntsyan, J.-C. Jaskula, P. Deuar, et al. “Violation of the Cauchy-Schwarz Inequality with Matter Waves”. In: *Phys. Rev. Lett.* 108 (26 June 2012), p. 260401.

[105]J. R. M. de Nova, F. Sols, and I. Zapata. “Violation of Cauchy-Schwarz inequalities by spontaneous Hawking radiation in resonant boson structures”. In: *Phys. Rev. A* 89 (4 Apr. 2014), p. 043808.

[106]R. J. Lewis-Swan and K. V. Kheruntsyan. “Proposal for demonstrating the Hong–Ou–Mandel effect with matter waves”. In: *Nature Communications* 5.1 (Apr. 2014), p. 3752.

[107]C. Sánchez Muñoz, E. del Valle, C. Tejedor, and F. P. Laussy. “Violation of classical inequalities by photon frequency filtering”. In: *Phys. Rev. A* 90 (5 Nov. 2014), p. 052111.

[108]T Wasak, P. Szańkowski, P Ziń, M. Trippenbach, and J. Chwedeńczuk. “Cauchy-Schwarz inequality and particle entanglement”. In: *Phys. Rev. A* 90 (3 Sept. 2014), p. 033616.

[109]E. Brambilla, A. Gatti, L. A. Lugiato, and M. I. Kolobov. “Quantum structures in traveling-wave spontaneous parametric down-conversion”. In: *The European Physical Journal D - Atomic, Molecular, Optical and Plasma Physics* 15.1 (July 2001), pp. 127–135.

[110]Tomasz Wasak, Piotr Szańkowski, Marek Trippenbach, and Jan Chwedeńczuk. “Cauchy–Schwarz inequality for general measurements as an entanglement criterion”. In: *Quantum Information Processing* 15.1 (Jan. 2016), pp. 269–278.

[111]Igor V. Volovich. “Cauchy–Schwarz inequality-based criteria for the non-classicality of sub-Poisson and antibunched light”. In: *Physics Letters A* 380.1 (2016), pp. 56–58.

[112]G. S. Agarwal. “Nonclassical statistics of fields in pair coherent states”. In: *J. Opt. Soc. Am. B* 5.9 (Sept. 1988), pp. 1940–1947.

[113]S. Datta. *Electronic Transport in Mesoscopic Systems*. 2nd ed. Cambridge University Press, 1999.

[114]E. Scheer J. C. Cueavas. *Molecular Electronics An Introduction to Theory and Experiment*. 1st ed. New Jersey: World Scientific Publishing Co. Pte. Ltd., 2015.

[115]K. Flensberg H. Bruus. *Many-body quantum theory in condensed matter physics: an introduction*. 2nd ed. Oxford: Oxford University Press, 2006.

[116]F. J. Dyson. “The S Matrix in Quantum Electrodynamics”. In: *Phys. Rev.* 75 (11 June 1949), pp. 1736–1755.

[117]Julian Schwinger. “On the Greens functions of quantized fields. I”. In: *Proceedings of the National Academy of Sciences* 37.7 (1951), pp. 452–455. eprint: `https://www.pnas.org/doi/pdf/10.1073/pnas.37.7.452`.

[118]J. Rammer. *Quantum Field Theory of Non-equilibrium States*. 1st ed. Cambridge: Cambridge University Press, 2007.

[119]J. Schwinger. “Brownian motion of a quantum oscillator”. In: *J. Math. Phys.* 2 (3 1961), p. 407.

[120]L. V. Keldysh. “Diagram technique for nonequilibrium processes”. In: *Zh. Eksp. Teor. Fiz.* 20 (4 Oct. 1965), pp. 1515–1527.

[121]R. P. Feynman. “Space-Time Approach to Quantum Electrodynamics”. In: *Phys. Rev.* 76 (6 Sept. 1949), pp. 769–789.

[122]R. D. Mattuck. *A Guide to Feynman Diagrams in the Many-Body Problem*. 2nd ed. New York, USA: Dover Publications, 1992.

[123]G. Stefanucci R. v. Leeuwen. *Nonequilibrium many-body theory of quantum systems: a modern introduction*. 1st ed. Cambridge: Cambridge University Press, 2013.

[125]J. Kuester and G. Muenster. “Tadpole Summation by Dyson-Schwinger Equations”. In: *arXiv* hep-th/9603145 ().

[126]C. Brouder. “Renormalization of QED in an external field”. In: *arXiv* physics/0202025 ().

[127]Mathias Wagner. “Expansions of nonequilibrium Green’s functions”. In: *Phys. Rev. B* 44 (12 Sept. 1991), pp. 6104–6117.

[128]Antti-Pekka Jauho, Ned S. Wingreen, and Yigal Meir. “Time-dependent transport in interacting and noninteracting resonant-tunneling systems”. In: *Phys. Rev. B* 50 (8 Aug. 1994), pp. 5528–5544.

[129]In contrast, when interdot Coulomb interaction is included, the two levels exhibit an energy splitting renormalization that scales logarithmically with the Coulomb energy, even for the spinless fermion model. This subject was studied in Ref. [130].

[130]Daniel Boese, Walter Hofstetter, and Herbert Schoeller. “Interference and interaction effects in multilevel quantum dots”. In: *Phys. Rev. B* 64 (12 Sept. 2001), p. 125309.

[131]T. V. Shahbazyan and M. E. Raikh. “Two-channel resonant tunneling”. In: *Phys. Rev. B* 49 (24 June 1994), pp. 17123–17129.

[132]B. Kubala and J. König. “Flux-dependent level attraction in double-dot Aharonov-Bohm interferometers”. In: *Phys. Rev. B* 65.24 (Mar. 2002), p. 245301.

[133]Yigal Meir and Ned S. Wingreen. “Landauer formula for the current through an interacting electron region”. In: *Phys. Rev. Lett.* 68 (16 Apr. 1992), pp. 2512–2515.

[134]M Sumetskii. “Modelling of complicated nanometre resonant tunnelling devices with quantum dots”. In: *Journal of Physics: Condensed Matter* 3.16 (Apr. 1991), pp. 2651–2654.

[135]D. Zwillinger, V. Moll, I.S. Gradshteyn, and I.M. Ryzhik. *Table of Integrals, Series, and Products*. 8th ed. Cambridge: Academic Press, 2014.

[136]David C. Langreth. *Linear and Nonlinear Electron Transport in Solids*. Ed. by J. T. Devreese and V. E. van Doren. Boston, MA: Springer US, 1976.

[137]A. Mitra, I. Aleiner, and A. J. Millis. “Phonon effects in molecular transistors: Quantal and classical treatment”. In: *Phys. Rev. B* 69 (24 June 2004), p. 245302.

[138]P. Stadler, W. Belzig, and G. Rastelli. “Ground-State Cooling of a Carbon Nanomechanical Resonator by Spin-Polarized Current”. In: *Phys. Rev. Lett.* 113 (4 July 2014), p. 047201.

[139]Vera Sazonova, Yuval Yaish, Hande Üstünel, et al. “A tunable carbon nanotube electromechanical oscillator”. In: *Nature* 431.7006 (Sept. 2004), pp. 284–287.

[140]A. Eichler, J. Moser, J. Chaste, et al. “Nonlinear damping in mechanical resonators made from carbon nanotubes and graphene”. In: *Nature Nanotechnology* 6.6 (June 2011), pp. 339–342.

[141]J. Scott Bunch, Arend M. van der Zande, Scott S. Verbridge, et al. “Electromechanical Resonators from Graphene Sheets”. In: *Science* 315.5811 (2007), pp. 490–493. eprint: https://www.science.org/doi/pdf/10.1126/science.1136836.

[142]Xianghui Zhang, Reimar Waitz, Fan Yang, et al. “Vibrational modes of ultrathin carbon nanomembrane mechanical resonators”. In: *Applied Physics Letters* 106.6 (2015), p. 063107. eprint: https://doi.org/10.1063/1.4908058.

[143]I. Mahboob and H. Yamaguchi. “Bit storage and bit flip operations in an electromechanical oscillator”. In: *Nature Nanotechnology* 3.5 (May 2008), pp. 275–279.

[144]D. Rugar and P. Grütter. “Mechanical parametric amplification and thermomechanical noise squeezing”. In: *Phys. Rev. Lett.* 67 (6 Aug. 1991), pp. 699–702.

[145]Anina Leuch, Luca Papariello, Oded Zilberberg, et al. “Parametric Symmetry Breaking in a Nonlinear Resonator”. In: *Phys. Rev. Lett.* 117 (21 Nov. 2016), p. 214101.

[146]James M.L. Miller, Dongsuk D. Shin, Hyun-Keun Kwon, Steven W. Shaw, and Thomas W. Kenny. “Phase Control of Self-Excited Parametric Resonators”. In: *Phys. Rev. Applied* 12 (4 Oct. 2019), p. 044053.

[147]Maximilian J. Seitner, Mehdi Abdi, Alessandro Ridolfo, Michael J. Hartmann, and Eva M. Weig. “Parametric Oscillation, Frequency Mixing, and Injection Locking of Strongly Coupled Nanomechanical Resonator Modes”. In: *Phys. Rev. Lett.* 118 (25 June 2017), p. 254301.

[148]S. Houri, D. Hatanaka, M. Asano, and H. Yamaguchi. “Demonstration of Multiple Internal Resonances in a Microelectromechanical Self-Sustained Oscillator”. In: *Phys. Rev. Applied* 13 (1 Jan. 2020), p. 014049.

[149]David A. Czaplewski, Changyao Chen, Daniel Lopez, et al. “Bifurcation Generated Mechanical Frequency Comb”. In: *Phys. Rev. Lett.* 121 (24 Dec. 2018), p. 244302.

[150]David A. Czaplewski, Scott Strachan, Oriel Shoshani, Steven W. Shaw, and Daniel López. “Bifurcation diagram and dynamic response of a MEMS resonator with a 1:3 internal resonance”. In: *Applied Physics Letters* 114.25 (2019), p. 254104. eprint: https://doi.org/10.1063/1.5099459.

[151]S. Houri, D. Hatanaka, M. Asano, R. Ohta, and H. Yamaguchi. “Limit cycles and bifurcations in a nonlinear MEMS resonator with a 1:3 internal resonance”. In: *Applied Physics Letters* 114.10 (2019), p. 103103. eprint: https://doi.org/10.1063/1.5085219.

[152]Yukihiro Tadokoro, Hiroya Tanaka, and M. I. Dykman. “Driven nonlinear nanomechanical resonators as digital signal detectors”. In: *Scientific Reports* 8.1 (July 2018), p. 11284.

[153]Behrouz Arash, Jin-Wu Jiang, and Timon Rabczuk. “A review on nanomechanical resonators and their applications in sensors and molecular transportation”. In: *Applied Physics Reviews* 2.2 (2015), p. 021301. eprint: https://doi.org/10.1063/1.4916728.

[154]Vadim Puller, Brahim Lounis, and Fabio Pistolesi. “Single Molecule Detection of Nanomechanical Motion”. In: *Phys. Rev. Lett.* 110 (12 Mar. 2013), p. 125501.

[155]Lei Li, Hanbiao Liu, Mingyu Shao, and Chicheng Ma. “A Novel Frequency Stabilization Approach for Mass Detection in Nonlinear Mechanically Coupled Resonant Sensors”. In: *Micromachines* 12.2 (2021).

[156]M. Selim Hanay, Scott I. Kelber, Cathal D. O’Connell, et al. “Inertial imaging with nanomechanical systems”. In: *Nature Nanotechnology* 10.4 (Apr. 2015), pp. 339–344.

[157]H. Kim, J. Park, Z. Aksamija, M. Arbulu, and R. H. Blick. “Ultrananocrystalline Diamond Membranes for Detection of High-Mass Proteins”. In: *Phys. Rev. Applied* 6 (6 Dec. 2016), p. 064031.

[158]Jonghoo Park, Zlatan Aksamija, Hyun-Cheol Shin, Hyunseok Kim, and Robert H. Blick. “Phonon-Assisted Field Emission in Silicon Nanomembranes for Time-of-Flight Mass Spectrometry of Proteins”. In: *Nano Letters* 13.6 (2013). PMID: 23621694, pp. 2698–2703. eprint: `https://doi.org/10.1021/nl400873m`.

[159]Ya Zhang, Ryoka Kondo, Boqi Qiu, Xin Liu, and Kazuhiko Hirakawa. “Giant Enhancement in the Thermal Responsivity of Microelectromechanical Resonators by Internal Mode Coupling”. In: *Phys. Rev. Applied* 14 (1 July 2020), p. 014019.

[160]R. B. Karabalin, Ron Lifshitz, M. C. Cross, et al. “Signal Amplification by Sensitive Control of Bifurcation Topology”. In: *Phys. Rev. Lett.* 106 (9 Feb. 2011), p. 094102.

[161]P. Weber, J. Güttinger, A. Noury, J. Vergara-Cruz, and A. Bachtold. “Force sensitivity of multilayer graphene optomechanical devices”. In: *Nature Communications* 7.1 (Aug. 2016), p. 12496.

[162]S. L. de Bonis, C. Urgell, W. Yang, et al. “Ultrasensitive Displacement Noise Measurement of Carbon Nanotube Mechanical Resonators”. In: *Nano Letters* 18.8 (2018). PMID: 30062893, pp. 5324–5328. eprint: `https://doi.org/10.1021/acs.nanolett.8b02437`.

[163]Avishek Chowdhury, Marcel G. Clerc, Sylvain Barbay, Isabelle Robert-Philip, and Remy Braive. “Weak signal enhancement by nonlinear resonance control in a forced nano-electromechanical resonator”. In: *Nature Communications* 11.1 (May 2020), p. 2400.

[164]J. S. Huber, G. Rastelli, M. J. Seitner, et al. “Spectral Evidence of Squeezing of a Weakly Damped Driven Nanomechanical Mode”. In: *Phys. Rev. X* 10 (2 June 2020), p. 021066.

[165]Luca Papariello, Oded Zilberberg, Alexander Eichler, and R. Chitra. “Ultrasensitive hysteretic force sensing with parametric nonlinear oscillators”. In: *Phys. Rev. E* 94 (2 Aug. 2016), p. 022201.

[166]J. Moser, J. Güttinger, A. Eichler, et al. “Ultrasensitive force detection with a nanotube mechanical resonator”. In: *Nature Nanotechnology* 8.7 (July 2013), pp. 493–496.

[167]Yukihiro Tadokoro and Hiroya Tanaka. “Highly Sensitive Implementation of Logic Gates with a Nonlinear Nanomechanical Resonator”. In: *Phys. Rev. Applied* 15 (2 Feb. 2021), p. 024058.

[168]Diego N. Guerra, Adi R. Bulsara, William L. Ditto, et al. “A Noise-Assisted Reprogrammable Nanomechanical Logic Gate”. In: *Nano Letters* 10.4 (2010). PMID: 20218630, pp. 1168–1171. eprint: `https://doi.org/10.1021/nl9034175`.

[169]Yu Jia, Sijun Du, and Ashwin A Seshia. “Twenty-Eight Orders of Parametric Resonance in a Microelectromechanical Device for Multi-band Vibration Energy Harvesting”. In: *Scientific Reports* 6.1 (July 2016), p. 30167.

[170] Stephan Camerer, Maria Korppi, Andreas Jöckel, et al. “Realization of an Optomechanical Interface Between Ultracold Atoms and a Membrane”. In: *Phys. Rev. Lett.* 107 (22 Nov. 2011), p. 223001.

[171] Andreas Jöckel, Aline Faber, Tobias Kampschulte, et al. “Sympathetic cooling of a membrane oscillator in a hybrid mechanical–atomic system”. In: *Nature Nanotechnology* 10.1 (Jan. 2015), pp. 55–59.

[172] Thomas M. Karg, Baptiste Gouraud, Chun Tat Ngai, et al. “Light-mediated strong coupling between a mechanical oscillator and atomic spins 1 meter apart”. In: *Science* 369.6500 (2020), pp. 174–179. eprint: `https://www.science.org/doi/pdf/10.1126/science.abb0328`.

[173] Markus Aspelmeyer, Tobias J. Kippenberg, and Florian Marquardt. “Cavity optomechanics”. In: *Rev. Mod. Phys.* 86 (4 Dec. 2014), pp. 1391–1452.

[174] J. C. Sankey, C. Yang, B. M. Zwickl, A. M. Jayich, and J. G. E. Harris. “Strong and tunable nonlinear optomechanical coupling in a low-loss system”. In: *Nature Physics* 6.9 (Sept. 2010), pp. 707–712.

[175] N. S. Kampel, R. W. Peterson, R. Fischer, et al. “Improving Broadband Displacement Detection with Quantum Correlations”. In: *Phys. Rev. X* 7 (2 Apr. 2017), p. 021008.

[176] T. P. Purdy, R. W. Peterson, and C. A. Regal. “Observation of Radiation Pressure Shot Noise on a Macroscopic Object”. In: *Science* 339.6121 (2013), pp. 801–804. eprint: `https://www.science.org/doi/pdf/10.1126/science.1231282`.

[177] R. W. Andrews, R. W. Peterson, T. P. Purdy, et al. “Bidirectional and efficient conversion between microwave and optical light”. In: *Nature Physics* 10.4 (Apr. 2014), pp. 321–326.

[178] Adarsh Ganesan, Cuong Do, and Ashwin Seshia. “Phononic Frequency Comb via Intrinsic Three-Wave Mixing”. In: *Phys. Rev. Lett.* 118 (3 Jan. 2017), p. 033903.

[179] Adarsh Ganesan, Cuong Do, and Ashwin Seshia. “Excitation of coupled phononic frequency combs via two-mode parametric three-wave mixing”. In: *Phys. Rev. B* 97 (1 Jan. 2018), p. 014302.

[180] H. J. R. Westra, M. Poot, H. S. J. van der Zant, and W. J. Venstra. “Nonlinear Modal Interactions in Clamped-Clamped Mechanical Resonators”. In: *Phys. Rev. Lett.* 105 (11 Sept. 2010), p. 117205.

[181] Dario Antonio, Damián H. Zanette, and Daniel López. “Frequency stabilization in nonlinear micromechanical oscillators”. In: *Nature Communications* 3.1 (May 2012), p. 806.

[182] O. Shoshani, S. W. Shaw, and M. I. Dykman. “Anomalous Decay of Nanomechanical Modes Going Through Nonlinear Resonance”. In: *Scientific Reports* 7.1 (Dec. 2017), p. 18091.

[183] Sungwan Cho, Sung Un Cho, Myunglae Jo, et al. “Strong Two-Mode Parametric Interaction and Amplification in a Nanomechanical Resonator”. In: *Phys. Rev. Applied* 9 (6 June 2018), p. 064023.

[184] C van der Avoort, R van der Hout, J J M Bontemps, et al. “Amplitude saturation of MEMS resonators explained by autoparametric resonance”. In: *Journal of Micromechanics and Microengineering* 20.10 (Sept. 2010), p. 105012.

[185]Johannes Güttinger, Adrien Noury, Peter Weber, et al. “Energy-dependent path of dissipation in nanomechanical resonators”. In: *Nature Nanotechnology* 12.7 (July 2017), pp. 631–636.

[186]Changyao Chen, Damián H. Zanette, David A. Czaplewski, Steven Shaw, and Daniel López. “Direct observation of coherent energy transfer in nonlinear micromechanical oscillators”. In: *Nature Communications* 8.1 (May 2017), p. 15523.

[187]Wenyao Luo, Naikun Gao, and Duo Liu. “Multimode Nonlinear Coupling Induced by Internal Resonance in a Microcantilever Resonator”. In: *Nano Letters* 21.2 (2021). PMID: 33443433, pp. 1062–1067. eprint: `https://doi.org/10.1021/acs.nanolett.0c04301`.

[188]A. Eichler, M. del Álamo Ruiz, J. A. Plaza, and A. Bachtold. “Strong Coupling between Mechanical Modes in a Nanotube Resonator”. In: *Phys. Rev. Lett.* 109 (2 July 2012), p. 025503.

[189]a. H. Nayfeh and D. T. Mook. *Nonlinear Oscillations*. 2nd ed. Weinheim: WILEY-VCH Verlag, 1995.

[190]M. Lewenstein, Ph. Balcou, M. Yu. Ivanov, Anne L’Huillier, and P. B. Corkum. “Theory of high-harmonic generation by low-frequency laser fields”. In: *Phys. Rev. A* 49 (3 Mar. 1994), pp. 2117–2132.

[191]P. A. Franken, A. E. Hill, C. W. Peters, and G. Weinreich. “Generation of Optical Harmonics”. In: *Phys. Rev. Lett.* 7 (4 Aug. 1961), pp. 118–119.

[192]J. A. Armstrong, N. Bloembergen, J. Ducuing, and P. S. Pershan. “Interactions between Light Waves in a Nonlinear Dielectric”. In: *Phys. Rev.* 127 (6 Sept. 1962), pp. 1918–1939.

[193]M. Dykman. *Fluctuating nonlinear oscillators : from nanomechanics to quantum superconducting circuits*. 1st ed. Oxford: Oxford University Press, 2012.

[194]G. Duffing. *Erzwungene Schwingungen bei veränderlicher Eigenfrequenz und ihre technische BBedeutung*. 1st ed. Braunschweig: F. Vieweg and Sohn, 1918.

[195]Émile Mathieu. “Mémoire sur le mouvement vibratoire d’une membrane de forme elliptique.” fre. In: *Journal de Mathématiques Pures et Appliquées* 13 (1868), pp. 137–203.

[196]G. Floquet. “Sur les équations différentielles linéaires à coefficients périodiques”. fr. In: *Annales scientifiques de l’École Normale Supérieure* 2e série, 12 (1883), pp. 47–88.

[197]Eugene I. Butikov. “Analytical expressions for stability regions in the Ince–Strutt diagram of Mathieu equation”. In: *American Journal of Physics* 86.4 (2018), pp. 257–267. eprint: `https://doi.org/10.1119/1.5021895`.

[198]S. H. Strogatz. *NONLINEAR DYNAMICS AND CHAOS*. 1st ed. Cambridge: Westview Press, 2004.

[199]Fan Yang, Felicitas Hellbach, Felix Rochau, et al. “Persistent Response in an Ultrastrongly Driven Mechanical Membrane Resonator”. In: *Phys. Rev. Lett.* 127 (1 July 2021), p. 014304.

[200]Fan Yang, Felicitas Hellbach, Felix Rochau, et al. “Suplemental Material for Persistent Response in an Ultrastrongly Driven Mechanical Membrane Resonator”. In: *Phys. Rev. Lett.* 127 (1 July 2021), p. 014304.

[201]Fan Yang, Felix Rochau, Jana S. Huber, et al. “Spatial Modulation of Nonlinear Flexural Vibrations of Membrane Resonators”. In: *Phys. Rev. Lett.* 122 (15 Apr. 2019), p. 154301.

[202]R. HANBURY BROWN and R. Q. TWISS. “Correlation between Photons in two Coherent Beams of Light”. In: *Nature* 177.4497 (Jan. 1956), pp. 27–29.

[203]Roy J. Glauber. “Photon Correlations”. In: *Phys. Rev. Lett.* 10 (3 Feb. 1963), pp. 84–86.

[204]L. Mandel and E. Wolf. “Correlation in the Fluctuating Outputs from Two Square-Law Detectors Illuminated by Light of Any State of Coherence and Polarization”. In: *Phys. Rev.* 124 (6 Dec. 1961), pp. 1696–1702.

[205]L Mandel. “Fluctuations of Photon Beams and their Correlations”. In: *Proceedings of the Physical Society* 72.6 (Dec. 1958), pp. 1037–1048.

[206]L Mandel. “Fluctuations of Photon Beams: The Distribution of the Photo-Electrons”. In: *Proceedings of the Physical Society* 74.3 (Sept. 1959), pp. 233–243.

[207]Horace P. Yuen. “Multimode two-photon coherent states and unitary representation of the symplectic group”. In: *Nuclear Physics B - Proceedings Supplements* 6 (1989), pp. 309–313.

[208]Roy J. Glauber. “Coherent and Incoherent States of the Radiation Field”. In: *Phys. Rev.* 131 (6 Sept. 1963), pp. 2766–2788.

[209]Horace P. Yuen. “Two-photon coherent states of the radiation field”. In: *Phys. Rev. A* 13 (6 June 1976), pp. 2226–2243.

[210]R. E. Slusher, L. W. Hollberg, B. Yurke, J. C. Mertz, and J. F. Valley. “Observation of Squeezed States Generated by Four-Wave Mixing in an Optical Cavity”. In: *Phys. Rev. Lett.* 55 (22 Nov. 1985), pp. 2409–2412.

[211]Y. Yamamoto, S. Machida, and O. Nilsson. “Amplitude squeezing in a pump-noise-suppressed laser oscillator”. In: *Phys. Rev. A* 34 (5 Nov. 1986), pp. 4025–4042.

[212]Roy S. Bondurant and Jeffrey H. Shapiro. “Squeezed states in phase-sensing interferometers”. In: *Phys. Rev. D* 30 (12 Dec. 1984), pp. 2548–2556.

[213]E. S. Polzik, J. Carri, and H. J. Kimble. “Spectroscopy with squeezed light”. In: *Phys. Rev. Lett.* 68 (20 May 1992), pp. 3020–3023.

[214]J. Aasi, J. Abadie, B. P. Abbott, et al. “Enhanced sensitivity of the LIGO gravitational wave detector by using squeezed states of light”. In: *Nature Photonics* 7.8 (Aug. 2013), pp. 613–619.

[215]A. A. Reynoso, G. Usaj, D. L. Chafatinos, et al. “Optomechanical parametric oscillation of a quantum light-fluid lattice”. In: *Phys. Rev. B* 105 (19 May 2022), p. 195310.

[216]Michael Saur, *Nonlinear interacting quantum Duffing resonators* (2020), submitted to obtain the degree Bachelor of Science (B.Sc.).

[217]J. S. Huber, G. Rastelli, M. J. Seitner, et al. “Supplemental Material: Spectral Evidence of Squeezing of a Weakly Damped Driven Nanomechanical Mode”. In: *Phys. Rev. X* 10 (2 June 2020), p. 021066.

Webpages

[@124]*'Diagramology' Types of Feynman Diagram*. 2018. URL: https://www.imperial.ac.uk/media/imperial-college/research-centres-and-groups/theoretical-physics/msc/current/qft/handouts/qftdiagramtypes.pdf.